Etude des mécanismes d'oxydation et de frittage de poudres de silicium en vue d'applications photovoltaïques

Jean-Marie Lebrun

▶ To cite this version:

UNIVERSITÉ DE GRENOBLE

THÈSE

Pour obtenir le grade de

DOCTEUR DE L'UNIVERSITÉ DE GRENOBLE

Spécialité : **Matériaux, Mécanique, Génie Civil, Electrochimie**

Arrêté ministériel : 7 août 2006

Présentée par

Jean-Marie LEBRUN

Thèse dirigée par **Jean-Michel MISSIAEN** et
co-dirigée par **Céline PASCAL**

préparée au sein du **Laboratoire SIMaP**
dans **l'École Doctorale IMEP²**

Etude des mécanismes d'oxydation et de frittage de poudres de silicium en vue d'applications photovoltaïques

Thèse soutenue publiquement le **24 Octobre 2012**
devant le jury composé de :

M. Alexis DESCHAMPS
Professeur à Grenoble INP, Président
M. Raj BORDIA
Professeur à l'Université de Washington, Rapporteur
Mme Michèle PIJOLAT
Professeur à l'ENS des Mines de St Etienne, Rapporteur
M. Jean-Michel MISSIAEN
Professeur à Grenoble INP, Directeur de thèse
Mme Céline PASCAL
Maître de conférences à l'UJF, Co-Directeur de thèse
M. Alain STRABONI
Directeur de l'entreprise S'Tile à Poitiers, Examinateur
M. Gilbert FANTOZZI
Professeur Emérite à l'INSA de Lyon, Examinateur
M. Jean-Paul GARANDET
Ingénieur Chercheur à INES, Chambéry, Co-Encadrant de thèse

Remerciements

T out débuta un jour de Juillet 2009, un transfuge du CEA venait de me convaincre de réaliser une thèse dans un laboratoire de recherche académique, le SIMaP. Dès le lendemain, je partais à la rencontre de ceux avec qui j'allais partager trois ans d'une vie professionnelle et amicale !

Alors que je franchissais l'entrée du bâtiment Thermo, la vision des murs défraichis retint d'abord mon attention. Cette vision ne tarda pas à s'affirmer comme l'image d'une ambition devenue singulière : celle de concentrer des moyens à la pratique d'une recherche scientifique de qualité, dans la plus grande simplicité.

Je commençai par rencontrer mes deux encadrant de thèse, Jean-Michel et Céline, avec qui j'allais partager des réunions régulières, toujours pleines de rigueur scientifique mais aussi d'humour, moins scientifique celui-là. Merci à eux donc, à leur patience et leurs conseils qui m'ont été indispensables pour en arriver là.

Ces réunions étaient aussi l'occasion d'en préparer de nouvelles, avec l'ensemble des partenaires de la thèse. Nos agents du CEA, qui auront su se rendre disponibles et participer à ma formation. Jean-Paul, dit le transfuge, qui n'aurait surtout pas manqué de breveter la roue s'il était né en 3500 av. JC. Florence, ensuite, qui eu la chance en même temps que moi de saisir tout l'intérêt de ces fameux « diagrammes d'Ashby ». Cyril, enfin, qui n'était jamais avare d'une idée sur le comportement de cette fameuse couche de silice ! Nos collègues de l'INSA de Lyon, aussi, dont les portes étaient toujours ouvertes pour une manip. Guillaume Bonnefont pour du SPS, ou encore Vincent Garnier pour du HIP. Gilbert Fantozzi quant à lui ne manquait jamais d'aborder une difficulté scientifique, de la plus haute importance !

L'encadrement fut donc complet, les idées et conseils nombreux. Heureusement, le laboratoire recèle de nombreuses personnes très compétentes avec qui j'ai pu confronter nos belles idées aux dures réalités de la Physique. Parmi eux, Nikos Eustathopoulos, qui le premier a su nous mettre sur la piste de Carl Wagner, co-disciple de Jean Besson (un ancien chercheur bien de chez nous !). Raphaël Boichot, grâce à qui notre modèle de transport de matière, initialement écrit en coordonnées cylindriques, passa du jour au lendemain en coordonnées cartésiennes. Détail diront certains, mais tout de même… Mais c'est surtout en frittage que les besoins se sont fait ressentir et en la matière les protagonistes ne manquent pas. Jean-Michel d'abord, avec qui je passai tant et tant de temps à comprendre l'origine de ces fameux deux pics (merci pour ta persévérance !). Céline ensuite, pour qui le modèle de la cacahouète® n'a plus aucun secret. Jean-Marc aussi, qui lorsqu'il s'agit de parler cinétique est peut être le premier à aller consulter. Paul, qui malheureusement n'a jamais été vraiment convaincu par les diagrammes d'Ashby. Sabine, toujours prête pour une observation MET. Christophe, avec qui il faudra un jour que je fasse du dp3d. Didier, qui lui m'a convaincu qu'un modèle, surtout quand c'est du Monte-Carlo, c'est avant tout fait pour publier ! Merci enfin à tous les séminaristes du GPM2, toujours à l'affût de la bonne question !

Les idées, une fois passées sous le regard des scientifiques, et brevetées par le CEA, devaient alors être confrontées à l'expérience ! C'est alors que les choses se gâtaient presque toujours… même pour les blonds, enfin surtout pour blondie… le service technique rentrait alors dans la bataille ! Jean-Jacques a toujours su me dégoter la bonne pièce au bon moment. Quant à Alain et Charles, ils m'ont prouvé par la pratique qu'une ATG et un dilato se déménagent sans encombre dans un kangoo ! Michel D. et Guy étaient nos fournisseurs officiels de céramiques et verres en tous genres et surtout à façon. Michel B. reste le compacteur de poudre le plus efficace (sans masque s'il vous plaît) et Lionel le M. granulomètre du CEA. Toute ma reconnaissance aussi à ma voisine Magali, alias la « Feffe » des tech du SIMaP. Je note aussi qu'il était souvent nécessaire d'acheter une pièce manquante, auprès des gestionnaires, toujours disponibles pour nous aider. Merci donc à Nathalie, Claire, Claude et Jacqueline (c'est quand qu'on se fait un pamplemousse ?).

Malheureusement cela n'a pas empêché quelques ratés expérimentaux… dans ces situations rien ne pouvait remplacer un rafraichissement à EVE ou la Bobine, ou encore une partie de tarot autour de collègues bien souvent dans la même situation que vous. Merci donc à tous les doctorants et post-doctorants que j'ai côtoyé au cours ce ces trois ans. Je commence d'abord par présenter mes plus plates excuses à mes collègues de bureau (successifs) qui ont dû supporter les embardées parfois surprenantes, toujours surprenantes en fait, d'un « faux calme ». Je pense à Coco, ma première collègue de bureau, qui comme moi parle toute seule, à Aurélie, que j'ai rejoint avec **Audrey** et

Philippe au bureau 109, à **<u>Mathilde</u>** (et ses gâteaux), Thibault, Assuczena et Nathalia que nous avons rejoint en salle verte au GPM2, puis à Clairette (et son plaid), Ismaël et Milan que j'ai fini par rejoindre à SIR. Viennent ensuite ceux qui ont eu la chance de ne pas partager mon bureau, en Thermo d'abord, là où tout a commencé. Je pense aux anciens, Jean-Joël, Sylvain, Céline, Benjamin, Oussama (un couscous ?), Coraline, Benoit, Jean-Philippe (un café ?) et Sébastien (mon acolyte sur le silicium) qui nous ont initiés à la tradition, qui perdure toujours, du tarot. Merci aussi aux contemporains. Guilhem notamment, que je retrouvais chaque lundi matin quelque peu affecté par son dernier match de rugby (aïe, aïe !). Thomas, mon partenaire de via ferrata et d'escalade, Quentin, sans qui mon pot de thèse aurait été sans alcool, et Jean et Natasha, nos post-docs modèles ! Je remercie aussi les plus jeunes, Fanny et Nicolas, mes compagnons de course à pied, Laurent et ses biscuits au pain d'épices et enfin Eva et Olivier. Passons ensuite au GPM2 et aux doctorants des salles bleue et blanche : Lionel (c'est moi qui ai la clef de la plateforme !), Achraf, Denis, Zi Lin, Jérémy, Magali, Pavel, Benjamin et Edouard (pas mal le Fuji, hein ?). Une petite dédicace enfin à Tahiti Bob et son EBM. Vient enfin le bâtiment Recherche et Maelig, Nicolas, Julien, Adrien Maxime et Lulu (Gigi pense bien à toi !). Une pensée enfin pour les stagiaires, Thomas, Victor, Adel avec qui j'ai passé de très bons moments.

Je remercie aussi le jury de thèse pour avoir lu et critiqué ce travail. Le président du jury, Alexis Deschamps, les rapporteurs, Michèle Pijolat et Raj Bordia et les examinateurs, Alain Straboni et Gilbert Fantozzi.

Sur un plan plus personnel, je suis très reconnaissant envers ma famille et mes amis qui m'ont toujours soutenu.

<div align="right">Jean-Jean.</div>

Table of contents

Chapter V.   Silicon sintering processes towards photovoltaic applications
201

Appendix C.   Initial sintering stage equations   *269*

C.1   **Geometrical assumptions**   **269**

C.2   **Sintering mechanism kinetic equations**   **271**

List of symbols

Symbol	Unit	Description
a	m	Particle radius
A	m²	Atomic flux surface area
c	-	Correlation factor
c_i	m	Polyhedron diagonal length of angular particles
C_j	mol m^{-3}	Concentration of the specie j
CTE_j	°C^{-1}	Coefficient of Thermal Expansion of the material j
d_j	m	Molecular diameter of the specie j
D	m² s^{-1}	Carrier diffusion coefficient
D_j	m² s^{-1}	Diffusion coefficient of the specie j
D_j^{eff}	m² s^{-1}	Effective diffusion coefficient of the specie j
D_j^{mol}	m² s^{-1}	Molecular diffusion coefficient of the specie j in the gas phase
$D_j^{Knudsen}$	m² s^{-1}	Knudsen diffusion coefficient of the specie j in the gas phase
D_j^{out}	m² s^{-1}	Diffusion coefficient of the specie j outside the compact

| D_j^{in} | m² s⁻¹ | Diffusion coefficient of the specie j inside the compact |

D_j^{in} m² s⁻¹   Diffusion coefficient of the specie j inside the compact

$D_j^{gb} = D_j^{gb,S}$ m² s⁻¹   Grain boundary diffusion coefficient in the solid S

$D_j^{l} = D_j^{l,S}$ m² s⁻¹   Lattice diffusion coefficient in the solid S

$D_j^{s} = D_j^{s,S}$ m² s⁻¹   Surface diffusion coefficient at the surface of the solid S

e_{SiO_2} nm   Silica layer thickness

E_a KJ mol⁻¹   Activation energy

$f(\omega)$ -   Geometrical factor for heterogeneous nucleation

F_j m   Characteristic length $= \dfrac{\gamma^{s\text{-}v}\Omega_j}{RT}$ (typically of magnitude 1×10^{-8} m)

G m   Grain size

h m   Height of the powder compact

i m   Interpenetration (or rapprochement) parameter

j_j mol m⁻² s⁻¹   Molar flux of the specie j

j_j^{out} mol m⁻² s⁻¹   Molar flux of the specie j outside the compact

j_j^{in} mol m⁻² s⁻¹   Molar flux of the specie j inside the compact

k_B J K⁻¹   Boltzmann constant

K_n -   Equilibrium constant of the reaction R_n

l m   Jumping length

l_p m   Length of the cylindrical pore

L m   Carrier diffusion length

m_j	g	Mass content of the specie j
m^{loss}	g	Mass loss in thermogravimetric analysis
m^{gain}	g	Mass gain in thermogravimetric analysis
M_j	g mol^{-1}	Molar mass of the specie j
n	-	Shape factor
n_c	-	Coordination number
N_A	mol^{-1}	Avogadro's number
p	-	Volume fraction of pores in the powder compact
P	Pa	Total pressure
P°	Pa	Standard pressure (~1 atm)
P_j	Pa	Partial pressure of the specie j
P_j^0	Pa	Solid vapor equilibrium partial pressure of the specie j
$P_j^{R_n}$	Pa	Equilibrium partial pressure of the specie j from the reaction R_n
P_j^z	Pa	Partial of the specie j at a given position z
$P_{H_2O}^{z_f}$	Pa	Water vapor partial pressure at the z_f position (diffusion length)
$P_{H_2O}^{z_f*}$	Pa	Critical water vapor pressure to be controlled at the z_f position (diffusion length) in order to stabilize the silica layer
$P_{H_2O}^{Probe}$	Pa	Water vapor partial pressure at the probe position, in the incoming gas flux
$P_{H_2O}^{Probe*}$	Pa	Critical water vapor pressure to be controlled in the incoming gas flux in order to stabilize the silica layer

Q	l h^{-1}	Volume gas flux
r	m	Radial position inside the powder compact
r_c	m	Powder compact radius
r_r	m	Radial reaction front position in the powder compact
r_g	m	Grain coarsening front position in the compact
R	J K^{-1} mol^{-1}	Gas constant
R$_n$	-	Chemical reaction
S^{tube}	m²	Furnace tube section
S^{out}	m²	Section of the flux outside the powder compact (twice the furnace tube section)
S^{in}	m²	Section of the entrance flux inside the powder compact (cylinder compact surface)
SD_j	$\%TD_j$	Sample density made of specie j
t	s	Time
T	°C	Temperature
T^S	°C	Sintering temperature
$T_{pyrometer}$	°C	Pyrometer temperature in SPS
$T_{A\rightarrow P}^{W}$	°C	Temperature of the active to passive transition as defined by Wagner [Wag58], the silicon surface being free of silica
$T_{P\rightarrow A}^{W}$	°C	Temperature of the passive to active transition as defined by Wagner [Wag58], the silicon surface being covered by passive layer of silica
$T_{A\rightarrow P}^{Wm}$	°C	Temperature at which the mass loss rate should be nil during the active to passive transition as defined by Wagner [Wag58]

$T_{P\rightarrow A}^{Wm}$	°C	Temperature at which the mass loss rate should be nil during the passive to active transition as defined by Wagner [Wag58]
T^{*}	°C	Transition temperature at which the molar flux of water equals the molar flux of silicon monoxide
$T_{A\rightarrow P}^{*}$	°C	Temperature at which the molar flux of water equals the molar flux of silicon monoxide during the active to passive transition
$T_{P\rightarrow A}^{*}$	°C	Temperature at which the molar flux of water equals the molar flux of silicon monoxide during the passive to active transition
T^{*m}	°C	Temperature at which the mass loss rate is nil, *i.e.* the mass flux of water equals the mass flux of silicon monoxide
$T_{A\rightarrow P}^{*m}$	°C	Temperature at which the mass loss rate is nil during the active to passive transition
$T_{P\rightarrow A}^{*m}$	°C	Temperature at which the mass loss rate is nil during the passive to active transition
TD_{j}	g cm^{-3}	Theoretical density of the specie j
V_{i}	m^{3}	Particle volume
V_{j}	mol m^{-3} s^{-1}	Rate of volume production of molecules j
V_{p}	m^{3}	Volume of the pore cylinders
V_{t}	m^{3}	Volume of the tetrakaidecahedron
x	m	Neck radius
$\dot{x}$	m s^{-1}	Neck growth rate
z	m	Height in the furnace (origin at the center position of the sample)
z_{f}	m	Uniform temperature height in the furnace
α	-	Sticking coefficient

β	-	Supersaturation coefficient
γ^{SV}	J m^{-2}	Solid vapor energy
$\gamma^{S_1 S_2}$	J m^{-2}	Interfacial energy between the solid S$_1$ and the solid S$_2$
$\delta^{gb} = \delta^{gb,S}$	m	Grain boundary thickness of the solid S
$\delta^{s} = \delta^{s,S}$	m	Surface layer thickness of the solid S
ΔG_f	J	Free energy for the formation of the defect (vacancy)
ΔG_m	J	Free energy for the defect (vacancy) migration
ΔV_f	m^3	Volume variation due to the formation of the defect (vacancy)
ΔV_m	m^3	Volume variation due to the migration of the defect (vacancy)
ΔP	Pa	Pressure drop due to the presence of tensile stresses in the silica layer
ε_j	J	Lennard-Jones energy parameter
Φ	-	Surface area fraction of holes in the silica layer at the particle surface
θ	°	Angle between two contacting spheres
κ	m^{-1}	Curvature difference
κ_d	m^{-1}	Curvature difference for densifying mechanisms
κ_{nd}	m^{-1}	Curvature difference for non-densifying mechanisms
λ_j	m	Mean molecular free path
ν	s^{-1}	Atomic frequency vibration
ρ	m	Radius of curvature
ρ_d	m	Radius of curvature for densifying mechanisms

ρ_{nd}	m	Radius of curvature for non-densifying mechanisms
ρ_p	m	Radius of the cylindrical pores
σ_j	Å	Lennard-Jones collison diameter
τ	-	Tortuosity
l	s	Carrier lifetime
μ_j	J mol^{-1}	Chemical potential
υ_j	m s^{-1}	Mean molecular speed
ω	°	Equilibrium contact angle
$\Omega_j = \Omega_j^S$	m^3 mol^{-1}	Molar volume of the solid specie j
Ω_j^V	m^3 mol^{-1}	Molar volume of the vapor specie j
ζ_j	mol m^{-2} s^{-1}	Wall collision frequency
Ψ_e	°	Equilibrium dihedral angle
Z	-	Number of neighboring atoms

Résumé étendu en Français

Introduction

L e rayonnement solaire est la ressource énergétique la plus abondante sur terre. Chaque année, notre planète reçoit dix fois plus d'énergie depuis le soleil que celle qui pourrait y être produite de part l'utilisation de l'ensemble des ressources non renouvelables, fossiles et fissiles, disponibles.

La conversion photovoltaïque permet de récupérer une partie de cette énergie, sous forme d'électricité, qui peut alors être produite localement. Cependant, cette production locale n'est pas continue et nécessite l'utilisation de moyens de stockage performants, dans les zones non connectées au réseau conventionnel ou la mise en place de réseaux dit « intelligents », dans les zones connectées.

L'industrie photovoltaïque (PV) connaît une croissance exponentielle. Si aux premiers jours de cette industrie, plus d'énergie était nécessaire à la réalisation d'un panneau qu'il ne pouvait en produire au cours de sa vie, un module est aujourd'hui rentabilisé énergétiquement en deux à trois ans, selon le lieu d'utilisation. Comparativement, la durée de vie d'un panneau est aujourd'hui supérieure à 25 ans, au moins pour ce qui concerne la technologie dite sur silicium cristallin (c-Si).

Cette technologie domine l'industrie PV (Figure 1). Largement basée sur des rebuts et procédés issus de l'industrie microélectronique jusque dans les années 2000, cette filière est aujourd'hui indépendante. Depuis lors, la multiplication des moyens de production du silicium dans les pays en voie de développement (essentiellement la Chine), ont permis de réduire les coûts de production des plaquettes de silicium, qui représentent environ la moitié des coûts de production d'un module. L'autre moitié est liée aux procédés d'élaboration de la cellule en salle blanche et à l'encapsulation de ces cellules en panneaux solaires. Les améliorations apportées à ces procédés, ont elles aussi participé à la diminution des coûts de

production de l'électricité photovoltaïque qui s'établissent aux alentours de 2 €/Wc[1] pour cette technologie.
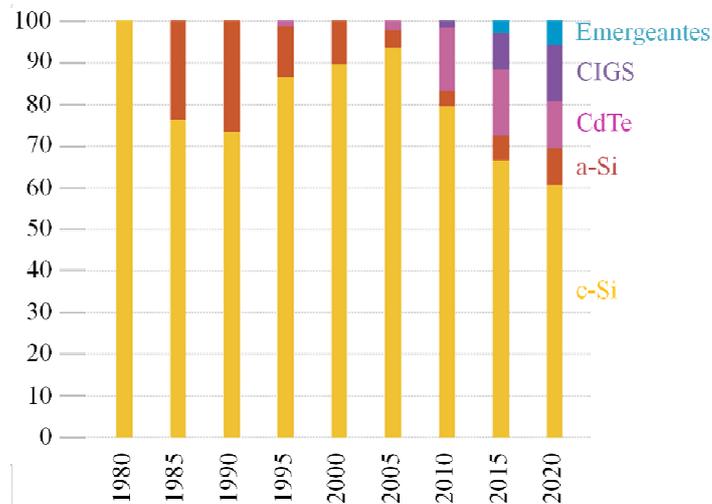
Figure 1 : Répartition actuelle et future des parts de marchés (en %), pour chacune des technologies photovoltaïques [Ass11].

Plus récemment, de nouvelles technologies basées sur des matériaux déposés en couches minces et à basses températures (< 500 °C) ont été envisagées (Figure 1). Les cellules en silicium amorphe (a-Si) ont notamment été développées dans les années 80 mais restent marginales du fait de performances relativement faibles. Comparativement, les cellules en tellure de cadmium (CdTe) et en cuivre, indium, gallium et sélénium (CIGS) captent des parts de marchés importantes, leurs performances ayant continuellement augmenté avec des coûts de production en constante baisse. Les cellules en CdTe permettent notamment de produire de l'électricité à environ 1 €/Wc et concurrencent donc fortement la filière c-Si.

Cependant, les technologies sur silicium resteront *a priori* dominantes. Le silicium est l'élément le plus abondant de l'écorce terrestre après l'oxygène et il est non toxique. Si de nombreuses économies d'échelles ont permis jusqu'ici de réduire les coûts de cette technologie, les améliorations futures nécessitent la mise en place de ruptures technologiques, afin d'atteindre des coûts de productions équivalents à ceux de l'électricité conventionnelle, aux alentours de 0,5 €/Wc.

Parmi les coûts de production difficilement compressibles lors la production d'une cellule, on peut noter ceux liés à la réalisation de la plaquette en silicium, qui représentent donc 50 % du prix d'un module photovoltaïque. Le matériau silicium, obtenu par réduction de la silice dans des fours à arc, est d'abord purifié à 99,999 %, puis fondu et recristallisé en lingots à des

---

[1] Le Wc, dit Watt crête, est l'unité de puissance délivrée par une cellule solaire sous plein ensoleillement.

températures supérieures à 1400 °C. Ceux-ci sont ensuite découpés en plaquettes. Cette étape de sciage est une des plus coûteuses puisque la moitié environ du silicium y est perdue.

Dans le but d'éviter cette étape de sciage, la société S'Tile localisée à Poitiers développe un nouveau procédé de fabrication de plaquettes de silicium multi-cristallin par frittage sous charge. Une poudre de silicium est alors chauffée sous contrainte, en dessous de sa température de fusion (1414 °C), afin de la consolider et de la densifier. Le principal avantage de cette technique est d'obtenir une plaquette directement mise en forme sans perte de matière.

La société S'Tile envisage d'utiliser cette plaquette frittée de deux façons :
- La première est de la transformer en cellule solaire comme dans le procédé conventionnel. Dans ce cas, un matériau de très haute pureté sans porosité résiduelle doit être produit, afin de faciliter le déplacement et la collecte des porteurs photo-générés dans la plaquette.

- La seconde voie, privilégiée par S'Tile, consiste à utiliser cette plaquette comme substrat, sur lequel est réalisé une couche mince de 20 à 50 μm d'épaisseur en silicium multi-cristallin, qui servira de composant actif à la cellule. Le principal intérêt de cette approche est d'offrir un substrat bas coût, compatible avec la réalisation de cellules couches minces en silicium cristallin, à des températures élevées, supérieures à 1000 °C. En effet, contrairement aux substrats bas coûts proposés dans la littérature, le matériau utilisé ici est en silicium et permet donc de préserver l'intégrité chimique et mécanique de la couche active tout au long du procédé. La société S'Tile ambitionne d'atteindre des rendements de 14 %, proches des rendements actuels de cellules multi-cristallines (16-18 %), par un procédé deux fois moins coûteux.

Au cours de cette thèse, nous envisageons l'élaboration de ces plaquettes par frittage naturel au lieu du frittage sous charge. Le frittage naturel consiste d'abord à compacter la poudre à froid puis à la consolider ensuite lors d'un traitement thermique dans un four. Ce type de frittage, s'il s'avérait réalisable, représenterait un gain de productivité par rapport au frittage sous charge. En effet, le frittage sous charge ne permet de fritter qu'un lot de plaquettes à la fois, ce qui ralentit considérablement la cadence de production.

Matériaux et problématique

P lusieurs poudres de granulométries différentes ont été étudiées au cours de cette thèse (Chapter II.1). Dans ce résumé, nous nous focaliserons sur le comportement d'une poudre fine, notée VF, constituée de particules élémentaires sphériques d'environ 220 nm de diamètre, estimé par la méthode BET (Figure 2). Cette poudre contient moins de 1 ppm d'impuretés métalliques mais est naturellement contaminée avec de l'oxygène à une hauteur de 0,61 % massique. Cet oxygène est présent sous forme d'une couche native de silice, SiO_2, à la surface des particules et correspond à une épaisseur équivalente, calculée à partir du diamètre BET, de 0,43 nm. La poudre est le plus souvent compactée sous forme de cylindres d'environ 8 mm de hauteur et 7 mm ou 15 mm de diamètre avec une densité initiale de 54 % TD_{Si}.

1 µm   200 nm
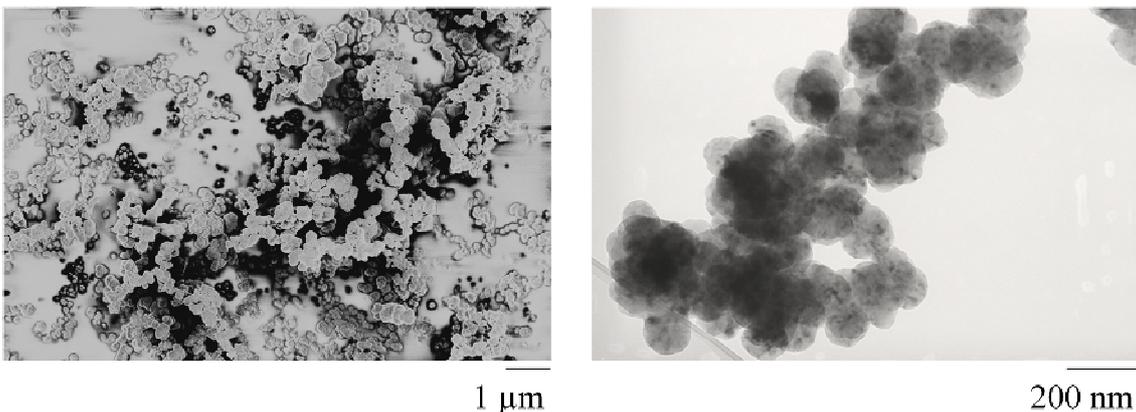
Figure 2 : Micrographies de la poudre VF, à droite : image en électrons secondaires au microscope électronique à balayage (FEG-SEM), à gauche : image en microscopie électronique à transmission (TEM).

Lorsque ces comprimés sont frittés à 1350 °C, pendant 3 h, sous atmosphère neutre ou hydrogénée, une perte de masse de quelques pourcents est observée. Cette perte de masse est attribuée à la réduction de la silice au cours de la montée en température.

Pour les comprimés de 7 mm de diamètre, Φ_7, la perte de masse relative est de 2,8 % et la densité finale est de 64 % TD_{Si}. La microstructure finale est homogène au sein du comprimé et très grossière, avec une taille de grain environ 50 fois supérieure à la taille initiale des particules (Figure 3).

Pour les comprimés de 15 mm de diamètre, Φ_{15}, la perte de masse relative est moindre, 2 %, et la densité finale supérieure, 76 % TD_{Si}. Contrairement aux comprimés de 7 mm de diamètre la microstructure n'est pas homogène. Le centre du comprimé est relativement dense (80-85 % TD_{Si}, par analyse d'images) avec une taille de grain d'environ 500 nm. Cette zone dense est entourée d'une zone plus grossière et poreuse (~65 % TD_{Si}, par analyse d'image), similaire à celle développée dans les comprimés de 7 mm de diamètre (Figure 3).
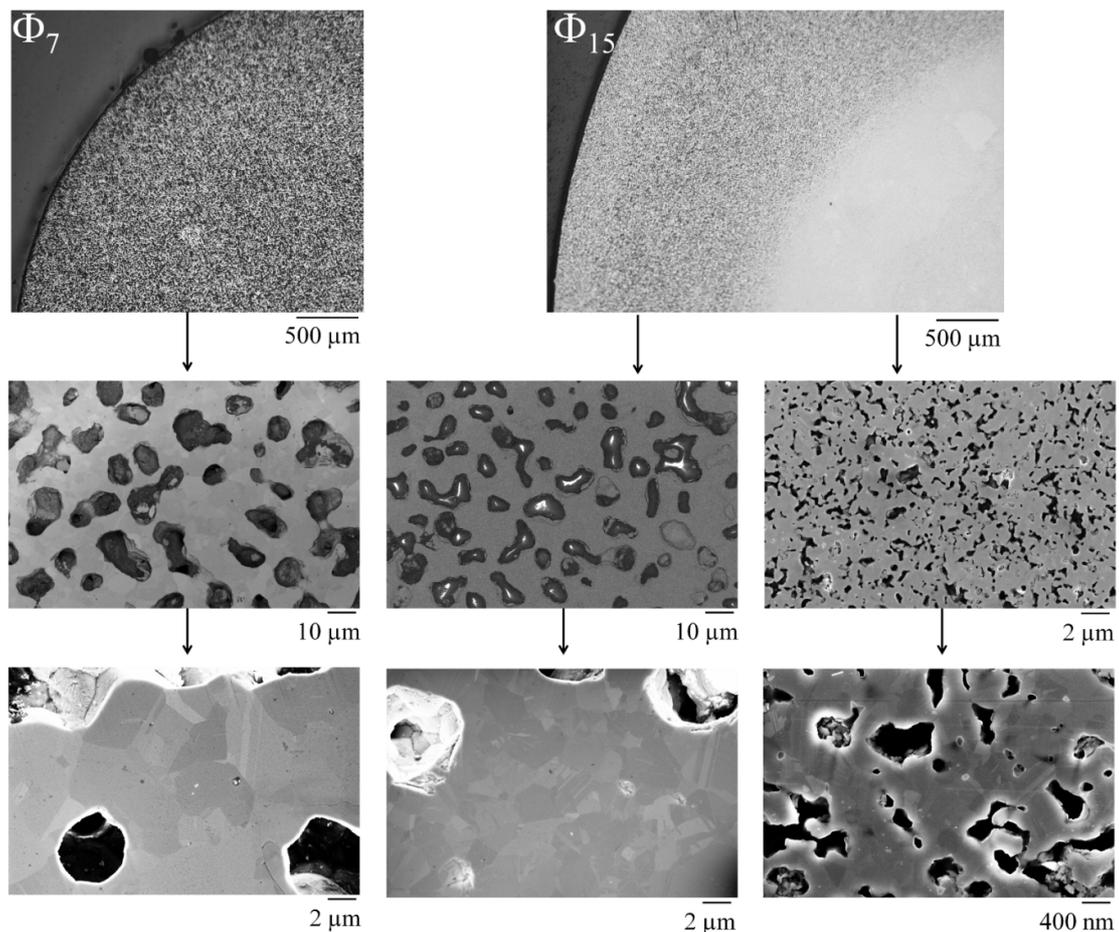
Figure 3 : Observation par microscopie optique et électronique des échantillons Φ_7 et Φ_{15}, après frittage à 1350 °C pendant 3 h sous He-4mol.% H_2.

L'évolution de la microstructure, de la périphérie vers le cœur de l'échantillon, montre que l'atmosphère entourant celui-ci affecte considérablement le frittage. Associées aux pertes de masse, que nous pouvons attribuer à la réduction de la silice, ces micrographies tendent à montrer que la présence d'une couche de silice à la surface des particules affecte considérablement les mécanismes et cinétiques de grossissement de grains.

Ces premières observations sont en accord avec les résultats de la littérature [GR76, SH83, MW85, Cob90], sans pour autant que le rôle de la couche de silice à la surface des particules n'y soit clairement défini. De fait, nos investigations visent à clarifier ce rôle :

- En focalisant notre attention sur les cinétiques de réduction de la couche de silice à la surface des particules et en étudiant le couplage avec l'évolution de la microstructure.

- En identifiant les paramètres qui contrôlent la température et les cinétiques de réduction de la silice. Des solutions seront alors proposées et testées afin de stabiliser la silice à haute température et d'en observer les conséquences sur le frittage (grossissement de grains et densité).

- En estimant les cinétiques de chacun des mécanismes de frittage en présence ou non de silice à la surface des particules. Des cartes de frittage seront alors tracées permettant de rendre compte des cinétiques de grossissement de grains et de densification observées expérimentalement.

Cinétiques de réduction de la silice

L es premiers travaux théoriques sur la réduction d'une couche de silice à la surface du silicium, sous atmosphère neutre, furent présentés par Carl Wagner [Wag58]. Ici, cette approche est appliquée au cas de particules de silicium recouvertes d'une fine couche de silice et placées sous une atmosphère hydrogénée.

Dans le cas général, Carl Wagner considère deux configurations (Figure 4) :

- (a) Dans une première configuration, la surface du silicium est à nu. Cette configuration est équivalente au cas d'une particule de silicium recouverte d'une couche de silice fragmentée, ou si fine, que la diffusion des espèces oxygénées (H_2O et SiO) dans la couche est rapide au regard du transport des ces mêmes espèces dans le gaz environnant. La réduction de la silice par le silicium sous forme de monoxyde de silicium gazeux ($SiO_{(g)}$) en réaction (R_5), est alors rendue possible par le départ progressif, par diffusion depuis l'interface silicium silice, de cette espèce.

$$Si_{(s)} + SiO_{2(s)} = 2SiO_{(g)} \tag{R_5}$$

- (b) Dans une deuxième configuration, la surface du silicium est recouverte d'une couche de silice, dite passive, c'est-à-dire que la diffusion des espèces oxygénées à travers la couche est infiniment lente au regard du transport de ces mêmes espèces dans le gaz environnant. La réduction de la silice ne peut alors avoir lieu que par réduction de la silice par l'hydrogène présent dans le gaz sous forme de monoxyde de silicium et d'eau, en réaction (R_6).

$$SiO_{2(s)} + H_{2(g)} = SiO_{(g)} + H_2O_{(g)} \tag{R_6}$$

$$Si_{(s)} + SiO_{2(s)} = 2SiO_{(g)} \ (R_5) \qquad SiO_{2(s)} + H_{2(g)} = SiO_{(g)} + H_2O_{(g)} \ (R_6)$$
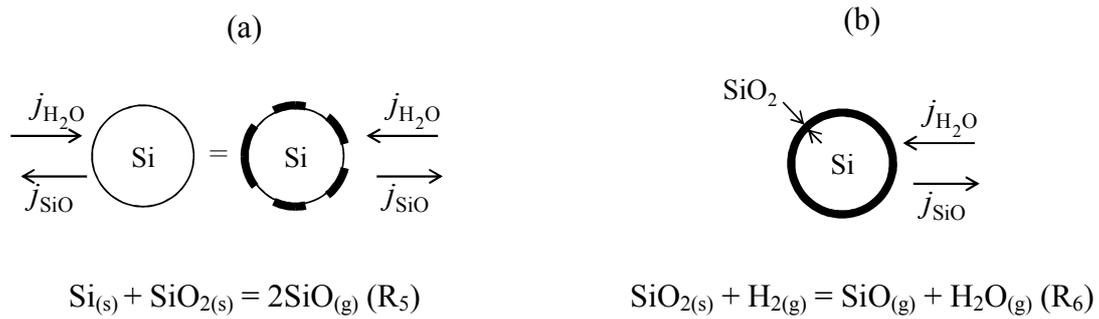
Figure 4 : Mécanismes de réduction de la silice envisagés pour deux configurations : (a) *une couche de silice fragmentée à la surface de la particule de silicium,* (b) *une couche de silice continue et passive à la surface de la particule de silicium.*

En faisant l'hypothèse d'un équilibre thermodynamique atteint et d'un régime stationnaire de diffusion des espèces oxygénées, la température de réduction de la silice, par chacun des deux mécanismes et donc pour chacunes des deux configurations, peut être calculée en fonction de la pression partielle en eau autour de l'échantillon (Figure 5).
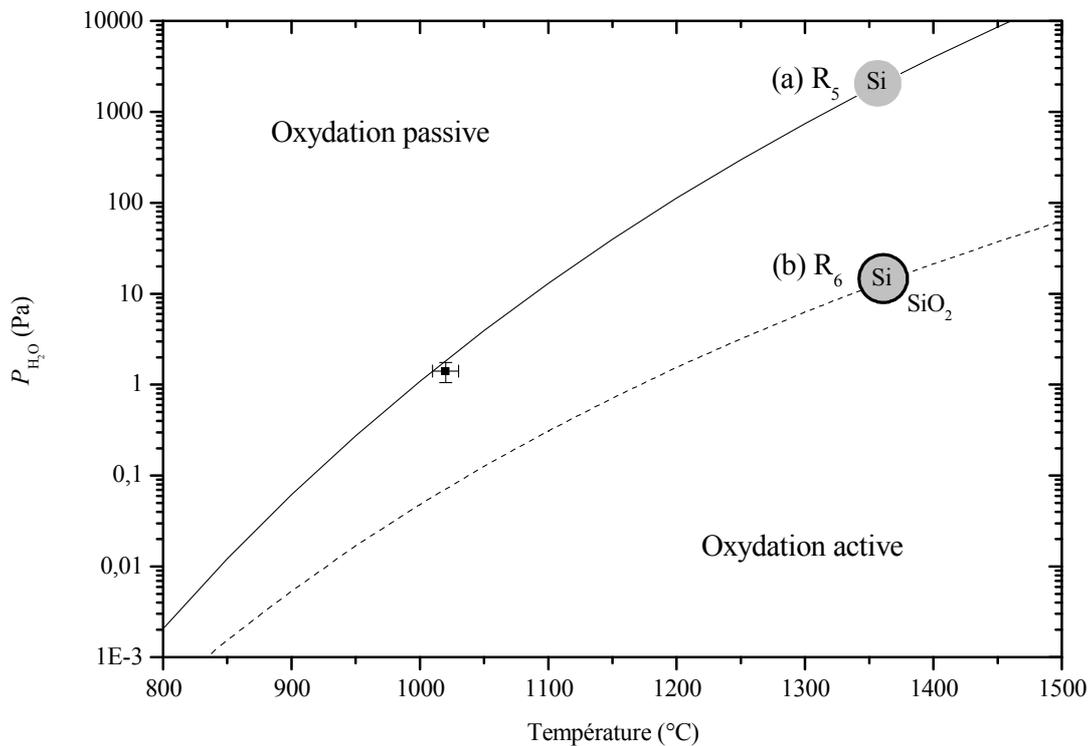
Figure 5 : Température de réduction de la silice attendue pour les deux configurations envisagées, (a) *une couche de silice fragmentée,* (b) *une couche de silice continue et passive. Température de réduction de la silice mesurée sous He-4mol.% H$_2$.*

Dans nos conditions expérimentales (atmosphère d'He-4mol.% H$_2$), la pression d'eau autour de l'échantillon est d'environ quelques Pa, ce qui correspond à une température de début de réduction de la silice d'environ 1020 °C dans le cas d'une couche de silice fragmentée (a) et d'environ 1200 °C dans le cas d'une couche de silice continue et passive (b).

La température de début de réduction de la silice peut être estimée expérimentalement par analyse thermogravimétrique. Un échantillon de silicium est alors suspendu, dans un four vertical, à l'aide de suspensions en tungstène, à un fléau en équilibre. La déviation du fléau permet alors de remonter au gain ou à la perte de masse subie par l'échantillon, tout au long du cycle thermique étudié.

Sur la Figure 6, la variation de masse subie par un échantillon chauffé à une vitesse de 1,25 °C min^{-1} à 1350 °C est tracée. La courbe obtenue peut être séparée en trois étapes :

    i.   Entre la température ambiante et 1025 °C, un gain de masse, lié à l'oxydation passive du silicium par l'eau sous forme de silice, est mesuré.

$$Si_{(s)} + 2H_2O_{(g)} = SiO_{2(s)} + 2H_{2(g)} \tag{R$_1$}$$

    ii.   Entre 1025 °C et le début de l'arrivée au palier à 1350 °C une perte de masse est mesurée, et attribuée à une réduction de la silice.

$$Si_{(s)} + SiO_{2(s)} = 2SiO_{(g)} \tag{R$_5$}$$
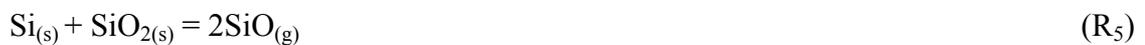
    iii.   A l'arrivée au palier à 1350 °C, une diminution brutale de la vitesse de perte de masse est observée, puisque la silice est maintenant entièrement réduite. L'échantillon est alors placé dans un régime d'oxydation active au cours duquel le silicium est progressivement consommé sous forme de monoxyde de silicium par l'eau.

$$Si_{(s)} + H_2O_{(g)} = SiO_{(g)} + H_{2(g)} \tag{R$_2$}$$

La température de début de perte de masse (1025 °C) est donc en accord avec un mécanisme de réduction de la silice par le silicium sous forme de monoxyde de silicium (R$_5$). La perte de masse globale mesurée au cours de la réduction de la silice est elle aussi en accord avec la stœchiométrie de la réaction (R$_5$) et la quantité d'oxygène initialement présent dans la poudre. Ceci tend à montrer que la couche de silice à la surface des particules de silicium est soit fragmentée, soit suffisamment fine ou défectueuse pour permettre la diffusion rapide du monoxyde de silicium. Ceci fait encore l'objet d'un débat comme mentionné au Chapitre III.4.
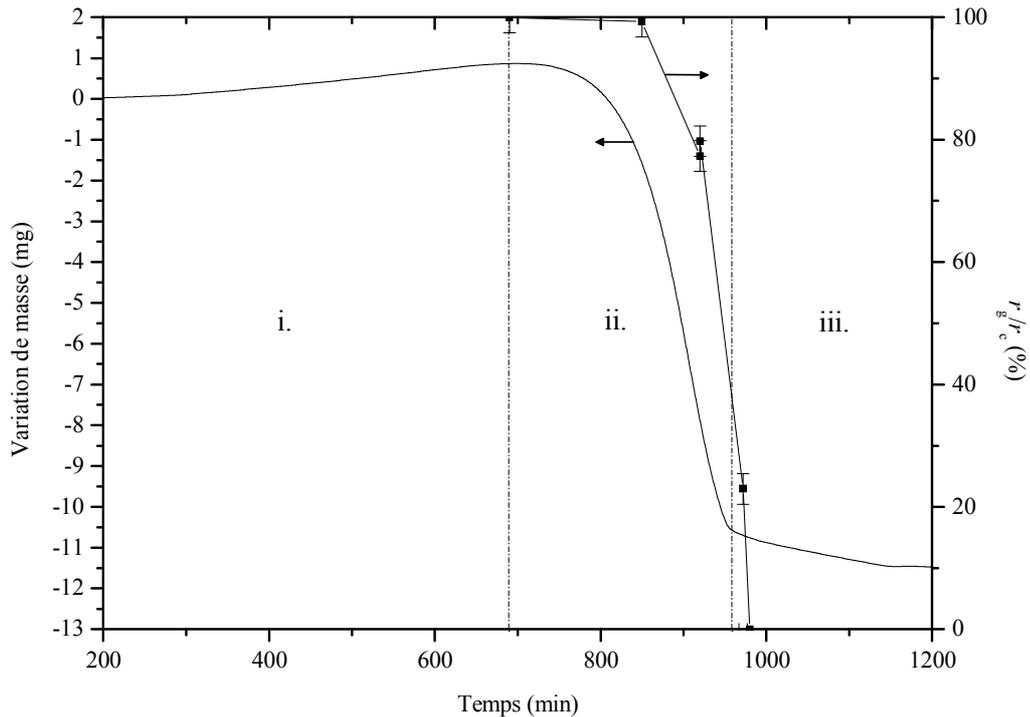
Figure 6 : A gauche : Mesure de la variation de masse d'un échantillon de silicium, Φ_7, par analyse thermogravimétrique, lors d'une montée à 1350 °C à une vitesse de 1,25 °C min^{-1} pendant 3 h sous He-4mol.% H_2. A droite : Mesure de la position du front de grossissement de grains au cours de la réduction de la silice.

Sur la Figure 7, la microstructure d'un échantillon trempé à 1315 °C au cours de la réduction de la silice est aussi représentée. Cette microstructure est inhomogène. A la périphérie de l'échantillon, une zone poreuse à gros grains apparait, alors qu'au centre de l'échantillon, les particules de silicium sont proches de leur taille initiale (200 nm).

Au cours de la réduction de la silice, la zone à gros grains s'étend progressivement au détriment de la zone à grains fins. Sur la Figure 6, le mouvement du front de grossissement de grain (r_g), par rapport au rayon du comprimé (r_c), est aussi tracé. On note que :

- Le début du grossissement de grain coïncide avec le début de la réduction de la silice.

- La fin du grossissement de grain correspond aussi à la fin de la réduction de la silice.

Le front de grossissement de grain est donc concomitant avec un front de réduction de la silice avançant progressivement depuis la surface externe du comprimé vers son centre. La zone à gros grains correspond de fait à une zone où la silice a été réduite, alors que la zone à grains fins correspond à une zone où la silice est encore présente. Ceci est confimé par les

profils d'analyse dispersive en énergie (EDS) qui montrent que la zone à grains fins est plus riche en oxygène que la zone à gros grains.
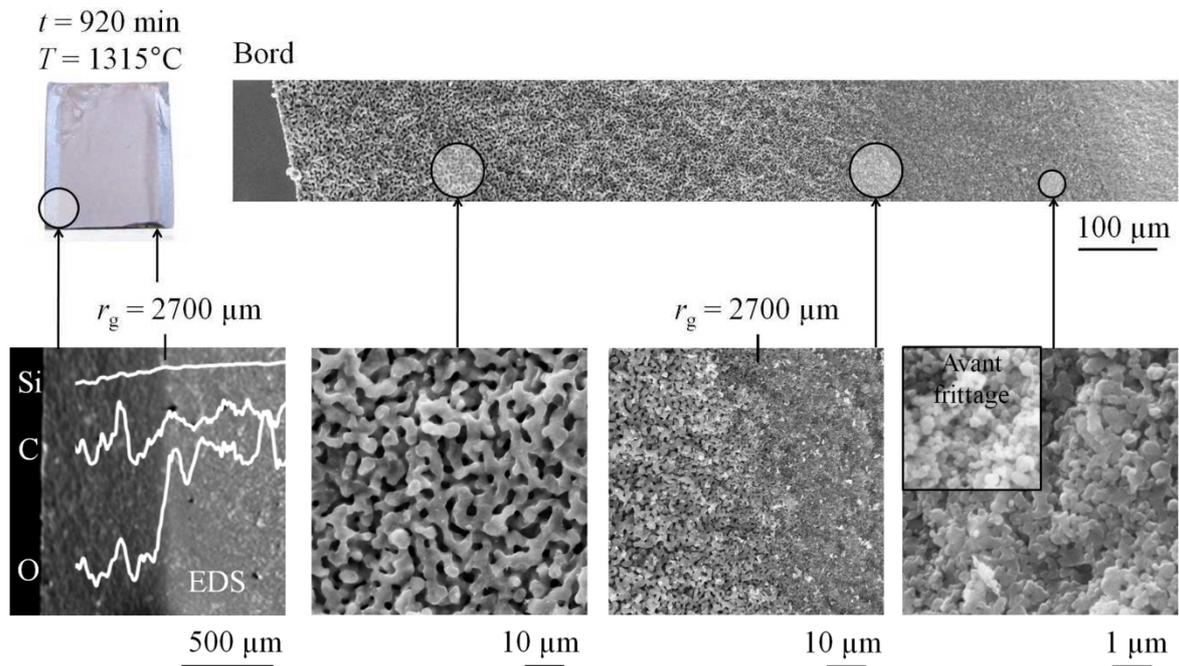
Figure 7 : Photographie et micrographies d'un échantillon trempé à 1315 °C (t = 920 min) au cours de la réduction de la silice. Profils EDS au niveau du front de grossissement de grain.

En conclusion de cette première partie, nous avons montré que la réduction de la silice activait un mécanisme de grossissement de grain et affectait donc les mécanismes de frittage. Ce grossissement de grain est la marque d'un mécanisme de frittage non densifiant, très rapide, opérant une fois la couche de silice réduite.

A l'aide de mesures thermogravimétriques, nous avons aussi déterminé la température de début de réduction de la silice qui dépend de la pression d'eau environnant l'échantillon. Dans nos conditions expérimentales, cette température est en accord avec un mécanisme de réduction de la silice par le silicium sous forme de monoxyde de silicium (R_5).

$$Si_{(s)} + SiO_{2(s)} = 2SiO_{(g)} \tag{R_5}$$

Dans le manuscrit rédigé en Anglais, un modèle cinétique de réduction de la silice est détaillé (Chapter III). Il permet de décrire l'ensemble des étapes d'oxydation subies par les comprimés de silicium en tenant compte de la contamination initiale en oxygène de la poudre, de la morphologie des pores, de la pression partielle en espèces oxydantes autour du comprimé, ainsi que de la géométrie du four. Finalement, ce modèle rend bien compte de la

vitesse de perte de masse mesurée pour les comprimés Φ_7, et à un degré moindre pour les comprimés Φ_{15}.

Stabilisation de la silice à haute température

A la suite des observations faites lors de l'étude de la réduction de la silice, nous avons étudié l'effet d'une stabilisation de la couche silice à plus haute température sur les mécanismes de grossissement de grains et de frittage. Pour cela il est nécessaire d'augmenter la pression partielle en eau autour de l'échantillon, ce qui peut être rendu possible par un contrôle de la pression partielle en eau dans le gaz vecteur. La question sous-jacente est donc la suivante : pour une température de frittage donnée, à laquelle nous souhaitons stabiliser la couche de silice, qu'elle doit être la pression d'eau dans le gaz entrant (Figure 8) ?
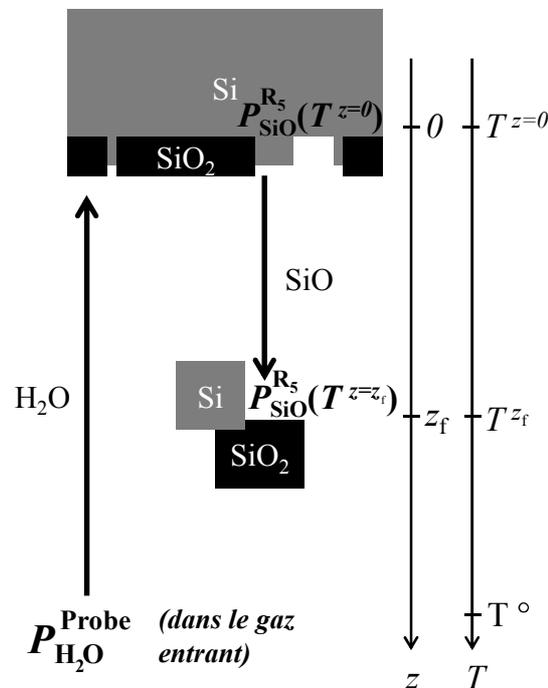
Figure 8 : Représentation des transports de matières impliqués dans le tube du four lors de la stabilisation de la couche de silice à la surface des particules de silicium.

Considérons pour cela une pression d'eau contrôlée, $P_{H_2O}^{Probe}$, dans le gaz vecteur. Dans l'hypothèse où toute l'eau apportée est consommée pour former de la silice à la surface de l'échantillon, le flux d'eau consommée, j_{H_2O}, peut s'écrire selon l'Equation (1) où, S^{tube} correspond à la section du tube du four, Q, au débit de gaz, T°, à la température ambiante et R à la constante des gaz parfaits.

$$j_{H_2O} = -\frac{Q}{2S^{tube}RT°}P_{H_2O}^{Probe}$$

(1)

Dans le même temps, à la surface de l'échantillon, la silice est réduite par le silicium sous forme de $SiO_{(g)}$. La pression partielle de $SiO_{(g)}$ est alors donnée par l'équilibre (R_5).

$$Si_{(s)} + SiO_{2(s)} = 2SiO_{(g)}$$

(R_5)

Le $SiO_{(g)}$ formé diffuse vers les parties froides du four où, du fait d'une surconcentration par rapport à l'équilibre (R_5), il condense sous forme de silicium et de silice. Le flux de départ de $SiO_{(g)}$ peut alors être exprimé selon l'Equation (2), pour une atmosphère dite « quasi-stagnante », comme cela a pu être vérifié en Annexe B. Dans cette équation on retrouve, le coefficient de diffusion moléculaire du SiO, D_{SiO}^{mol}, la longueur de diffusion entre l'échantillon et les zones froides du four, z_f, ainsi que les pressions à l'équilibre de SiO au voisinage de l'échantillon ($z = 0$) et sur les zones froides ($z = z_f$). La pression de SiO sur les zones froides, $P_{SiO}^{R_5}(T^{z=z_f})$, peut par ailleurs être néglégigée devant la pression de SiO au voisinage de l'échantillon, $P_{SiO}^{R_5}(T^{z=0})$.

$$j_{SiO} = -\frac{D_{SiO}^{mol}}{RT}\frac{P_{SiO}^{R_5}(T^{z=z_f}) - P_{SiO}^{R_5}(T^{z=0})}{z_f} \approx \frac{D_{SiO}^{mol}}{RT}\frac{P_{SiO}^{R_5}(T^{z=0})}{z_f}$$

(2)

Dans le cas où le flux d'eau consommé est égal au flux de $SiO_{(g)}$ généré par l'échantillon, la couche est stabilisée. Pour une température de frittage donnée, $T^{z=0}$, à laquelle nous souhaitons stabiliser la couche de silice, la pression d'eau à contrôler dans le gaz vecteur, $P_{H_2O}^{Probe*}$, peut donc être estimée à l'aide des Equations (1) et (2) et dépend essentiellement de la longueur de diffusion, z_f (Equation (3) et Figure 9).

$$P_{H_2O}^{Probe*} = 2\frac{M_{SiO}}{M_O}\frac{D_{SiO}^{mol}(T^{*m})S^{tube}}{Qz_f}\frac{T°}{T^{z=0}}P_{SiO}^{R_5}(T^{z=0})$$

(3)

Par thermogravimétrie, la température de début de réduction de la silice est mesurée pour différentes valeurs de pressions d'eau contrôlées dans le gaz vecteur à l'aide d'un régulateur présenté dans le Chapitre II.2.4. Une fois reportées sur la Figure 9, ces mesures suivent sensiblement celles attendues par l'Equation (3), moyennant une longueur de diffusion de $SiO_{(g)}$ approximativement égale à 25 mm. Cette longueur de diffusion est cohérente avec la zone de température homogène donnée par le constructeur du four (± 15 mm).
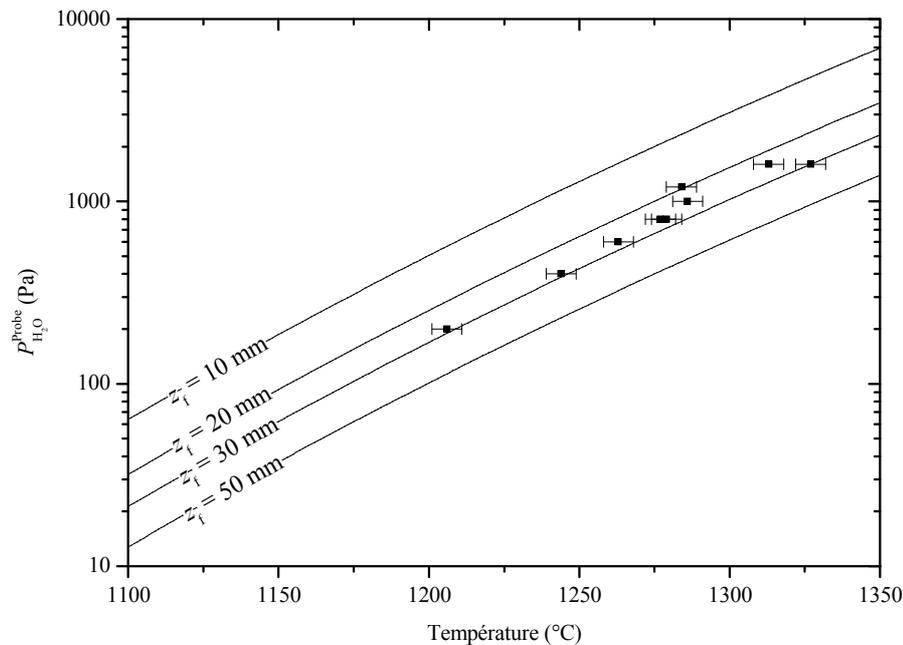
Figure 9 : Pression partielle d'eau à contrôler dans le gaz entrant afin de stabiliser la couche de silice à la surface des particules de silicium en fonction de la température de l'échantillon. Cette pression est estimée à l'aide de l'Equation (3) pour plusieurs longueurs de diffusion (traits continus). Cette pression est aussi mesurée expérimentalement par thermogravimétrie (carrés noirs).

Une fois ces mesures effectuées, les valeurs de pressions d'eau dans le gaz vecteur sont choisies (400, 800 et 1600 Pa), en fonction des températures de frittage étudiées (1225, 1260 et 1315 °C) pour les échantillons a*, b* et c* respectivement. Les essais de frittage sous pression d'eau sont ensuite comparés à des essais réalisés aux mêmes températures, sous atmosphère réductrice, c'est-à-dire sous gaz sec, pour les échantillons a, b et c. Les résultats de ces essais sont donnés sur la Figure 10, où l'on peut constater l'effet de la stabilisation de la couche de silice sur l'évolution de la microstructure et de la densité.

- La stabilisation de la couche de silice inhibe le grossissement de grains et donc le mécanisme non densifiant qui en est à l'origine.

- La stabilisation de la couche de silice permet une meilleure densification des échantillons. Cette amélioration est d'autant plus élevée que la température de frittage est importante.
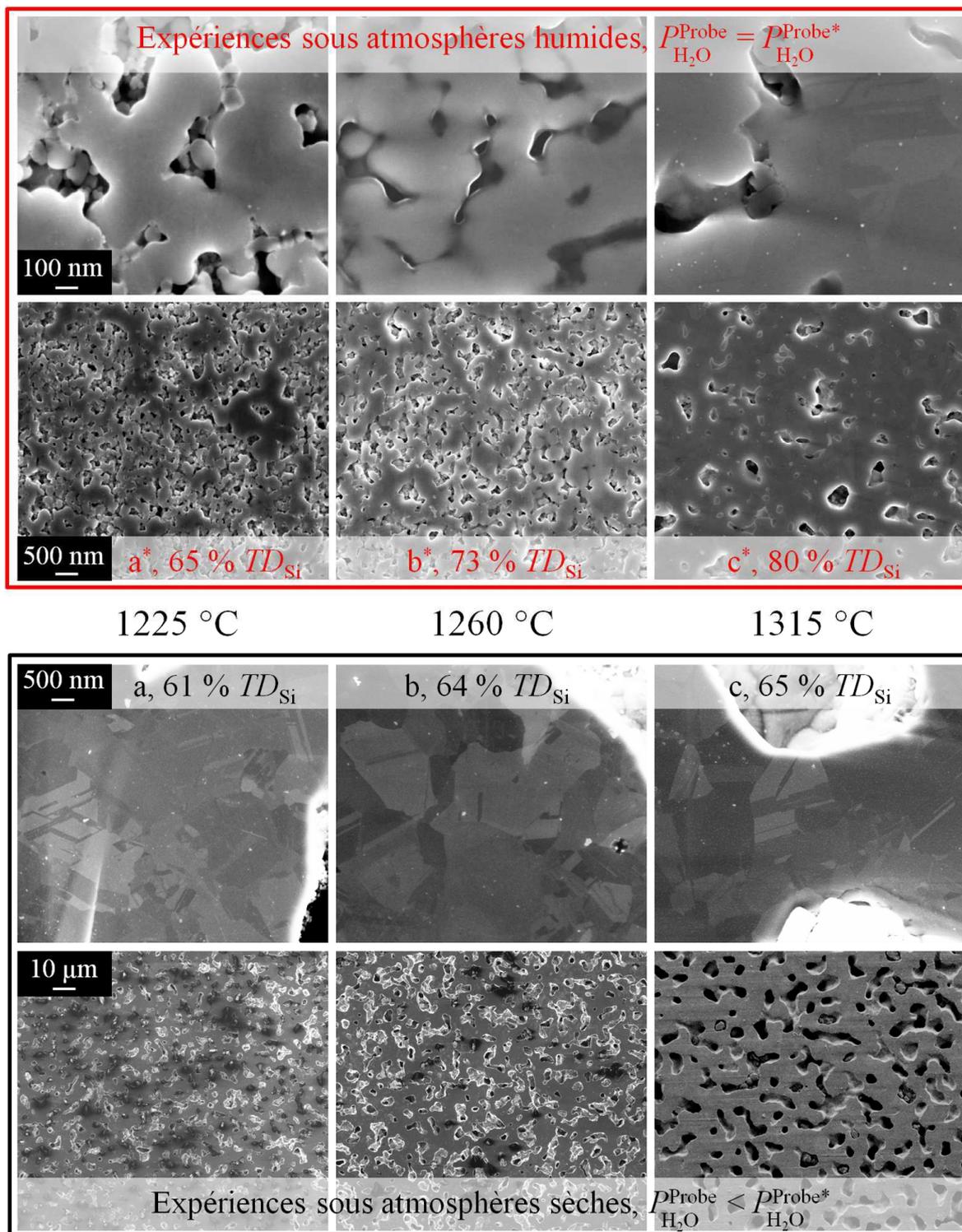
Figure 10 : Cadre rouge, en haut : microstructures et densités des échantillons a*, b* *et* c*, *frittés sous atmosphères humides, durant 3 h, à respectivement 1125, 1260 et 1315 °C. Cadre noir, en bas : microstructures et densités des échantillons* a, b *et* c, *frittés aux mêmes températures mais sous atmosphères sèches. La vitesse de montée en température est de 40 °C min⁻¹ et le gaz porteur est un flux de 2 l h⁻¹ d'He-4mol.% H₂.*

En conclusion de cette deuxième partie, nous avons identifié les moyens de contrôle d'une couche de silice à la surface de particules de silicium. Ceux-ci sont principalement la pression partielle en espèces oxydantes autour de l'échantillon et la longueur de diffusion de ces mêmes espèces dans le four.

Ici, la température de début de réduction de la silice a été maîtrisée à l'aide d'un contrôle de la pression partielle en eau dans le gaz entrant. Sous atmosphère humide, la stabilisation de la silice a permis d'inhiber le mécanisme de grossissement de grain, non densifiant, couramment observé sous atmosphère sèche. A température égale, le frittage en présence de silice permet aux mécanismes densifiant d'opérer puisque une densité finale plus élevée est mesurée.

Néanmoins, le frittage en atmosphère humide est responsable de pertes de matières importantes lorsque le flux d'eau, à l'origine de la stabilisation de la silice, est trop élevé. Il apparait donc plus approprié de contrôler la longueur de diffusion des expèces oxydantes, en maîtrisant le profil thermique du four utilisé.

Un autre moyen de stabilisation de la couche de silice consiste à placer l'échantillon sous un lit de poudres de silicium et de silice. Ce lit de poudres génère alors tout au long du frittage la pression partielle à l'équilibre de $SiO_{(g)}$ de la réaction (R_5), ce qui permet de stabiliser la silice au sein de l'échantillon. C'est cette solution qui sera envisagée par la suite pour étudier le frittage du silicium en présence de silice.

Identification des mécanismes de frittage en présence ou non de silice

A la suite des observations faites dans la partie précédente, deux interrogations méritent une attention particulière :

- Pour quelle raison la couche de silice inhibe-t-elle le grossissement de grain ?
- Pourquoi, contre toute attente, une stabilisation de cette couche permet elle aussi d'améliorer la densification ?

Ces deux questions sont en réalité étroitement liées et ne peuvent être traitées indépendament l'une de l'autre. Pour cela, il est nécessaire de considérer les mécanismes de premier stade du frittage, c'est-à-dire ceux qui contrôlent le début de la formation des cous entre deux particules, sous l'effet des gradients de courbures locaux et de la diffusion atomique à haute température.

Le modèle géométrique couramment utilisé est celui de deux particules sphériques de rayon a, connectées par un cou de rayon x (Figure 11).

Les gradients de courbure entre les surfaces convexes des particules, en compression, et les surfaces concaves du cou, en traction, induisent des gradients de lacunes dans la phase solide et des gradients de pression de vapeur dans la phase gazeuse. Ces gradients sont à l'origine d'une diffusion atomique dans la phase solide et dans la phase gazeuse, à l'origine d'une croissance de cou sans rapprochement du centre des deux particules, *i.e.* sans densification. Dans la phase solide, la diffusion peut avoir lieu *via* le volume ou la surface. Dans la phase gazeuse, sous pression atmosphérique et pour les tailles de particules considérées ici ($2a$ =

220 nm), l'étape de diffusion est limitée par la condensation du gaz sur les surfaces concaves du cou.

Des gradients de lacunes entre le joint de grain, en compression, et la surface du cou, en traction, existent et induisent eux aussi une diffusion atomique qui contribue à la croissance des cous entre particules. A la différence des mécanismes de diffusion depuis la surface des particules, ceux-ci sont à l'origine d'un rapprochement des particules et donc d'une densification. Ici la diffusion peut avoir lieu *via* le volume ou le long du joint de grain.
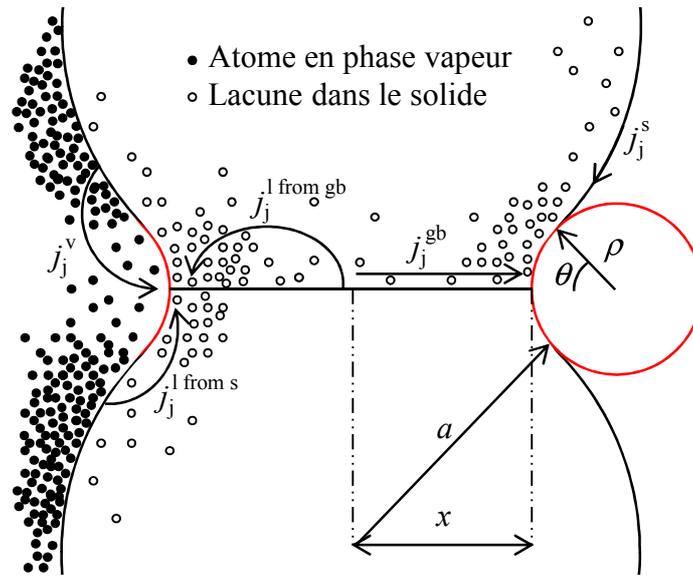
Figure 11 : Modèle à deux sphères couramment utilisé pour décrire le premier stade du frittage. Le transport de matière est induit par la courbure négative du cou entre les deux particules (en rouge). A cet endroit, la concentration en lacunes, dans le solide, y est plus élevée et la concentration en atomes, dans la phase vapeur, y est plus faible. Les flux de matières peuvent alors suivre cinq chemins différents. Trois d'entre eux sont originaires de la surface des particules et sont donc non-densifiant : le transport vapeur, j_j^v, la diffusion de surface, j_j^s, et la diffusion en volume depuis la surface des particules, $j_j^{l\,from\,s}$. Deux d'entre eux sont originaires du joint de grain, ils induisent alors un rapprochement des particules et sont donc densifiant : la diffusion au joint de grain, j_j^{gb}, et la diffusion en volume depuis le joint de grain, $j_j^{l\,from\,gb}$.

Tous ces mécanismes sont en compétition tout au long du frittage et contrôlent la vitesse de croissance des cous entre particules et l'évolution de la microstructure :
-   Si les mécanismes non-densifiant dominent, alors ils contribuent à une croissance des cous sans rapprochement des particules et finissent par générer un grossissement de grains et de pores. Les surfaces libres ayant été consommées au

profit du grossissement, la force motrice des mécanismes de frittage disparait progressivement sans qu'aucune densification n'ait pu et ne puisse plus avoir lieu.

-   Si les mécanismes densifiant dominent, au moins en partie, alors une croissance des cous avec densification et sans grossissement à lieu jusqu'à fermeture de la porosité, lorsque l'échantillon atteint environ 92 % de la densité théorique. Ensuite, un grossissement de la microstructure peut éventuellement avoir lieu si les joints de grains sont suffisamment mobiles.

Dans le cas du silicium pur, non recouvert de silice, un mécanisme de diffusion de surface, très rapide, est en fait responsable du grossissement de grains, sans densification, observé. Le coefficient de diffusion à la surface du silicium pur, $D_{Si}^{s,Si}$, a été mesuré dans la littérature par Robertson [Rob81] et Coblenz [Cob90], à l'aide de mesures cinétiques de gravures thermiques de joints de grains. Ce coefficient est particulièrement élevé et permet d'expliquer les vitesses très rapides de croissance de cou observées dès 1020 °C, une fois la silice réduite (Figure 10 et Figure 12).
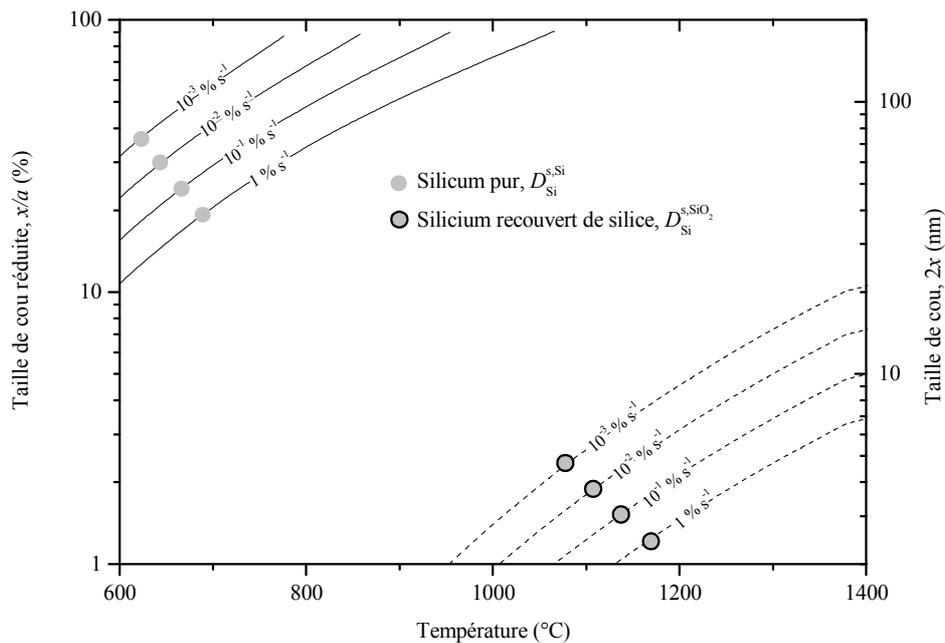
Figure 12 : Courbes de vitesse de croissance de taille de cou pour le mécanisme de diffusion de surface dans le cas du silicium pur et du silicium recouvert de silice. La taille des particules (2a = 220 nm) est représentative de la poudre VF utilisée.

Dans le cas du silicium recouvert de silice, le coefficient de diffusion de surface à considérer est celui du silicium à la surface de la silice, D_{Si}^{s,SiO_2}. D'après la littérature [BSS+80, GC85], ce coefficient est considérablement plus faible que celui du silicium à la surface du silicium.

Dans ce cas, les vitesses de croissance de cou par diffusion de surface estimées sont beaucoup plus faibles et expliquent l'inhibition du grossissement de grains observé en présence de silice (Figure 10 et Figure 12).

Dans le cas du silicium pur, le mécanisme de diffusion de surface est si rapide qu'il devance tous les autres, les empêchant ainsi d'opérer. Fortement ralenti dans le cas de particules de silicium recouvertes de silice, il n'est plus prédominant. Une compétition s'engage alors entre les autres mécanismes, non-densifiant d'une part, et densifiant d'autre part. Au cours de cette compétition, la vitesse de chacun des mécanismes contrôle à la fois les vitesses de croissance de cou et de densification observées.

Dans le Chapitre IV.3, les vitesses de croissance de cou et de retrait en présence de silice à la surface des particules de silicium ont pu être estimées à l'aide d'un modèle adapté, permettant de rendre compte de l'évolution de la microstructure, de la densité et de la taille moyenne des pores, tout au long du frittage. Ce modèle permet de montrer qu'une compétition entre un mécanisme densifiant, de diffusion en volume et un mécanisme non-densifiant, de transport vapeur a lieu. Cette compétition est à l'origine de la présence inhabituelle de deux pics, sur les courbes de retrait mesurées par dilatométrie (Figure 13). Dans ce cas, l'échantillon de silicium est placé sous un lit de poudres de silicium et de silice permettant de stabiliser la silice dans le comprimé tout au long du frittage.

- Le mécanisme de diffusion en volume depuis le joint de grain est prédominant au début du premier stade et permet de rendre compte de la première accélération observée sur les courbes de retrait. Ce mécanisme est perturbé par la présence de silice à la surface des particules, qui ralentit la diffusion du silicium.

- A mesure que les cous croissent, le mécanisme de transport vapeur, non-densifiant et opérant *via* la phase $SiO_{(g)}$, domine peu à peu le mécanisme de diffusion en volume et la vitesse de retrait diminue.

- A la fin du premier stade, la majorité des surfaces convexes ont disparu. Celles-ci étaient à l'origine du phénomène de transport vapeur. De fait, ce mécanisme non-densifiant disparait, permettant ainsi au mécanisme densifiant, toujours conduit par les surfaces concaves, de dominer à nouveau. Au fur et à mesure que la température augmente, la vitesse de retrait, thermiquement activée, augmente à nouveau lorsque le matériau rentre dans le deuxième stade du frittage.

- Au cours du deuxième stade de frittage, le matériau est constitué d'une porosité allongée et interconnectée. La dispersion en taille des pores, à l'origine de nouveaux gradients de courbures, explique la réapparition d'un mécanisme de transport vapeur entre pores. La pression partielle en $SiO_{(g)}$ étant plus élevée dans les gros pores que dans les petits, un flux de matière depuis les gros pores,

qui grossissent, remplit peu à peu les petits pores qui se bouchent. La taille moyenne des pores augmente donc. Cette augmentation, visible sur les microstructures, est à l'origine du ralentissement de la vitesse de retrait observé, alors même que la densité du matériau reste inférieure à 88 % TD_{Si}.
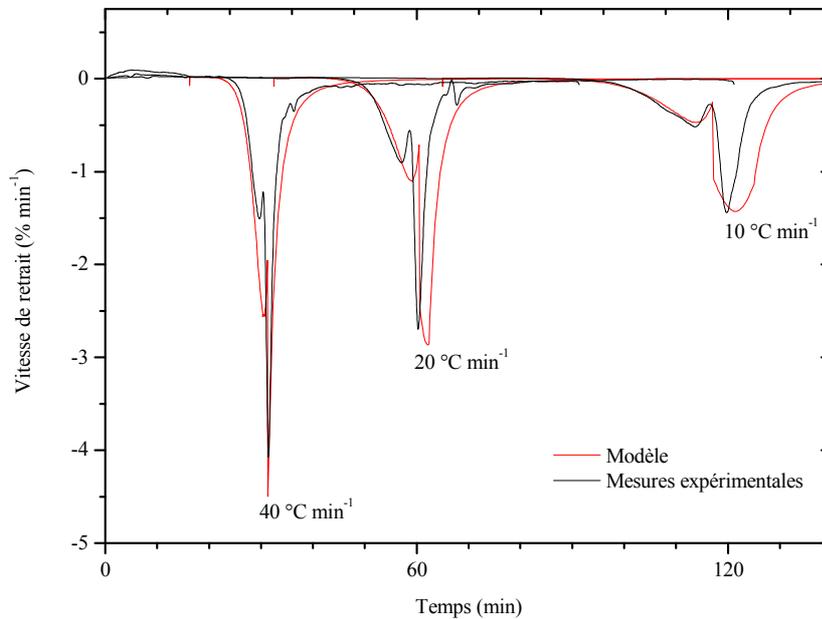
Figure 13 : En noir : vitesses de retrait mesurées en dilatométrie pour des vitesses de montée à 1400 °C de 10, 20 et 40 °C min^{-1} sous atmosphère contrôlée de SiO$_{(g)}$. Lors de ces expériences, la couche de silice à la surface des particules de silicium est stabilisée à l'aide d'un lit de poudres de silicium et de silice entourant l'échantillon. En rouge : vitesses de retrait modélisées dans le Chapitre IV.3.

Les principaux résultats de ces modèles cinétiques peuvent être rassemblés sur des cartes de frittage, tracées pour des particules de silicium de différents diamètres recouvertes ou non de silice. Sur ces cartes, sont représentés les mécanismes de frittage qui dominent dans des domaines de température/taille de cou. Dans ces domaines, sont tracées des lignes « isotemps » de frittage. Elles donnent, à une température donnée, le temps nécessaire pour atteindre un certain avancement dans le frittage, c'est-à-dire une certaine taille de cou.

- *Silicium pur*

Pour le silicium pur, les cartes de frittage sont relativement simples (Figure 14). Quelle que soit la taille des particules, la diffusion de surface (non-densifiant, nd) domine les cinétiques de frittage à toutes températures et tailles de cous. Cette conclusion est en accord avec les observations microstructurales où un grossissement grain important sans densification est observé.

Figure 14 : Cartes de frittage du silicium pur, sans silice, pour différentes tailles de particules.

Silicium pur – 2*a* = 100 nm

Silicium pur – 2*a* = 220 nm – Poudre VF
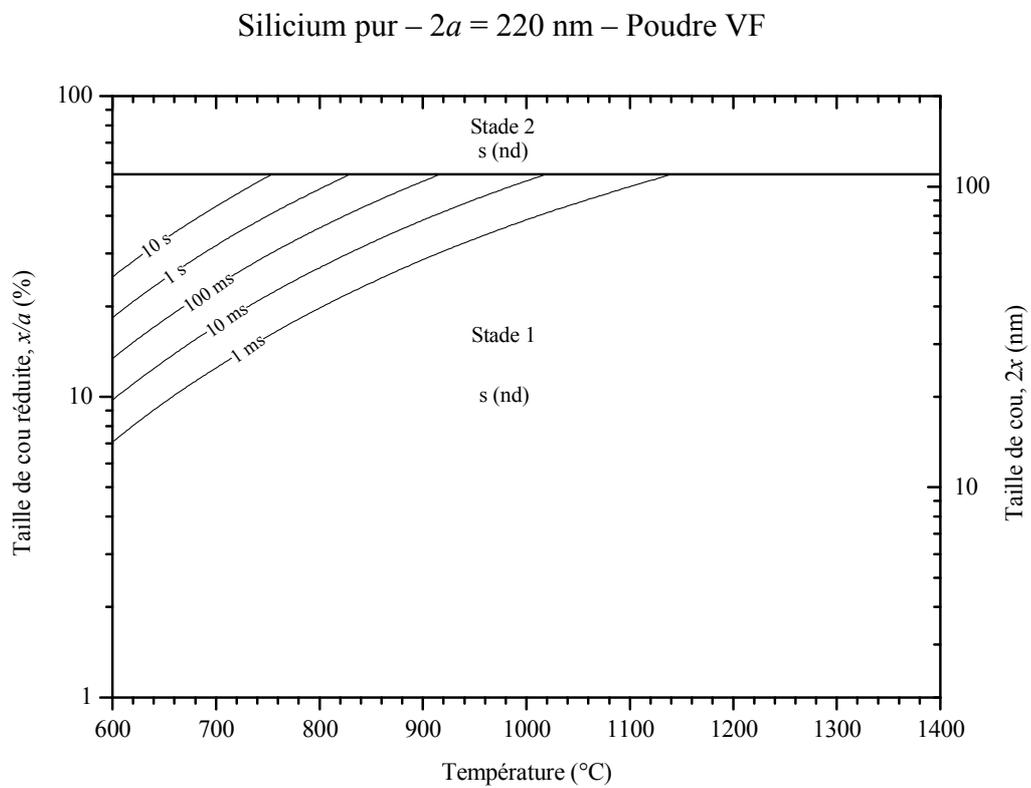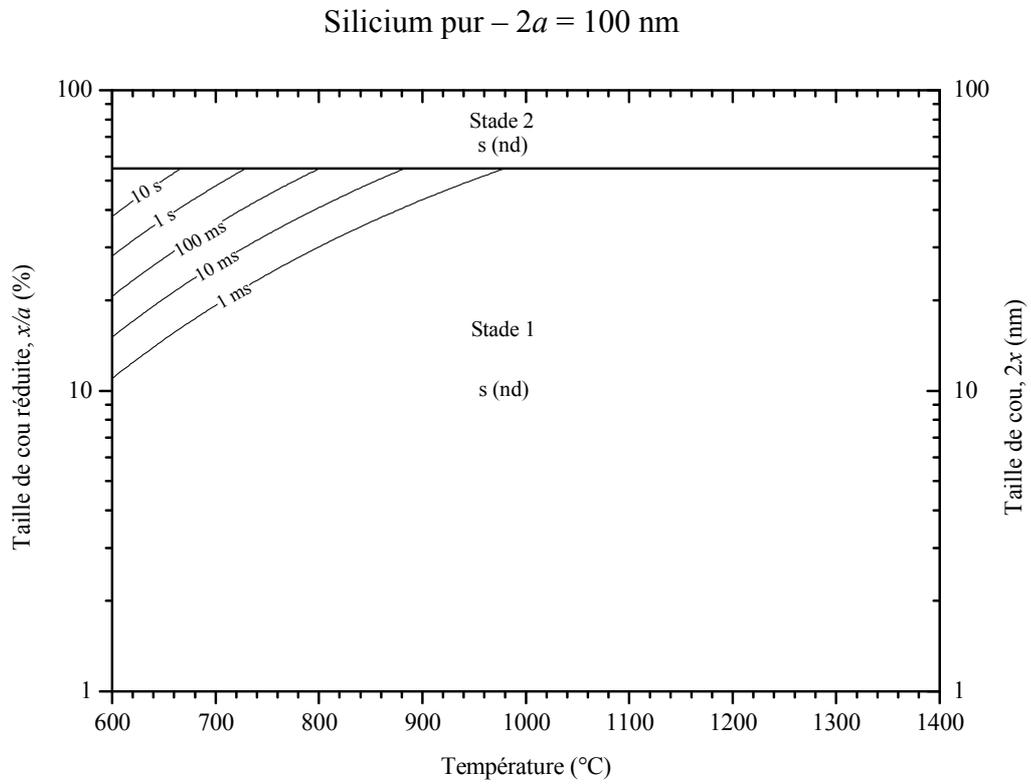
Figure 14 : (suite) Cartes de frittage du silicium pur, sans silice, pour différentes tailles de particules.

Silicium pur – 2*a* = 1 μm

Silicium pur – 2*a* = 10 μm
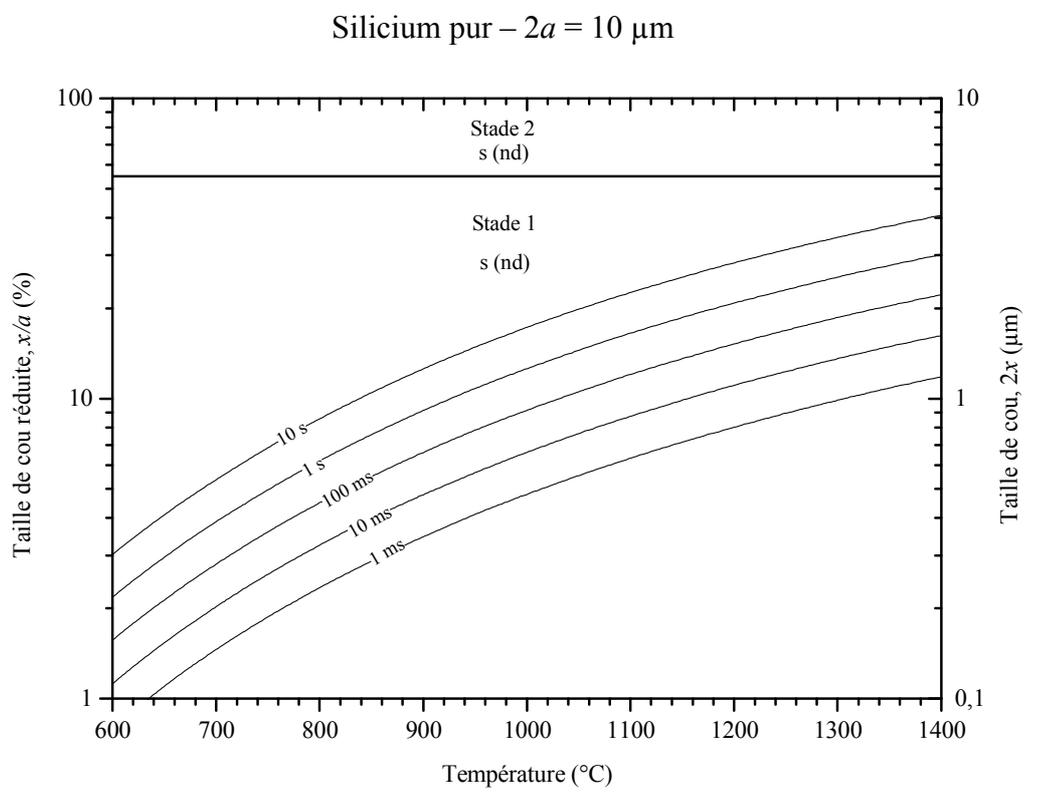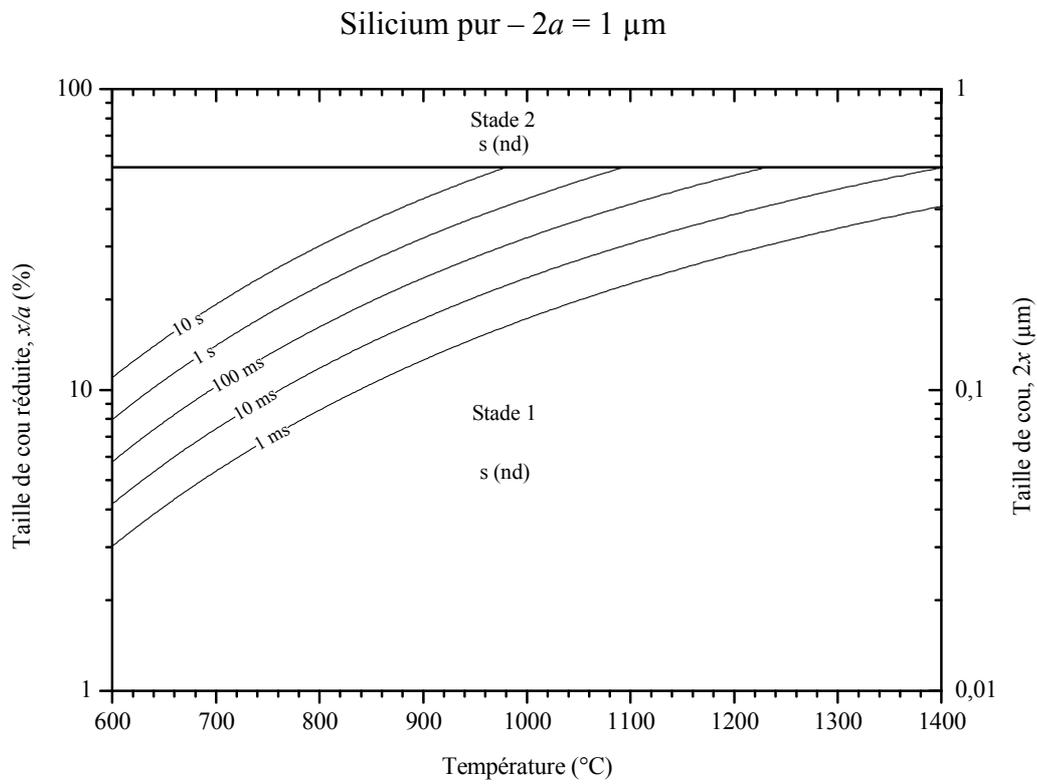
- *Silicium recouvert de silice*

Dans le cas de particules de silicium recouvertes de silice, les cinétiques de frittage sont plus complexes (Figure 15). Pour des particules relativement fines ($2a < 500$ nm), plusieurs mécanismes de frittage sont en compétition :

- La diffusion de surface (non-densifiant, s (nd)) domine les premières étapes du frittage, mais est fortement ralentie en comparaison du silicium pur. De fait, les vitesses de croissance de cous sont fortement diminuées en comparaison du silicium pur.

- A mesure que les cous grossissent, les mécanismes de transport vapeur (v (nd)) et de diffusion en volume finissent par dominer la diffusion de surface. Entre le domaine de diffusion de surface (s (nd)) et celui de diffusion en volume depuis le joint de grain (densifiant, l (d)), la diffusion en volume depuis la surface (l (nd)) domine. La diffusion en volume depuis le joint de grain (l (d)) ne domine le transport vapeur (v nd) que pour les hautes températures et les faibles avancements de frittage.

- Enfin, pour des tailles de cou supérieures à 55 % de la taille des particules, le frittage rentre dans son second stade. Une compétition entre densification, par diffusion en volume (l (d)), et grossissement des pores, par transport vapeur (v (nd)), a lieu.

Pour des particules de silicium recouvertes de silice, un changement de la taille des particules change significativement la position de chacun des domaines de frittage considérés plus haut.

Lorsque la taille des particules diminue, le domaine de diffusion de surface (s (nd)) grossit au détriment du domaine de transport vapeur (v (nd)). Pour des particules de diamètres supérieurs à 1 μm, le domaine de transport vapeur domine le frittage à toutes températures et tailles de cou.

Les domaines de diffusion en volume (l (nd) et l (d)) sont compris entre les domaines de diffusion de surface (s (nd) et de transport vapeur (v (nd)), pour des températures plus élevées que ~1300 °C. Lorsque la taille des particules diminue, les domaines de diffusion en volume (l (d) et l (nd)) se déplacent vers les basses températures et des avancements de frittage plus élevés pour concurrencer le transport vapeur. Pour des tailles de particules inférieures à 1 μm, la diffusion en volume a majoritairement lieu depuis le joint de grain alors qu'elle est majoritairement originaire de la surface des particules pour des tailles supérieures. La densification, qui ne peut avoir lieu que par diffusion depuis le joint de grain, ne peut donc se produire que pour des particules suffisamment fines ($2a < 500$ nm) et couvertes de silice, ce qui est accord avec les résultats présentés dans la littérature.

Figure 15 : Cartes de frittage du silicium recouvert de silice pour différentes tailles de particules.

Particules de silicium recouvertes de silice – 2*a* = 100 nm
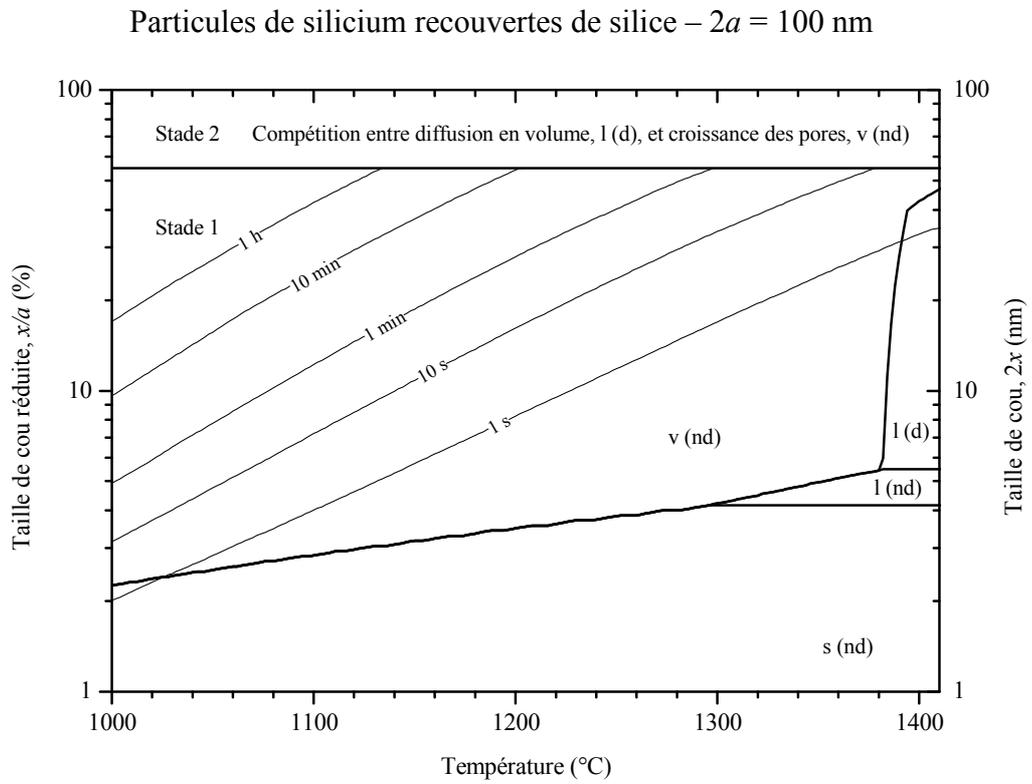
Particules de silicium recouvertes de silice – 2*a* = 220 nm – Poudre VF
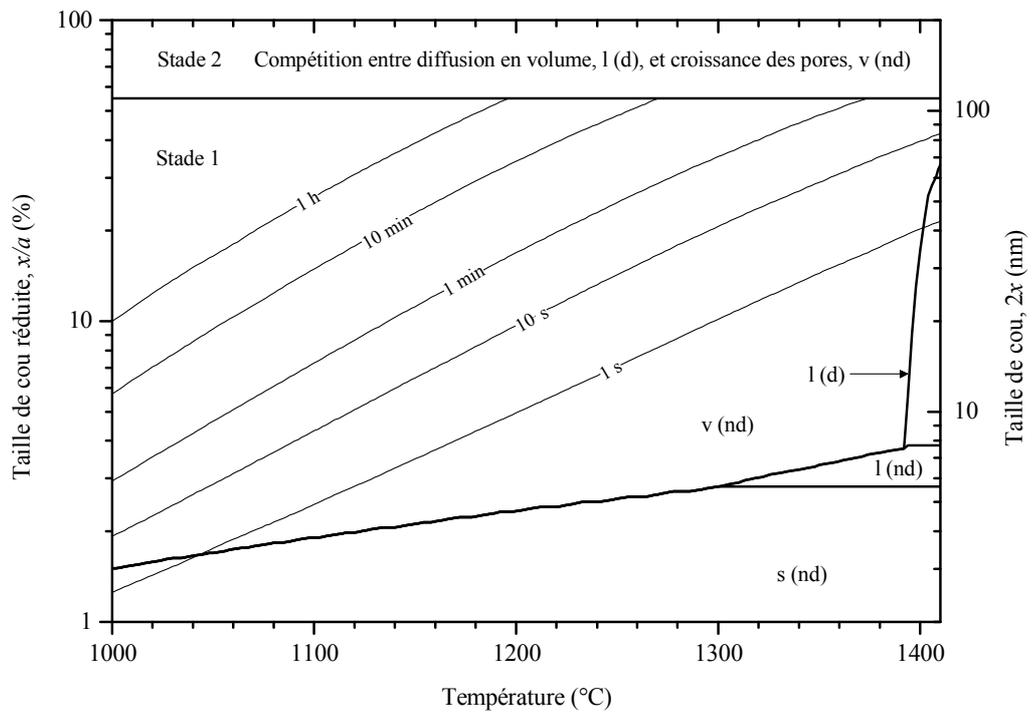
Figure 15 : (suite) Cartes de frittage du silicium recouvert de silice pour différentes tailles de particules.

Particules de silicium recouvertes de silice – $2a = 1$ μm

Particules de silicium recouvertes de silice – $2a = 10$ μm
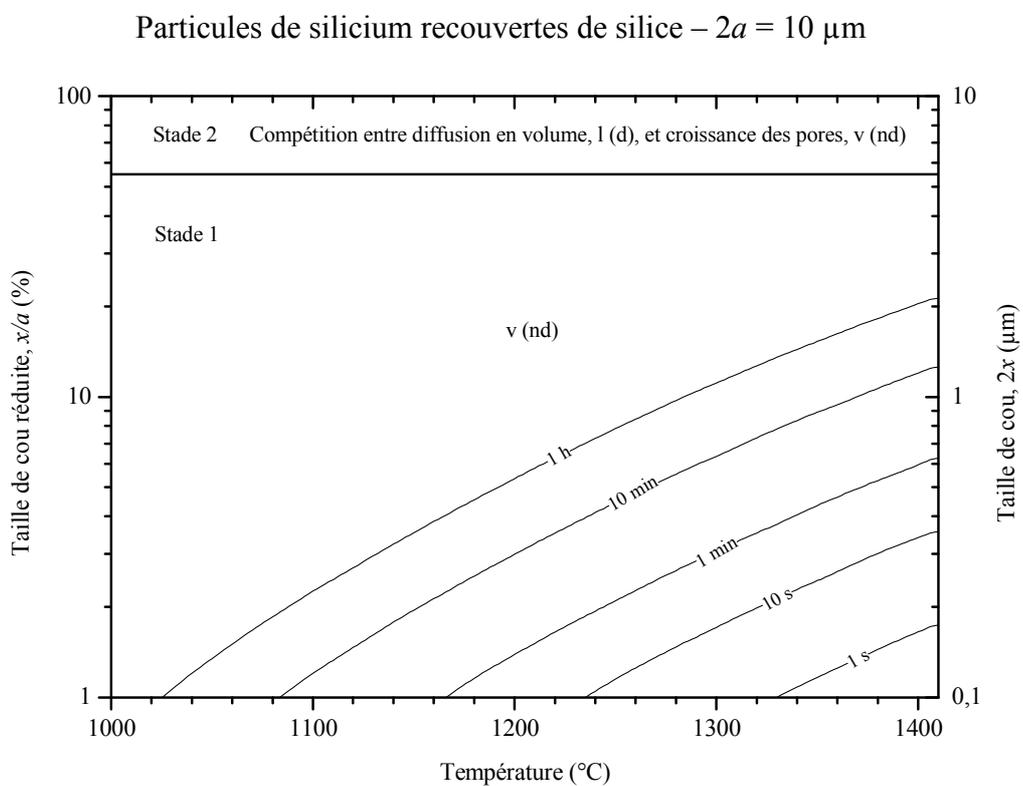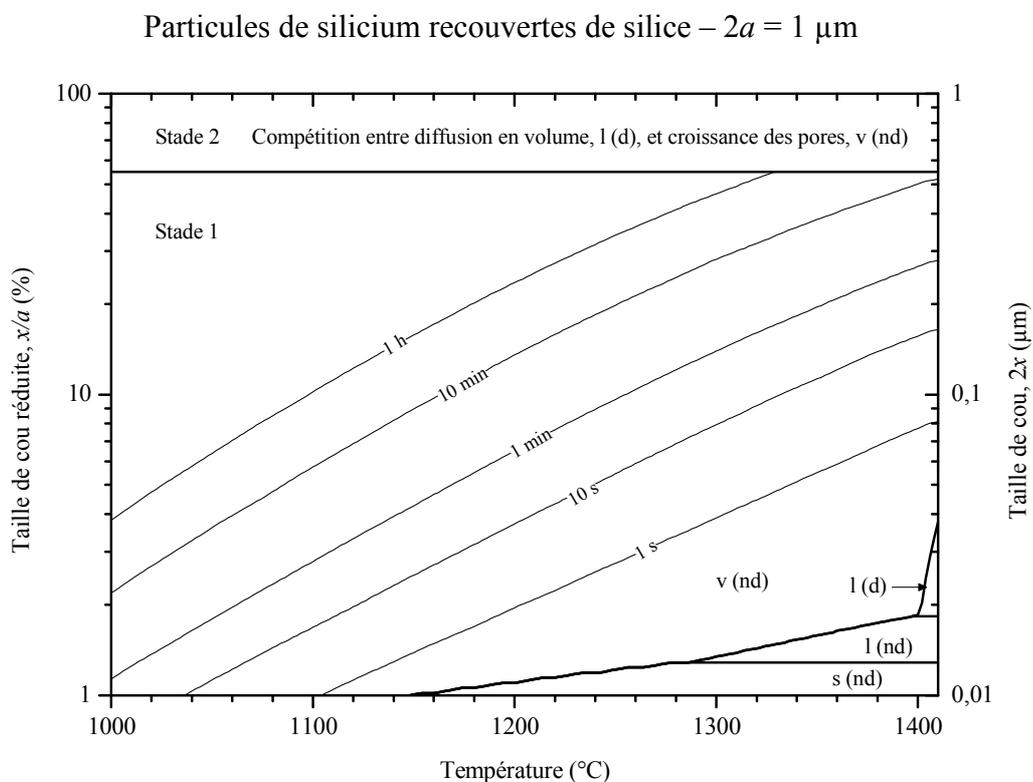
Conclusion et perspectives

L e défi à relever pour la filière silicium cristallin est la réalisation de wafers de silicium bas-coûts. La métallurgie des poudres est une des solutions envisagées à cette fin puisque cette technique permet de s'affranchir au moins des étapes de cristallisation et de découpe qui représentent jusqu'à un quart du prix d'un module.

Au cours de cette thèse, notre travail s'est focalisé sur une voie de frittage dite naturelle, qui permettrait de réduire considérablement les coûts de production, car le matériau pourrait alors être élaboré par un procédé continu.

Dans la littérature, l'identification des mécanismes de frittage du silicium était sujette à controverse. En particulier, le rôle de la couche de silice à la surface des particules de silicium restait incompris. De ce fait, nous avons commencé par identifier les mécanismes qui contrôlent la stabilité de cette couche en fonction de la température et de la pression partielle en espèce oxydante autour de l'échantillon. Dans nos conditions expérimentales (gaz sec, P_{H_2O} ~1 Pa), la température de début de réduction de la silice (~1020 °C) est en accord avec un mécanisme de réduction de la silice par le silicium sous forme de monoxyde de silicium (R_5).

$$Si_{(s)} + SiO_{2(s)} = 2SiO_{(g)} \tag{R_5}$$

Des observations microstructurales, effectuées à différents avancement du frittage et du processus de réduction de la silice, ont permis de montrer que la couche de silice à la surface des particules affectait fortement les mécanismes de frittage. Pour cette raison, des essais ont été réalisés à différentes températures, sous atmosphère sèche, et donc sans couche de silice. Ces essais ont été comparés à d'autres essais de frittage réalisés sous pression d'eau contrôlée, afin de stabiliser la dite couche, aux mêmes températures.

Les observations expérimentales, associées à des interprétations cinétiques basées sur des données de la littérature, permettent de conclure de la manière suivante :

- Dans le cas où la couche de silice est réduite, un mécanisme de diffusion de surface, non-densifiant et très rapide, est responsable d'un grossissement de grain important qui empêche toute densification par un autre mécanisme.

- Dans le cas où la couche de silice est stabilisée, ce mécanisme de diffusion de surface est fortement ralenti par la présence de silice qui bloque donc le grossissement de grain. De fait, d'autres mécanismes, dont certains ont un caractère densifiant, peuvent prendre place à plus haute température et améliorer la densification.

A la suite de ces observations, les cinétiques de densification en présence de silice ont été étudiées plus en détails à l'aide d'essais de dilatométrie. Le comportement lors du frittage a pu être divisé en deux étapes clairement identifiables sur les courbes de vitesse retrait par deux pics. Ce résultat est inattendu dans le cas du frittage d'un matériau monophasé tel que le silicium. Cependant, il a pu être expliqué avec l'aide d'un modèle cinétique utilisant des simplifications géométriques appropriées pour rendre compte de l'évolution de la microstructure observée expérimentalement.

Ces résultats ont été rassemblés sur de cartes de frittage afin de prévoir les effets d'une évolution de la taille initiale des particules sur les mécanismes de frittage. Pour des particules de silicium pur, le mécanisme de diffusion de surface domine quelle que soit la taille des particules et aucune densification n'est donc attendue. Pour des particules de silicium recouvertes de silice, le mécanisme de transport vapeur domine pour des tailles supérieures à 1 μm. Pour des particules plus fines ($2a < 500$ nm), un mécanisme de diffusion en volume peut concurrencer ce mécanisme de transport vapeur, au moins dans les débuts du premier et du second stade, et mener à une densification au moins partielle de l'échantillon.

Durant cette thèse, notre attention s'est portée sur la compréhension des mécanismes de frittage du silicium qui affectent essentiellement la densité, la pureté et la taille de grain du matériau. Ces paramètres affecteront directement le procédé d'élaboration de la cellule solaire. Idéalement, un matériau sans porosité résiduelle, de très haute pureté et possédant de très gros grains est recherché.

Le frittage du silicium pur est en réalité dominé par un mécanisme de grossissement de grains (la diffusion de surface) qui empêche toute densification. Cependant, une avancée majeure de notre étude est que ce grossissement de grain peut être évité, et la densification améliorée en stabilisant la couche de silice native à la surface des particules à haute température sous

atmosphère contrôlée. Au cours de ce travail, la densité a été augmentée de 63 % TD_{Si}, sous atmosphère réductrice conventionnelle, à 87 % TD_{Si} sous atmosphère contrôlée (1400 °C – 3 h), pour de fines particules de silicium de 220 nm de diamètre. Mais une densification complète requiert l'utilisation de particules encore plus fines qui ne sont pas disponibles commercialement. Dans tous les cas, le matériau final, toujours poreux, contient des niveaux d'oxygène important et une taille de grain d'environ 10 µm, qui ne sont pas favorables à l'élaboration de cellules solaires traditionnelles en silicium multi-cristallin.

Néanmoins, ces matériaux de silicium, élaborés à bas-coût, peuvent être envisagés comme substrats pour la réalisation de cellules solaires de silicium en couche mince. Cette approche à l'avantage de réduire le cahier des charges à remplir pour le matériau fritté. Des matériaux poreux et quelques peu contaminés en oxygène, carbone, bore ou phosphore, peuvent être envisagés, faisant du procédé de frittage naturel, facile à mettre en œuvre, un candidat sérieux et attractif.

Des matériaux plus denses, exempts d'impuretés métalliques, avec des tailles de grains de quelques centaines de µm en surface, seraient notamment très intéressants, car ils pourraient être envisagés pour la réalisation de cellules « couche mince » par un procédé relativement simple. Pour atteindre cet objectif, les développements suivants peuvent être proposés :

- L'étude des procédés de mise en forme afin d'augmenter la densité initiale des matériaux et de limiter l'effet néfaste du transport vapeur sur la densification. D'autre part, les défis à relever pour cette étape sont importants compte tenu de l'épaisseur et de la taille des substrats à réaliser.

- Le frittage de substrats de grandes tailles dans des fours industriels mettant en jeu des problématiques de génie des procédés majeures. Les cinétiques de réduction de la silice affectant fortement le frittage, une attention particulière doit être apportée au profil thermique du four, à l'atmosphère et aux pressions partielles de gaz oxydant.

- La recristallisation à l'état solide des matériaux obtenus par frittage. Ceci permettrait d'augmenter la taille des grains sans passer par des étapes de fusion locale du matériau souvent néfastes à la productivité du procédé.

- Enfin, des procédés nouveaux, tels que le frittage par induction ou le frittage sous courant pourraient être envisagés, dans le but d'augmenter à la fois la productivité et la densité finale des matériaux. Des essais de Spark Plasma Sintering (SPS) ont d'ores et déjà été réalisés et permis d'atteindre des densités de 100 % TD_{Si} avec des durées de frittage très courtes, de l'ordre de quelques minutes. Néanmoins, les problématiques liées à la contamination du matériau par

les éléments en contact au cours du frittage et aux cinétiques de réduction de la silice doivent être étudiées plus en détail.

English Manuscript

Introduction

Solar radiation is the most abundant renewable energy resource on earth. The sun emits energy at a rate of $3.8×10^{23}$ kW. Only a tiny fraction, approximately $1.08×10^{14}$ kW, reaches the surface of the earth. Even if only 0.01 % of this power could be recovered, it would be four times the world's total generating capacity of about 3000 GW [Cou10].

The annual solar radiation reaching the earth's surface is an order of magnitude greater than all the estimated (discovered and undiscovered) non-renewable energy resources, including fossil fuels and nuclear. However, as shown in Figure 1 [Age11a], 80 % of the present worldwide energy use is based on fossil fuels (coal, oil, natural gas) and several risks are associated with their use.

The global demand for fossil energies is boosted by the continuous growth of the BRIC countries (Brazil, Russia, India and China). It is expected to exceed annual production, probably within the next two decades. Since fossil resources are not homogenously distributed at the surface of the earth, shortages are expected to induce international economic and political conflicts. Moreover, burning fossil fuels releases emissions such as carbon dioxide or nitrogen oxides which affect the local regional and global environment.

Nuclear energy provides about 6 % of the world's energy with very low emission levels of carbon dioxide. In opposition to other energies, such as hydrology or biofuels and waste, its market share could be considerably increased, at least for a few hundred years, by building new power plants. However, there is an ongoing debate about the use of nuclear energy. Uranium is not sustainable and its production generates potential threats to environment and people, including health hazards and political conflicts. Moreover, the Fukushima Daiichi nuclear disaster has recently shown that the production of electricity from nuclear power plants, even in highly developed countries, is not completely safe. In addition, the production of long life nuclear waste is another issue that is far from being solved.
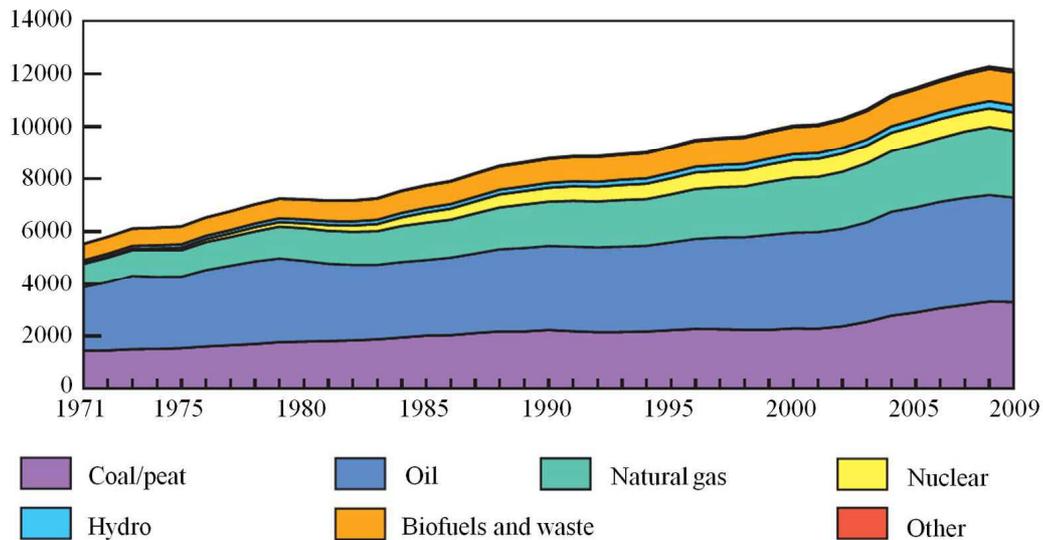
Figure 1: World total primary energy supply from 1971 to 2009 in Mega tons equivalent petrol (Mtep) [Age11a].

Comparatively, alternative energies represent less than 0.8 % of the global energy mix. An underlying reason is that they are relatively low-density and intermittent energies that require the use of economical and efficient storage. But most of their disadvantages are attributed to high installation costs that make them comparatively more expensive than fossil and fissile energies. Reducing the cost and improving the efficiency of conversion systems would then increase their proportion in the global energy mix to a significant extent. The European Union has policies and plans to obtain 20% of its energy needs through renewable energy by 2020. Analyses of resources in the future have been conducted and points to a major contribution by solar energy to global energy needs in the long term [Cou10, Age11b].

A major contribution to this ambitious objective can then be expected from photovoltaic conversion. Photovoltaic is a technology that generates direct current (DC) electrical power from semiconductors when they are illuminated by photons. This energy can be produced locally and can be directly used in a wide range of applications. However, its inherent attributes require the use of widespread suitable facilities that are not yet available: economical and efficient energy storage in off-grid areas and smart networks for grid-connected systems. Photovoltaic panels are solid-state and are therefore very rugged, with a long life. In the early days of solar cells in the 1960s and 1970s, more energy was required to produce a cell than it could ever deliver during its lifetime. Since then, dramatic improvements have taken place in their efficiency and manufacturing methods. The energy payback period has been reduced to about 2-4 years [BPP11], depending on the location of use, while panel lifetime has increased to over 25 years at least for crystalline silicon technologies [Cou10].

The solar photovoltaic proportion in the global energy market is insignificant but is growing rapidly. This growth is fueled by the European market, most particularly Germany that accounts for 43 % of the world output installed, which is represented in Figure 2 in Mega Watt peak (MWp) [Ass12]. The Watt peak refers to the unit of power delivered under full solar radiation. During the last decades, German and Japanese industries dominated the global photovoltaic market. From now on, thanks to lower production costs, China accounts for almost 50 % of the solar cell modules production although it represents less than 5 % of world output installed capacity [Age11b].
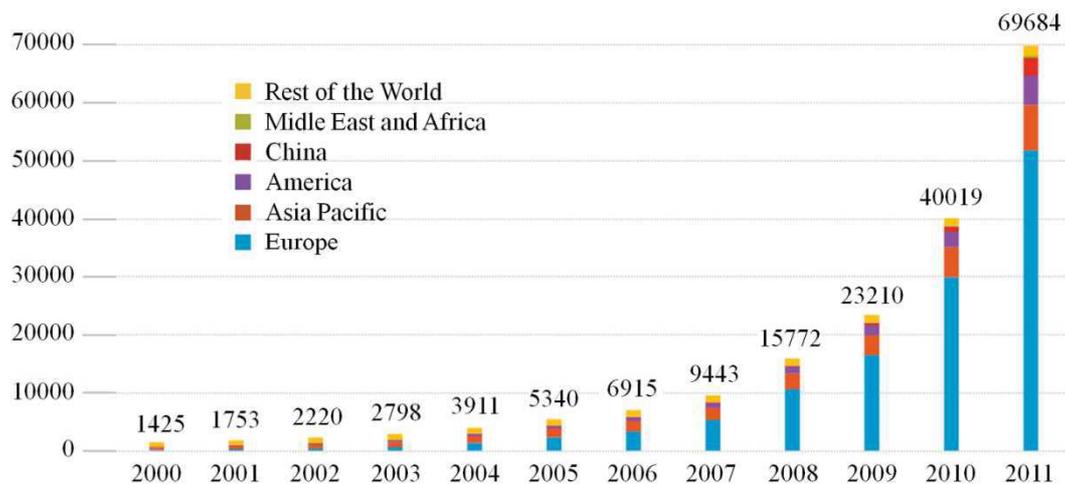
Figure 2: Evolution of global cumulative installed capacity from 2000 to 2011 in MWp [Ass12].

The driving force for the development of photovoltaic energy then relies on the reduction of the production cost measured in Euros per Watt peak (€/Wp). The final objective is to achieve a price that is equivalent to the electricity originating from conventional resources with a final cost of approximately 0.5 €/Wp. As can be seen in Figure 3, panels based on crystalline and polycrystalline silicon solar cells (c-Si) are the most common. Their retail price came down from about 30 €/Wp about 30 years ago to about 1.8 €/Wp in 2010.

More recently, thin-film solar panels emerged as new solutions because of their lower costs as they use lower amount of material. Amorphous silicon based solar cells (a-Si) were developed in the 1980s, but have not gained significant market share recently because of lower performances as compared to c-Si based technologies. Comparatively, cadmium telluride (CdTe) and copper indium gallium diselenide (CIGS) technologies are growing fast. Their efficiencies have gradually increased, while costs have decreased. Thin-film solar cells based on CdTe have now production costs less than 1 €/Wp. High efficiency multi-junction solar cells are also worth noting for concentrating photovoltaic applications (CPV). The light being

concentrated, the surface of the solar cell, which is composed of highly priced multiple band-gap material, is largely reduced and so is the electricity production cost.
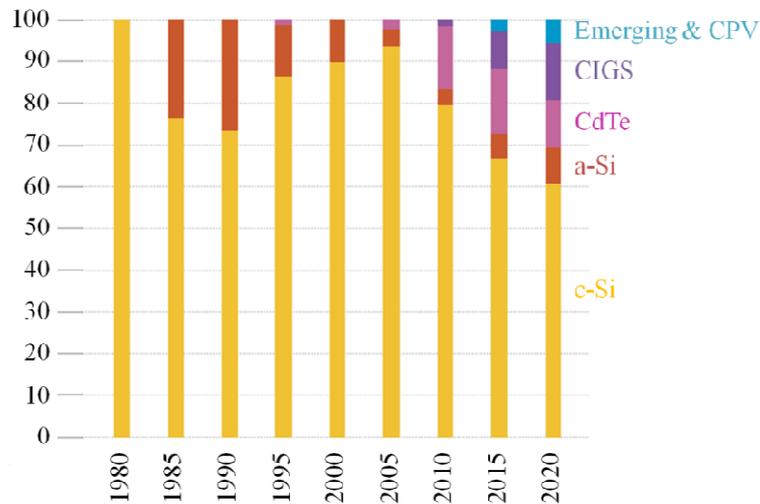
Figure 3: Evolution of technology market share and future trends in % [Ass11].

However, silicon based technologies are expected to remain largely dominant in the following years. Silicon being the second most common element of the earth's crust, it is a widely available and non-toxic material. During the last decades, the elaboration cost has been decreased mainly thanks to scale economies and incremental improvements during the solar cell elaboration process. However, as can be seen in Figure 4, the wafer cost, including the silicon raw material, the ingot crystallization and the wafering, accounts for more than 50 % of the module cost. These steps are now highly detrimental as they are hardly compressible.
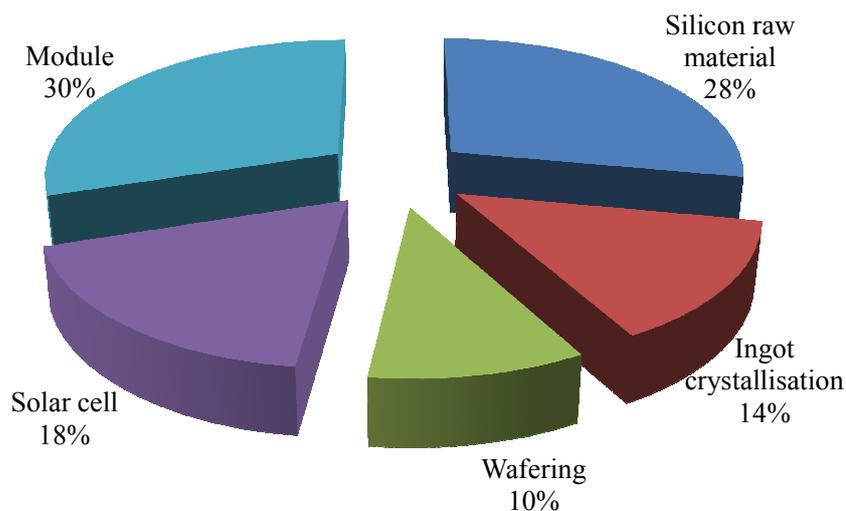
Figure 4: Repartition of the production cost of crystalline silicon solar cells in %
[Sun10, Vei11].

During this thesis, new processes for the elaboration of crystalline silicon wafers that fit for the elaboration of solar cells are investigated. These are based on the elaboration of low cost silicon substrates. Approximately 25 % of the module price being lost during crystallization and wafering, the basic idea is to avoid these steps using a powder metallurgy route. Powder metallurgy is based on the blending of fine powdered materials which are pressed into a desired shape (compaction), and then heated in a controlled atmosphere to bond the material in the solid state (sintering[2]).

The first chapter introduces the elaboration process of standard ingot based crystalline silicon solar cells. Basically, the steps presented in Figure 4 are described in greater details. Although large material losses are involved, this process is largely dominating the market mainly thanks to its robustness. But Crystalline Silicon Thin Film (CSiTF) solar cells emerge as alternative solutions to ingot based photovoltaic technologies. The material is the same as for standard silicon solar cells but with a thickness far less important; typically 10 to 50 μm instead of 250 μm. Then, CSiTF solar cells make their own of the advantages of silicon technologies including high efficiency, long-term reliability, material abundance and non-toxicity. However, they require low-cost substrates with thermo-mechanical and chemical properties as close as possible to silicon. From the literature experience, only silicon based materials fit these needs. The silicon powder metallurgy route is then peculiarly suitable since it avoids the need for at least wafering and crystallization. A hot pressing method has been investigated by the start-up S'Tile that allows achieving 9.2 % efficiency with a non-optimized 4 cm² Crystalline Silicon Thin Film solar cell, which is very encouraging result. But, pressure-less sintering methods are expected to be more competitive as the substrates can be produced and processed continuously. This is the method investigated in this manuscript.

The second chapter describes the experimental methods and materials used throughout this study. High temperature measurement techniques employed for the monitoring of the sintering process are presented. The selected powders are also characterized in terms of morphology, size and purity. Among the impurity considered, a particular attention is dedicated to oxygen contamination. Silicon powders are stored under Ar glove box but processed under air, their surface is then naturally covered by a thin layer of silica which is characterized in terms of thickness.

The third chapter focuses on the stability of this silica layer during high-temperature processing under He-H_2 atmosphere. Oxidation kinetics is then discussed. Thermochemical

---

[2] Actually sintering processes can be divided into two types: solid state sintering and liquid phase sintering. Solid state sintering occurs when the powder compact is processed wholly in a solid state at the sintering temperature, while liquid phase sintering occurs when a liquid phase is present in the powder compact during sintering. In the case of pure silicon, only one phase is involved which remains in its solid state. Then, in this manuscript "sintering" will refer to as "solid state sintering".

analyses along with thermogravimetric experiments are performed on un-compacted powders. Mechanisms involved during the reduction of the silica are identified and the initial silica layer thickness is estimated. Eventually, silica reduction kinetics is analyzed in silicon powder compacts and associated with microstructure evolution as a first route for the identification of silicon sintering mechanisms. The silica layer actually plays an important role by affecting sintering mechanisms.

The fourth chapter is dedicated to the elucidation of silicon sintering mechanisms. Solid state sintering mechanisms are first described and general kinetic equations introduced. Then, a literature review of silicon sintering studies is performed, showing that the identification of silicon sintering mechanisms is controversial. Especially, the role of the native silica layer at the particle surfaces is not fully understood. Densification kinetics is then measured for pure silicon and for silicon particles covered with silica using appropriate dilatometric measurement techniques. These experiments are compared to a sintering kinetic model taking into account the presence of silica at the particle surface. It is then possible to conclude on the role of the silica layer on silicon densification kinetics during sintering. Eventually, main results are summarized using Ashby sintering map formalism.

The fifth chapter investigates new sintering processes for silicon. A processing route based on TPS (Temperature Pressure Sintering) diagrams and involving a control of the silica layer stability is proposed in order to control the final density and microstructure of the material. Sintering of thin layer bimodal powder compact is also addressed. The objective here is to find the better compromise between the sinterability and the required final microstructure and geometry for photovoltaic applications. Eventually, another sintering method, so called Spark Plasma Sintering, is proposed in order to overcome the difficulties regarding silicon densification.

Chapter I. Context

T he development of the photovoltaic energy will depend on the reduction of the elaboration costs measured in €/Wp. New technologies, such as CIGS, CdTe or CPV, are currently under development and allow drastic reductions of the production costs. However, crystalline silicon solar cell technologies will still dominate the market in the next 25 years. Silicon material being largely abundant and non-toxic, it is a resource that can certainly meet the continuous growth of the photovoltaic industry.

In this chapter, the elaboration process of ingot based silicon solar cells is presented. The silicon material accounting for half the module price, new solutions based on Crystalline Silicon Thin Films (CSiTF) processes, which are less material consuming, are proposed as a solution for the reduction of the production costs. Eventually, issues regarding the substrate on which these thin layers must be attached are discussed.

I.1 **Silicon production**

I.1.1   Metallurgical Grade silicon (MG-Si)

Silicon is the second most common element of the earth's crust in weight, oxygen being the largest. It is usually combined with oxygen, forming silica and silicates. The carbothermic reduction of silica is the first step involved in the production of all types of silicon grades [CL03, Pro06].

$$SiO_{2(s)} + 2C_{(s)} = Si_{(l)} + 2CO_{(g)}$$
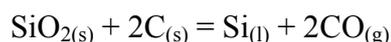
This reduction takes place at temperatures of 1900 to 2100 °C in electric arc furnaces filled with silica chunks (10-100 mm size) and carbon material. This leads to the production of liquid silicon metal so called "Metallurgical Grade silicon", with a typical purity of 98-99%. Most common impurities are Fe, Al, Ca, Ti, Mg and C.

Metallurgical grade silicon [CL03, Cor09] is mainly used as an alloying material in the aluminum industry or as a starting element for the production of poly-silicones in the chemical industry. Both segments represent approximately half of the worldwide production of Metallurgical grade silicon that reached 1.7 million tons in 2009.

Comparatively, the use of semi-conductor silicon in the electronic and photovoltaic industry in terms of volume is far less important. However, it is a high value product. Metallurgical silicon grade is detrimental as regards semi-conducting and solar conversion properties of the material. Upgrading processes are then required and result an increment of the silicon cost which is multiplied by a factor 30 to 50.

Slag based techniques are then used to partially refine the material. Dissolved elements less noble than silicon (Al, Ca and Mg) can be oxidized using an oxidizing gas or silica. From thermodynamic considerations, it is theoretically possible to remove Al and Ca to very low levels. In practice, this operation leads to partial oxidation of silicon resulting in significant material losses. Carbon is either dissolved or associated with silicon in the form of SiC carbides. As the liquid metal is cooled down, the carbon solubility in silicon decreases and the fraction of SiC carbides increases. These carbides are then captured in the slag phase and removed. The refined melt is eventually separated from the slag phase and cast in an iron mold or preferably onto a silicon powder bed in order to avoid any metallic contamination. Nevertheless, slag methods are not sufficient for high silicon refining, neither for Electronic Grade (EG-Si), nor for Solar Grade Silicon (SoG-Si).

I.1.2   Electronic Grade silicon (EG-Si)

Ultra-high purity silicon, in the range of ppb-ppt, is required for electronic industry. This is achieved by the preparation of a volatile silicon hydrochloride and its purification through fractional distillation. The hydrochloride is then decomposed as pure elemental silicon by reductive pyrolysis or chemical vapor deposition [CL03].

The most famous purification process to obtain EG-Si has been developed in the late fifties and is commonly referred to as the Siemens process. This process is based on the strong affinity of silicon for chloride (Cl). MG-Si reacts with chloridric acid (HCl) to give several chlorosilane by-products and mainly trichlorosilane ($SiHCl_3$) which is extracted using a distillation process. Trichorosilane is then vaporized, diluted with high purity hydrogen and introduced into the deposition reactor. The gas is thermally decomposed onto the surface of electrically heated (1100 °C) ultra-pure silicon seed rods, growing large rods of hyper-pure silicon (Figure I.1). Silicon rods are then crushed to give silicon chunks (Figure I.2).

During the Siemens process, powder particles often nucleate and are referred to as fines. These are detrimental as regards the process efficiency since they actually correspond to

material losses. Some powders studied during this thesis (F and VF powders, Chapter II) are probably recycled particles from this process.

A tie-in Siemens process is the Union Carbide process which involves the purification of trichlorosilane in silane (SiH_4) prior to its decomposition into elemental silicon using hydrogen. This results in a silicon deposit of extremely high purity. Other advantages of using SiH_4 instead of $SiHCl_3$ are that the pyrolisis may be operated at lower temperature (600-800 °C) with higher conversion efficiency and without the production of corrosive by-products. But silane based processes result in higher cost as additional steps are required to convert $SiHCl_3$ in SiH_4.

Both processes are highly energy consuming batched processes. The high energy consumption originates from the pyrolisis process during which silicon rods are placed in steel bell jars. The inner surface of the jars is cooled in order to avoid nucleation of fines and 90 % of the power supplied is then thermally lost.

Figure I.1: Photograph of silicon rods obtained through the Siemens process [Pro06].

I.1.3 Solar Grade silicon (SoG-Si)

Solar Grade silicon (SoG-Si) is defined as any silicon material that can be used for the fabrication of silicon solar cells. Although purity requirements for solar cells are not as stringent as for semiconductors, the silicon for photovoltaic industry was supplied by the microelectronic industry up to the year 2005. EG-Si production was then large enough to supply the photovoltaic industry in discarded materials which were sold at very competitive prices. Since then, the expansion of the photovoltaic industry led to supply shortages and

prices increased dramatically from 60 €/kg in 2004 to 300 €/kg in 2007. In the meantime, new silicon production plants were developed and silicon returned to lower prices (< 50 €/kg). The industry has thus been forced to select its silicon raw material from various second-grade elaboration processes, being less expensive than prime-grade processes [BMZ+08].

- *Siemens-derived processes*

Some processing routes are refinements of the chemical purification methods involving the use of volatile silicon hydrides. These routes referred to as "Siemens-based processes" are usually performed in a Fluidized Bed Reactor, where silane is decomposed on silicon seed powder particles sustained in a gas stream of silane and hydrogen. Pure silicon is collected in the form of silicon spheres that fall down under the effect of gravity at the bottom of the reactor. Energy losses and operating costs are considerably reduced compared to the conventional Siemens process as the reactor temperature is homogeneous and as the whole process can be run continuously. End products are small granules of poly-silicon (Figure I.2) which is a strong advantage compared to silicon chunks, as the feeding of the crucibles for ingot crystallization is improved [REC12].

Figure I.2: Photograph of silicon granules obtained in Fluidized Bed Reactor and silicon chunks obtained from milled silicon rods [REC12].

- *Upgraded metallurgical processes*

Metallurgical processes are other promising routes to achieve adequate purity, large production ability and acceptable costs. Unlike Siemens based processes, the upgraded metallurgical routes do not involve distillation steps and are *de facto* less dangerous [MG09]

and less energy consuming. These processes take advantage of the directional solidification step during which impurities can be segregated in the liquid phase where they are usually more soluble than in the solid phase. For most of the metallic impurities, the equilibrium distribution coefficient, k, defined as the ratio of the equilibrium solid and liquid compositions is less than 10^{-4}. Therefore, by controlling the heat flux within the solidification device, the amount of impurities in the solid phase can be decreased drastically. However, some elements (B, P) have an equilibrium distribution coefficient in silicon close to 1, making it difficult to separate them from the solid phase. These are electronic doping element for silicon and their concentration must then be closely controlled during all steps of the manufacturing process. Selection of raw materials (quartz and carbon) containing acceptable amount of these impurities is then crucial.

Multiple routes are currently investigated in order to control the amount of boron which is the impurity that is the most difficult to segregate ($k = 0,8$). Some routes use highly pure raw materials dedicated to the photovoltaic industry. Although it is a very cost effective process (25-30 €/kg), the final material often contains too many impurities and is then not suitable for the direct production of solar cells. The Elkem route proposes a ladle extraction method followed by a chemical leaching post-treatment [MG09, Sve11]. The final material cost is less than 25-30 €/kg and solar cell efficiencies higher than 16 % can be achieved. The Photosil process uses a plasma torch treatment in order to reduce the amount of boron. The expected final cost of the material is as low as 15 €/kg [KDC+10] and solar cell efficiencies around 17 % are currently obtained.

- *Other processes*

Among the other techniques available, electrolysis, electrolytic purification methods, metallic reduction of silicon are worth noting [CL03, YO10, YSO11]. Although revisited in the literature, these methods do not seem to have been the subject of extensive new programs since the eighties.

I.2 Bulk crystalline silicon solar cells

In this section, the conventional elaboration process of first generation solar cells is described. This process involves the production of approximately 200-250 μm thick crystallized silicon wafers [KEF+03] which are then processed using conventional methods adapted from the electronic industry [TDCA03].

I.2.1   Silicon crystallization and wafering

- *Silicon crystallization*

EG-Si or SoG-Si chunks are first melted and crystallized. Two crystallization processes are mainly used. The Czochralski process (Figure I.3) allows the production of cylindrical mono-crystalline silicon ingots while the Gradient Freeze process (Figure I.4) produces parallelepiped multi-crystalline silicon ingots [KEF+03].

In the Czochralski process, a mono-crystalline seed is first made to contact silicon melt. Then the seed (usually <100>-oriented) is slowly withdrawn vertically to the melt surface whereby the liquid crystallizes at the seed. Owing to the clockwise seed rotation and counter-clockwise crucible rotation the crystal cross section is mostly circular. The temperature of the melt and the withdrawal speed are controlled in order to achieve a dislocation-free ingot with a given diameter. After crystallization, the ingot sides are cut in order to obtain pseudo-square shaped ingots that yield to a better utilization of the module area.
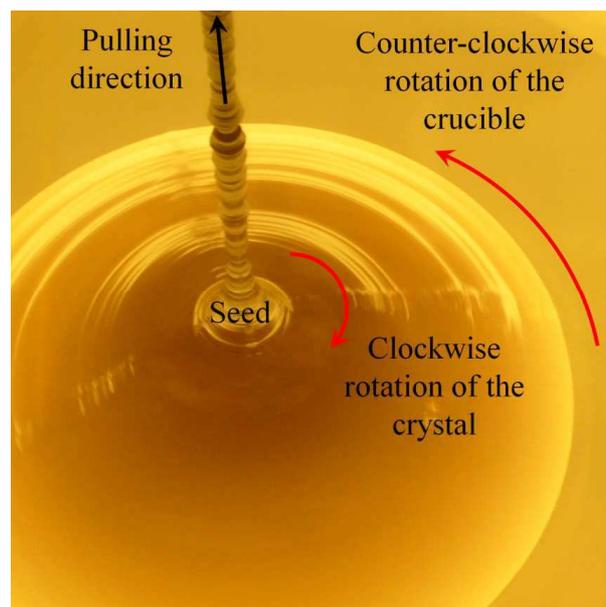
Figure I.3: Crystallization of silicon during the Czochralski process [Vei11].

The Gradient Freeze process corresponds to the directional crystallization of the silicon melt in a quartz crucible. Crystallization starts at the bottom of the crucible where the heat is extracted. Then the crystallization front moves progressively from the bottom to the top of the crucible. A parallelepiped ingot with elongated grains along the vertical direction is then obtained. If the crystallization is initiated on a mono-crystalline seed, it is theoretically possible to achieve mono-crystalline ingots. However, the use of large crucibles in the industry makes it difficult to achieve this in practice; the technique is then often referred to as

"quasi-mono" or "mono-like" solidification. At the end of the crystallization, the sides of the ingot are discarded, as they contain impurities that diffused from the crucible (bottom and lateral sides of the ingot) or that were segregated during the crystallization (top of the ingot). Then, the crystallized ingots are separated in smaller parallelepiped pieces, called bricks, with a section compatible with the standard of the solar cell industry.
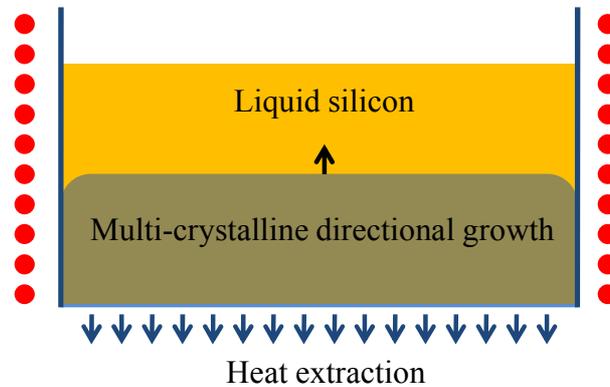
Figure I.4: Crystallization of silicon during the Gradient Freeze process.

Although the crystallization front rate in the Gradient Freeze process (~1 cm/h) is lower than in the Czochralski process (~10 cm/h), the global rate of crystallization is larger (~10 kg/h compared to ~2 kg/h) as the section of the ingot is much larger. Nowadays, Gradient Freeze processes allow to elaborate 25 bricks in a single solidification run as ingots of more than 600 kg can be achieved. This process is then less energy consuming than the Czochralski process. The main crystalline defects in multi-crystalline silicon are grain boundaries and dislocations. For a given silicon grade, the Gradient Freeze technique is less expensive and is now dominating the photovoltaic market.

- *Wafering*

The silicon parts are then glued to a substrate holder and placed in a multi-wire saw that slices them into final wafers (Figure I.5). Cutting is achieved by abrasive slurry (Figure I.6), which is supplied through nozzles over the wire and carried by the wire into the sawing channel. The slurry consists of a suspension of hard grinding particles usually made of SiC. Today, another technique under development uses diamond abrasive glued to the metallic wire. Both materials are very expensive and account for 25 to 35 % of the total slicing cost [KEF+03]. Silicon material is continuously removed through the interaction of the SiC particles below the moving wire and the silicon surface. The silicon material loss represents 40 % of the whole material and is referred to as the kerf loss (Figure I.6). After sawing the surface of the wafer is damaged from the abrasive process over a thickness of 5 to 10 µm and contaminated

with organic and inorganic remnants from the slurry. Therefore, the wafers have to be cleaned and the saw damage removed by etching before a solar cell can be fabricated.
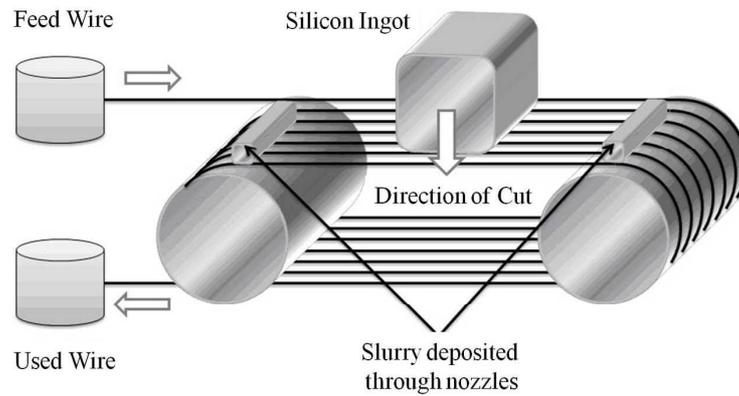
Figure I.5: Schematic diagram depicting the principle of the multi-wire sawing technique.
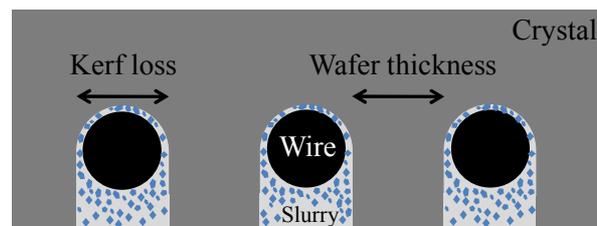
Figure I.6: Cross section of wire, slurry with abrasive and crystal in the cutting zone, showing the Kerf loss.

The sawing performance has been improved by reducing the amount of slurry and improving the wire life time. However, the slicing cost accounts for half of the wafer price and is really damaging as regards the development of the photovoltaic industry [KEF+03].

I.2.2   Solar cell fabrication steps

The structure of a conventional solar cell is represented in Figure I.7. Generally p-type wafer are used (boron doped ingots) and so called the base.
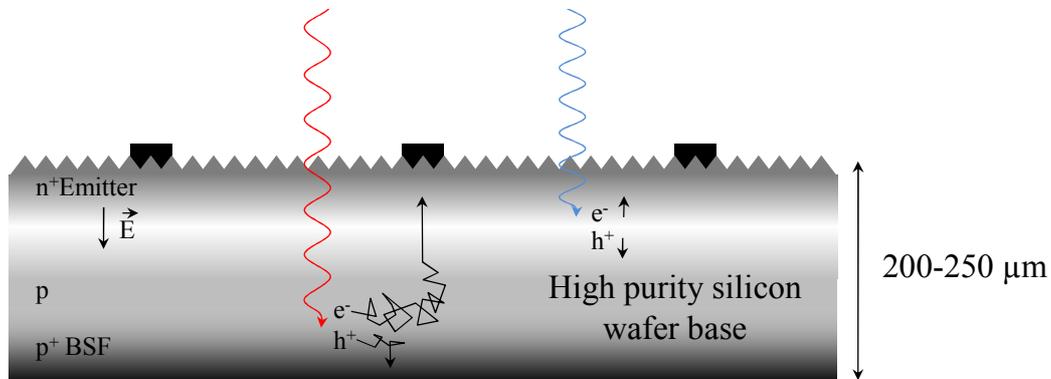
Figure I.7: Structure of a standard silicon solar cell.

The elaboration process involves the following steps [TDCA03]:

- *Texturing*

Silicon wafers are first textured. Basically, alkaline (KOH or NaOH-based) or acid solutions etch anisotropically the silicon surface to give square-base pyramids, whose size is adjusted to a few microns by controlling etching time and temperature. In a textured surface, a ray can be reflected towards a neighboring pyramid and hence absorption of photons is enhanced.

- *Phosphorous diffusion*

The silicon substrate obtained from crystallization is usually p-type, *i.e.* the majority carriers are holes. In order to collect the minority carriers (electrons), which are generated in the substrate, a p-n junction must be created. Phosphorus is generally used as the n-type doping element and diffused at the surface of the wafer which is then called the emitter (n^+ region).

- *Anti-reflection coating*

A PECVD (Plasma-Enhanced Chemical Vapor Deposition) deposit of hydrogenated silicon nitride is performed in order to decrease the reflectivity of the surface. This material also passivates the surface, *i.e.* saturates the dangling bonds with hydrogen in order to avoid the trapping of generated carriers.

- *Contacts*

Metal contacts are then screen printed. Silver lines are deposited as front contacts while aluminum is used as a back contact. Contacts are then co-fired to obtain an ohmic behavior. The aluminum back contact makes a eutectic with silicon that over-dopes (p^+) the wafer surface and creates a Back Surface Field that repulses electrons.

- *General considerations*

All these process steps aimed to improve:
- The absorption of the light. The material must absorb the largest part of the solar spectrum. For wavelength lower than 365 nm, the absorption is readily induced in silicon, as a direct transition is available for the photons which are then absorbed within the first angstrom of the solar cell [HB98]. For higher wavelength, the band gap is indirect and the absorption must be assisted by a phonon. The absorption coefficient decreases by several decades. The whole wafer thickness is then needed to absorb the photons (Figure I.8).
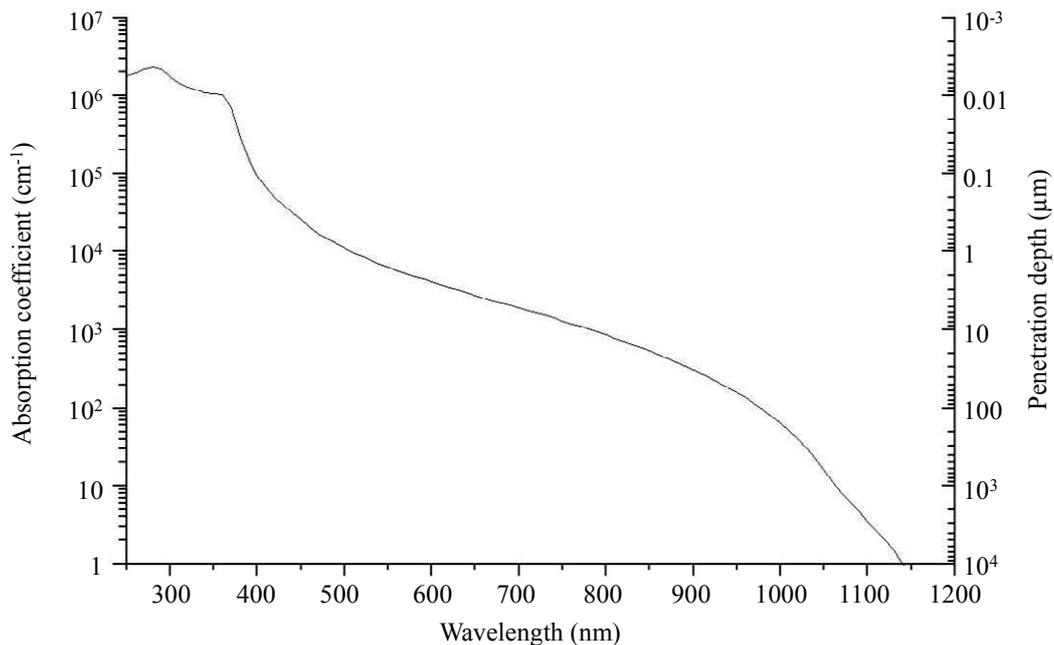
Figure I.8: Absorption coefficient and penetration depth of the light in crystalline silicon depending on the wavelength at room temperature [HB98].

- The conversion of the photons in chemical energy *via* the creation and the transport of free carriers (electrons and holes). Once created, minority carriers (holes in the n part of the material and electrons in the p part) have to diffuse towards the vicinity of the p-n junction where they are collected under the effect

of the electric field (Figure I.7). The key issue is that minority carriers can recombine before they are collected, resulting in detrimental energy conversion. The minority carrier diffusion length, *L*, is conventionally defined with respect to minority carrier life time, *ι*, and diffusion coefficient, *D*, in Equation (I.1) [HB98].

$$L = \sqrt{D\iota} \tag{I.1}$$

As a rule of thumb, the carrier diffusion length must be 2-3 times larger than the cell thickness to ensure good collection efficiency. The life time, mobility and then diffusion length of the minority carriers depend on:

- o Defect and impurity levels that strongly affect the bulk recombination.

- o Surface dangling bonds that affect surface recombination. Surface can be then passivated with hydrogenated silicon nitride.

In first generation solar cells, volume recombination plays an important role as the thickness of the cell, and then the distance for electrons to reach the junction is important.

I.3   Thin film crystalline silicon solar cells

The main advantage of the first generation solar cells is the robustness of the elaboration process. During the last decades, the elaboration cost in €/Wp has been decreased mainly thanks to scale economies and incremental improvements. However, the material cost and waste during the wafering are detrimental as regards the development of the photovoltaic industry.

In this section, crystalline silicon thin film solar cells, a new generation of silicon solar cells, will be considered. The material structure is the same as for bulk silicon solar cells but with a thickness far less important: typically, 10 to 50 μm instead of 250 μm. Such thin layers must be attached to a low cost substrate. The sawing step being circumvolved, appreciable cost diminution can be expected.

However, such technological breakthrough significantly affects the behavior of the solar cell. New requirements apply and are first discussed. Then, developments on thin film silicon solar cells deposited on high grade silicon substrates are presented to show the potential of this new approach. Eventually, the issue regarding the substrate to which the solar cell is to be attached is addressed.

I.3.1   Crystalline Silicon Thin Film solar cells (CSiTF) particularities

The basic structure of Crystalline Silicon Thin Film solar cells is introduced in Figure I.9.
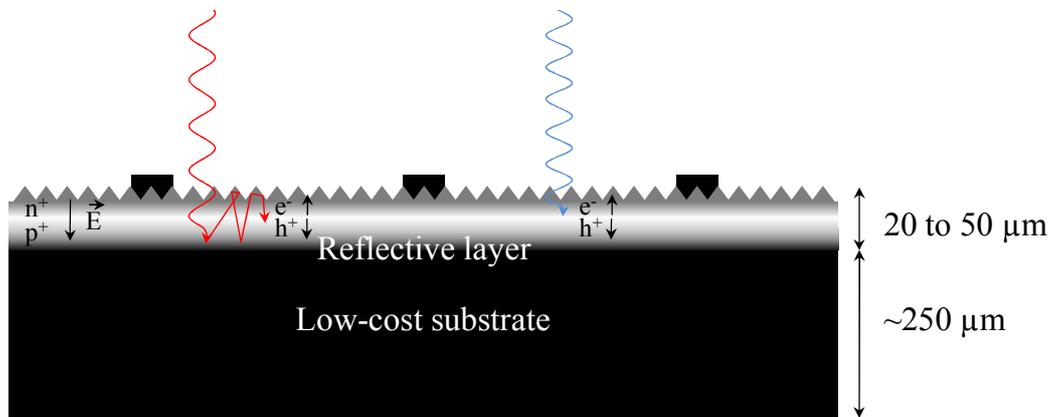
Figure I.9: Structure of a Crystalline Silicon Thin Film solar cell structure.

The main differences compared to bulk silicon solar cells presented in Figure I.7 are:

- *Lower bulk recombination rates*

Thinner silicon solar cells offer a performance advantage by decreasing the length that the minority carriers have to cross towards the junction. For a given material quality, *i.e.* a given minority carrier diffusion length, the bulk-carrier recombination would be reduced and the voltage delivered by the cell would be improved by simply reducing the thickness of the material [Sop03].

- *Higher surface recombination rates*

As the cell thickness is reduced, the surface recombination becomes significantly important with respect to bulk recombination. The important conclusion is that although a reduction in thickness can lead to a performance increase, it can have an opposite effect if surface recombination is not also reduced [Sop03].

- *Lower absorption properties*

As the silicon thickness is decreased, the number of absorbed photons is reduced. For low wavelength, typically less than 400-500 nm, the difference will be negligible. But for higher wavelength, as the absorption coefficient is much lower, a large part of the solar energy is expected to be lost. Antireflection coatings and front-side texturing play a critical role by increasing the path of the light rays. These losses can be also avoided using light trapping methods, such as back-side Bragg arrays that act as a reflective layer (Figure I.9).

- *Deposition techniques*

High crystalline quality active layer deposition techniques are required. The fabrication of crystalline thin film solar cells usually involves the epitaxial growth of silicon through high temperature Chemical Vapor Deposition (CVD) techniques. Such process is currently used in the electronic industry but suffers from low production rates and high production costs that are detrimental as regards their development in the photovoltaic industry. The main issue concerns the elaboration of low cost substrates that meet the requirements discussed in the next section.

I.3.2   The needs for low cost substrates

The best result on CSiTF has been obtained by the University of New South Wales by progressive thinning of a conventional silicon wafer through chemical etching. The efficiency of the 50 μm thick self-supporting silicon solar cell is 21.5 % that must be compared to 25 % maximal efficiency obtained on a standard silicon substrate [WZWG96]. In this study, the objective was not to propose a solution that can be transferred to industry, but rather to show that high efficiency can be obtained. Therefore, the issue relies on the low cost production of crystalline silicon thin layers. The material substrate properties actually determine the range of accessible processes and the final efficiency of the produced solar cells.

- *Low temperature substrates*

First, low cost approaches addressed low temperature substrates such as silica or metallic substrates [RCJMJWWB01]. These substrates do not allow treatments at temperatures higher than 600-700 °C. Therefore, melting re-crystallization or high temperature epitaxial growth methods cannot be used. Such substrates are then restricted to the elaboration of amorphous or nano-crystalline silicon thin film materials deposited through low temperature processes such as Physical Vapor Deposition (PVD). Processes are numerous and all have their particular advantages [Sop03]. Usually, solid phase crystallization methods such as low temperature (550-600 °C) and long time (60-70 h) annealing or metal induced crystallization are proposed to improve the crystalline quality of the silicon layer. However, because of the poor electronic properties of the re-crystallized layer, solar cell efficiencies higher than 10 % are not expected.

Layer transfer methods have also been proposed. Basically the idea is to grow the epitaxial layer on a mono-crystalline substrate of which surface has been porosified by HF-etching. High temperature processing steps, namely the epitaxial growth and phosphorous diffusion, are then realized before the layer is separated from the silicon substrate and transferred to the low temperature substrate. However, these processes are not easily applied to large surface

silicon solar cells and to industrial scales as the separation and transfer steps are highly unreliable.

- *High temperature substrates*

The high temperature approach allows the deposition of silicon with high crystalline quality through epitaxial growth (Liquid or Vapor Phase Epitaxy). This approach is often referred to as the Wafer Equivalent concept (Figure I.10), first addressed by ISE Fraunhofer (Fraunhofer Institut for Solar Energy Systems) [RHEW04].

The Epitaxial Wafer Equivalent (EpiWE) [RHEW04] is one of the simplest methods to realize a CSiTF solar cell. It is based on the use of a low-cost silicon substrate, on which the thin active silicon base layer is deposited epitaxially (Figure I.10). Its main advantages are obvious: only one processing step, namely the silicon epitaxy, is needed for its manufacture, and it is fully compatible with all industrial processing steps used today. An efficiency of 17.6 % has been achieved on a 4 cm² and 37 μm thick EpiWE solar cell grown on a mono-crystalline substrate [FHHS98]. For higher solar cell surfaces (92 cm²), the efficiency drops to 15.1 % on a mono-crystalline substrate and to 14 % on multi-crystalline [SSR07]. However, the challenge for its realization is still related to a suitable substrate, which has to feature sufficiently high crystal quality for low-defect epitaxial growth and low impurity content at low cost. Proposed substrates are typically the ribbon or cast silicon substrates [KEF+03].
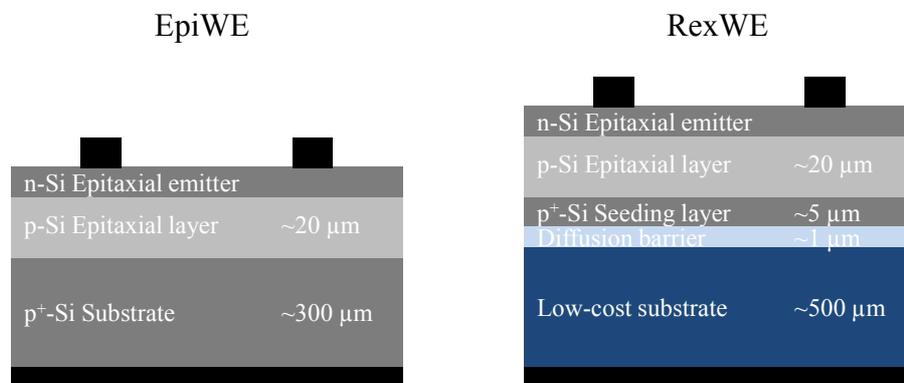
Figure I.10: Structures of an epitaxial wafer equivalent (left) and re-crystallized wafer equivalent (right) solar cells, from [RHEW04].

With a somewhat equivalent structure, IMEC (Interuniversity Microelectronics Centre in Leuven, Belgium) developed a CSiTF solar cell with a porous Bragg reflector produced by electro-anodizing of the silicon substrate surface [NPKF+09]. The reflector is annealed under hydrogen at 1130 °C before the epitaxial growth and a closed pore surface is obtained with the same crystallographic orientation as the substrate (Figure I.11). This is necessary as

regards both the epitaxial growth and the resistivity of the reflector that affects the quality of the back contact.

Epitaxial layer

Reorganized porous silicon stack

Highly doped mono-crystalline substrate
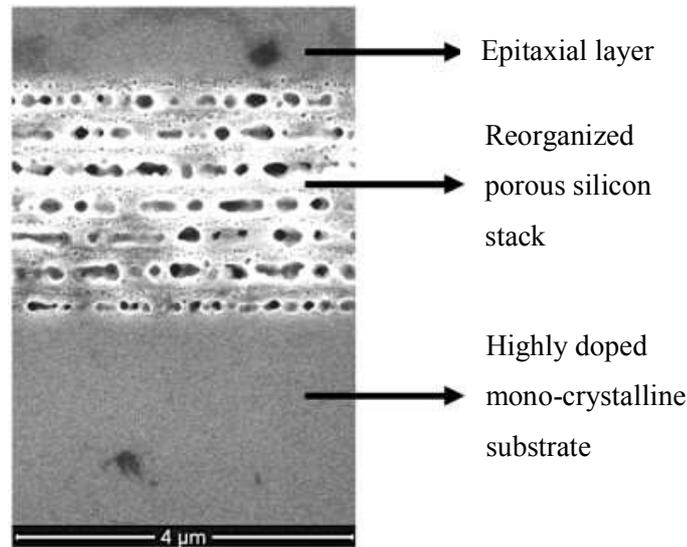
Figure I.11: SEM micrograph picture of a reorganized porous silicon reflector with epitaxial layer on top of the porous silicon stack realized by IMEC [NPKF+09].

Another process, referred to as Recrystallized Wafer Equivalent (RexWE) [RHEW04], has been proposed by ISE Fraunhofer in order to apply the Wafer Equivalent approach to foreign substrate materials (Figure I.10). Substrates are typically ceramic materials that match the thermal expansion coefficient of silicon and that are chemically inert with respect to silicon. The substrate is first encapsulated in a diffusion barrier layer. Barrier materials are insulating materials (silica) or advantageously a conductive material (doped SiC, SiN) that protects the silicon layer from the diffusion of impurities possibly originating from the low cost substrate. Then, a 1 to 5 µm thick silicon layer is deposited and re-crystallized by Zone Melting Re-crystallization. Then, an epitaxial silicon layer is deposited on the now large-grained (few cm²) seeding layer and the former forms the active light absorber of the solar cell.

Numerous foreign materials have been tested as low cost substrates [RCJMJWWB01]. ISE Fraunhofer achieved a 10.7 % solar cell efficiency using a silicon carbide substrate infiltrated with silicon [Bau03]. The best solar cell efficiency of 11 % has been obtained on a graphite substrate encapsulated in silicon carbide by ZAE Bayern [KBGA08]. Mullite ($3Al_2O_3$-$2SiO_2$) materials have also been investigated as substrate materials, but up to now, efficiencies higher than 8.2 % have never been reached [SBBP02]. Alumina substrate has also been proposed by IMEC, using a distinct process of solar cell elaboration based on aluminum induced crystallization. However, the efficiency remains as low as 8 % showing that this material is not suitable for photovoltaic application [GCG+08]. Comparatively, if the RexWE process is applied to a silicon substrate, the achieved efficiency is 13.5 % [KPES03].

- *Summary*

A large number of processes have been proposed to realize CSiTF solar cells. The presentation has focused on high temperature substrates which are expected to give the higher solar cell efficiencies and a competitive production cost.

Lower efficiencies are usually obtained on foreign substrates. This is attributed to thermo-mechanical mismatches between the substrate and the grown layer which generates stresses and defects inside and at the interface with the grown layer that are detrimental to its electrical properties.

The conclusion is that silicon materials are the best substrates for the epitaxial growth of silicon. The issue then relies on the production cost and crystalline quality of the substrate. In the next section, a new process for the low cost production of silicon substrates is proposed.

I.4   S'Tile process: silicon sintered substrates for the PV industry

S'Tile is a start-up founded in 2007 in Poitiers by Pr. Alain Straboni which aims to develop solar cell fabrication processes using sintered silicon substrates. The basic idea is to circumvolve the wafering step that is highly detrimental as regards the reduction of the photovoltaic electricity cost. Instead of being obtained through the slicing silicon of ingots, the material is directly shaped using a powder metallurgy route [Str04].

I.4.1   Solar cell structures and substrate requirements

Two silicon solar cell processing routes have been investigated by the company [Bel10, Gra12] (Table I.1).

The original idea was to use the sintered multi-crystalline material as a bulk silicon wafer for the production of standard silicon solar cells [Bel10]. Its main advantage is obvious: highly reliable conventional solar cell processes presented in section I.2 can be directly applied to this wafer. However, the material should meet the standard multi-crystalline quality requirements, that is to say, high purity levels (< ppm in metallic impurities) and large grain sizes (mm² to cm²).

The second investigated route proposes to solve the issue regarding the elaboration of low cost substrates for CSiTF solar cells [Gra12]. Two major alternative processes can be proposed:
- An EpiWE-like process can be used. In this case, the grain size at the substrate surface must be at least a few times larger than the thickness of the epitaxial layer that will be grown on top. The impurity contamination levels must remain as low as possible since no diffusion barrier protect the epitaxial layer.

- A RexWE-like process can also be proposed. Although the elaboration is comparatively more complex than the EpiWE-like process, it bypasses the need for high crystalline quality (large grain size, no dislocations…) and high purity levels. Silicon powders obtained from metallurgical routes or recycled from the standard wafering process can be used.

Process	Impurities		Grain size	Density	Advantages / Drawbacks
	Metallic ppm	O / C ppm			
Conventional (bulk)	< 1	< 10	> 1 mm	Full density	The conventional process is highly reliable. Complete wafer re-crystallization needed
EpiWE	< 1	< 100	> 100 µm at the surface	Pore closure 92 % TD_{Si}	High potential efficiencies (19 % on mono-crystalline Si) Surface re-crystallization needed
RexWE	< 10-100	< 1000	-	Pore closure 92 % TD_{Si}	Allow the use of recycled silicon powders Complex elaboration process

Table I.1: Material requirements depending on the silicon solar cell elaboration process envisaged.

The material requirements for the elaboration of conventional solar cells are highly difficult to achieve by low cost processing like the Powder Metallurgy route. As will be shown in this manuscript and as already shown in previous thesis and literature [MW85, Der06, Bel10], it is impossible to obtain a wafer of high crystalline quality using only the sintering route. Full wafer re-crystallization through melting processes has then been proposed to enlarge the grain size. This usually leads to high level of contamination or defects in the substrate which are inappropriate for the production of bulk silicon solar cells. The solar cell efficiency is then limited to 8.9 % with a production cost that is drastically increased due to the re-crystallization step [Bel10].

Wafer Equivalent concepts have comparatively a higher potential efficiency. Using the RexWE concept, S'Tile achieved 9.2 % efficiency with a non-optimized (no texturing and no light trapping) 4 cm² solar cell [GBL+09]. The open circuit voltage obtained is as large as 580 mV which is a very encouraging result as CSiTF on low cost substrates usually suffer from too small open voltage values. It indicates that the sintered silicon substrate is appropriate to obtain high quality wafer equivalent. Using this approach the company estimates that the production cost of a solar cell can be divided by two [Gra12] (Table I.2).

	Conventional solar cell	S'Tile solar cell
Silicon raw material	0.30	0.05
Ingot	0.05	-
Wafer	0.29	0.05
Cell	0.29	0.35
Total	0.93	0.45

Table I.2: Estimated production cost in €/Wc of a RexWE S'Tile solar cell compared to a conventional solar cell.

To our knowledge, the EpiWE approach has never been investigated on low cost crystalline silicon substrates. However, this approach would be very competitive as only one processing step, namely the silicon epitaxy, is needed for its manufacture. The issue actually relies on the low cost realization of a large grain seeding layer at the top surface with low-defect and low impurity levels for the epitaxial growth of the thin film material.

I.4.2   Substrate elaboration process – Technological and scientific issues

Sintering is a solid state thermal process in which isolated particles bond together to give a consolidated material. The basic phenomena occurring during this process are neck growth between particles, densification and coarsening.

The main advantage of this process is that it avoids silicon waste originating from wire sawing. For a given purity of raw silicon material, this makes the sintering process cost lower than the conventional block casting and sawing process. Also, there is no theoretical limit for the size of the sample, so that the limitation would be the same as for regular wafers.

The elaboration process investigated by S'Tile is a hot pressing method. The silicon sample composed of micrometric powders is processed below the melting point of silicon under an applied pressure about of 30 to 40 MPa. Under the effect of the pressure, plastic deformation occurs leading to neck growth between particles and to densification up to 100 % of the theoretical density (TD_{Si}).

The method investigated in this thesis is a pressure-less sintering route. Neck growth between particles occurs only under the effect of the temperature and curvature gradients at the scale of the particles. The pressure-less sintering route will not allow full densification of the sample. However, regarding the application, the elaboration of pore free wafers is not always necessary (Table I.1). Bulk solar cell processes require full densification mainly because the wafer must be completely re-crystallized by melting. More precisely, melting of the substrate creates bubbles that drastically damage the wafer shape.

EpiWE or RexWE processes are not as stringent as regards the porosity of the substrate. If surface melting re-crystallization is needed (EpiWE), it is assumed that the porosity must be closed (density higher than 92 % TD_{Si}), so that infiltration of the substrate by the melt does not occur.

The contamination of the specimen by the specimen holder is thought to be less stringent in the case of pressure-less sintering. But as a major difference with hot-pressing, the sample must be shaped before the sintering process. Eventually, pressure-less sintering is comparatively more competitive as the material can be produced and processed continuously.

I.5 Conclusion

The photovoltaic energy suffers from high processing cost that makes the electricity comparatively more expensive than the electricity produced from nuclear plants in France. In this chapter, the processing route for the production of standard silicon solar cells has been introduced. Half of the module price arising from the elaboration of the wafer (silicon purification, crystallization, and wafering), significant cost reductions are expected if at least one of these processing steps can be avoided.

Crystalline Silicon Thin Film (CSiTF) technologies emerge as alternative solutions to wafer based photovoltaic technologies. They make their own of the advantages of silicon technologies including high efficiency, long-term reliability, material abundance and non-toxicity. However, they require low-cost substrates with thermo-mechanical and chemical properties as close as possible from silicon. From the literature, only silicon based materials fulfil these needs.

The silicon powder metallurgy route is *a priori* peculiarly suitable since it avoids the need for at least wafering and crystallization. If a barrier diffusion layer is added between the substrate and the CSiTF solar cell, it even avoids, at least partially, highly expensive purification processes.

Chapter II. Starting materials and methods

T his chapter describes the experimental methods and materials used throughout this study. The selected powders are first characterized in terms of morphology, size and purity. Then high temperature measurement techniques employed for the study of the sintering process are presented. Eventually, this chapter focuses on the metallographic procedures used for the microstructural observations of the sintered materials.

II.1 Powders and characteristics

During this study, four different silicon powders are used. These powders are named, C (Coarse), M (Medium), F (Fine) and VF (Very Fine) as listed in Table II.1 with their main characteristics.

The VF powder is supplied by S'Tile (see Chapter I.4) and comes from silane decomposition in a Fluidized Bed Reactor (FBR). C, M and F powders are supplied by Alfa Aesar. Powders origin is unclear. However, from particle morphology studies in section II.1.1, the fabrication process is deduced. C and M powders are obtained from milling processes while F certainly originates from a Siemens-based process (see Chapter I.1).

Powders are chosen such as to cover a wide range of particle size. Using appropriate measurement techniques, in section II.1.2, the particle size is estimated. As regards the application, the use of large particles is of great interest in order to reach large grain sizes after sintering. To this purpose, C and M powders were selected. However, as regards the sintering process, the use of finer particles is needed. First, finer particles, of higher specific surface area, often undergo better densification. Then, the study of sintering mechanisms and kinetics requires mono-dispersed powders made of spherical shape particles such as the VF ones. Finally, F powders were chosen from their relatively good compressibility behavior as will be seen in section II.1.4.

All the selected powders verify the photovoltaic purity criteria and contain less than one ppm of metallic impurities. However, these powders are contaminated with carbon and oxygen. As will be seen in section II.1.3, the oxygen content can be related to an equivalent silica layer thickness at the silicon particle surface (e_{SiO_2} in Table II.1) that strongly affects sintering mechanisms.

Powder	Supplier	Size (μm)	Morphology	Elaboration process	Initial conditioning	e_{SiO_2} (nm)
C	Alfa Aesar Ref: 36212	120	Angular	Milling	Under air	1 ± 3
M	Alfa Aesar Ref: 35662	2 to 35	Angular	Milling	Under air	2.2 ± 0.3
F	Alfa Aesar Ref: 35662	0.3 to 20	Spherical	Siemens derivate	Under Argon	0.7 ± 0.1
VF	S'Tile	0.22	Spherical	Siemens derivate	Under Argon	0.4 ± 0.1

Table II.1: Main characteristics of the powders.

II.1.1   Powder morphologies

The powder morphologies (Figure II.1) were observed by standard Scanning Electron Microscopy (SEM, LEO STEREOSCAN 440) or Field Emission Gun Scanning Electron Microscopy (FEG-SEM, CARL ZEISS ULTRA55) for the finest one. These microscopes were also used for metallographic observations and coupled with Energy Dispersive Spectroscopy profiles (EDS, EDAX Phoenix). Some observations were also performed using Transmission Electron Microscopy (TEM, JEOL 3010-LaB6).

C and M powders are made of angular particles, most probably obtained through milling of discarded wafers from the electronic or photovoltaic industry.

F powder is made of spherical agglomerates (10 μm) that contain finer particles. This powder most probably originates from a Siemens-based process (see Chapter I.1) during which fine powders are often collected on the cold wall of the reactor [CHC95]. Observed agglomerates

might originate from a spray drying process often used to improve the castability of fine powders.

VF powder comes from silane decomposition in a Fluidized Bed Reactor (FBR). This powder is made of "chain like" agglomerates constituted of very fine and mono-dispersed spherical primary particles of 200 nm diameter.

C - 200 µm

M - 100 µm

F - 10 µm
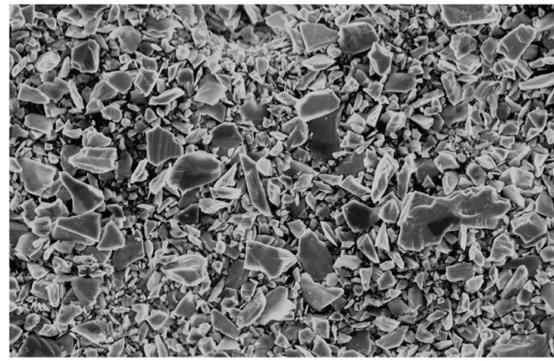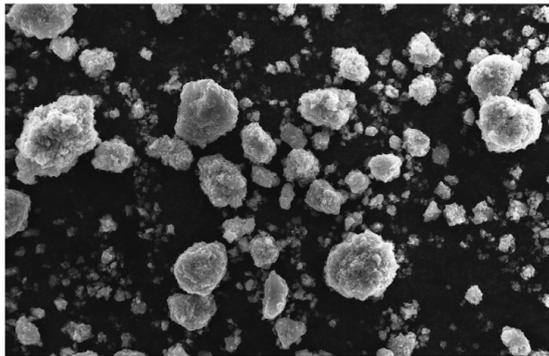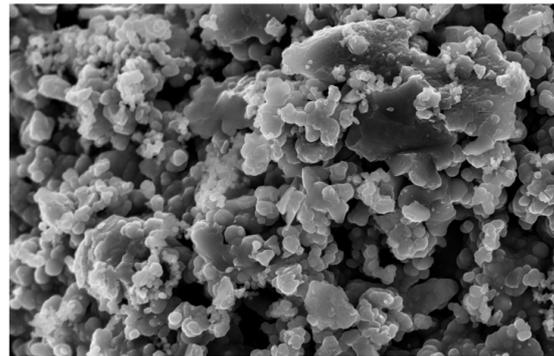
F - 500 nm

VF - 1 µm

VF - 200 nm

Figure II.1: SEM and TEM micrographs of the powders (SEM: C and M, FEG-SEM: F and VF, TEM: VF).

II.1.2   Particle size characterization

Powders consist of particles of various dimensions and complex shapes. The estimation of a particle size is thus equivocal and depends on the measurement technique. However, combination of several techniques can bring interesting results as regards the size, size dispersion and shape factor of the particles (Table II.2). In this study, Brunauer–Emmett–Teller (BET, Micromeritics ASAP 2020) and laser granulometry (Malvern Instruments mastersizer) are carried out to determine the specific area and particle sizes. The specific surface area (*SSA*) of a powder is the solid-vapor surface with respect to the sample mass (directly related to the volume) in $m^2\ g^{-1}$.

Powder	SSA_{BET}	SSA_{laser}^{sphere}	Shape factor, n	Estimated primary particle diameter, $2a$
	\($m^2\ g^{-1}$\)			\(μm\)
C	0.09	0.02	polyhedron $n = 5.6$	$2a_{BET}^{polyhedron} = 120$
M	3.0	0.95	polyhedron $n = 4.2$	$2a_{laser}^{V,10\%}$ to $2a_{laser}^{V,90\%}$ $= 2$ to 35
F	2.6	2.4 to 3.1	sphere	$2a_{laser}^{V,10\%}$ to $2a_{laser}^{V,90\%}$ $= 0.3$ to 20
VF	11.7	~~7.4~~*	sphere	$2a_{BET}^{sphere} = 0.22$

*Struck out value refers to an inappropriate estimation.

Table II.2: Measured specific surface area (SSA) from BET and laser granulometry as well as estimated particle size.

a)   Specific surface area from BET

BET specific surface area measurement is based on the amount of gas adsorbed at the powder particle surface versus the partial pressure. The BET technique actually measures the quantity

of gas needed to saturate the particle surface. By assuming that each gas molecule occupies a precise area, the surface area of the powder can be calculated from the adsorption behavior.

Silicon powders are placed in a sealed sample tube. The powder particle surface is first desorbed under vacuum by increasing the temperature up to 150 °C. The tube under vacuum is then cooled down in liquid nitrogen. Nitrogen gas, inserted in the sample tube, is finally used as an adsorbing gas. The specific surface area, SSA_{BET}, given in Table II.2, is then deduced from the plot of the adsorbed volume as a function of gas pressure. In the case of spherical particles, the particle size can be roughly estimated from the diameter of a sphere of equivalent volume in Equation (II.1), where TD_{Si} is the theoretical density of silicon [Ger94].

$$2\,a_{BET}^{sphere} = \frac{6}{TD_{Si}\,SSA_{BET}} \tag{II.1}$$

b)   Specific surface area from laser granulometry

Laser granulometry is a technique that provides the powder particle size dispersion in volume over a wide size range (from 300 nm to 1 mm). This technique is based on the scattering of a monochromatic and coherent light (laser) by moving dispersed particles. The data are collected using a photodiode detector array. From wave optics analysis, the scattering angle varies inversely with the gyration diameter of the particles. The intensity of the scattered signal is proportional to the number of analyzed particles and to the square of the particle diameter. Computer analysis of the intensity versus angle data shall determine the particle size distribution which is generally expressed as the volume of analyzed particles versus the size of the particle.

In this study, silicon powders are dispersed in ethanol with an ultrasonic device. The laser wavelength is 632.8 nm (He-Ne), the threshold limit is thus approximately 300 nm. Size distributions are given in volume percentage as well as cumulated volume percentage in Figure II.2. Values of practical use are, $2a_{laser}^{V,10\%}$, $2a_{laser}^{V,50\%}$ and $2a_{laser}^{V,90\%}$, that gives a good representation of the particle size dispersion. These values represent the upper size limit for respectively 10 %, 50 % and 90 % of the particle volume.

In laser measurements, the particle size is referred as the gyration diameter of the particle. Assuming that the particle is a sphere, the specific surface area of the powder, SSA_{laser}^{sphere}, is estimated from Equation (II.2) and can be compared to SSA_{BET} in Table II.2. TD_{Si} corresponds to the theoretical density of silicon, N_i to the number of particles in a given class, S_i to their total surface, V_i to their volume and a_i to their radius.

$$SSA_{laser}^{sphere} = \frac{\sum_i N_i S_i}{TD_{Si} \sum_i N_i V_i} = \frac{3\sum_i N_i a_i^2}{TD_{Si} \sum_i N_i a_i^3} \tag{II.2}$$
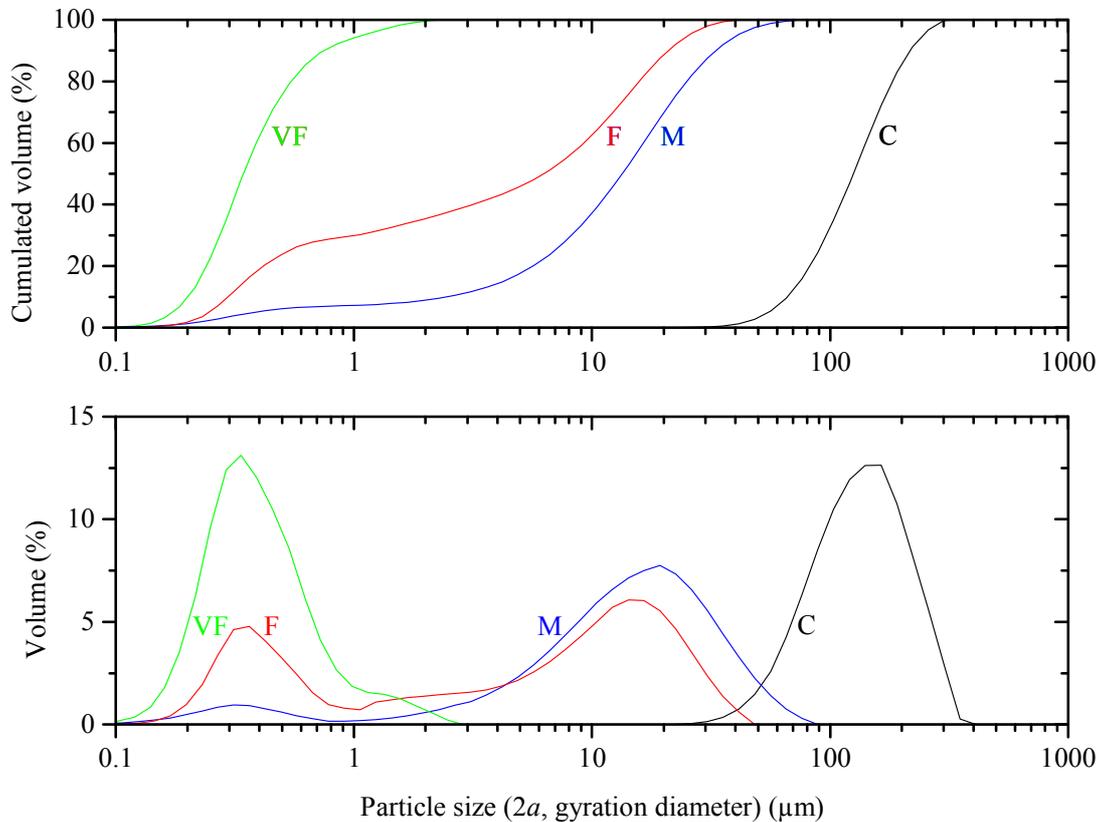
Figure II.2: Laser granulometry curves realized on powders dispersed in ethanol with an ultrasonic device for 1 min.

c)   **Combination of laser granulometry and BET measurements**

From laser measurements, C and VF powders show a mono-dispersed like behavior, while M and F powders are poly-dispersed over a wide size range. It is then difficult to set a particle size for these last two powders. Rather, a particle size range is given in Table II.2.

In the following, the particle size is analyzed with respect to the morphology of the powder particles.

- *Angular particles, C and M powders*

From laser measurements, C powder particle size is centered around 130 µm (Figure II.2). M powders are constituted of large particles centered around 20 µm and of finer particles about

300 nm in size (Figure II.2). These measurements are consistent with SEM observations (Figure II.1). However, large discrepancies are observed between the specific surface area measured from laser granulometry, SSA_{laser}^{sphere}, and BET, SSA_{BET}. During laser measurements, it can be assumed that the powder is well dispersed as the particles are coarse. The inconsistency is easily removed when considering the powder particle shape which is angular. Assuming that the particles are polyhedrons with a shape factor n, the specific surface area, $SSA^{polyhedron}$, is given in Equation (II.3). This surface is related to the usual specific surface area measured from laser granulometry, SSA_{laser}^{sphere}, assuming spherical particles of gyration radius, a_i. This radius corresponds to half the polyhedron diagonal that can be approximated to the longest side of the polyhedron, c_i (Figure II.3).

$$SSA^{polyhedron} = \frac{\sum_i N_i \left(4 c_i^2 / n + 2 c_i^2 / n^2\right)}{TD_{Si} \sum_i N_i \left(c_i^3 / n^2\right)}$$

$$SSA^{polyhedron} = \sqrt{\frac{2}{n^2} + 1} \, \frac{2n+1}{3} SSA_{laser}^{sphere} \xrightarrow[n>3]{c \to a} \frac{2n+1}{3} SSA_{laser}^{sphere}$$

(II.3)
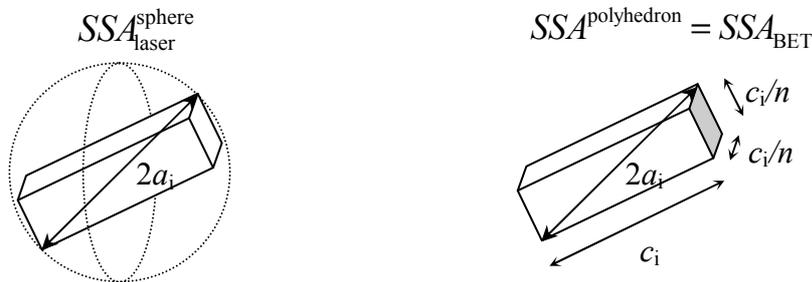
Figure II.3: Schematic representation of the specific surface area estimated from laser granulometry when particle are assimilated to spheres (left) or polyhedrons (right).

By equaling $SSA^{polyhedron}$ with the specific surface area measured from BET, SSA_{BET}, shape factors of 5.6 and 4.2 are respectively found for the C and M powders. These values seem in agreement with the powder morphology in Figure II.1. From these observations, size of angular particles can be roughly related to the specific surface area measured with BET using Equation (II.4) and a shape factor, $n \# 5$.

$$2a_{\mathrm{BET}}^{\mathrm{polyhedron}} = 2\sqrt{\frac{2}{n^2}+1}\ \frac{(2n+1)}{TD_{\mathrm{Si}}SSA_{\mathrm{BET}}} \approx \frac{22.8}{TD_{\mathrm{Si}}SSA_{\mathrm{BET}}} \tag{II.4}$$

- *Spherical particles, F and VF powders*

From granulometry, the F powder is made of large particles about 15 μm as well as finer particles about 350 nm (Figure II.2). Large particles correspond to spherical agglomerates of the primary particles, as observed by SEM (Figure II.1). BET measurements realized on this powder are in very good agreement with the specific surface area estimated from laser granulometry (Table II.2). The powder is homogeneously dispersed during laser measurements and particles can be correctly referred as objects of spherical shape. The use of Equation (II.1) to estimate the particle diameter from BET measurements is then appropriate in this case.

From laser granulometry, the VF powder shows a mono-dispersed behavior with particles about 300 nm (Figure II.2). This technique is actually not accurate to measure the particle size of this powder, as the detection threshold of 300 nm is higher than the particle size observed by SEM (Figure II.1). This leads to an underestimation of the specific surface area. Considering the size and the spherical shape of the particles, the specific area measured from BET, SSA_{BET}, is more suitable. This corresponds to spheres of 220 nm equivalent diameter from Equation (II.1), in agreement with SEM observations.

- *Conclusion*

In Figure II.4, the equivalent sizes, $2a$, of angular (Equation (II.4)) and spherical (Equation (II.1)) particles are plotted versus the specific surface area measured from BET. The particle sizes, $2a_{\mathrm{laser}}^{\mathrm{V},10\%}$, $2a_{\mathrm{laser}}^{\mathrm{V},50\%}$ and $2a_{\mathrm{laser}}^{\mathrm{V},90\%}$, of C, M and F powders measured from laser granulometry, are also added while the particle size of the VF powder is roughly estimated from SEM and TEM observations.

Estimations from Equations (II.1) and (II.4) are in good agreement with the experimental data of C and VF powders respectively. As for M and F powders, estimations are less satisfying because of the large distribution of particle sizes. Comparing a particle size estimated from a volume distribution (laser granulometry) to a particle size estimated from a surface measurement (BET) is then meaningless.

Still the particle size of fine powders (F) is lower than the particle size of medium ones (M). However, the specific surface area measured from BET is higher for M than for F powders. In any case, this is consistent with the polyhedron and spherical particle models (Equations (II.1) and (II.4)).
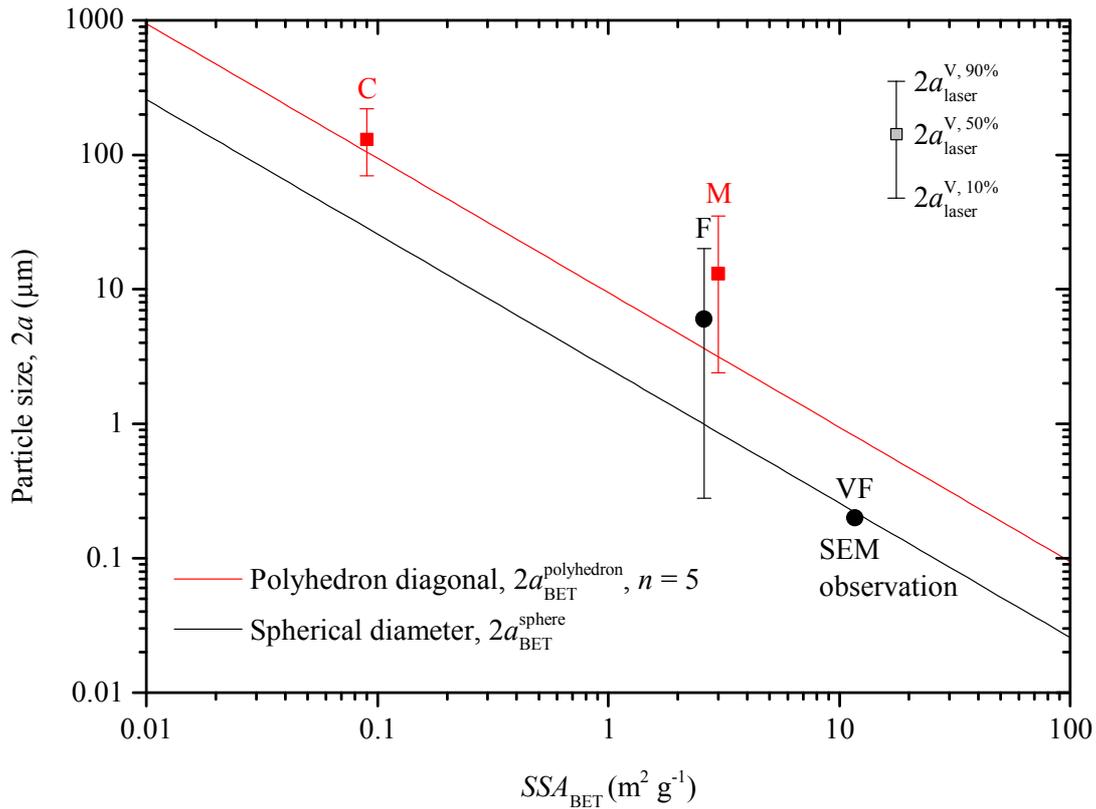
Figure II.4: Particle size estimated from laser granulometry versus the specific surface area estimated from BET, SSA_{BET} . Experimental values are compared to estimations from the specific surface area of ideal particle shapes: polyhedrons and spheres.

II.1.3   Powder purity

a)   Metallic impurities

All powders selected are less than 1 ppm of metallic impurities from Glow Discharge Mass Spectroscopy measurements (GDMS, VG 9000, Thermo Fisher Scientific). This is a requirement as regards both, the application and the study of sintering mechanisms.

b)   Oxygen contamination

The oxygen contamination was measured with an Instrumental Gas Analyzer (IGA ELTRA ON900). The equilibrium concentration of oxygen in silicon at the melting temperature is between 20 and 40 ppm in weight [Bea09, IN85]. The amount of oxygen measured on the powders, a few weight percent, is much larger. As will be seen in Chapter III, it actually corresponds to silica (SiO_2) grown at the particle surface, as silicon naturally oxidizes when manipulated under air.

Silicon powder oxidation is assumed to strongly depend on the elaboration process and packing atmospheres. When received, C and M powders were initially packed under air while F and VF powders were packed under argon. All powders were actually transferred in an argon glove-box but processed under atmospheric conditions prior to any experimental procedure.

The first step of oxidation is fairly rapid and the silica layer reaches a steady state thickness of several angstroms in a few seconds [MOH+90]. Then, the silica previously grown precludes the diffusion of oxidizing species towards the $Si_{(s)}$-$SiO_{2(s)}$ interface and drastically slows down oxidation kinetics. This was verified on some VF powder which was kept under atmospheric conditions. The increment of oxygen contamination measured using IGA only slightly increased with time (Figure II.5).

Assuming a silica layer uniformly distributed at the particle surface, the amount of oxygen can be converted into an equivalent silica layer thickness, e_{SiO_2} in Table II.1, using Equation (II.5), where it relies on the specific surface area measured by BET, SSA_{BET}, the molar masses of silica and oxygen, M_{SiO_2} and M_O, and the theoretical density of silica, TD_{SiO_2}. When looking at C, F and VF powders, in Figure II.5, the global amount of oxygen contamination is found greater for fine powders than for coarse powders as the specific surface area is higher. But, it usually corresponds to a lower equivalent silica layer thickness. For fine powders, agglomerates are assumed to retard oxidation of particles in their core, and accordingly a lower equivalent silica layer thickness is estimated. M powder is comparatively more oxidized than other powders. This certainly originates from the elaboration process.

$$e_{SiO_2} = \frac{\text{Oxygen mass}(\%) \times \dfrac{M_{SiO_2}}{2M_O}}{TD_{SiO_2} \times SSA_{BET}} \qquad (II.5)$$
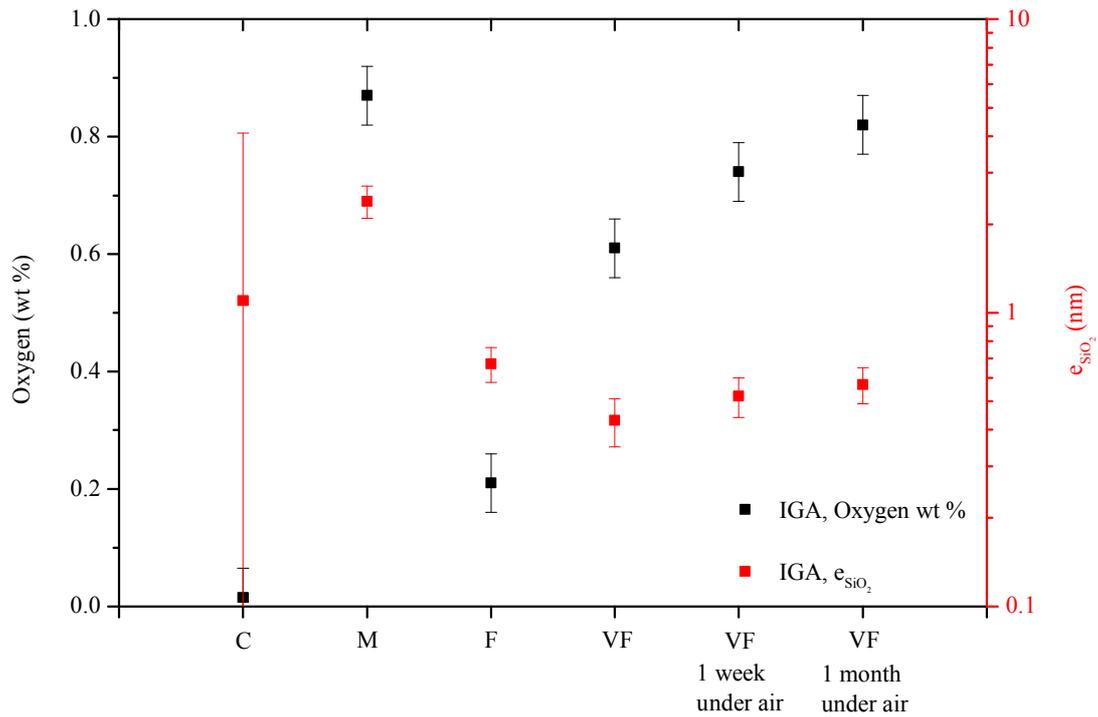
Figure II.5: Oxygen contamination in weight percent (black squares) from IGA and equivalent silica layer thickness (red squares).

For specific experiments, the silica layer could be removed by dipping silicon powders in a HF:ethanol (40:60) solution. This chemical etching was inspired by procedures used in the semiconductor industry to clean silicon surfaces and adapted to powder technology [BLCC07]. It ensures the protection against native oxidation for several minutes by the formation of Si-H or Si-F terminations at the particle surfaces [Pie95]. The suspension was filtered and powders were dried to be processed a few minutes later. These powders will be referred to as etched powders in the following.

II.1.4   Powder castability and sinterability

Sintering is experimentally studied on cylindrical compacts. Such compacts are prepared through die pressing in a mould made of hardened steel that can bear compaction pressure up to 1000 MPa. Two moulds are used depending on the compact diameter (8 or 16 mm). In this section, powders castability, compressibility and sinterability are briefly presented by measuring the tapped, green and sintered density (Figure II.6).
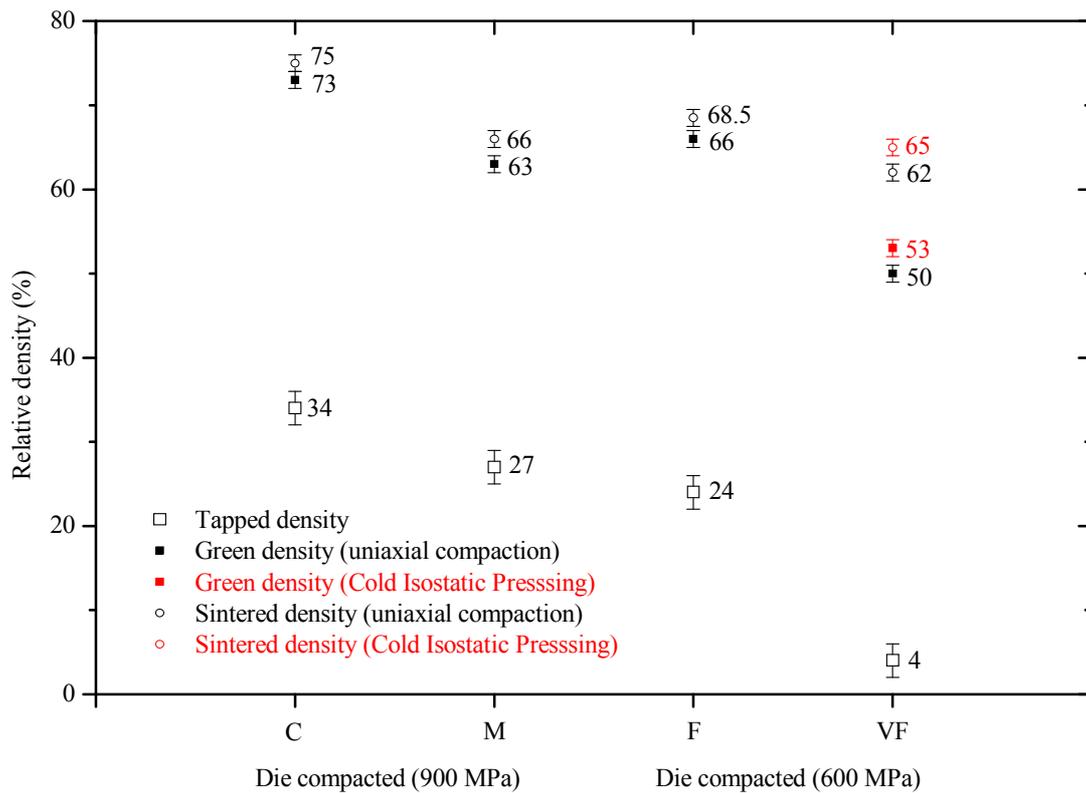
Figure II.6: Relative density of the tapped powders and green compacts. The final compact densities after pressure-less sintering are also given (1350°C - 3h - 2 l h⁻¹ He-4mol.% H₂).

a)   Compressibility

The large particle size and the plate like shape of C and M particles enable very good powder castability. Accordingly, the tapped densities (34 and 27 % respectively) as well as the green densities are relatively high. However, compacts are very brittle. For this reason, a 900 MPa minimal pressure must be applied to reach green densities of 73 and 63 % for the C and M powders respectively.

F powder shows a very good castability that relies on the micrometric agglomerates observed in Figure II.1. The tapped and green densities are then quite high (24 and 66 % respectively) even though initial primary particle diameter is as low as 300 nm. A 600 MPa compaction pressure is enough to obtain a relatively good green strength.

As can be seen on the measured tapped density (4 %), the VF powder castability is poor. This is easily explained when considering the particle size and the morphology of the "chain like" agglomerates. The green density is therefore quite low (50 %). A pressure higher than

600 MPa cannot be applied during compaction because of the risk of die punch jamming in the mould.

In order to improve the green density of VF compact, Cold Isostatic Pressing (CIP) is used. 50 MPa die compacted samples are placed in a watertight plastic bag that is submerged in a pressure vessel filled with oil, where the pressure is increased up to 450 MPa. A 3 % increase in the green density is observed compared to 600 MPa die pressed sample. The VF compacts used throughout this study were then prepared by CIP and had a green density of 53 %. In this case, samples of 8 and 16 mm diameter respectively become approximately 7.5 and 15 mm after CIP and are named, Φ_7 and Φ_{15}, in the following.

b)   Sinterability

The effect of a standard sintering cycle (1350°C − 3 h) on the sample densification is also given in Figure II.6. Compacts are sintered under a $2\,l\,h^{-1}$ He-4mol.% H_2 atmosphere, but similar results are obtained under Ar.

First results show the difficulty to densify silicon through pressure-less sintering. Indeed, C, M and F powder compacts show very little densification (less than 3 %). On the contrary, VF powder compacts undergo better densification (12 %). All samples experienced a mass loss of a few percent.

In order to study densification and mass loss kinetics, high temperature treatments are performed in dilatometric and thermogravimetric equipments that are presented below.

II.2 **High temperature treatments**

Silicon is a highly reactive material at high temperature and is commonly used in metallurgy as a melting point depressant. Phase diagrams including silicon are then numerous and very useful when designing a high temperature process including silicon. The choice of the material and atmosphere at the sample surrounding is thus crucial and will be discussed. Then experimental methods (thermogravimetry and dilatometry) will be presented. Finally, the water vapor partial pressure controller that has been designed specifically for our experiments is described.

II.2.1   Furnace geometry and materials at the sample surroundings

Sintering experiments are carried out in a Setaram dilatometric and thermogravimetric apparatus that are similarly designed. The furnace tube of these equipments is schematically represented in Figure II.7.

Measurement probe and electronics, TGA (Thermogravimetric Analysis) or Dilatometry

Gas inlet
Water cooling

Graphite resistor under Ar

Alumina furnace tube

$\pm z_f$: Diffusion length

$\pm z_h$: Heated zone

Sample, $z = 0$

W-Re 5%/26% thermocouple

Water cooling
Gas outlet

18 mm

280 mm

He-4mol.% H_2 - 2 l h^{-1}

z
z_f
z_h

r
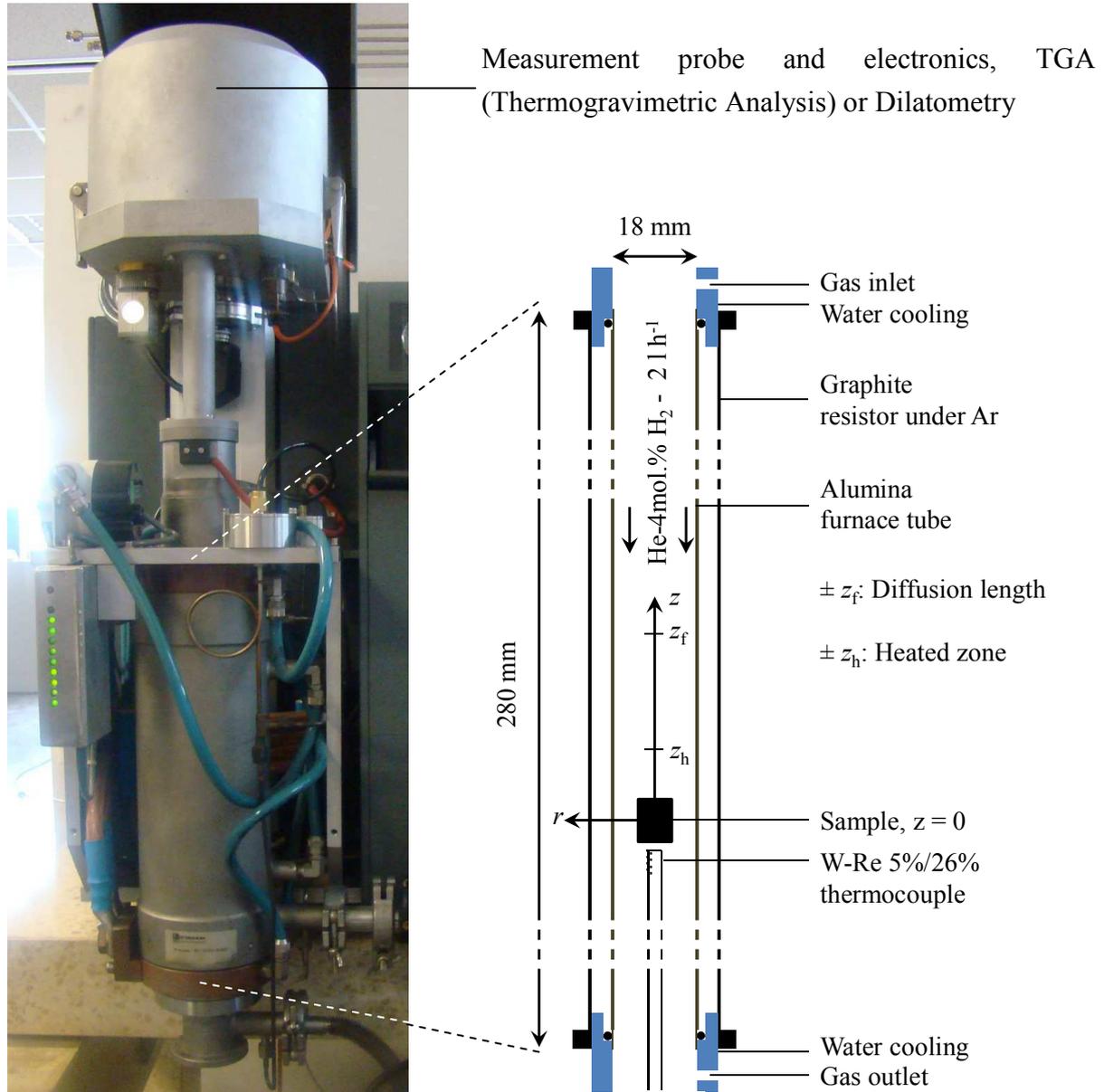
Figure II.7: Picture of a Setaram equipment (Setsys) and schematic representation of the furnace tube.

The furnace tube (280 mm height and 18 mm diameter) is made of alumina and is located in a graphite resistor. Platinum is commonly used as a thermocouple material because of its high reliability. However, Pt is not suitable as a surrounding material for silicon because of the existence of low temperature eutectics. This is the reason for the use of a tungsten-rhenium thermocouple (5%/26%) located at the sample underneath. The temperature is homogeneous over a height $\pm z_h$ ($\pm$ 15 mm) from the center of the tube and tube ends are cooled by water flowing.

Vacuum is performed in the furnace tube at room temperature before each experiment. The tube is first filled with Ar and vacuum is applied a second time before filling with the carrier gas at 150 °C. A $2 \, l \, h^{-1}$ gas flow is commonly used as a carrier gas. We shall later on show that for such small flow conditions, the gas mixture can be considered as stagnant (Appendix B.3.3). In most of the experiments, He-4 mol.% H_2 (supplied by Air Liquide, mélange crystal) gas mixture was used. Oxygen impurities are water molecules and their amount is less than 5 ppm (0,5 Pa) from supplier specifications. In some experiments a $2 \, l \, h^{-1}$ Ar (Air Liquide, Ar1) gas flow is used. In this case, oxygen impurities are typically O_2 molecules and are also less than 5 ppm.

II.2.2   Thermogravimetry

Silicon powder compacts undergo mass loss during sintering. As will be seen in Chapter III, Thermogravimetric Analysis (TGA) is a highly suitable technique in order to follow mass variation during the whole thermal process. The thermogravimetric equipment used is a Setaram Setsys apparatus that is schematically represented in Figure II.8.
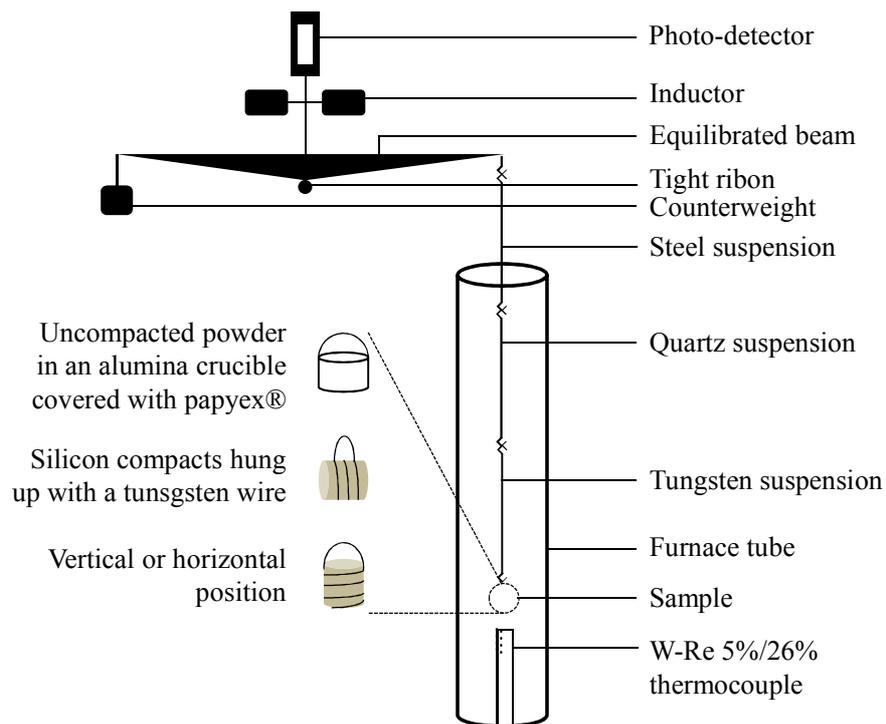
Figure II.8: TGA equipment and sample configurations.

The sample is hung up to suspensions that are connected to a beam equilibrated on a tight ribbon. Any sample mass deviation induces a slight rotation of the beam that is measured by a photo-detector associated with a laser diode. The deviation is instantaneously corrected by inductors that apply a counter electromagnetic force. The beam being always in its

equilibrium position, the electromagnetic force applied to the beam is directly related to the sample mass.

Suspensions used are successively made of steel, quartz and tungsten from the measurement to the heated area of the TGA. In this case, the use of a hydrogenated atmosphere is a requirement as tungsten would oxidize because of the presence of O_2 traces under neutral atmosphere. The behavior of un-compacted powders is first studied in Chapter III.2. In this case, powders are placed in an alumina crucible covered with papyex®. Powder compact oxidation kinetics is also studied. Compacts are then hold in a tungsten wire and are either in a horizontal (Chapter III.2) or vertical (Chapter V.2) position.

Suspension and crucible mass variations (~ 0.1 mg) are measured after each experiment and are much less than the sample mass variation (~ 10 mg). TGA experimental curves are corrected with a blank that corresponds to a TGA measurement along the same thermal cycle without sample. The W-Re (5%/26%) thermocouple is regularly calibrated by measuring the melting temperature of pure metals using the Differential Thermal Analysis (DTA) equipment which can be introduced in the same tube.

II.2.3   Dilatometry

Shrinkage kinetics during sintering is studied in a Setaram TMA92 vertical dilatometer that is schematically represented in Figure II.9. The sample is placed on an alumina support and sandwiched by appropriate spacers to avoid any chemical interaction. An alumina pushrod is in contact with the top spacer and follows the course of the sample during the thermal cycle. The load applied by the pushrod on the sample (typically 5 g) is controlled by inductors at the top of the equipment. The applied load takes into account the pushrod weight that is previously measured.

The measured signal, Δz, depends on the compact dilation and shrinkage, $\Delta z|_{compact}$, as well as the dilation of the pushrod, $\Delta z|_{pushrod}$, and of the alumina tube, $\Delta z|_{tube}$, in Equation (II.6).

$$\Delta z = \Delta z|_{compact} + \Delta z|_{pushrod} - \Delta z|_{tube} \tag{II.6}$$

During blank experiments, the pushrod is in contact with the bottom of the alumina tube. The measured signal, $\Delta z|_{blank}$, then becomes Equation (II.7).

$$\Delta z|_{blank} = \Delta z|_{pushrod} - \Delta z|_{tube} \tag{II.7}$$

To obtain the compact dilation and shrinkage, $\Delta z|_{compact}$, the measured signal, Δz, is thus corrected with the blank using Equation (II.8), where the term $CTE_{Al_2O_3}.h.\Delta T$ accounts for the dilation of the pushrod on the sample height, h, $CTE_{Al_2O_3}$ being the coefficient of thermal expansion of alumina and ΔT the difference between the actual and initial temperature.

$$\Delta z|_{compact} = \Delta z|_{compact} - \Delta z|_{blank} + CTE_{Al_2O_3}.h.\Delta T \tag{II.8}$$
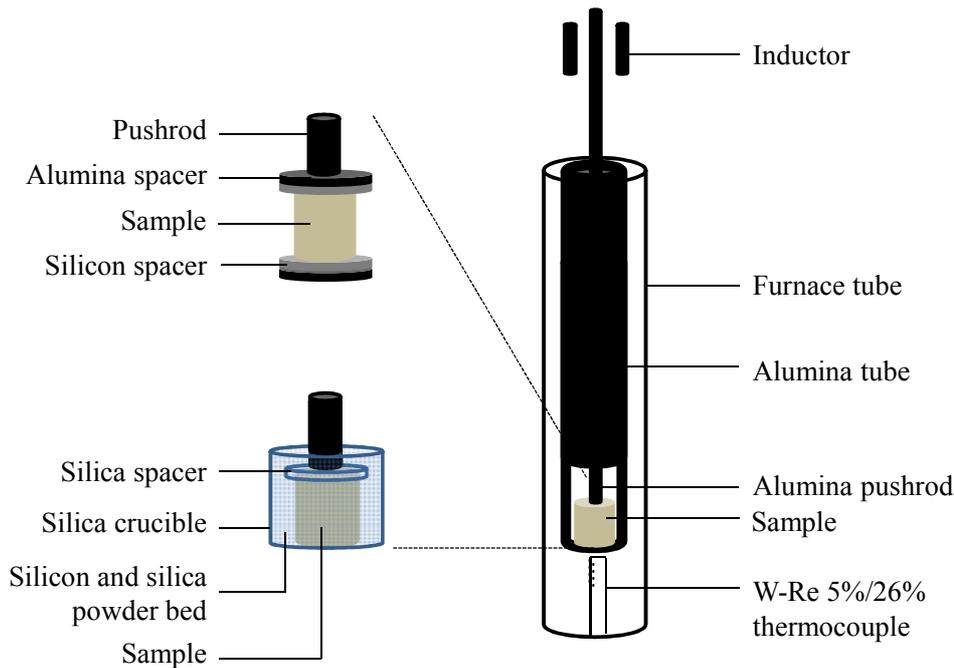
Figure II.9: Vertical dilatometer and sample configurations.

The W-Re (5%/26%) thermocouple is regularly calibrated by measuring the transition temperatures and associated size changes of a pure iron sample.

Shrinkage is first studied under standard reducing atmosphere (Chapter III) as explained in section II.2.1. The sample is then sandwiched by silicon and alumina spacers to avoid contact between the silicon powder compact and alumina (Figure II.9). Spacers are replaced for each new experiment performed. Sintering kinetics is also studied under controlled silicon monoxide atmosphere (Chapter IV). The compact with a silica spacer is then placed in a silica crucible filled with a mix of silicon and silica powders (Figure II.9). In the following, these conditions will be respectively referred to as "sintering under reducing atmosphere" and "sintering under silicon-silica powder bed".

II.2.4   Water vapor partial pressure controller

For some experiments, variable water vapor pressure at the sample surroundings are used by monitoring the water vapor in the gas flux upstream, at the tube inlet. The water vapor pressure is monitored with a humidity controller system made of two gas lines and schematically represented in Figure II.10. One line is composed of dry gas while the other is composed of humidified gas bubbled in a water container. Both gases are mixed and a humidity probe (Vaisala HUMIDICAP® HMT333) associated with a controller (West N8800) allows to regulate thermal mass flow (Brooks SLA5850S) to give a water vapor pressure, $P_{H_2O}^{Probe}$, comprised between 100 and 2000 Pa. We shall see from modeling arguments in Chapter V.2 that these water vapor pressures actually correspond to approximately 10 and 200 Pa at the sample surrounding.
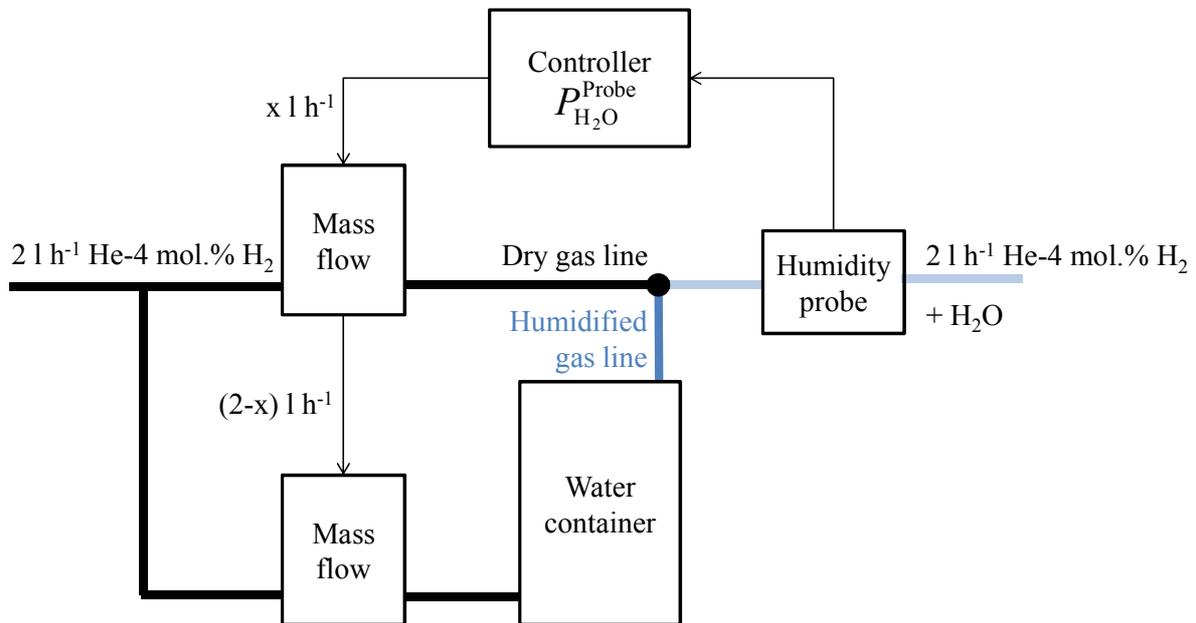
Figure II.10: Water vapor pressure controller designed during this study.

II.3   **Metallographic procedures**

Densities are measured on sintered samples using Archimedes' method in ethanol. Then, samples are fractured or cut to be observed by SEM.

Finally, cut samples are mounted under vacuum and polished according to the following procedure:

- Polishing on abrasive papers (~ 10 μm, 2400 grains per inch²).

- Polishing on woven cloth (RAM cloth, PRESI) with 6, 3 and 1 µm polycrystalline diamond paste suspensions.

- Polishing on flock cloth (NT cloth, PRESI) with ¼ µm polycrystalline diamond paste suspension.

- Finishing and developing with colloidal suspension made of 20 nm silica particles (SUPRA 5 cloth, PRESI).

Between each steps the sample is cleaned with ethanol in an ultrasonic bath and rinsed under water.

After SEM observation, image analysis was sometimes performed on micrographs using Image J.

Chapter III.   Oxidation kinetics

- Silica reduction and silicon oxidation -

Identification of mechanisms involved during sintering of silicon is controversial [Cob90, GR76, SH83]. Especially, the role of the native oxide layer (SiO_2) at the particle surfaces is not fully understood.

According to Shaw and Heuer [SH83], the silicon monoxide vapor, $SiO_{(g)}$, released during the reduction of this silica layer would enhance surface vapor transport during sintering (*i.e.* non-densifying mechanisms). On the contrary, Coblenz [Cob90] proposed that the silica layer would inhibit surface transport occurring through surface diffusion, and allow volume transport (*i.e.* densifying mechanisms) to compete during sintering.

Prior to the discussion about sintering mechanisms, the silica layer stability at the silicon particle surface is characterized during high-temperature processing under He-H_2 atmosphere. Silicon oxidation is first described according to Wagner's approach [Wag58]. Then, thermochemical analyses along with thermogravimetric experiments are performed on un-compacted powders. Mechanisms involved during the reduction of the silica are identified and the initial silica layer thickness is estimated. Eventually, silica reduction kinetics is analyzed in silicon powder compacts and associated with microstructure evolution as a first route for the identification of silicon sintering mechanisms.

III.1 **Passive and active oxidation of silicon**

In literature, high temperature oxidation of silicon has been studied on dense silicon wafer materials [Wag58, GAB66, LM62, GCG01, GJ01]. Two kinds of oxidation mechanisms, active or passive, can occur depending on the temperature and partial pressures of oxidizing species. Under inert atmosphere, the oxidizing species are dioxygen, $O_{2(g)}$, while under hydrogenated atmosphere the stable oxidizing species are water molecules, $H_2O_{(g)}$ (Table III.1).

i.   At low temperature and high oxygen pressure, passive oxidation of silicon occurs, which means that the formation of solid silica, $SiO_{2(s)}$, is promoted according to reactions (R_1) or (R_3) (equilibrium constant K_1 or K_3) depending on the atmosphere

ii.   At high temperature and low oxygen pressure, active oxidation occurs. It corresponds to the formation of gaseous silicon monoxide, $SiO_{(g)}$, according to reactions (R_2) or (R_4) (equilibrium constant K_2 or K_4) depending on the atmosphere

Gas flow		H$_2$ atmosphere	Inert atmosphere
Mechanisms and oxidation type	(i.) and (ii.)	$Si_{(s)} + 2H_2O_{(g)} = SiO_{2(s)} + 2H_{2(g)}$ (R$_1$) passive $Si_{(s)} + H_2O_{(g)} = SiO_{(g)} + H_{2(g)}$ (R$_2$) active	$Si_{(s)} + O_{2(g)} = SiO_{2(s)}$ (R$_3$) passive $Si_{(s)} + \frac{1}{2} O_{2(g)} = SiO_{(g)}$ (R$_4$) active
Transition type — Active – Passive	(iii.)	$Si_{(s)} + SiO_{2(s)} = 2SiO_{(g)}$ (R$_5$) $P_{SiO}^{R_5} = P^{\circ} K_5^{1/2}$ (III.1)	$Si_{(s)} + SiO_{2(s)} = 2SiO_{(g)}$ (R$_5$) $P_{SiO}^{R_5} = P^{\circ} K_5^{1/2}$ (III.1)
Transition type — Passive – Active	(iv.)	$SiO_{2(s)} + H_{2(g)} = SiO_{(g)} + H_2O_{(g)}$ (R$_6$) $P_{SiO}^{R_6} = P^{\circ} P_{H_2} P_{H_2O}^{-1} K_6$ (III.2)	$SiO_{2(s)} = SiO_{(g)} + \frac{1}{2} O_{2(g)}$ (R$_7$) $P_{SiO}^{R_7} = P^{\circ 3/2} P_{O_2}^{-1/2} K_7$ (III.3)

Table III.1: Passive and active oxidation reactions of silicon under hydrogenated and inert atmospheres. Equilibrium constant are estimated from Malcolm and Chase Thermochemical data [MC98]. P° (~1atm) corresponds to the standard gas pressure.

Wagner [Wag58] was the first to predict the conditions of active and passive oxidation, under an inert gas flow, by considering two distinct cases (Table III.1):

    iii.   The first one in which the silicon surface is initially free from its oxide.

    iv.   The second one in which the silicon is initially covered with a continuous layer of silica.

In the first case (iii.), the competition between the formation of solid silica (R_3) and gaseous silicon monoxide (R_4) is discussed. The combination of both reactions gives reaction (R_5) of which equilibrium partial pressure, $P_{SiO}^{R_5}$, determines the transition between active and passive oxidation (Table III.1). As long as the effective partial pressure of silicon monoxide, P_{SiO}, remains lower than the equilibrium partial pressure, $P_{SiO}^{R_5}$ (Equation (III.1)), the silicon surface remains bare. But, once this partial pressure exceeds $P_{SiO}^{R_5}$ (Equation (III.1)), a silica layer starts to develop.

In the second case (iv.), a protective silica layer perfectly covers the silicon surface. Silica cannot be reduced by silicon according to reaction (R_5) in that case, since silicon monoxide cannot leave the $Si_{(s)}$-$SiO_{2(s)}$ interface. Wagner considers that silica reduction occurs through reaction (R_7). In the same way as discussed above, $P_{SiO}^{R_7}$ (Equation (III.3)) determines the transition between passive and active oxidation.

Thermogravimetric experiments have been carried out by different authors to characterize the active to passive [GAB66] and passive to active [GCG01, GJ01] transitions for bulk silicon, but only under vacuum conditions. Actually, authors noticed that both transitions were controlled by reaction (R_5) and that silica would not act as a diffusion barrier during the passive to active transition. Gulbransen and Janson [GJ01] assumed the presence of cracks in the $SiO_{2(s)}$ layer while Gelain *et al.* [GCG01] considered the formation of blisters by $SiO_{(g)}$ at the silicon-silica interface which cause the rupture of the silica layer. Healing of the silica layer by reaction (R_1) is no longer possible after the transition and the system is shifted to the active oxidation state where vacuum conditions were thought to allow a rapid removal of the oxide.

The thermochemical approach of Wagner is extended to a stagnant hydrogenated atmosphere in Appendix A. Reactions (R_5) and (R_6) are considered as references to determine the temperatures of active to passive and passive to active transitions, $T_{A \rightarrow P}^{W}$ and $T_{P \rightarrow A}^{W}$, respectively. During thermogravimetric analysis (TGA), the transition can be identified when the mass loss rate is nil as the mass flux of water equals that of silicon monoxide. The active to passive and passive to active transition temperatures are then called, $T_{A \rightarrow P}^{Wm}$ and $T_{P \rightarrow A}^{Wm}$. Assuming a steady-state diffusion of oxidizing species in a furnace tube, these temperatures

can be determined in terms of a surrounding water vapor partial pressure, P_{H_2O}, in Equations (III.4) and (III.5) respectively, where M_j and D_j are respectively the molar mass and the molecular diffusion coefficient of the species j (Appendix A).

$$P_{H_2O}^{WR_5} = \frac{M_{SiO} D_{SiO}^{mol}}{M_O D_{H_2O}^{mol}} P^\circ \left(K_5 \left(T_{P \to A}^{Wm} \right) \right)^{1/2} \tag{III.4}$$

$$P_{H_2O}^{WR_6} = 2 \left(\frac{M_{SiO} D_{SiO}^{mol}}{M_O D_{H_2O}^{mol}} \right)^{1/2} P_{H_2}^{1/2} P^{\circ 1/2} \times \left(K_6 \left(T_{A \to P}^{Wm} \right) \right)^{1/2} \tag{III.5}$$

In Figure III.1, the expected $T_{A \to P}^{Wm}$ and $T_{P \to A}^{Wm}$ are plotted as a function of the surrounding water vapor pressure. In the next section, these will be compared with TGA measurements as a reference for the elucidation of silicon powder oxidation mechanism.
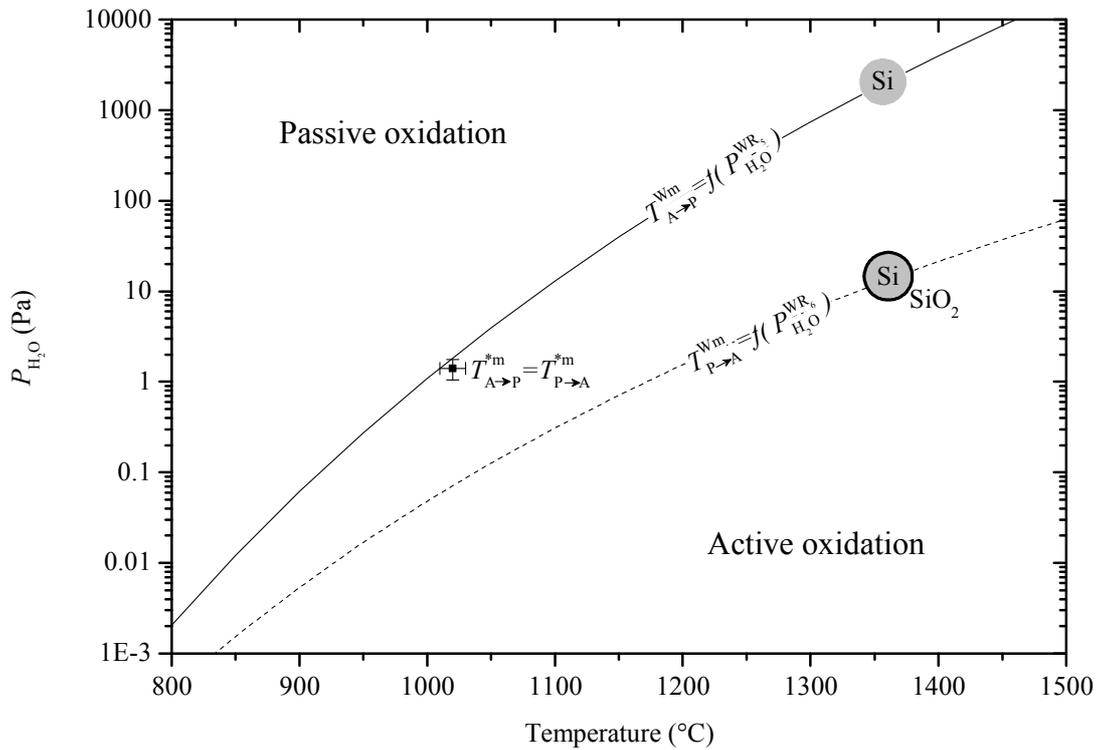
Figure III.1: Expected active to passive ($T_{A \to P}^{Wm}$, bare silicon surface, full line) and passive to active ($T_{P \to A}^{Wm}$, silicon surface covered with silica, dashed line) transition temperatures as a function of the surrounding water vapor pressure from Wagner's approach (Appendix A). Measured passive to active, $T_{P \to A}^{*m}$, as well as active to passive, $T_{A \to P}^{*m}$, transition temperatures and surrounding water vapor pressure (dot).

III.2 **Elucidation of silicon powder oxidation mechanisms**

III.2.1 Experimental approach

Under atmospheric conditions, the water vapor pressure is largely higher than $P_{H_2O}^{WR_5}$. On initially bare silicon surfaces, the formation of a native silica layer is favored until the silica layer reaches several angstroms and precludes the diffusion of oxidizing species towards the $Si_{(s)}$-$SiO_{2(s)}$ interface. On single crystal wafers, layer-by-layer growth occurs from 0.2 to 1 nm in approximately 10 h time exposure and requires the coexistence of oxygen and water [MOH+90]. IGA measurements of the oxygen powder content allows to estimate the silica layer thickness, e_{SiO_2}, which is of the same order of magnitude (see section II.1.3 and Table II.1).

The silica mass fraction is estimated in Equation (III.6) depending on the specific surface area, SSA_{BET} (or the corresponding equivalent spherical particle size, $2a$), the silica layer thickness, e_{SiO_2}, and the theoretical densities of silica and silicon, TD_{SiO_2} and TD_{Si}. Then, the expected mass loss during thermogravimetric experiments are calculated according to the mass balance of the mechanisms involved during the silica layer reduction under hydrogenated atmospheres, (R$_5$) (Equation (III.7)) or (R$_6$) (Equation (III.8)) and reported in Figure III.2.

$$\text{Silica}\,(\text{wt \%}) = \frac{100 \times m_{SiO_2}}{m_{Si} + m_{SiO_2}} = 100 \times \left(1 + \frac{TD_{Si}}{TD_{SiO_2}} \left(\left(\frac{a + e_{SiO_2}}{a}\right)^3 - 1\right)^{-1}\right)^{-1} \tag{III.6}$$

$$\text{Mass loss R}_5\,(\%) = \frac{2 M_{SiO}}{M_{SiO_2}} \times \text{Silica mass}\,(\%) \tag{III.7}$$

$$\text{Mass loss R}_6\,(\%) = \text{Silica mass}(\%) \tag{III.8}$$

Sample mass are typically of 100 mg and the mass loss detection amplitude of the thermogravimetric system is about 0.05 mg, giving a detection threshold of 0.05 %. TGA is thus well suited to estimate silica layers of nanometric thickness for specific surface areas higher than 1 m^2 g^{-1}.

Powders are placed in an alumina crucible of 12 mm diameter covered with Papyex® such as to limit interactions between silicon and alumina (see Figure II.8 in Chapter II). These are heated up to 1350 °C for 3 h under 2 l h^{-1} He-4mol.% H$_2$ atmosphere with a heating rate of 5 °C min^{-1}. For specific experiments, the native silica layer is removed by dipping silicon powders in a HF:ethanol (40:60) solution (see Chapter II.1.3b).

Equivalent polyhedron diagonal, C and M powders (n=5), $2a$ (µm)

Equivalent spherical diameter, F and VF powders, $2a$ (µm)
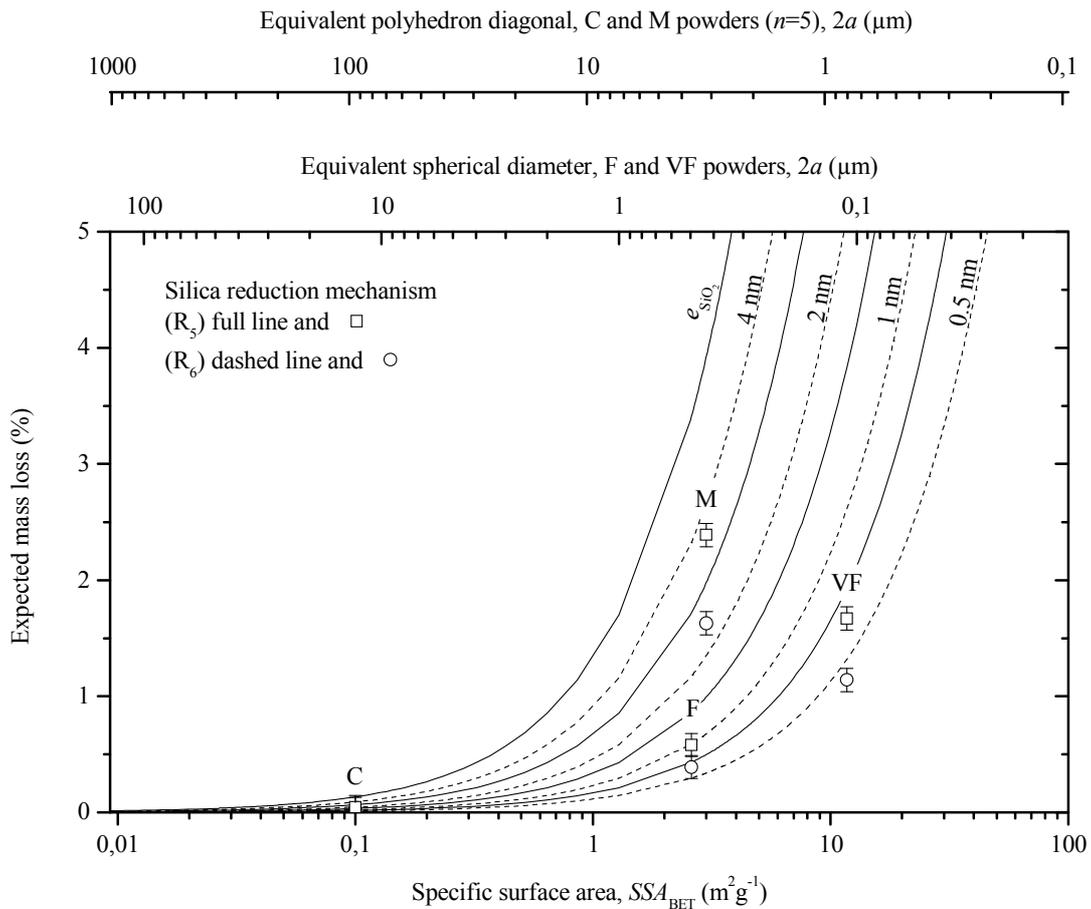
Figure III.2: Expected mass loss as function of the BET specific surface area of the powder depending on the silica layer thickness and the reduction mechanisms involved. The specific surface area of the powder can be read as an equivalent spherical diameter or as an equivalent polyhedron diagonal depending on the particle shape. Studied powders, C, M, F and VF are placed on the graph.

III.2.2 Experimental results

Four steps are identified for all the powders on the thermogravimetric curves as shown in Figure III.3 for the VF powder:

v.   Below 400 °C, a mass loss is observed which is related to desorption of adsorbed species on the powder.

vi.   Between 400 and 1025°C, a mass gain is measured which is due to the formation of $SiO_{2(s)}$ according to reaction (R_1), since the temperature is initially lower than the active to passive transition. The silica growth is then controlled by the surrounding water vapor pressure, the water solubility into the silica layer and its diffusion towards the silicon surface. According to the literature [DG65], the silica growth rate is enhanced under humidified atmospheres compared to dry atmospheres because the

equilibrium concentration of water is higher than the equilibrium concentration of oxygen in silica.

vii. Above 1025 °C, the samples start to experience a massive weight loss, which is attributed to $SiO_{(g)}$ release during the decomposition of the silica layer.

viii. At higher temperatures, the rate of mass loss suddenly collapses. The constant mass loss rate observed (about 3×10^{-3} mg min^{-1}) is related to the active oxidation of silicon according to reaction (R$_2$), as the silica layer has been removed. Assuming that the reaction is controlled by the diffusion of water vapor to the powder bed, the rate of weight loss is simply proportional to the surrounding water partial pressure, $P_{H_2O}^{z_f}$. Considering a diffusion length, z_f, between 30 and 50 mm (see section III.3.3 and Appendix B.3.4), the values of 1.8 and 1 Pa are respectively deduced for $P_{H_2O}^{z_f}$.
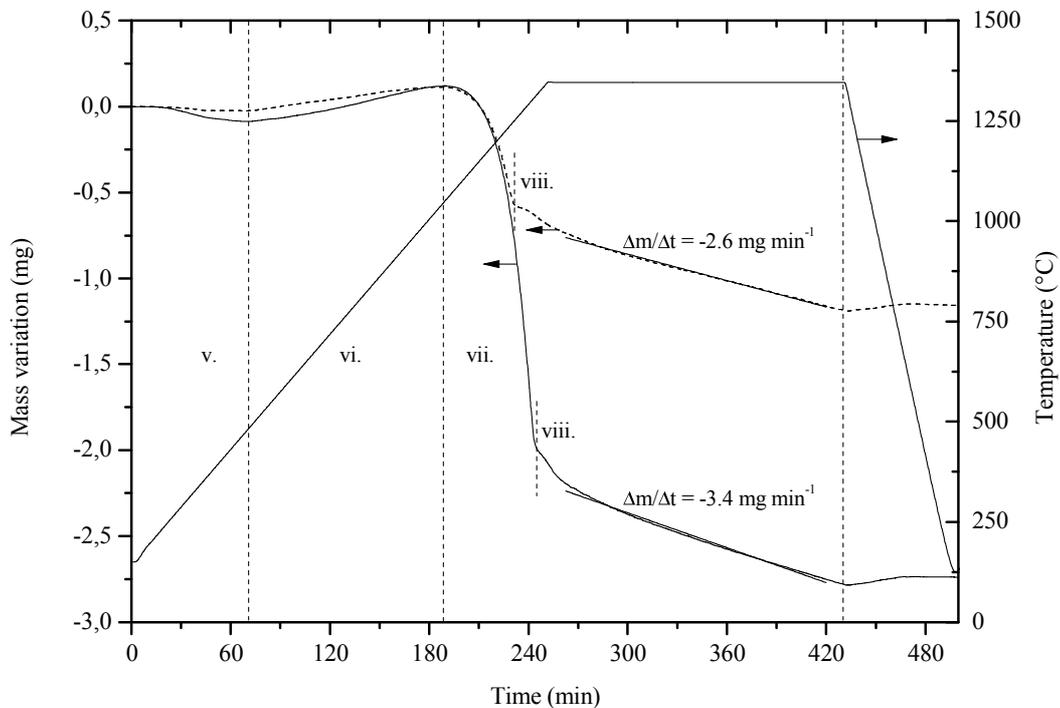
Figure III.3: Thermogravimetric curves of VF as-received powder (full line) and previously etched (dashed line), heated up to 1350 °C with a heating rate of 5 °C min^{-1} and a holding time of 3 h under 2 l h^{-1} He-4mol.% H$_2$ atmosphere.

The partial pressure of water impurities deduced is larger than the gas specifications (0.5 Pa). However, under stagnant gas conditions, it should even be lower as water would be rapidly consumed by silicon. Actually, the water is probably supplied by a condensate film that is observed 70 mm underneath the sample position, on the furnace tube and on the thermocouple (Figure III.4, Appendix B.3.4). According to XRD measurements, this condensate is made of

silicon, cristobalite (crystallized silica) and an amorphous phase, probably silica glass. It is assumed that $SiO_{(g)}$ crystallizes in the form of silicon and silica on the cold wall of the tube and on the tungsten thermocouple according to reaction (R_5).

The onset of weight loss which corresponds to the measured passive active transition, $T_{P \to A}^{*m}$, is observed at 1025 °C (Figure III.3). Referring to Figure III.1 (dot), the mechanism involved for the passive to active transition can be determined with the water partial pressure calculated above (# 1.4 Pa). The prediction is consistent with the reduction of silica by silicon through reaction (R_5) rather than the reduction of silica by hydrogen through reaction (R_6). Active to passive, $T_{A \to P}^{*m}$, and passive to active, $T_{P \to A}^{*m}$, transitions are equal and correspond to the active to passive transition calculated by Wagner, $T_{A \to P}^{Wm}$. Actually, active to passive and passive to active transitions are controlled by the same mechanism which is reaction (R_5).
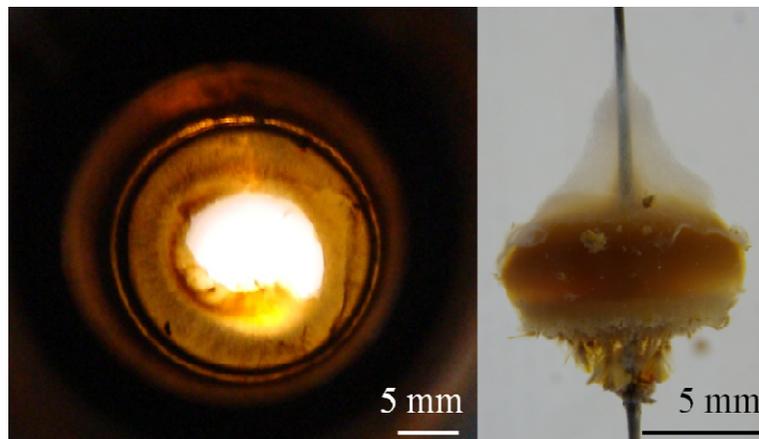
Figure III.4 : Silicon monoxide condensate film on the furnace tube (left), on the thermocouple (right).

Another evidence of the previous statement is the ratio between mass gain and mass loss measured on etched powders (dashed line in Figure III.3), on which the amount of silica grown during passive oxidation should equal the amount of silica reduced further. The ratio of mass loss and mass gain, about 2.8, is close to what is expected from reaction (R_5) $M_{SiO}/M_O = 2.75$ and is different from what is expected from reaction (R_6) $M_{SiO_2}/2M_O = 1.87$.

Eventually, the initial masses of native oxide, $m_{SiO_2}^{R_5}$ or $m_{SiO_2}^{R_6}$, are estimated according to Equation (III.9) or (III.10) assuming respectively reaction (R_5) or (R_6) as the mechanisms involved for the oxide reduction. The global mass loss, m^{loss}, depends on the initial silica layer thickness as estimated in Figure III.2 but also on the silica grown during passive

oxidation as seen on etched powders. The mass gain, m^{gain}, occurring during passive oxidation according to reaction (R$_1$) is thus taken into account in the calculation. IGA measurements (Chapter II.1.3) are consistent with estimations predicted from the mechanism (R$_5$) as can be seen in Figure III.5.

$$m_{\text{SiO}_2}^{\text{R}_5} = \frac{M_{\text{SiO}_2}}{2M_{\text{SiO}}} \times m^{\text{loss}} - \frac{M_{\text{SiO}_2}}{2M_{\text{O}}} \times m^{\text{gain}} \tag{III.9}$$

$$m_{\text{SiO}_2}^{\text{R}_6} = m^{\text{loss}} - \frac{M_{\text{SiO}_2}}{2M_{\text{O}}} \times m^{\text{gain}} \tag{III.10}$$
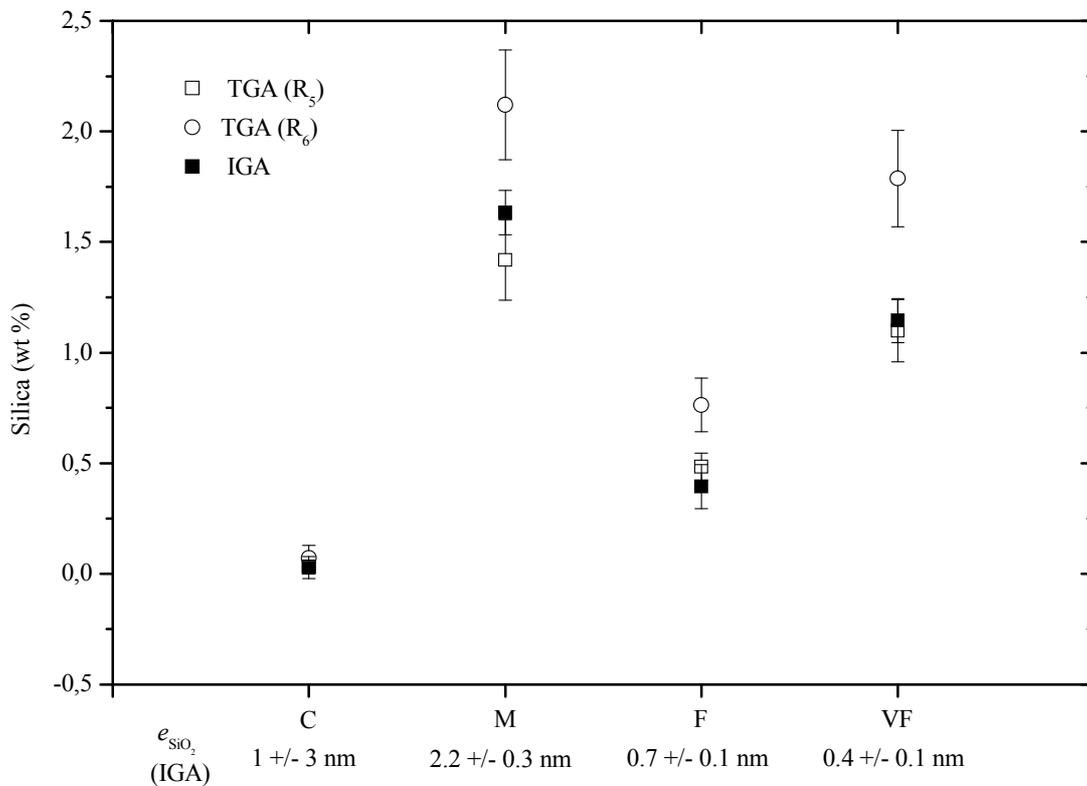
Figure III.5: Measured silica mass percent from two distinct methods: TGA, assuming reaction (R$_5$) or (R$_6$) as the mechanisms involved during the reduction of the silica layer, and IGA.

III.2.3 Summary

From Wagner approach [Wag58], if a protective silica layer were covering the silicon particles, reduction should be controlled by reaction with hydrogen (R$_6$). However, our experimental results show that active to passive and passive to active transitions are controlled by the same mechanism, which is the reduction of silica by silicon into silicon monoxide (R$_5$). Three distinct observations support this conclusion:

- The experimental passive to active transition temperature equals the active to passive temperature estimated from the equilibrium constant of reaction (R_5) and surrounding water vapor pressure.

- When considering reaction (R_5) as the silica reduction mechanism, TGA measurements corroborate IGA measurements of the oxygen contamination in starting powders.

- Mass loss ratios of passive and active oxidation on previously etched powders are coherent with the balance of reaction (R_5).

Reaction (R_5) is possible at temperatures as low as 1000-1100 °C and hydrogenated atmospheres are not an aid as regard to silica elimination. Vacuum conditions might change the kinetics but are not necessary for the oxide removal.

III.3 Silica reduction kinetics in silicon powder compacts

III.3.1 Experimental approach

Oxidation kinetics is now analyzed on VF silicon powder compacts using TGA associated with dilatometric experiments in order to analyze the possible effect of the silica layer on silicon sintering. Three different rates are used (0.625, 1.25 and 2.5 °C min^{-1}) to heat up the samples to 1350 °C with a holding time of 3 h, under He-4mol.% H_2 atmosphere.

Silica reduction kinetics is thought to be affected by the sample dimensions. Two types of cylindrical compacts of approximately 8 mm height, Φ_7 and Φ_{15}, are prepared with a respective diameter of 7 mm and 15 mm. Compact densities of 53 % TD_{Si} are obtained by uniaxial compaction at 50 MPa followed by cold isostatic pressing at 450 MPa.

The microstructure development is observed on fractured or polished surfaces. Reduction of the native silica covering particles is modeled and connected with densification and microstructure evolution over the compacts.

III.3.2 Experimental results on Φ_7 samples

a)   Thermogravimetric and dilatometric experiments

The rate of mass variation for the 1.25 °C min^{-1} cycle is plotted in Figure III.6. Three steps (vi., vii. and viii.) are identified which are related to the silicon oxidation behavior as explained in section III.2.2. The shrinkage rate is also plotted.

    ix.   Below 950 °C, the slight dilation is attributed to the thermal expansion of silicon and to the formation of a silica layer at the surface of the sample according to reaction (R_1).

    x.   Above 950 °C, the sample starts to shrink. A shoulder is observed after the maximum on the main shrinkage peak.

   xi.   At high temperatures, the rate of shrinkage tends to zero after the decomposition of the silica layer (end of step vii. on the curve of mass loss rate).

During sintering, the relative density is estimated from mass variation and shrinkage which is assumed isotropic. The silicon powder density is taken as the bulk one (2.33 g cm^{-3}). The actual value is very close since the silica amount is small and its theoretical density is similar (2.27 g cm^{-3} for amorphous silica). The final relative density is 64 % and does not increase during the 3 h holding at 1350 °C. Similar observations are made for the 0.625 and 2.5 °C min^{-1} cycles.
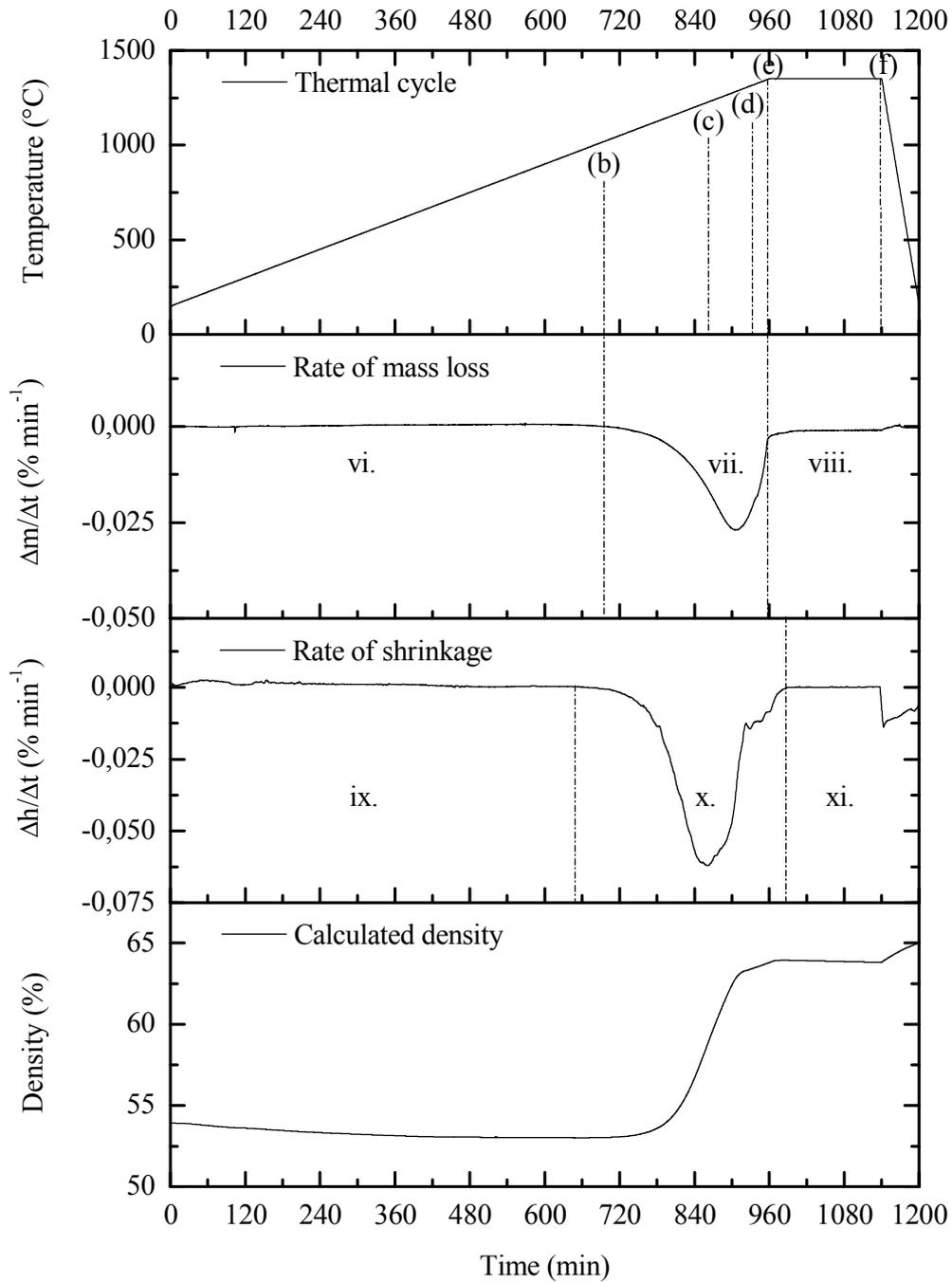
Figure III.6 : Temperature cycle, rate of mass loss, rate of shrinkage and calculated relative density of a silicon powder compact, heated up to 1350 °C with a heating rate of 1.25 °C min^{-1} and a holding time of 3 h under He-4 mol.% H$_2$. The relative density of the compact is deduced from the rate of mass loss and the rate of shrinkage, assuming an isotropic shrinkage. Quenches realized along the thermal cycle are marked out by letters and referenced into the text.

b) **Microstructural observations**

Samples heated at 1.25 °C min^{-1} are quenched at different steps of the sintering process and referenced on the temperature cycle in Figure III.6:

(a) As compacted sample.

(b) Quenched at 1025 °C, just before the beginning of the silica dissociation.

(c) Quenched at 1230 °C, at the maximum of the shrinkage rate.

(d) Quenched at 1315 °C, on the shoulder of the shrinkage peak.

(e) Quenched at 1350 °C, at the end of shrinkage.

(f) Quenched after 3 h at 1350 °C.

SEM observations of fractured sample are given in Figure III.7. No change is observed up to 1025 °C in samples (a) and (b). A grain coarsening area growing from the edge to the core of the compact is observed between 1230 and 1350 °C in samples (c), (d) and (e). The radial position of the grain coarsening area from the center (r_g) was systematically measured on SEM micrographs. The position of the grain coarseniong area was even visible on the macroscopic sample (d). Eventually, at the center of samples (d) and (e), neck growth is observed associated with particles center-to-center approach. Grain coarsening concerns the entire sample after 3 h at 1350 °C and grains as large as 10 µm are identified (f).

On sample (d), the SEM micrograph is associated with EDS profiles showing that the grain coarsening position, r_g, also corresponds to a sudden change in oxygen concentration, which is related to the reduction of silica at the edge of the sample. The grain coarsening area is then referred to as the "reduced area", while the fine grain area is referred to as the "non-reduced area".

> *Following double pages, Figure III.7: Pictures and SEM microstructures at the edge and center of fractured silicon compacts quenched at several steps of the 1.25 °C min^{-1} cycle.*

(a) As compacted — Edge / Center, 1 μm

(b) 1025°C — Edge / Center, 1 μm

(c) 1230°C — Edge, $r_g = 3475\ \mu m$, 10 μm, 2 μm / 1 μm, As compacted

(d)
1315°C

Edge

r_g = 2700 µm

Si
C
O
EDS

500 µm

r_g = 2700 µm

10 µm

10 µm

As compacted

1 µm

100 µm

(e)
1350°C

r_g = 840 µm

Edge

10 µm

Center

r_g = 840 µm

As compacted

As compacted

1 µm

(f)
1350°C
3h

As compacted

Edge

10 µm

Edge

100 µm

Center

Center

100 µm
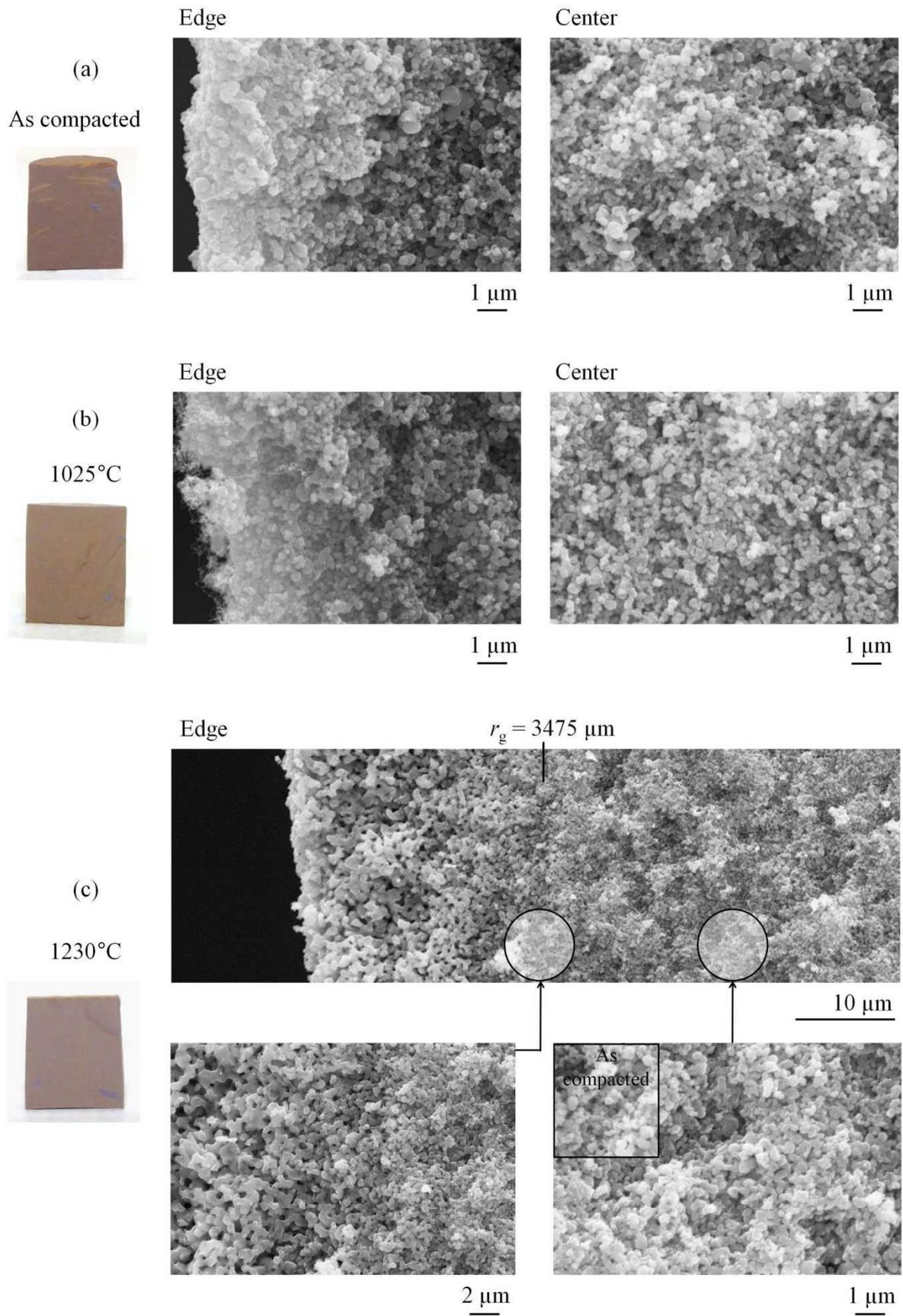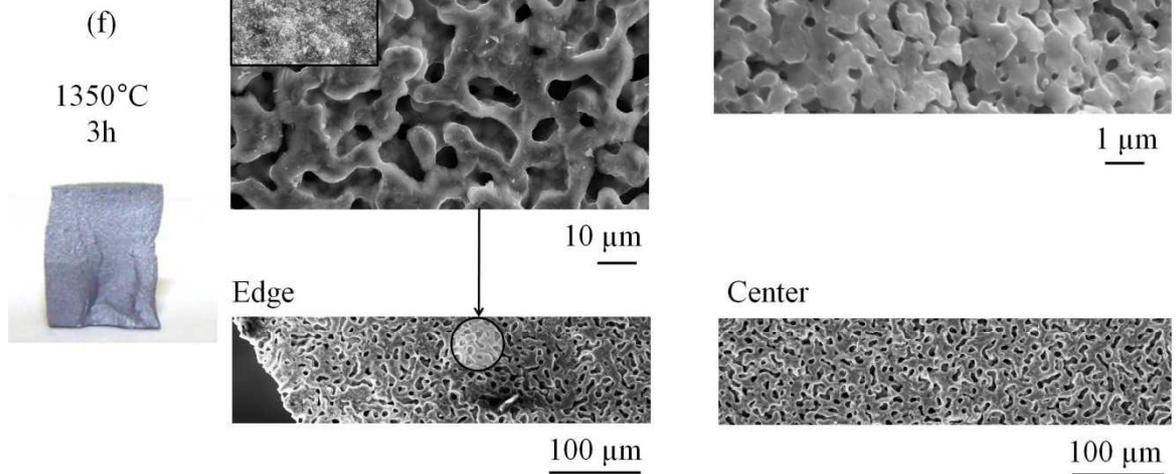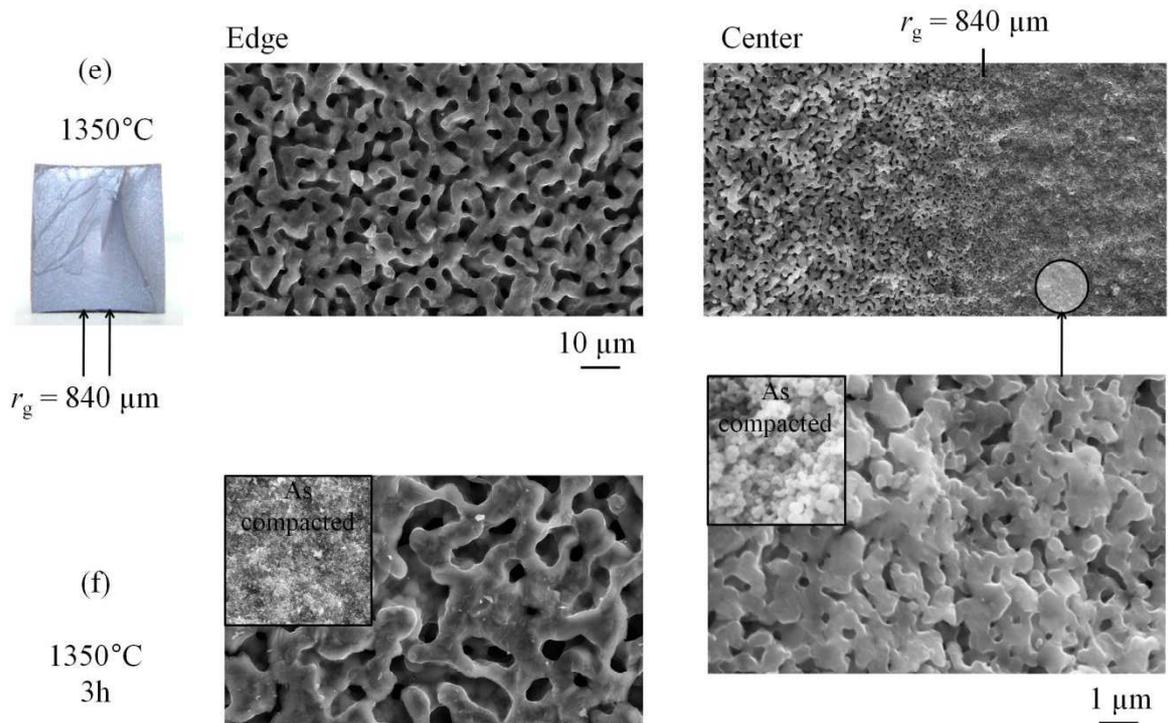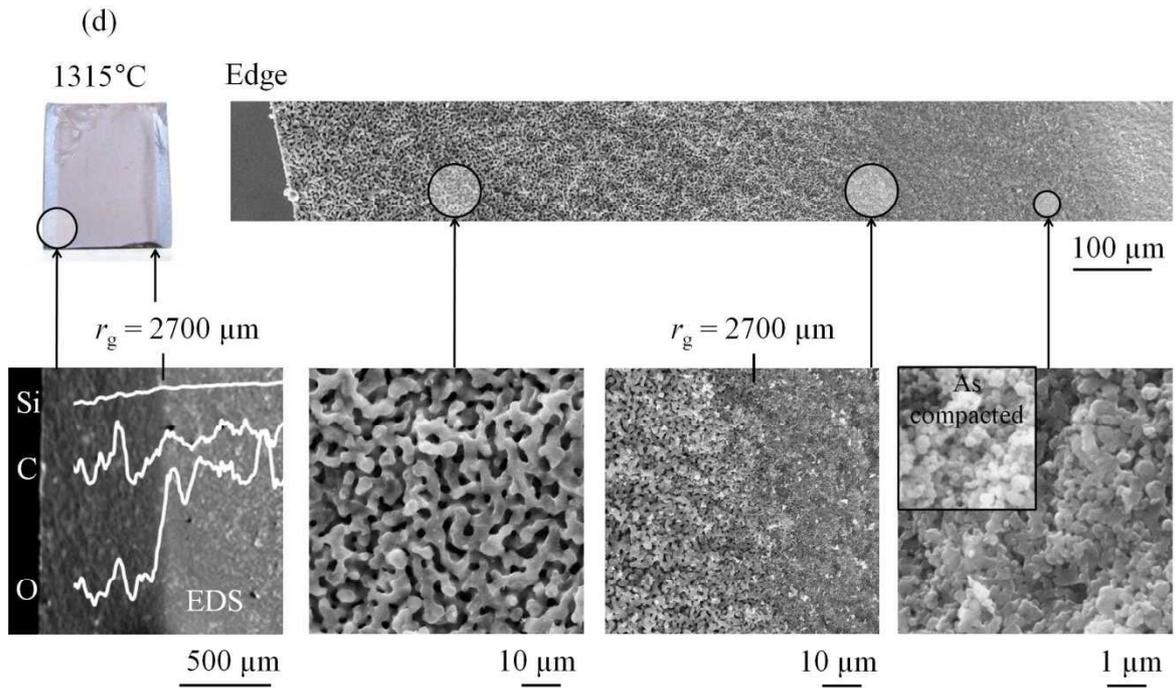
III.3.3 Model for silicon compact oxidation

a)   Basics

According to the previous section III.2, oxidation of silicon is controlled by reaction (R_5), assuming that the silica layer does not preclude the release of $SiO_{(g)}$ from the silicon-silica interface.

$$Si_{(s)} + SiO_{2(s)} = 2SiO_{(g)} \tag{R_5}$$

This reaction is a combination of two others, (R_1) and (R_2), that describes the oxidation state of silicon depending on the transition temperature, T^{*m}, or corresponding water vapor pressure surrounding the sample at the transition, $P_{H_2O}(T^{*m})$ (Figure III.1).

For temperatures lower than T^{*m}, a mass gain is observed and is related to passive oxidation of silicon according to the following reaction:

$$Si_{(s)} + 2H_2O_{(g)} = SiO_{2(s)} + 2H_{2(g)} \tag{R_1}$$

For temperatures higher than T^{*m}, a mass loss is observed and is related to the dissociation of silica (R_5) and active oxidation of silicon according to reaction:

$$Si_{(s)} + H_2O_{(g)} = SiO_{(g)} + H_{2(g)} \tag{R_2}$$

The mass transport kinetics can be entirely described in three steps as sketched on Figure III.8 for a compact in horizontal position:

(Step 1) The diffusion through a silica layer of nanometric thickness on the silicon particles in the non-reduced area. This step is assumed to not limit the departure of $SiO_{(g)}$ after the passive to active transition as the layer is assumed porous or cracked. But it certainly limits passive oxidation kinetics of silicon at low temperature. However, the silica growth at the sample surface is small under the water vapor pressure considered here. Diffusion kinetics of water through the silica layer is then not taken into account and passive oxidation kinetics is overestimated.

(Step 2) The molecular/Knudsen diffusion of $SiO_{(g)}$ and $H_2O_{(g)}$ in the porosity of the reduced area. A reduction front, at the radial position r_r, moves from the edge ($r_r = r_c$) to the center ($r_r = 0$) of the cylindrical compact. r_r can be related to the position r_g of the grain coarsening area, as observed on Figure III.7, since surface diffusion and then grain coarsening would become dominant after the silica removal [Cob90].

(Step 3) The molecular diffusion of $H_2O_{(g)}$ and $SiO_{(g)}$ outside the compact over a height z_f, along the furnace tube. (Appendix B.3.3).

As a first approximation, the shrinkage is neglected and the radius of the cylinder compact, r_c, is assumed constant.
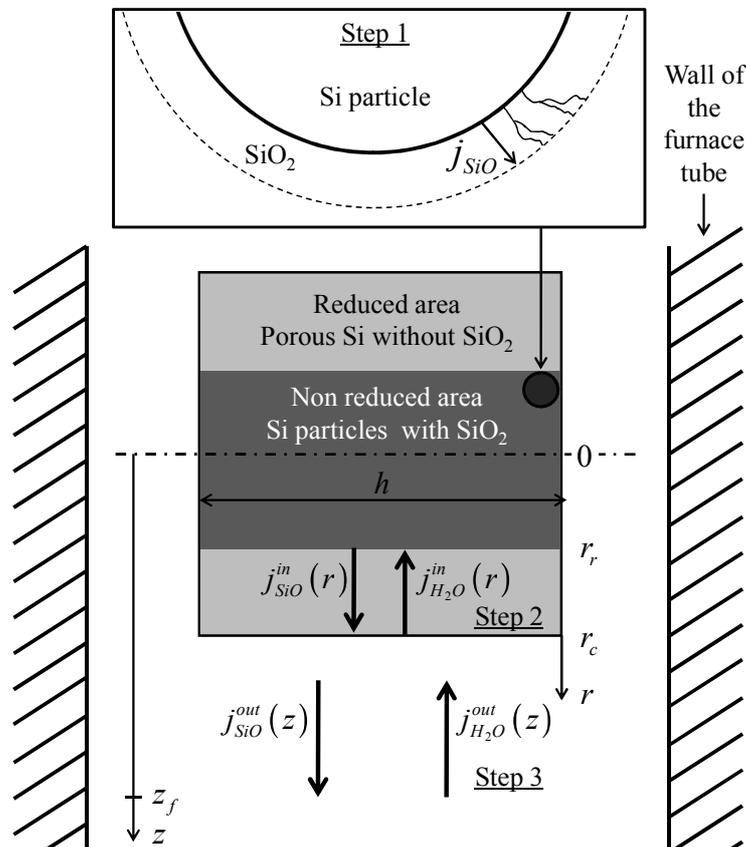
Figure III.8 : Schematic representation of the model derived. The fluxes of gases involved during the thermal oxidation of silicon compacts are represented. At the particle surface (Step 1), the diffusion of silicon monoxide occurs through holes or solid state diffusion. Inside the cylindrical compact, between 0 and r_r, silicon particles are covered with silica and the equilibrium (R_5) controls the rate of $SiO_{(g)}$ release (non-reduced area). Between r_r and r_c, silicon particles are free from oxide (reduced area) and gaseous species diffuse inside pores (Step 2). Out of the compact, gaseous species diffuse in the furnace tube in a stagnant mixture of He-4 mol.% H_2 (Step 3).

b)   Model equations

A kinetic model for diffusion is derived inside (Step 2) and outside (Step 3) the porous compact (Figure III.8), assuming steady-state conditions as verified in Appendix B.3.2.

The diffusion flux density of gaseous species j, j_j, is given by Equation (III.11), where ∇P_j is the pressure gradient of the species j, D_j, their diffusion coefficient, R the gas constant and T the temperature.

$$j_j = -\frac{D_j}{RT}\nabla P_j \qquad\qquad (III.11)$$

The diffusion flux densities $j_{H_2O}^{in}$ and j_{SiO}^{in} of $H_2O_{(g)}$ and $SiO_{(g)}$ inside the porosity of the reduced area (Step 2) are derived in cylindrical coordinates in Equations (III.12) and (III.13), r being the radial position in the cylindrical compact, $D_{H_2O}^{in}$ and D_{SiO}^{in} the diffusion coefficients inside the porosity of the reduced area.

$$j_{H_2O}^{in} = -\frac{D_{H_2O}^{in}}{RT}\frac{P_{H_2O}^{r_c} - P_{H_2O}^{r_r}}{\ln\left(\dfrac{r_c}{r_r}\right)}\frac{1}{r} \qquad\qquad (III.12)$$

$$j_{SiO}^{in} = -\frac{D_{SiO}^{in}}{RT}\frac{P_{SiO}^{r_c} - P_{SiO}^{r_r}}{\ln\left(\dfrac{r_c}{r_r}\right)}\frac{1}{r} \qquad\qquad (III.13)$$

The diffusion flux densities $j_{H_2O}^{out}$ and j_{SiO}^{out} of $H_2O_{(g)}$ and $SiO_{(g)}$ out of the compact (Step 3) are derived in linear coordinates in Equations (III.14) and (III.15), z being the vertical position in the furnace tube, $D_{H_2O}^{out}$ and D_{SiO}^{out} the diffusion coefficients outside the compact.

$$j_{H_2O}^{out} = -\frac{D_{H_2O}^{out}}{RT}\frac{P_{H_2O}^{z} - P_{H_2O}^{r_c}}{z} \qquad\qquad (III.14)$$

$$j_{SiO}^{out} = -\frac{D_{SiO}^{out}}{RT}\frac{P_{SiO}^{z} - P_{SiO}^{r_c}}{z} \qquad\qquad (III.15)$$

c)   Boundary conditions

At the reaction front position, r_r, there is competition between the formation of silica and silicon monoxide according to the monovariant equilibrium (R5). Thus, fixing the temperature, the pressure of silicon monoxide at the reaction front position, $P_{SiO}^{r_r}$, is given by the equilibrium pressure of reaction (R5), in Equation (III.16), where $P°$ is the standard pressure.

$$P_{SiO}^{r_c} = P_{SiO}^{R_5} = P° K_5^{1/2}$$ (III.16)

In the reduced area, particles are no longer covered with silica. Reaction (R_2) of equilibrium constant K_2 controls the pressures of silicon monoxide and water inside the sample.

$$Si_{(s)} + H_2O_{(g)} = SiO_{(g)} + H_{2(g)}$$ (R₂)

From Equation (III.17), the vapor pressure of water is found negligible as regards the pressure of silicon monoxide, in the temperature range of active oxidation (T > 1000 °C).

$$P_{H_2O}^r = \frac{P_{H_2}^r P_{SiO}^r}{P° K_2} < 2.10^{-3} P_{SiO}^r \quad \text{then} \quad P_{H_2O}^r \ll P_{SiO}^r$$ (III.17)

Since $D_{H_2O}^{in}$ and D_{SiO}^{in} are of the same order of magnitude, $j_{H_2O}^{in}$ can be neglected with respect to j_{SiO}^{in} (Equations (III.12) and (III.13)).

Since the water vapor pressure in the compact is much lower than the silicon monoxide one (Equation (III.17)), water is entirely consumed at the surface of the compact through the silicon oxidation. The water vapor pressure at the surface of the compact, $P_{H_2O}^{r_c}$, can be neglected with respect to the value far from the compact, $P_{H_2O}^{z_f}$. Indeed, $P_{SiO}^{r_c}$ cannot be superior to $P_{SiO}^{R_5}$ and Equation (III.18) can be written for temperatures below 1400 °C.

$$P_{H_2O}^{r_c} = \frac{P_{H_2}^{r_c} P_{SiO}^{r_c}}{P° K_2} < \frac{P_{H_2}^{r_c} P_{SiO}^{R_5}}{P° K_2} < 6.10^{-2} \text{ Pa} \quad \text{then} \quad P_{H_2O}^{r_c} \ll P_{H_2O}^{z_f} = 1 - 1.8 \text{ Pa}$$ (III.18)

Far from the sample, the temperature is low, silicon monoxide condensate in the form of silicon and silica and the partial pressure, $P_{SiO}^{z_f}$, becomes negligible as regards $P_{SiO}^{r_c}$, while the partial pressure of $H_2O_{(g)}$, $P_{H_2O}^{z_f}$, is at least the value in the experimental gas mixture (see Appendix B.3.4).

d)   Model derivation

Under steady-state conditions, the net transport of oxygen atoms reaching and leaving the sample vanishes (Equation (III.19)) and the silicon monoxide pressure at the surface of the cylinder, $P_{SiO}^{r_c}$ (Equation (III.20)), is deduced from Equations (III.12) to (III.19), S^{in} being the lateral cylindrical sample surface. S^{out} is twice the furnace tube section to take into account for the diffusion in the lower part as well as in the upper part of the tube.

$$\left(j_{SiO}^{out} + j_{H_2O}^{out}\right) \times S^{out} = j_{SiO}^{in} \times S^{in} \tag{III.19}$$

$$P_{SiO}^{r_c} = P_{SiO}^{R_5} \frac{D_{SiO}^{in}}{D_{SiO}^{in} + D_{SiO}^{out} \ln\left(\frac{r_c}{r_r}\right)\frac{r_c}{z_f}\frac{S^{out}}{S^{in}}} + P_{H_2O}^{z_f} \frac{D_{H_2O}^{out} \ln\left(\frac{r_c}{r_r}\right)\frac{r_c}{z_f}\frac{S^{out}}{S^{in}}}{D_{SiO}^{in} + D_{SiO}^{out} \ln\left(\frac{r_c}{r_r}\right)\frac{r_c}{z_f}\frac{S^{out}}{S^{in}}} \tag{III.20}$$

The mass loss rate is derived in Equation (III.21) considering that H_2O arrival is responsible for a mass gain and SiO departure for a mass loss. M_j is the molar mass of a specie j.

$$\frac{\Delta m}{\Delta t} = \left(-j_{H_2O}^{out}(r_c) \times M_O - j_{SiO}^{out}(r_c) \times M_{SiO}\right) \times S^{out}$$

$$= \frac{S^{out}}{RT \times z_f} \left[\begin{array}{c} P_{H_2O}^{z_f} D_{H_2O}^{out} M_O - P_{SiO}^{R_5} \dfrac{D_{SiO}^{out} D_{SiO}^{in}}{D_{SiO}^{in} + D_{SiO}^{out} \ln\left(\frac{r_c}{r_r}\right)\frac{r_c}{z_f}\frac{S^{out}}{S^{in}}} M_{SiO} \\[2em] - P_{H_2O}^{z_f} \dfrac{D_{SiO}^{out} D_{H_2O}^{out} \ln\left(\frac{r_c}{r_r}\right)\frac{r_c}{z_f}\frac{S^{out}}{S^{in}}}{D_{SiO}^{in} + D_{SiO}^{out} \ln\left(\frac{r_c}{r_r}\right)\frac{r_c}{z_f}\frac{S^{out}}{S^{in}}} M_{SiO} \end{array} \right] \tag{III.21}$$

In the same way, the silica mass variation in the compact is assessed in Equation (III.22), by considering that the molar variation of silica is half the oxygen one.

$$\frac{\Delta m_{SiO_2}}{\Delta t} = \frac{S^{out}}{RT \times z_f}\frac{1}{2} M_{SiO_2} \left[\begin{array}{c} P_{H_2O}^{z_f} D_{H_2O}^{out} - P_{SiO}^{R_5} \dfrac{D_{SiO}^{out} D_{SiO}^{in}}{D_{SiO}^{in} + D_{SiO}^{out} \ln\left(\frac{r_c}{r_r}\right)\frac{r_c}{z_f}\frac{S^{out}}{S^{in}}} \\[2em] - P_{H_2O}^{z_f} \dfrac{D_{SiO}^{out} D_{H_2O}^{out} \ln\left(\frac{r_c}{r_r}\right)\frac{r_c}{z_f}\frac{S^{out}}{S^{in}}}{D_{SiO}^{in} + D_{SiO}^{out} \ln\left(\frac{r_c}{r_r}\right)\frac{r_c}{z_f}\frac{S^{out}}{S^{in}}} \end{array} \right] \tag{III.22}$$

e) Application to the description of silicon oxidation sequences

During the passive oxidation of the compact, the model is reduced to a more simple expression where the influxes, j_j^{in}, do not exist. Equilibrium (R$_5$) is always realized at the edge of the sample ($r_r = r_c$). Equations (III.20), (III.21) and (III.22) can be written in a more simple way in Equations (III.23), (III.24) and (III.25), respectively.

$$P_{SiO}^{r_c} = P_{SiO}^{R_5} \tag{III.23}$$

$$\frac{\Delta m}{\Delta t} = \frac{S^{\text{out}}}{RT \times z_f}\left(P_{H_2O}^{z_f}D_{H_2O}^{\text{out}}M_O - P_{SiO}^{R_5}D_{SiO}^{\text{out}}M_{SiO}\right) \tag{III.24}$$

$$\frac{\Delta m_{SiO_2}}{\Delta t} = \frac{S^{\text{out}}}{RT \times z_f}\frac{1}{2}M_{SiO_2}\left(P_{H_2O}^{z_f}D_{H_2O}^{\text{out}} - P_{SiO}^{R_5}D_{SiO}^{\text{out}}\right) \tag{III.25}$$

The rate of mass loss (Equation (III.24)) is nil at a temperature T^{*m}, where the water vapor pressure far from the sample, $P_{H_2O}^{z_f}$, can be deduced from Equation (III.26) and corresponds to the water partial pressure, $P_{H_2O}^{WR_5}$, found in section III.1 (Equation (III.4) and Figure III.1).

$$P_{H_2O}^{z_f} = \frac{M_{SiO}}{M_O}\frac{D_{SiO}^{\text{out}}}{D_{H_2O}^{\text{out}}}P_{SiO}^{R_5}\left(T^{*m}\right) \tag{III.26}$$

For the 1.25 °C min^{-1} cycle, the rate of mass loss is nil at 1020 °C, thus giving a water pressure of 1.8 Pa far from the sample.

As the molar flux of silicon monoxide overpass the water vapor flux arriving at the surface of the compact, the silica starts to dissociate and the passive to active transition occurs as defined by Wagner [Wag58]. The reaction front position is located at r_c as long as the silica produced during the passive oxidation is not entirely reduced. Then, the reaction front starts to move to the center of the compact and the model is described by the general Equations (III.20), (III.21) and (III.22). The variation of the reaction front position (r_r) must be assessed in order to solve these equations. Assuming that the silica is initially uniformly distributed at the particle surfaces throughout the sample, the reaction front position as function of time, t, $r_r(t)$, is given by Equation (III.27).

$$r_r(t) = \sqrt{\frac{m_{SiO_2}(t)}{m_{SiO_2}(t=0)}}\, r_c \tag{III.27}$$

An iterative calculation is performed, $r_r(t)$ is sequentially uploaded in Equations (III.20), (III.21) and (III.22) thanks to Equation (III.27). The silica mass gradually decreases, causing the reaction front to move forward, which tends to reduce the rate of mass loss.

Finally, the silica mass and r_r position become nil, Equations (III.20), (III.21) and (III.22) simplify respectively in Equations (III.28), (III.29) and (III.30) during active oxidation (R$_2$). Equation (III.29) is simply the rate of mass loss as estimated by Wagner (Appendix A).

$$P_{SiO}^{r_c} = P_{H_2O}^{z_f}\frac{D_{H_2O}^{\text{out}}}{D_{SiO}^{\text{out}}} \tag{III.28}$$

$$\frac{\Delta m}{\Delta t} = -\frac{S^{\text{out}}}{RT \times z_f} P_{H_2O}^{z_f} D_{H_2O}^{\text{out}} M_{Si}$$ (III.29)

$$\frac{\Delta m_{SiO_2}}{\Delta t} = 0$$ (III.30)

The rate of mass loss no longer depends on the equilibrium constant of reaction (R$_5$). It is then monitored by the water vapor pressure in the gas mixture, $P_{H_2O}^{z_f}$, and the diffusion length of the species out of the compact, z_f. $P_{H_2O}^{z_f}$ being equal to 1.8 Pa, z_f is found to be 40 mm for the 1.25 °C min^{-1} cycle, a value slightly larger than the uniform temperature area in the furnace tube (30 mm) beyond which a condensate film of silicon and silica is observed (Figure III.4).

f)   Assessment of model parameters

Diffusion coefficients out of the compact, D_j^{out}, are the molecular diffusion coefficients (Equation (III.31)), estimated as a function of molecular characteristics and temperature from the semi-empiric approach of Chapman-Enskog [BSL01, AS62] in Appendix B.4.1.

$$D_j^{\text{out}} = D_j^{\text{mol}}$$ (III.31)

Diffusion coefficients inside the compact (Equation (III.32)) are function of the molecular diffusion coefficient, D_j^{mol}, and the Knudsen diffusion coefficient, D_j^{Knudsen}, accounting for the elastic collisions between gas molecules and the pore surface. D_j^{Knudsen} is calculated from the gas kinetic theory [BSL01] in Appendix B.4.2, replacing the molecular mean free path by the pore size estimated between 1 and 10 μm from SEM observations.

$$D_j^{\text{in}} = \frac{p}{\tau} \left(\frac{1}{D_j^{\text{mol}}} + \frac{1}{D_j^{\text{Knudsen}}} \right)^{-1}$$ (III.32)

The volume fraction of pores, p, is fixed as 40 %, a value comprised between the initial (47 %) and final (36 %) experimental values (density curve in Figure III.6). The pore tortuosity, τ, is at least equal to the minimal molecular path around spherical particles, *i.e.* $\frac{\pi}{2}$.

The initial amount of silica in the compact, $m_{SiO_2}(t=0)$ (Equation (III.27)), is related to the thickness of the oxide covering the particles and to the sample mass. This value is adjusted in the model to fit the experimental global mass loss and is consistent with the IGA

measurements. It corresponds to an initial thickness of 0.52 nm for the native oxide (0.43 ± 0.10 nm from IGA).

III.3.4 Application of the model to Φ_7 samples

Experimental and model results are displayed on Figure III.9 for the 1.25 °C min^{-1} cycle.
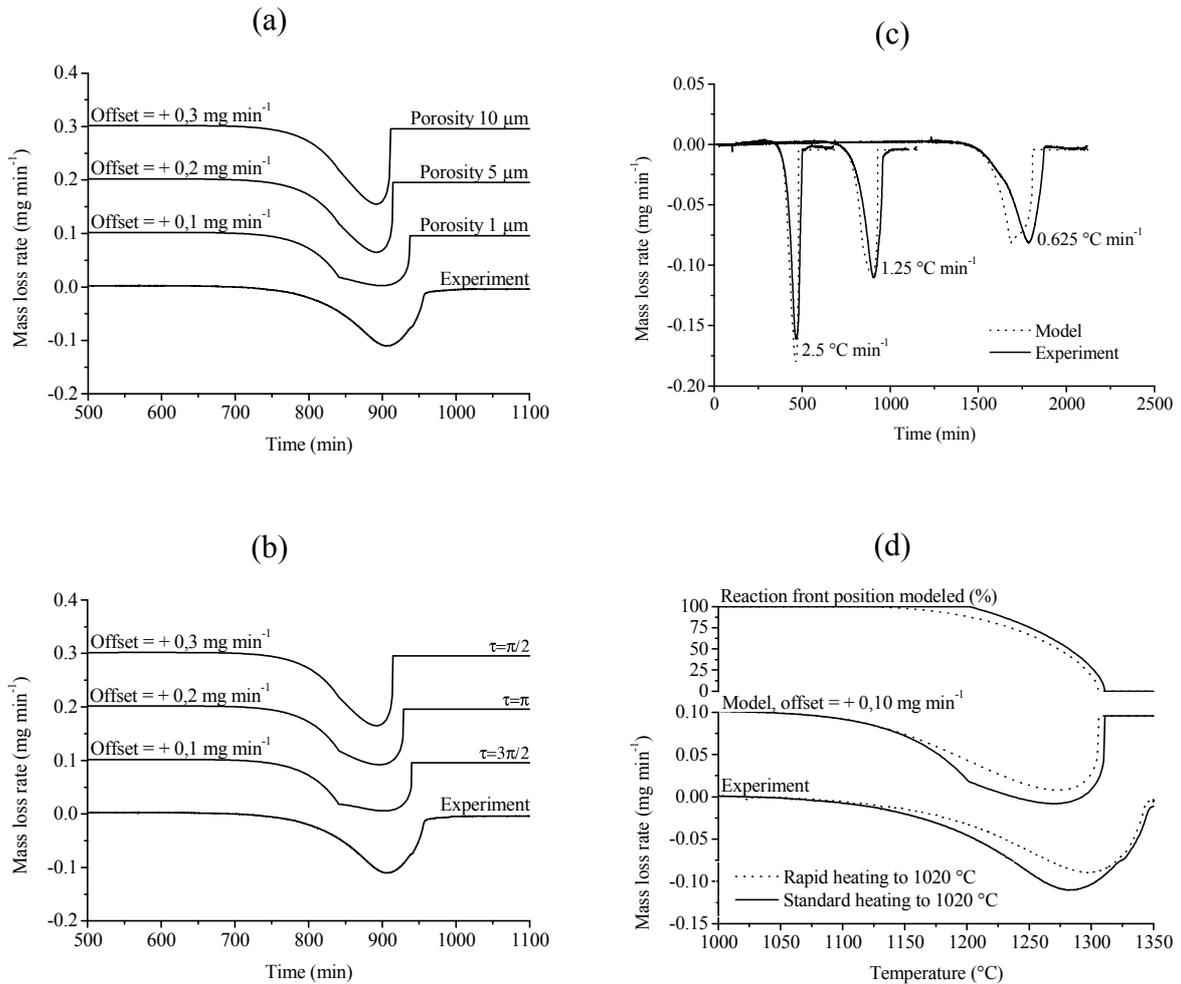
Figure III.9: Experimental and modeled rate of mass loss. Constant model parameters are p = 0.4, e_{SiO_2} = 0.52 nm, $P_{H_2O}^{z_f}$ = 1.8 Pa, and z_f = 40 mm. (a) Effect of the pore size for a heating rate of 1.25 °C min^{-1} and a tortuosity of π/2. (b) Effect of the tortuosity for an heating rate of 1.25 °C min^{-1} and a pore size of 5 μm. (c) Effect of the heating rate for a pore size of 5 μm and a tortuosity of π. (d) Effect of the passive oxidation, occurring below 1020 °C, on the reaction front position and the rate of mass loss during the silica reduction. Above 1020°C the heating rate is 1.25 °C min^{-1}. The pore size is 5 μm and the tortuosity π.

In Figure III.9 (a), three different pore sizes (1, 5 and 10 μm) and a tortuosity of $\pi/2$ were first considered. As the pore size is decreased, D_j^{in} (Equation (III.32)) decreases which slows

down the rate of mass loss. For a pore size of 5 μm, the model overestimates the rate of mass loss, probably because the tortuosity has been underestimated.

In Figure III.9 (b), experimental results are compared to the model for a pore size of 5 μm and tortuosities of $\pi/2$, π and $3\pi/2$. As the tortuosity is increased, D_j^{in} (Equation (III.32)) decreases which slows down the rate of mass loss. The pore size and the tortuosity increase with time in the reduced area, due to the microstructure coarsening and partial densification. These two effects have opposite consequences on the rate of mass loss. Afterwards, a constant pore size of 5 μm and a constant tortuosity of π will be used as it seems realistic values.

In Figure III.9 (c), the experimental rates of mass loss are given for the 0.625, 1.25 and 2.5 °C min^{-1} cycles. Even though simplifications have been made as regards the geometry or the grain size and tortuosity in the reduced area, the model fits the data pretty well and never underestimates the rate of mass loss. Close to the reaction front, the grain size evolution is not taken into account and may explain the slower experimental rate of mass loss measured at the beginning of the silica reduction, when the whole porosity is lower than 1 μm, as observed on SEM micrographs (Figure III.7 (c)).

It has been assumed that the silica is entirely produced at the sample surface during passive oxidation. To confirm this assumption a sample was rapidly heated (40 °C min^{-1}) to 1020 °C, to limit the passive oxidation, and then slowly heated to 1350 °C with the standard heating rate of 1.25 °C min^{-1} (Figure III.9 (d)). In these conditions, the reaction front position moves to the center of the compact sooner because the surface silica layer grown during heating is thinner. The model correctly predicts the sooner reduction of the rate of mass loss compared to the standard 1.25 °C min^{-1} cycle. The amount of silica to be eliminated is lower in this case, leading to a lower global mass loss.

III.3.5 Extension of the model to Φ_{15} samples

Experimental and modeled mass loss curves for the Φ_7 and Φ_{15} samples are given in Figure III.10 for the 1.25 °C min^{-1} cycle.
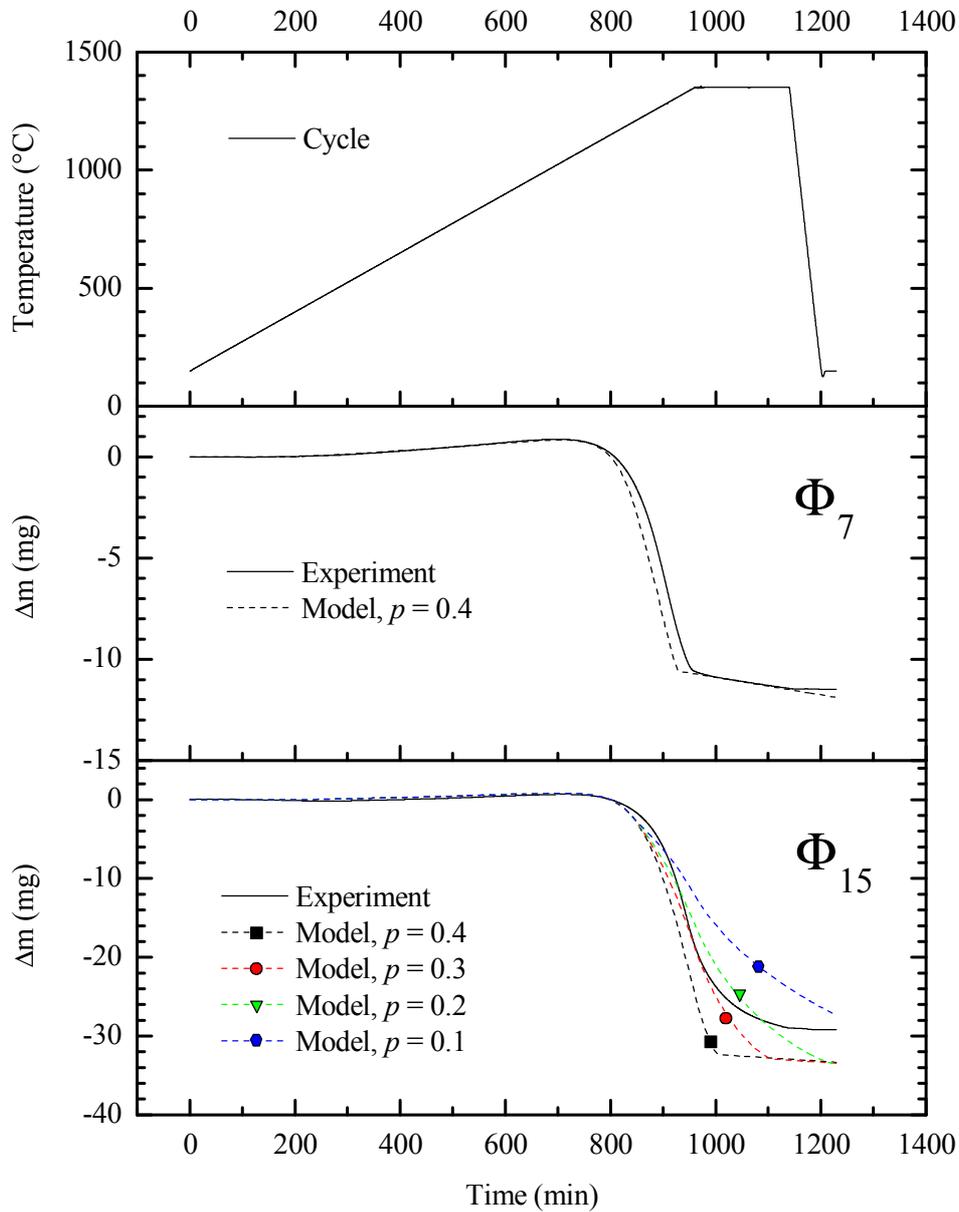
Figure III.10: Experimental curves (full line) and modeled curves (dashed lines) of the mass loss for the Φ_{15} and Φ_7 samples associated with the thermal cycle (1.25 °C min^{-1}, 1350 °C - 3 h - 2 l h^{-1} He-4 mol.% H_2). Constant model parameters are $\tau = \pi$, $e_{SiO_2} = 0.52$ nm, $P_{H_2O}^{z_f} = 1.8$ Pa, and $z_f = 40$ mm. For the Φ_{15} sample, the effect of the porosity decrease on the global mass loss of the sample is depicted.

- For the Φ_7 sample, the global mass loss is 2.8 % of the intial sample mass. The rate of mass loss suddenly collapses just before the dwell at 1350 °C. This corresponds to the end of the silica reduction since the mass loss rate becomes constant and is deduced using Equation (III.29) by putting $r_r = 0$ in Equation (III.21). The model predicts an earlier mass loss but accounts very well for the shape of the curve and the amplitude of the mass loss.

- For the Φ_{15} sample, the global mass loss is higher since the sample mass and thus the anount of silica to be reduced is also higher. A sudden collapse in the mass loss rate associated with a complete silica reduction is also predicted from the model. Experimentally, the global mass loss is only 2 % of the sample mass. The expected mass loss is then not measured and the sudden collapse is not observed, showing that the silica reduction is incomplete.

To explain the experiment and model inconsistency on the Φ_{15} curves, samples polished cross sections are observed and compared in Figure III.11.
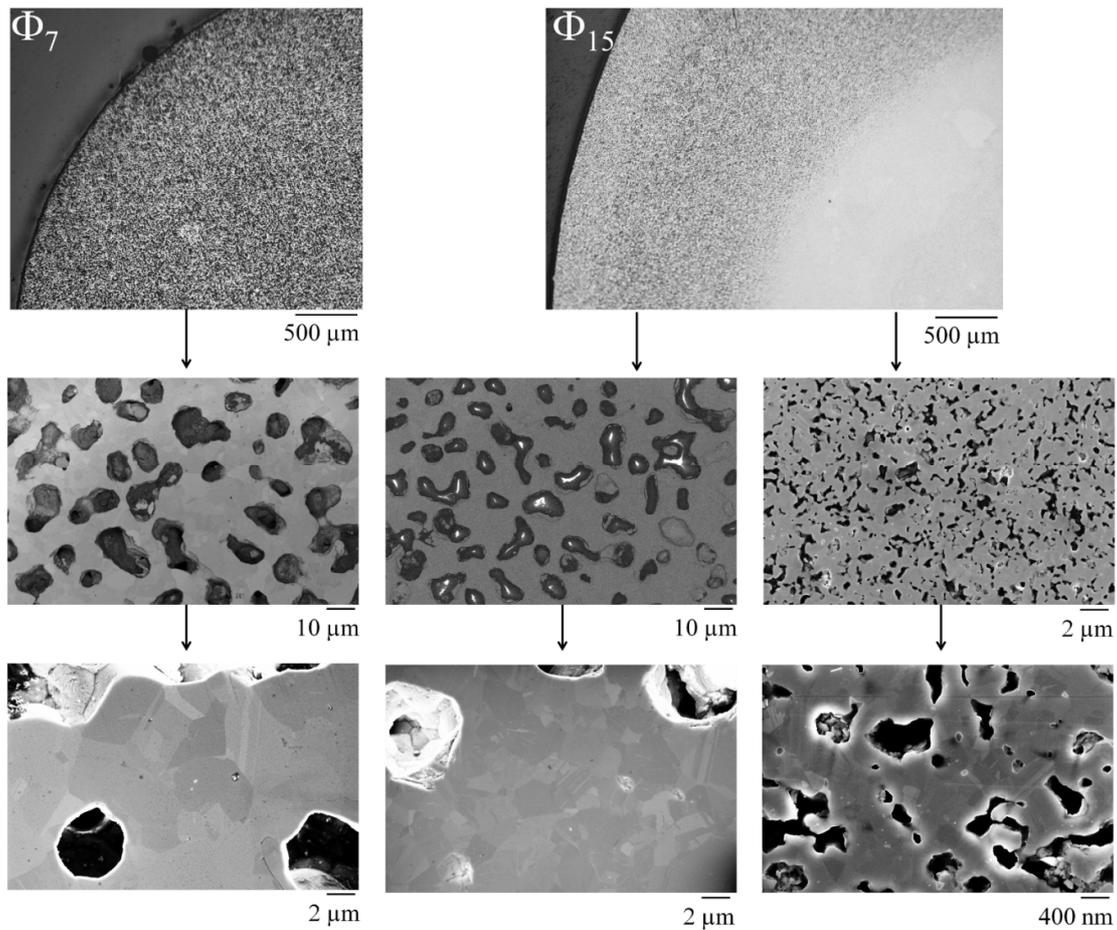
Figure III.11: Optical and SEM microstructures of Φ_7 and Φ_{15} polished samples.

- Φ_7 sample microstructure is homogeneous over the compact with large grains (2-5 µm) surrounded by coarser pores (5-10 µm) as observed on Figure III.7 (f).

- Φ_{15} sample microstructure is non-uniform as already observed by Shaw and Heuer [SH83] and Möller and Welsch [MW85]. A relatively dense inner core (80-85 % TD_{Si} from image analysis) with a fine grain size (~200 nm) is surrounded by a region of coarse grain and porosity (~65 % TD_{Si} from image analysis). The global density of the compact is 76 % TD_{Si}, comparatively higher than the density of Φ_7 sample which is 64 % TD_{Si}.

The silica reduction kinetics is strongly influenced by the microstructure evolution and *vice versa*. Indeed, for the Φ_{15} sample, decreasing the pore fraction in the model leads to a better fit of the mass loss curve (Figure III.10). However, this fit is actually not accurate since the pore fraction is not constant inside the compact as assumed in the model derivation. At the center of the compact, silica impedes grain and pore coarsening and allows densification of the sample. The porosity decrease is responsible for a diminution of the diffusion coefficient inside the compact, D_j^{in} (Equation (III.32)) and leads to a retardation of the silica reduction as observed on the Φ_{15} experimental mass loss curve.

III.3.6 Summary

The effect of the powder compact size on silica layer reduction kinetics, microstructure evolution and final density has been studied.

Thermogravimetric experiments have shown that the silica covering the silicon particles is easily reduced during sintering. A reduction front propagates from the edge to the center of the sample and kinetics is controlled by the diffusion of silicon monoxide released into the porous compact. After reduction of the silica layer, grain coarsening occurs and densification is precluded.

The silica reduction kinetics is strongly influenced by the microstructure evolution. In small compacts, thermogravimetric experiments have shown that the silica can be rapidly reduced leading to a very porous and coarse microstructure. In larger compacts, silica reduction is retarded, impeding coarsening. This leads to non-uniform final microstructures with higher densification of the core where the silica cannot be reduced.

A kinetic model describing the silicon oxidation steps has been developed taking into account the initial powder oxygen content, the pore morphology of the sintered samples, the partial pressure of oxidizing species and the furnace geometry. As regards silicon sintering process, the control of these two last parameters is crucial as will be seen in Chapter V.

III.4 **Discussion: continuity of the silica layer**

One of the most important assumption of the closed-form model derived above, is that the silica layer does not rate limit the elimination of $SiO_{(g)}$. Indeed, for reaction (R$_5$) to occur, the $SiO_{(g)}$ formed at the $Si_{(s)}$-$SiO_{2(s)}$ interface must be evacuated.

If the silica layer were perfectly continuous, this would occur by solid state diffusion through this layer. According to Sasse and König [SK90], the diffusion of the SiO molecular entity would control the kinetics. The diffusion coefficient in vitreous silica, D_{SiO}^{l,SiO_2}, is estimated as 3.2×10^{-20} and 2.7×10^{-19} m² s^{-1} at 1000 and 1100 °C respectively. These values are considerably lower than the molecular diffusion coefficient of silicon monoxide in the gas phase, D_{SiO}^{mol} (# 8×10^{-4} m² s^{-1}, Figure B.6 in Appendix B.4.1).

Assuming a serial diffusion of silicon monoxide in the silica layer (thickness, e_{SiO_2}) and in the gas phase (distance, z_f), an effective diffusion coefficient, D_{SiO}^{eff}, can be overestimated from Equation (III.33).

$$D_{SiO}^{eff} = \left(z_f + e_{SiO_2}\right)\left(\frac{e_{SiO_2}}{D_{SiO}^{l,SiO_2}} + \frac{z_f}{D_{SiO}^{mol}}\right)^{-1} \underset{e_{SiO_2}=1nm}{\approx} 1 \times 10^{-9} D_{SiO}^{mol} \qquad \text{(III.33)}$$

Even when considering the diffusion of silicon monoxide in a silica layer of nanometric thickness, the effective diffusion coefficient is much lower than the molecular diffusion coefficient, which is used in the model to describe the reduction kinetics in section III.3.3. Accordingly, if the silica layer were perfectly continuous, it would entirely preclude silica reduction through reaction (R$_5$). It is then fair to question the continuity of this layer.

From interfacial energy considerations, the silica layer should be stable and continuous. The surface energy of amorphous silica, $\gamma^{SiO_2 V}(T) = 0.307 - 0.0002 \times (T - 1720\,°C)$ J m^{-2} [END99], is much lower than the surface energy of silicon, $\gamma^{SiV}(T) = 1.08 - 0.0001 \times (T - 937\,°C)$ J m^{-2} [END99], as usually observed when comparing oxide to metal surface energies. The silicon-silica interfacial energy, $\gamma^{Si\,SiO_2}$, can be estimated from wettability measurements of silicon onto silica. The wetting is then unfavorable with an equilibrium contact angle, $\omega \sim 90° \pm 10°$ [WTT99]. Accordingly, the silicon-silica interfacial energy, $\gamma^{Si\,SiO_2}$, should be of the same order as the surface energy of amorphous silica, $\gamma^{SiO_2 V}$. As shown in Figure III.12, as the temperature increases, the global energy of a silica layer covering a silicon surface becomes even less than the energy of a free silicon surface. Accordingly, dewetting of silica on silicon particles is unlikely to occur.
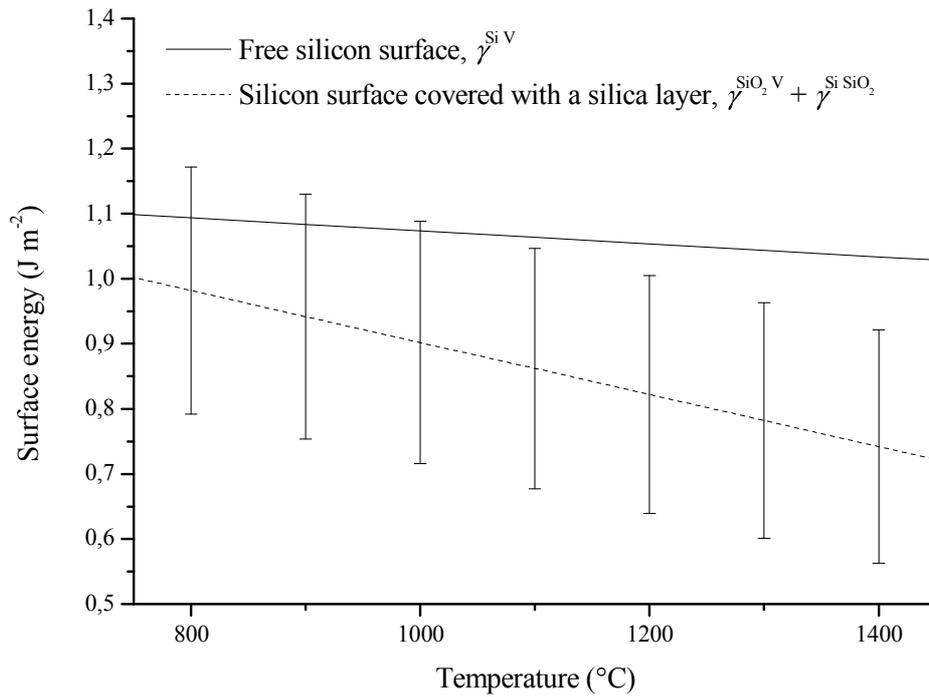
Figure III.12: Surface energy of a free silicon surface compared with the estimated surface energy of a silicon surface covered with a silica layer.

The inconsistency is removed by considering the presence of defects, such as oxygen vacancies or holes, in the silica layer. These defects could be initially present inside the native oxide or created during heating. However, during heating below the passive to active transition, continuous growth of the silica layer occurs through reaction (R_1). This growth should fill the holes and decrease the vacancy concentration in the layer.

$$Si_{(s)} + 2H_2O_{(g)} = SiO_{2(s)} + 2H_{2(g)} \tag{R_1}$$

But, once the passive to active transition temperature is overpassed, the overall vacancy concentration should increase and accelerate the diffusion of silicon monoxide molecules (Figure III.13 (a)).

Considering the thermal expansion coefficients of silicon (4.26×10^{-6} °C^{-1} [Hul99]) and vitreous silica (0.55×10^{-6} °C^{-1} [Smi83]) at 1000 °C, tensile stresses should also appear during heating and result in an increment of oxygen vacancies (Figure III.13 (b)) or even cracks or holes (Figure III.13 (c)).

Nevertheless, according to the Pilling-Bedworth ratio, which is defined as the ratio of the molar volume of silica to the molar volume of silicon, the silica layer is initially under

compressive stresses. Indeed, this ratio is close to 2.1 in the case of amorphous silica, tridymite or cristoballite, which are the most common crystalline strcutres proposed for thin native silica layers. The silica layer should be then initially continuous and passive, as observed expiremtally since silicon is usually protected against further oxidation once a native silica layer is formed.[3]

Another possible reason for the acceleration of the diffusion in the silica layer after the passive to active transition is the generation of vacancies by the reaction (R_5), itself, at the silicon-silica interface.

Whatever the origin of the defects, considering the thickness of the silica layer (0.5 nm, two or three silica tetrahedrons), these should rapidly propagates in non-healable holes (Figure III.13 (d)) as observed by Tromp *et al.* [TRB+85] under vacuum.
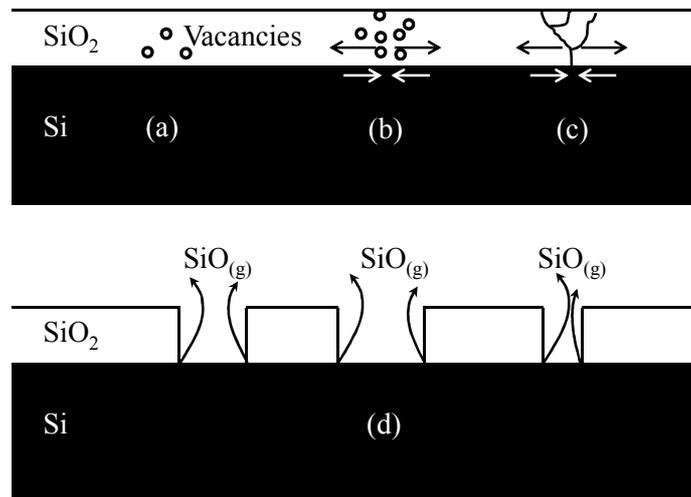
Figure III.13: Defects in a silica layer covering a silicon surface. (a) *Generation of vacancies,* (b and c) *Generation of vacancies, cracks or holes under the effect of thermal tensile stresses,* (d) *Non-healable holes.*

From the gas kinetic theory (Appendix B.4), the evaporation flux of silicon monoxide through the holes is given in Equation (III.34), where Φ is the surface area fraction of holes at the particle surface.

$$j_{SiO}^{v} = \frac{\Phi P_{SiO}^{R_5}}{\sqrt{2\pi M_{SiO} R T}}$$

(III.34)

---

[3] Paragraph added to the manuscript following a discussion with the comitee during the PhD defence.

The diffusion flux of silicon monoxide from the sample surface is roughly estimated in Equation (III.35) from discussion of section III.3.3.

$$j_{SiO}^{d} = \frac{D_{SiO}^{mol}}{RT} \frac{P_{SiO}^{R_5}}{z_f}$$
(III.35)

According to a mass balance, at the passive to active transition, the evaporation does not limit the silicon monoxide departure if Equation (III.36) is verified.

$$j_{SiO}^{v} = j_{SiO}^{d}$$
(III.36)

Using Equations (III.34) to (III.36), this is verified for surface area fraction of holes of approximately 4×10^{-5} as shown in Equation (III.37).

$$\Phi = \frac{D_{SiO}^{mol} \sqrt{2\pi M_{SiO}}}{z_f \sqrt{RT}}$$
(III.37)

From our results on silica reduction kinetics, it is fair to assume that the holes surface area fraction overpasses this limit as soon as the passive to active transition is overpassed. Cracks or holes then rapidly propagate in non-healable holes and silica reduction kinetics is limited by molecular diffusion in the gas phase.

III.5 **Conclusion**

Reaction (R_5) has been shown to control the stability of the silica layer depending on the temperature and on the surrounding partial pressure of oxidizing species.

$$Si_{(s)} + SiO_{2(s)} = 2SiO_{(g)}$$
(R_5)

The silica layer is assumed to be fragmented as the solid state diffusion of silicon (or silicon monoxide) through the silica layer cannot account for the rapidity of the silica removal, which is simply limited by the molecular diffusion of silicon monoxide and water in the gas phase.

A closed-form model has been developed and predicts well the experimental data of silica reductions kinetics in small compacts (Φ_7). However, in larger compacts (Φ_{15}), the model cannot account for the incomplete silica reduction as the densification of the inner part of the compact is not taken into account.

Even though very fine (about 0.5 nm), the silica layer strongly influences sintering kinetics. From the center of the compact to the reduction front (non-reduced area), silica prevents grain

coarsening (Φ_{15} center microstructure in Figure III.11) and facilitates densification. From the reduction front to the edge of the sample (reduced area), densification is impeded because of significant grain coarsening (Φ_7 microstructure in Figure III.11) and densities higher than 65 % TD_{Si} cannot be reached.

As regards silicon sintering process, the comprehension of the role of the silica layer on silicon sintering mechanisms is crucial and is going to be discussed in Chapter IV.2. Also, the establishment of a model relating silica reduction and microstructure evolution in porous layers would be of great interest in order to control the remaining oxygen content, the porosity and eventually the electrical properties of the final material.

Chapter IV.   Sintering kinetics

$\mathbf{S}$ intering corresponds to the minimization of the surface-interface energy as solid-vapor surfaces decrease at the expense of the solid-solid interfaces. Sintering and densification of covalent materials such as silicon were thought to be intrinsically limited by a high ratio of interfacial solid-solid, γ^{SS}, to solid-vapor energy, γ^{SV}. This energy ratio may be connected to the dihedral angle, Ψ_e, observed on microstructures using Equation (IV.1). A 2D pore surrounded by three grains (Figure IV.1) may shrink to closure only if the equilibrium dihedral angle is higher than 60°, *i.e.*, if $\gamma^{SS}/\gamma^{SV} < \sqrt{3}$.

$$\gamma^{SS} = 2\gamma^{SV} \cos\left(\frac{\Psi_e}{2}\right) \tag{IV.1}$$
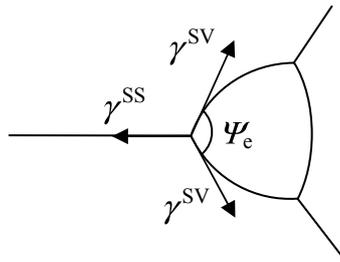
Figure IV.1: Pore surrounded by three grains. The equilibrium dihedral angle is given by interfacial tensions that control sintering.

During firing of silicon powder compacts, particle coarsening occurs as observed on SEM micrographs (Figure III.7 and Figure III.11). The specific surface area of the material (solid-vapor surface with respect to the sample mass, m² g^{-1}) largely decreases without densification and dihedral angles are higher than 60°, showing that sintering of silicon is not intrinsically limited by energy considerations as already shown by Greskovich [GR76].

Kinetic interpretations were then put forward to explain the poor densification of silicon. However, these interpretations are controversial [GR76, Cob90] and need to be revisited. Mass transport during sintering can occur by at least five different paths that define the mechanisms of sintering. Some mechanisms (referred to as densifying mechanisms) lead to densification of the powder system, whereas others (referred to as non-densifying mechanisms) do not. All of them lead to neck growth between particles and can occur simultaneously. They interact each other and influence the densification rate. However, in a first approach, these mechanisms will be considered separately.

One of the most important conclusions of Chapter III, is the inhibition of coarsening by the silica layer at the particle surface. Densification kinetics will be measured for pure silicon and for silicon particles covered with silica using appropriate dilatometric measurement techniques. These experiments will be compared to a sintering kinetic model taking into account the presence of silica at the particle surface. It will then be possible to conclude on the role of the silica layer on silicon densification kinetics during sintering.

Eventually, a processing route based on TPS (Temperature Pressure Sintering) diagrams and involving a control of the silica layer stability will be proposed in order to control the final density and microstructure of the material.

IV.1 **Sintering stage models**

IV.1.1 Sintering stage definitions

Sintering usually occurs through three sequential stages referred to as the initial stage, the intermediate stage and the final stage [Rah95, Kan05, BA93, Ger94, Ger96]. Each stage refers to an idealized geometrical model that roughly represents the microstructure of the powder compact.

The initial stage consists of particle to particle neck growth. The volume of individual particles is assumed constant, i.e, grain growth is not taken into account. The initial stage is assumed to last until the density has reached 60-65 %.

The intermediate stage begins when the pores have reached their equilibrium shapes, *i.e.*, a constant surface curvature with a dihedral angle equal to the equilibrium value, $\Psi = \Psi_e$ (Figure IV.1). The pores are interconnected. This sintering stage is assumed to correctly represent the microstructure for densities less than 90-95 %.

The final stage of sintering is considered when pores pinch off and become isolated, that is to say, for densities higher than 90-95 %.

First, only the initial stage of sintering will be considered to investigate the dominant sintering mechanisms. Then, we shall consider the second stage of sintering and its connection with the first one such as to predict the microstructure evolution (grain/pore growth) of the material.

Sintering kinetics is related to differences in bulk pressure (or vacancy concentration), in the solid phase, and vapor pressure, in the vapor phase, that act simultaneously. The effect of the particle and neck curvature on these three phenomena is discussed in the following section.

IV.1.2 Effect of interface curvature on solid and vapor phases

Consider one solid particle (S) made of a single specie j in equilibrium with a surrounding vapor phase (V) (Figure IV.2). An infinitesimal and reversible change between the solid and vapor phase results in infinitesimal change in chemical potentials, $d\mu_j^S$ and $d\mu_j^V$. The equilibrium condition states the equality of the chemical potentials of the two phases in Equation (IV.2).

$$d\mu_j^S = d\mu_j^V \tag{IV.2}$$

At a given temperature, the infinitesimal change in chemical potential, $d\mu_j$, can be related to an infinitesimal change in partial pressure, dP_j, in Equation (IV.3), which is equivalent to Equation (IV.4), where Ω corresponds to the phase molar volume and where P_j^V and P_j^S are respectively the equilibrium pressure in the vapor and solid phase near a curved interface.

$$\Omega_j^S dP_j^S = \Omega_j^V dP_j^V \tag{IV.3}$$

$$\left(\Omega_j^V - \Omega_j^S\right) dP_j^S - \Omega_j^V d\left(P_j^S - P_j^V\right) = 0 \tag{IV.4}$$

According to the Laplace Equation (IV.5), the solid-vapor interface curvature, κ, impose a pressure jump at the surface of the particle between the solid phase and the vapor phase.

$$P_j^S - P_j^V = 2\gamma^{SV}\kappa \tag{IV.5}$$

Combination of Equations (IV.3), (IV.4) and (IV.5) gives Equations (IV.6) and (IV.7).

$$dP_j^S = 2\frac{\Omega_j^V}{\Omega_j^V - \Omega_j^S}\gamma^{SV} d\kappa \tag{IV.6}$$

$$dP_j^V = 2\frac{\Omega_j^S}{\Omega_j^V - \Omega_j^S}\gamma^{SV} d\kappa \tag{IV.7}$$

Using $\Omega_j^V \gg \Omega_j^S$ and $\Omega_j^V = RT/P_j^V$, Equations (IV.6) and (IV.7) are simplified and integrated from 0 (curvature of the plane) to κ to give Equations (IV.8) and (IV.9), where P_j^0 is the equilibrium pressure near a plane interface and $F_j = \gamma^{SV}\Omega_j^S/RT$ is a characteristic length.

$$P_j^S - P_j^0 = 2\gamma^{SV}\kappa \tag{IV.8}$$

$$\ln\left(\frac{P_j^V}{P_j^0}\right) \approx \frac{P_j^V - P_j^0}{P_j^0} = 2\frac{\gamma^{SV}\Omega_j^S}{RT}\kappa = 2F_j\kappa \tag{IV.9}$$
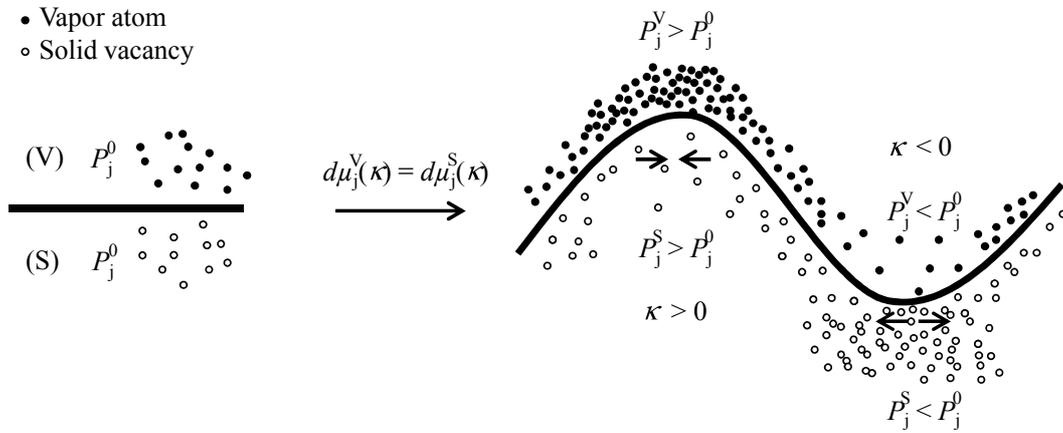
Figure IV.2: Plane and curved solid (S) - vapor (V) interface. The interface curvature induces a change in atom concentration in both phases in order to satisfy the equality of the chemical potentials.

In the vapor phase (Equation (IV.9)), a positive curvature (convex surface) results in a pressure increase, *i.e.* a higher atom vapor concentration, while a negative curvature (concave surface) results in a pressure drop, *i.e.* a lower atom vapor concentration (Figure IV.2).

In the solid phase (Equation (IV.8)), a positive curvature (convex surface) results also in a pressure increase that acts as a compressive stress on the lattice, while a negative curvature (concave surface) results in a pressure drop that acts as a tensile stress. Actually, the pressure difference, $\left(P_j^S - P_j^0\right)$, is also related to a chemical potential difference underneath the curved interface in Equation (IV.10), which in turns leads to an atomic concentration difference, $\left(C_j^S - C_j^0\right)$ in Equation (IV.11).

$$\Delta\mu_j^S = \Omega_j\left(P_j^S - P_j^0\right) = 2\gamma^{SV}\Omega_j\kappa \tag{IV.10}$$

$$\ln\left(\frac{C_j^S}{C_j^0}\right) \approx \frac{C_j^S - C_j^0}{C_j^0} = \frac{\Delta\mu_j^S}{RT} = 2\frac{\gamma^{SV}\Omega_j}{RT}\kappa = 2F_j\kappa \qquad \text{(IV.11)}$$

A positive curvature (convex surface) results in a higher concentration of atoms on lattice sites, while a negative curvature (concave surface) results in a lower concentration of atoms compared to the plane interface. The atom concentration difference is related to an opposite vacancy concentration difference on lattice sites (Figure IV.2).

To conclude, the driving force for sintering is the reduction of interfacial energy. The material transport is induced by differences in bulk pressure (or vacancy concentration) and vapor pressure that control sintering kinetics.

IV.1.3 Initial sintering stage: mechanisms and equations

The usual model for the initial stage consists of two spheres of equal radius a, connected with a neck of radius x. The negative curvature around the neck region induces matter transport towards this area and increases the neck size (Figure IV.3).

Sintering equations are derived in Appendix A by equaling the neck volume increase per unit time, dV/dt, and the net volume flux of atoms coming to the neck, which depends on the flux density of atoms j, j_j, the surface area of the flux, A, and the molar volume of the specie j, Ω_j, in Equation (IV.12).

$$\frac{dV}{dt} = j_j A\Omega_j \qquad \text{(IV.12)}$$

The atom flux density is related to the atom concentration difference in the solid phase (Equation (IV.11)) and to the vapor pressure difference in the vapor phase (Equation (IV.9)). Material transport either contributes to shrinkage or not, depending on the diffusion path (Figure IV.3).

Sintering equations are reported in Table IV.1 and Table IV.2 for non-densifying (nd) and densifying (d) mechanisms, respectively.
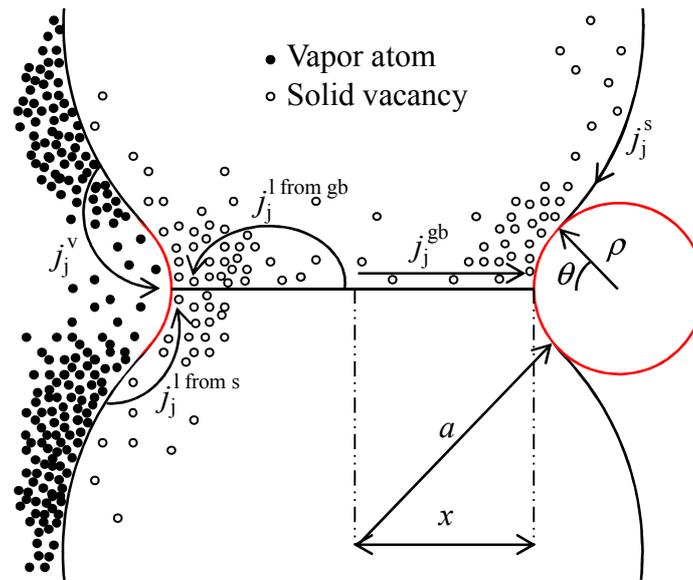
Figure IV.3: Two spherical particles model for initial sintering stage. Matter transport is driven by the negative curvature around the neck (in red), where the concentration of atom vacancies is higher in the solid phase and the concentration of vapor atoms is lower in the vapor phase. Matter transport can occur through five distinct paths. Three of them correspond to an atomic flux from the surface of the particles and are then non-densifying: vapor transport, j_j^v, surface diffusion, j_j^s, and lattice diffusion from the surface of the particles, $j_j^{l\,from\,s}$. Two of them correspond to an atomic flux from the grain boundary, they induce particles center to center and are then densifying: grain boundary diffusion, j_j^{gb}, and lattice diffusion from the grain boundary, $j_j^{l\,from\,gb}$.

Non-densifying mechanisms transport matter from one part of the pore to another and are driven by the difference in curvature between the convex surface of the particle and the concave surface around the neck. The transport can occur through the vapor phase. It is then controlled either by the evaporation-condensation rate on the solid surface (α is a sticking coefficient comprised between 0 and 1) or the molecular-Knudsen diffusion rate in the vapor phase. Solid state diffusion mechanisms can also occur at the surface of the particle (surface diffusion coefficient of the specie j, D_j^s, in a thickness, δ^s) and through lattice diffusion inside the particle (lattice diffusion from surface sources, lattice diffusion coefficient, D_j^l). When the neck size is small, the mean curvature difference, κ_{nd}, is given by Equation (IV.13).

$$\kappa_{nd} = \frac{1}{2}\left(\frac{1}{\rho_{nd}} - \frac{1}{x} + \frac{2}{a}\right) \tag{IV.13}$$

The geometry accounts for the particle size, a, and for the circular neck growth which affects the two main principal radius of curvature, x and ρ_{nd} (Equation (IV.14)), and θ which is an angle defined in Figure IV.3.

$$\rho_{nd} = \frac{x^2}{2(a-x)} \tag{IV.14}$$

Mechanism		Neck growth rate (s^{-1})	Equation reference
Vapor transport – v	Evaporation-condensation	$\dfrac{dx_{nd}^{v}}{dt} = 2\alpha \dfrac{P_j F_j \Omega_j}{\sqrt{2\pi M_j RT}} \kappa_{nd}$	(IV.15) or (C.10)
	Molecular diffusion	$\dfrac{dx_{nd}^{v}}{dt} = 2\dfrac{\sin\theta}{\theta^2} \dfrac{D_j^{mol}}{RT} \dfrac{P_j F_j \Omega_j}{\rho_{nd}} \kappa_{nd}$	(IV.16) or (C.13)
Surface diffusion – s		$\dfrac{dx_{nd}^{s}}{dt} = \dfrac{2}{\theta^2} \dfrac{D_j^{s} \delta^{s} F_j}{\rho_{nd}^2} \kappa_{nd}$	(IV.17) or (C.17)
Lattice diffusion – l		$\dfrac{dx_{nd}^{l}}{dt} = 2\dfrac{1-\cos\theta}{\theta^2} \dfrac{D_j^{l} F_j}{\rho_{nd}} \kappa_{nd}$	(IV.18) or (C.19)

Table IV.1: Neck growth rate for non-densifying mechanisms in the initial stage of sintering.

The grain boundary acts as a source of atoms for densifying mechanisms which can occur through solid state diffusion along the grain boundary (grain boundary diffusion coefficient, D_j^{gb}, in a thickness, δ^{gb}) or through lattice diffusion inside the particle (lattice diffusion from grain boundary sources, lattice diffusion coefficient, D_j^{l}). The curvature difference, κ_d, is calculated in Equation (IV.19).

$$\kappa_d = \frac{1}{2}\left(\frac{1}{\rho_d} - \frac{1}{x}\right) \tag{IV.19}$$

The geometry accounts for interpenetration of the spheres (*i.e.*, shrinkage) as well as neck growth and depends on the two principal radius of curvature of the neck, x and ρ_d (Equation (IV.20)).

$$\rho_{\rm d} = \frac{x^2}{4(a-x)} \tag{IV.20}$$

Mechanism	Neck growth rate (s^{-1})	Equation reference
Grain boundary diffusion – gb	$\dfrac{dx_{\rm d}^{\rm gb}}{dt} = \dfrac{4}{\theta}\dfrac{D_{\rm j}^{\rm gb}\delta^{\rm gb}F_{\rm j}}{\rho_{\rm d}x}\kappa_{\rm d}$	(IV.21) or (C.24)
Lattice diffusion – l	$\dfrac{dx_{\rm d}^{\rm l}}{dt} = 8\dfrac{\sin\theta}{\theta}\dfrac{D_{\rm j}^{\rm l}F_{\rm j}}{x}\kappa_{\rm d}$	(IV.22) or (C.25)

Table IV.2: Neck growth rate for densifying mechanisms in the initial stage of sintering.

IV.1.4 Intermediate and final sintering stage models

The intermediate stage begins when pores have reached their equilibrium shapes as dictated by the surface and interfacial energies of the system (Equation (IV.1)). The pores are still connected and shrink to reduce their cross section. Eventually, pores become unstable and pinch off. The system then shifts to the final stage as pores become isolated.

The model commonly used for the intermediate and final stage of sintering was proposed by Coble [Cob61]. The compact geometry is idealized by a network of equal-sized tetrakaidecahedra, each of which representing one particle. The structure is represented by a unit cell with cylindrical pores along its edges during the intermediate stage in Figure IV.4.

The volume of the tetrakaidecahedron, $V_{\rm t}$, is given in Equation (IV.23) where $l_{\rm p}$ is the pore segment length. The pore volume per tetrakaidecahedron, $V_{\rm p}$, is given in Equation (IV.24) where $\rho_{\rm p}$ is the radius of the pore. The volume, $V_{\rm p}$ - $V_{\rm t}$, remains constant as grain growth is neglected. The pore volume fraction is then defined as the ratio of $V_{\rm p}$ and $V_{\rm t}$ in Equation (IV.25) [Cob61].

$$V_{\rm t} = 8\sqrt{2}\, l_{\rm p}^{\,3} \tag{IV.23}$$

$$V_{\rm p} = 12\pi\rho_{\rm p}^{\,2}l_{\rm p} \tag{IV.24}$$

$$p = \frac{3\pi}{2\sqrt{2}}\left(\frac{\rho_{\rm p}}{l_{\rm p}}\right)^2 \tag{IV.25}$$
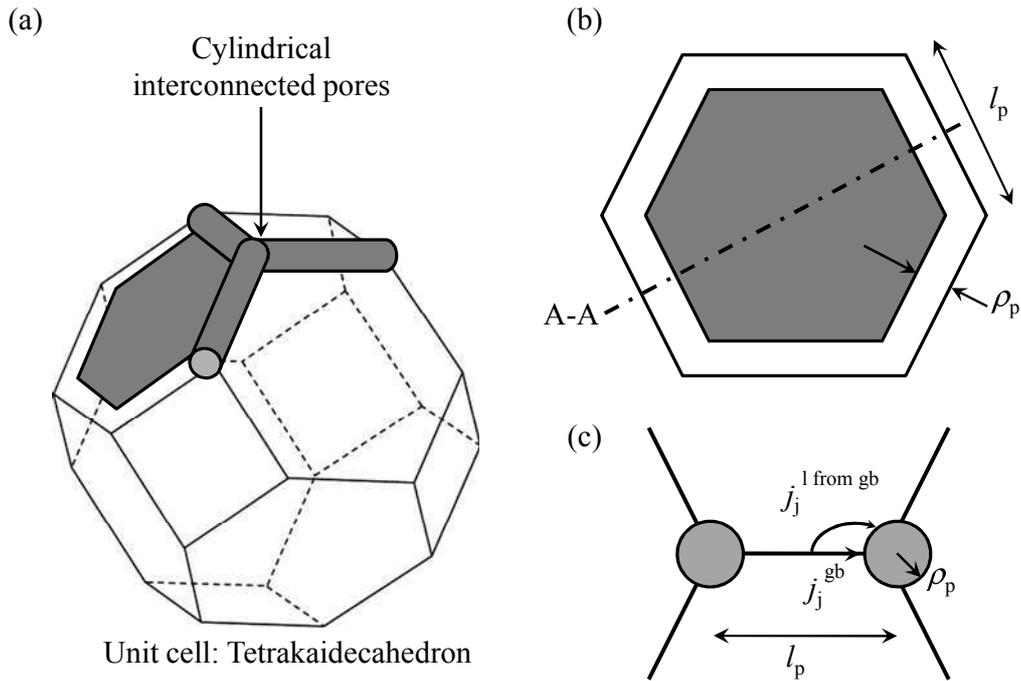
Figure IV.4: (a) *Model geometry for the second stage of sintering idealized by a tetrakaidecahedron with interconnected cylindrical pores along its edges.* (b) *Hexagonal face of the tetrakaidecahedron showing the length of cylindrical pore segments, l_p and the pore radius, ρ_p.* (c) *Section A-A, showing the neck with the atomic flux paths for grain boundary diffusion and lattice diffusion from the grain boundary.*

Since the model assumes that the pore curvature is uniform, non-densyfying mechanisms cannot operate as the chemical potential is the same everywhere at the surface. Therefore, only the densifying mechanisms, that is to say, lattice diffusion and grain boundary diffusion are considered.

By considering that atom fluxes are driven by the curvature of the pore, the pore shrinkage rate through lattice diffusion and grain boundary diffusion, dp^l/dt and dp^gb/dt, can be estimated from integration of the volume flux per tetrakaidecahedron, dV/dt, that depends on the lattice diffusion (Equation (IV.26)) and grain boundary diffusion (Equation (IV.27)) coefficients, respectively [Rah95].

$$\frac{dp^\mathrm{l}}{dt} = -7\pi\sqrt{2}\,\frac{D_\mathrm{j}^\mathrm{l} F_\mathrm{j}}{l_\mathrm{p}^{\,3}} \tag{IV.26}$$

$$\frac{dp^\mathrm{gb}}{dt} = \frac{2}{3}\left(\frac{2 D_\mathrm{j}^\mathrm{gb}\,\delta^\mathrm{gb} F_\mathrm{j}}{l_\mathrm{p}^{\,4}}\right)^{\!2/3} t^{-1/3} \tag{IV.27}$$

Here, only the second stage is presented. During the final stage, the geometry changes and spherical pores at the corner of the tetrakaidecahedron are considered.

Although non-densifying mechanisms cannot operate at the scale of one pore, microstructure changes, usually grain growth, increase the pore size, and therefore slow down densification kinetics. Coble's model can be then refined by taking into account the change in grain size from grain boundary mobility models [ZH92].

IV.2 **The role of silica during sintering of silicon**

IV.2.1 Literature analysis

Greskovich and Rosolowski [GR76] have shown that kinetic considerations explain the low densification of silicon powders by noticing that coarsening mechanisms are predominant with respect to shrinkage mechanisms. Depending on the authors, the coarsening mechanism would be vapor transport [GR76, SH83, MW85] or surface diffusion [Rob81, Cob90]. As for sintering, those mechanisms are responsible for grain growth without shrinkage.

Greskovich and Rosolowski attempted to identify the dominant coarsening mechanism using Herring's scaling laws [Her50]. A similar approach is used from simplification of the sintering rate equations introduced in the previous section IV.1.3. Curvatures for densifying and non-densifying mechanisms are assumed to be simply proportional to a/x^2. Neck growth rate equations are integrated and written in the following form in Equation (IV.28), where k is a constant with respect to the particle and neck size, a, and x, and to the time, t.

$$\left(\frac{x}{a}\right)^n = \frac{kt}{a^m} \tag{IV.28}$$

The principal conclusion of this approach is that the time, t, required to obtain a given neck growth, x/a, is directly related to the particle size to the power m, a^m, which depends on the dominant sintering mechanism (Table IV.3). The effect of change in particle size on the sintering rate of two competing mechanisms can then be foreseen.

Greskovich and Rosolowski actually observed that finer particles give rise to better densifications [GR76]. Indeed, Möller and Welsh [MW85] investigated the sinterability of ultrafine silicon powders of 20 to 100 nm and measured densities higher than 90 % TD_{Si} for compacts sintered 3 h at 1300 °C. The measured apparent activation energy for densification (500 kJ mol^{-1}) was close to silicon lattice self-diffusion activation energy (476 kJ mol^{-1}) [SUI07], leading the authors to conclude that lattice diffusion from grain boundary sources dominates sintering kinetics of fine particles. This mechanism is assumed to control densification kineticsfor fine particles in the following.

Sintering mechanism		n	m	$m_{d,l} - m_{nd}$
Vapor transport – v (nd)	Evaporation-condensation	3	2	1
	Molecular diffusion	5	3	0
Surface diffusion – s (nd)		7	4	-1
Lattice diffusion – l (nd)		5	3	0
Grain boundary diffusion – gb (d)		6	4	-
Lattice diffusion – l (d)		4	3	-

Table IV.3: Exponents for the scaling law depending on the mechanism considered.

When referring to Equation (IV.28), as the particle size, *a*, is decreased, the sintering rate of a given mechanism will increase even faster as *m* is higher. Returning to case of silicon, if a non-densifying mechanism were dominant for coarse particles, this mechanism would be hindered by lattice diffusion from grain boundary sources for finer particles only if $m_{d,l} - m_{nd}$ > 0. $m_{d,l}$ is the exponent *m* for lattice diffusion from grain boundary sources while m_{nd} is the exponent *m* for the competing non-densifying mechanism. As can be seen in Table IV.3 this condition is respected only for a vapor transport limited by evaporation-condensation. The authors then concluded that a vapor-phase mechanism is responsible for the non-densification of micrometric particles [GR76].

However, this conclusion is not consistent with grain boundary grooving experiments realized by Robertson [Rob81] and Coblenz [Cob90]. Surface diffusion was found to be the dominant mechanism in both studies and the diffusion coefficient for this mechanism was estimated. Associated with other data from the literature, Coblenz calculated the neck growth rate for different mechanisms and deduced that a surface diffusion mechanism should control the neck growth at all particle sizes of interest, even for fine particles, in agreement with Herring's scaling law approach. The grain boundary diffusion mechanism was not considered since no data were available in literature for the calculations. Coblenz also performed neck growth rate measurements on polycrystalline spheres of 150 to 250 μm. Kinetics was consistent with the surface diffusion model, but a small contribution from grain boundary diffusion could not be ruled out. The rapid surface diffusion transport would then explain the important coarsening of silicon powders.

Coblenz noticed that the rapid surface diffusion mechanism observed at all particle sizes cannot account for the better densification of fine powders. He removed this inconsistency by

considering that the silica layer at the particle surface might inhibit surface diffusion *i.e.* grain coarsening with respect to densifying mechanisms. Indeed, as observed in Chapter III, the presence of silica at the particle surface seems to strongly influence the sintering process. A grain coarsening front was observed, moving from the edge of the compact to the center. This coarsening front was related to a silica reduction front showing that the silica layer precludes grain coarsening, most probably through inhibition of surface diffusion. Möller and Welsh [MW85] as well as Shaw and Heuer [SH83] also observed a non-uniform microstructure on their final compacts but put forward that the reduction of native silica at the particle surface into gaseous silicon monoxide ($SiO_{(g)}$) would enhance vapor transport coarsening at the edge of the sample. However, they did not analyze the possible contribution of surface diffusion.

IV.2.2 Neck growth kinetics estimations

The role of silica during sintering of silicon is not clearly understood in the literature. The issue deals with the comprehension of the microstructure evolution during the silica removal.

In Figure IV.5, the grain coarsening position, r_g, is compared to the reaction front position, r_r, modeled in Chapter III.3. The reaction front position is slightly ahead of the measured grain coarsening position as the model always overestimates silica reduction kinetics. Actually the reaction front position, r_r, where the silica is reduced, corresponds to the grain coarsening position, r_g, as shown in the EDS profiles. This shows that sintering mechanisms are strongly affected by the presence of silica at the particle surface.

In order to tackle the issue, kinetics of the initial sintering stage is estimated using the formalism introduced in the previous section, taking into account the presence of a silica layer at the particle surface. The dissolution of silica into silicon during heating is not considered as the solubility of oxygen in silicon is very low [Bea09, IN85].
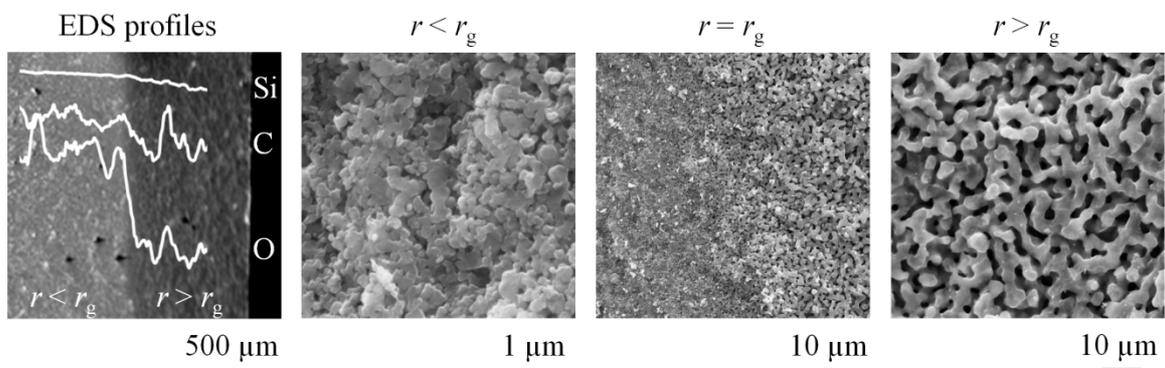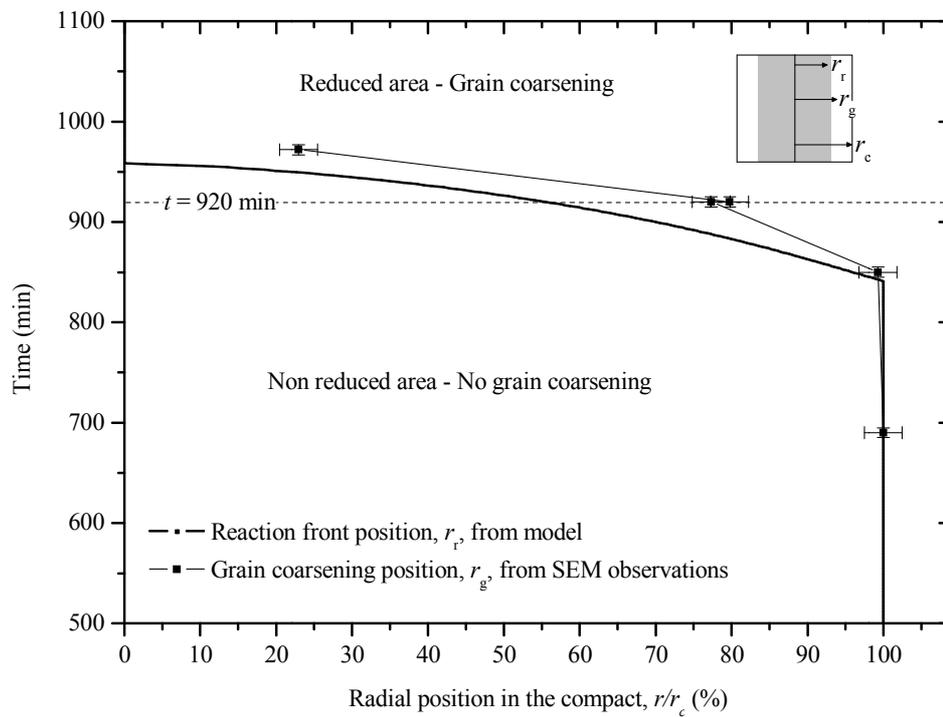
Figure IV.5: Grain coarsening position, r_g, and calculated reaction front position, r_r, as function of time for a silicon powder compact, heated up to 1350 °C with a heating rate of 1.25 °C min^{-1} and a holding time of 3 h under He-4 mol.% H_2. EDS profiles and silicon micrographs for a sample quenched at t = 920 min, T = 1315 °C, are given at different positions from the grain coarsening front position.

a)   Solid state diffusion coefficients in silicon and silica

Prior to the discussion of silicon sintering mechanisms, a brief review on the diffusion coefficients to be used in the sintering equations is performed.

- *Silicon*

Studies on the tracer diffusion of silicon in silicon are numerous [Gho66, FM67, KS79, HA79, NOT+03, SUI07]. The most recent and complete description is given by Shimizu *et al.* [SUI07]. The lattice diffusion coefficient estimated from this study, $D_{Si}^{l,Si}$, is given in Equation (IV.29).

$$D_{Si}^{l,Si} = 2.3 \times 10^{-7} \exp\left(\frac{-347 \text{ KJ mol}^{-1}}{RT}\right) + 2.2 \times 10^{-1} \exp\left(\frac{-477 \text{ KJ mol}^{-1}}{RT}\right) \text{m}^2\text{s}^{-1} \quad (IV.29)$$

According to Doremus [Dor01], oxidizing atmospheres accelerate the diffusion coefficient by a factor 2 or 3 compared to inert atmospheres. The diffusion would then occur through dissolved silicon monoxide in oxygen saturated silicon. However, there are only few evidences for this mechanism to occur, and its temperature dependence is not consistent with experimental observations. This possible acceleration is then not considered in the following.

The surface diffusion coefficient of silicon onto silicon, $D_{Si}^{s,Si}$, given in Equation (IV.30), was first estimated by Robertson [Rob81] using grain boundary grooving experiments.

$$D_{Si}^{s,Si} = 93.9 \exp\left(\frac{-298 \text{ KJ mol}^{-1}}{RT}\right) \text{m}^2\text{s}^{-1} \quad (IV.30)$$

This estimation is in agreement with Coblenz calculations and measurements [Cob90] and is then used in our calculations. This diffusion coefficient has lower activation energy than the lattice diffusion coefficient, as usually observed in conventional systems, where surface diffusion is often favored at low temperatures.

No data are available in the literature for the grain boundary diffusion coefficient of silicon, $D_{Si}^{gb,Si}$.

- *Silica*

The estimation of the silicon diffusion coefficient into silica is less obvious.

The first measurements of silicon diffusion coefficient into silica were made by Brebec *et al.* [BSS+80] by measuring diffusion profiles of a stable isotope Si^{30} in a silica bulk material. According to Doremus [Dor02], this measurement is consistent with the apparent activation energy for the silica viscosity. This diffusion coefficient, given in Equation (IV.31), is called the lattice diffusion coefficient of silicon into silica, D_{Si}^{l,SiO_2}.

$$D_{Si}^{l,SiO_2} = 3.3 \times 10^{-2} \exp\left(\frac{-579 \text{ KJ mol}^{-1}}{RT}\right) \text{m}^2\text{s}^{-1} \tag{IV.31}$$

However, another diffusion coefficient of silicon into silica is available in the literature. Sasse and Köning [SK90] measured the time required for the decomposition of silica layers of 1.5 nm thickness at the surface of silicon wafers under high-vacuum ($P = 1.10^{-11}$ Pa). The decomposition process takes place at the interface between the silicon and the silica layer according to reaction (R_5), as considered in Chapter III.

$$Si_{(s)} + SiO_{2(s)} = 2SiO_{(g)} \tag{R_5}$$

Down to a thickness of 0.6-0.7 nm, the decomposition rate is parabolic showing that it is initially controlled by the solid state diffusion of silicon and oxygen atoms in the silica layer. The deduced diffusion coefficient has lower apparent activation energy than the one measured by Brebec *et al.* (Equation (IV.31)) and is then approximately 10^4 times larger. Such rapid diffusion has also been proposed by Celler and Trimble to explain the thermo-migration of arsenic impurities in silica [CT89b, CT89a, CT88, TCWS89]. This fast diffusion was attributed to the movement of SiO molecular entities rather than the diffusion of Si and O atoms themselves. This diffusion coefficient, given in Equation (IV.32), is then called the chemical diffusion coefficient of silicon monoxide into silica, D_{SiO}^{l,SiO_2}.

$$D_{SiO}^{l,SiO_2} = 1.48 \times 10^{-7} \exp\left(\frac{-308 \text{ KJ mol}^{-1}}{RT}\right) \text{m}^2\text{s}^{-1} \tag{IV.32}$$

To our knowledge, no data is available for the surface diffusion coefficient of silicon onto silica. The diffusion coefficient is usually higher at the surface than in the bulk. According to Garofalini and Conover [GC85], the surface to bulk diffusion coefficients ratio for silica is ten for temperatures as high as 4000 °C. Even though uncertain, this ratio is used in our calculations (Equation (IV.33)).

$$D_{j}^{s,SiO_2} = 10 \times D_{j}^{l,SiO_2} \tag{IV.33}$$

b)   Sintering mechanisms

In this section, each sintering mechanism is considered separately. Kinetics for a given sintering mechanism is estimated by giving the corresponding lines of constant neck growth rate in a temperature / neck size diagram. These lines give the neck growth rate, $\dot{x}/a\,(\%)$, for a given sintering temperature, T, and neck to particle size ratio, $x/a\,(\%)$.

- *Surface diffusion – s (nd)*

Neck growth rate for surface diffusion is given by Equation (IV.17) for pure silicon and for silicon particles covered with silica. The relevant diffusion coefficient is the silicon surface diffusion coefficient, $D_{\mathrm{Si}}^{\mathrm{s,Si}}$ in the first case and the surface diffusion coefficient of silicon on silica, $D_{\mathrm{Si}}^{\mathrm{s,SiO_2}}$ in the second case. Neck growth rates for both cases are shown in Figure IV.6.
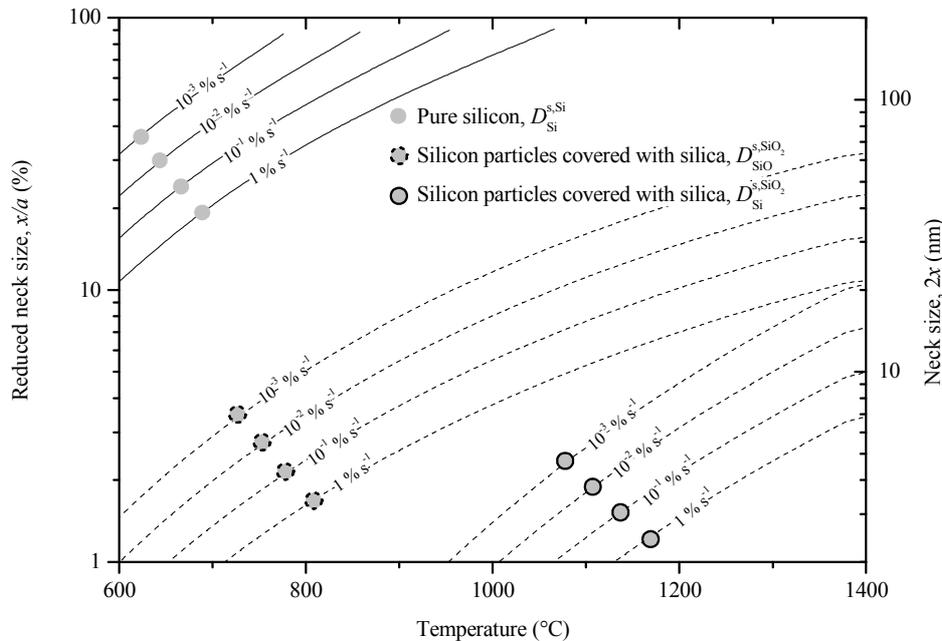
Figure IV.6: Lines of constant neck growth rate for the surface diffusion mechanism for pure silicon and for silicon covered with silica. The presence of silica at the particle surface is shown to strongly impede surface diffusion kinetics. The particle size (2a = 220 nm) is a typical value of the VF powder.

The surface diffusion coefficient of silicon onto silicon, $D_{\mathrm{Si}}^{\mathrm{s,Si}}$, is very high (Equation (IV.30)). When integrated in Equation (IV.17), neck growth rate through surface diffusion for pure silicon is found fairly rapid. As an example, according to this calculation, for 220 nm particles, the necks would grow of 70 % in less than 1 second at 1000 °C.

As for silicon particles covered with silica, D_{Si}^{s,SiO_2} [BSS+80] and D_{SiO}^{s,SiO_2} [SK90] coefficients are considerably lower than $D_{Si}^{s,Si}$, and surface diffusion is found to be strongly impeded by the presence of silica at the particle surface.

These estimations of surface diffusion kinetics for pure silicon and for silicon particles covered with silica are consistent with SEM observations in Figure IV.5, where silicon particles remain fine in the presence of silica (non-reduced area, $r < r_g$) and where a large grain coarsening is observed once the silica is reduced (reduced area, $r > r_g$). After the reduction of silica, surface diffusion is activated and leads to a rapid neck growth without densification. Pores rapidly reach their equilibrium shape $(x/a \approx 40-50\%)$ and sintering keeps going in a process where larger pores (or grains) grow at the expense of the smaller ones.

- *Vapor transport* – v (nd)

Under atmospheric pressure and for the particle size considered in this study, vapor transport around the particle neck is limited by the evaporation-condensation rate (Equation (IV.15)) as the diffusion length is lower than hundreds of nanometer (Appendix C.2.1).

For pure silicon, vapor transport is monitored by the silicon equilibrium vapor pressure, P_{Si}^0. The sticking coefficient, α, is assumed to be equal to one as the condensation of silicon vapor atoms on silicon solid surface is assumed to be highly favorable.

For silicon particles covered with silica, the silicon monoxide pressure, $P_{SiO}^{R_5}$, is approximately 10^5 times higher than P_{Si}^0. Assuming that silicon monoxide can participate in mass transport of silicon, the neck growth rate through vapor transport would be given by Equation (IV.34), where Φ is the efficient surface fraction for the condensation, *i.e.* the surface area fraction of defects or holes at the particle surface. In this equation, Φ is also assumed to account for the sticking coefficient, α.

$$\frac{dx_{nd}^v}{dt} = 2\Phi \frac{P_{SiO} F_{SiO} \Omega_{SiO}}{\sqrt{2\pi M_{SiO} RT}} \kappa_{nd} \tag{IV.34}$$

In the case where the surface area fraction would be close to one, that is to say, a mostly bare silicon surface, vapor transport would be strongly enhanced. As an example, necks would reach their equilibrium size ($\sim a$) in a few second at 1000 °C (Figure IV.7). Such neck growth is not observed at this temperature for silicon particles covered with silica (Figure IV.5, non-

reduced area, $r < r_g$), showing that the surface area fraction of holes is small and that the particle surface is mostly covered with silica, as shown in Chapter III.4.
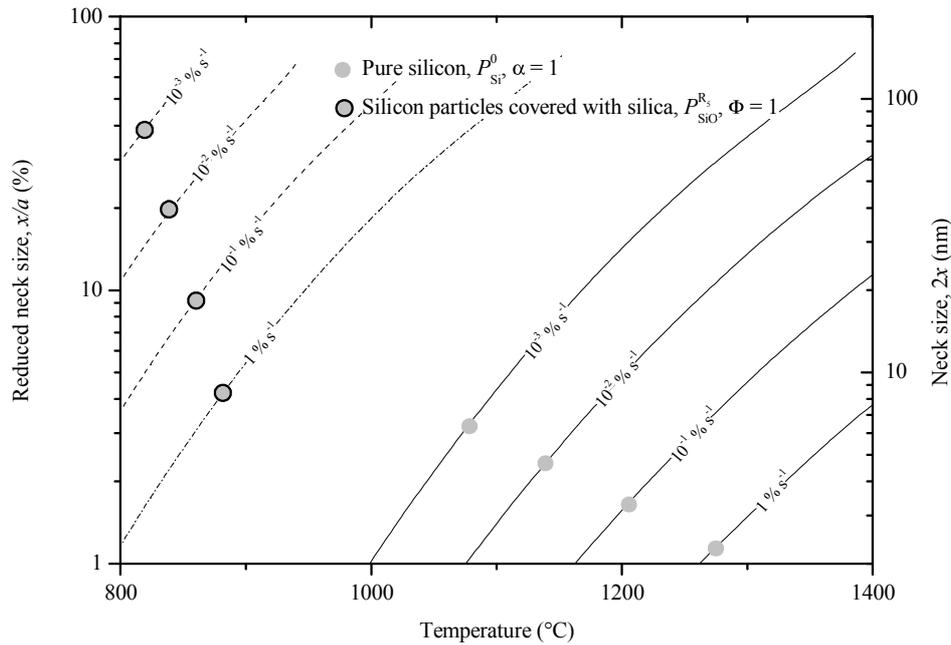
Figure IV.7: Lines of constant neck growth rate for the vapor transport mechanism. The particle size (2a = 220 nm) is a typical value of the VF powder.

In addition, for neck growth through vapor transport to occur continuously, the silica layer should not be an obstacle to the silicon surface migration. At the passive to active transition, $T^*_{P \to A}$, the healing of holes is still possible, as $P_{SiO} = P^{R_5}_{SiO}$, but inevitably ends up in the formation of new holes, since the healing SiO molecules originates from a surrounding region of the silica layer that is breaking out. Accordingly, the silica layer would continuously evaporate and condensates from one crack to another (Figure IV.8) and would not perclude particle neck growth through vapor transport of silicon monoxide.
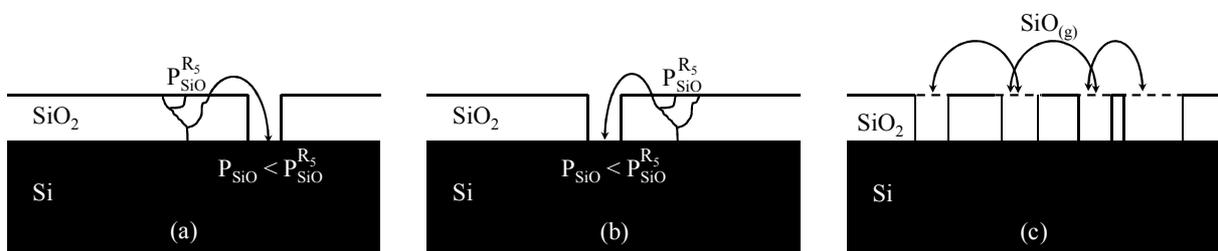
Figure IV.8: Healing of a large hole at the passive to active transition, $T^*_{P \to A}$, can only occur from $SiO_{(g)}$ produced by a neighboring crack (a) that in turns ends up in a large crack which is going to be healed by a new forming crack (b). Eventually the silica layer can be seen as a continuously evaporating and condensing material (c).

- *Lattice diffusion from the particle surface* – 1 (nd)

The neck growth rate through lattice diffusion from the particle surface is given in Equation (IV.18).

For pure silicon, neck growth rates are calculated using the lattice diffusion coefficient of silicon, $D_{Si}^{l,Si}$, as given in Equation (IV.29) from measurements of Shimizu *et al.* [SUI07].

In the presence of silica at the particle surface, neck growth requires the diffusion of silicon atoms through the particle volume and through the silica layer to the neck region. Munir [Mun79] proposed to estimate an effective diffusion coefficient assuming the serial diffusion of atoms in the particle volume and in the oxide thickness. This effective diffusion coefficient, $D_j^{l,eff}$ with j = Si or SiO, is then given by Equation (IV.35) where $\left(\theta\rho_{nd} - e_{SiO_2}\right)$ corresponds to the diffusion distance in the silicon particle volume, while e_{SiO_2} corresponds to the diffusion distance in the silica layer.

$$D_j^{l,eff} = \theta\rho_{nd}\left(\frac{e_{SiO_2}}{D_j^{l,SiO_2}} + \frac{\theta\rho_{nd} - e_{SiO_2}}{D_{Si}^{l,Si}}\right)^{-1}$$

(IV.35)

According to this approach, when the silica layer thickness, e_{SiO_2}, goes 0, the effective diffusion coefficient, $D_{Si}^{l,eff}$ equals the lattice diffusion coefficient of silicon into silicon, $D_{Si}^{l,Si}$. However, for a silica layer thickness of 0.5 nm (typical value of the VF powder), the value of $D_{Si}^{l,eff}$ strongly depends on the lattice diffusion coefficient for silicon (or silicon monoxide) into silica, D_j^{l,SiO_2} (Figure IV.9):

- If D_{Si}^{l,SiO_2} [BSS+80] (Equation (IV.31)) is chosen, neck growth kinetics through lattice diffusion is strongly slowed down by the presence of silica.

- If D_{SiO}^{l,SiO_2} [SK90] (Equation (IV.32)) is chosen, the presence of silica slightly affects lattice diffusion kinetics at the first step of sintering, *i.e.*, when $\theta\rho_{nd} \sim e_{SiO_2}$. In this case, lattice diffusion kinetics is found to be enhanced as D_{SiO}^{l,SiO_2} is higher than $D_{Si}^{l,Si}$.
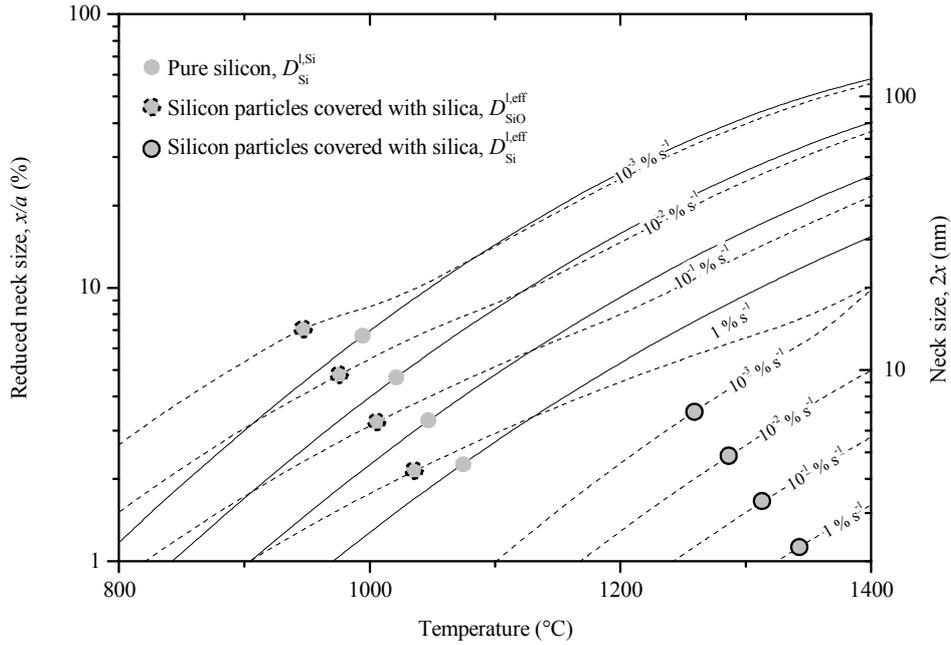
Figure IV.9: Lines of constant neck growth rate for the lattice diffusion mechanism from particle surface for pure silicon and for silicon covered with silica. In the presence of silica, neck growth kinetics is affected depending on the silicon diffusion coefficient through the silica layer, D_{Si}^{l,SiO_2} or $D_{SiO_2}^{l,SiO_2}$. The particle size (2a = 220 nm) and the silica layer thickness ($e_{SiO_2} = 0.5$ nm) are typical values of the VF powder.

- *Lattice diffusion from grain boundary* – l (d)

The neck growth rates through lattice diffusion from the grain boundary are calculated from Equation (IV.22) and given in Figure IV.10.

For pure silicon, the appropriate diffusion coefficient is the lattice diffusion coefficient of silicon into silicon, $D_{Si}^{l,Si}$, that is given in Equation (IV.29) from measurements of Shimizu *et al.* [SUI07].

In the presence of silica at the particle surface, neck growth requires the diffusion of silicon atoms through the particle volume and through the silica layer to the neck region. Munir's approach [Mun79] can still be used to estimate an effective diffusion coefficient, $D_j^{l,eff}$, given in Equation (IV.36), where $(x - e_{SiO_2})$ corresponds the diffusion distance in the silicon particle volume (neck radius) and e_{SiO_2} to the diffusion distance in the silica layer.

$$D_j^{l,eff} = x \left(\frac{e_{SiO_2}}{D_j^{l,SiO_2}} + \frac{x - e_{SiO_2}}{D_{Si}^{l,Si}} \right)^{-1}$$

(IV.36)

As shown in the previous section, for a silica layer thickness of 0.5 nm, the value of $D_{Si}^{l,Si-SiO_2}$ strongly depends on the chosen diffusion coefficient for silicon (or silicon monoxide) into silica, D_j^{l,SiO_2} (Figure IV.10):

- If D_{Si}^{l,SiO_2} [BSS+80] (Equation (IV.31)) is chosen, neck growth kinetics through lattice diffusion is strongly affected by the presence of silica. Neck growth and then densification should be strongly precluded.

- If D_{SiO}^{l,SiO_2} [SK90] (Equation (IV.32)) is chosen, the presence of silica only slightly affects lattice diffusion kinetics.
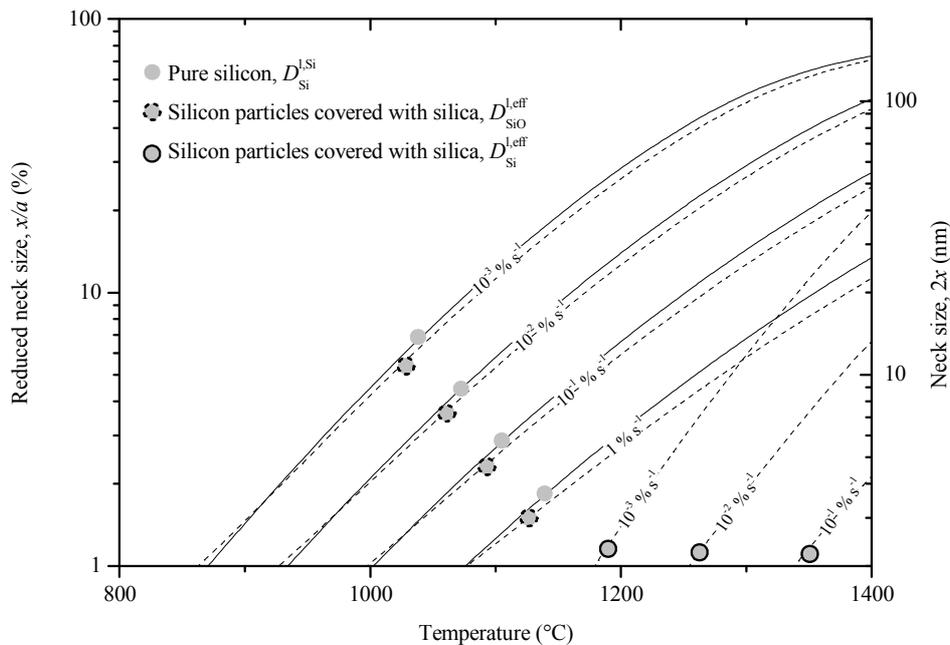
Figure IV.10: Lines of constant neck growth rate for the lattice diffusion mechanism from grain boundaries for pure silicon and for silicon covered with silica. In the presence of silica, neck growth kinetics is affected depending on the silicon diffusion coefficient through the silica layer, D_{Si}^{l,SiO_2} or D_{SiO}^{l,SiO_2}. The particle size (a = 110 nm) and the silica layer thickness (e_{SiO_2} = 0.5 nm) are typical values of the VF powder.

- *Grain boundary diffusion – gb (d)*

This mechanism probably never dominates sintering kinetics. For pure silicon, densification is not measured. Instead, grain coarsening is observed which is consistent with a dominant

surface diffusion mechanism. In the presence of a silica layer, surface diffusion is inhibited. Assuming that silica is also at least partly located at the grain boundary, grain boundary diffusion kinetics would probably be lowered as much as surface diffusion. Accordingly, grain boundary diffusion kinetics would be lower than any other mechanism.

c)   Summary: role of the silica layer

For pure silicon, surface diffusion dominates sintering and is responsible for a large grain growth.

In the presence of silica at the particle surface, surface diffusion and then grain coarsening is inhibited. This conclusion is confirmed by SEM observations and kinetics considerations. Grain boundary diffusion probably never dominates sintering kinetics. The effect on vapor transport and lattice diffusion kinetics is less obvious:

-      Vapor transport of silicon monoxide depends on the surface area fraction of holes, Φ, which is available for the condensation.

-      Depending on the diffusion coefficient considered for the diffusion of silicon into silica, $D_{\text{Si}}^{\text{l,SiO}_2}$ *(*Equation (IV.31)) [BSS+80] or $D_{\text{SiO}}^{\text{l,SiO}_2}$ (Equation (IV.32)) [SK90], lattice diffusion kinetics is respectively strongly slowed down or unaffected.

IV.2.3 Silicon sintering: experimental approach

In order to study the role of the silica layer on densification kinetics, *i.e.* lattice diffusion kinetics, dilatometric measurements are performed. A solution is proposed to stabilize the silica layer at any temperature in the compact. From Chapter III, reaction (R_5) determines the stability of the silica layer.

$$Si_{(s)} + SiO_{2(s)} = 2SiO_{(g)} \tag{R_5}$$

To prevent both growth and dissociation of the silica, the silicon monoxide equilibrium partial pressure of reaction (R_5), $P_{SiO}^{R_5}$, has to be maintained at the particle surface. The solution proposed is then to place the silicon powder compact in a crucible filled with an equimolar mix of silicon and silica powders, according to the experimental procedure described in Chapter II.2.3. As the temperature is increased the silicon-silica powder bed is progressively consumed, since the silicon monoxide vapor diffuse out of the crucilble and condensate on the cold surfaces of the furnace tube. But, as a major difference with a conventional silicon powder compact, the amount of silica to be reduced is as large as the amount of silicon. The molecular diffusion of silicon monoxide is not fast enough to consume entirely the silicon-silica powder bed. The silicon monoxide equilibrium partial pressure is maintained around the sample and the silica is never reduced in the compact.

In the following, sintering with a stabilized silica layer is referred to as sintering under a silicon-silica powder bed, while sintering with a reducing silica layer is referred to as sintering under reducing atmosphere. Dilatometric studies are first performed in the case of a stabilized silica layer and compared to conventional sintering under reducing atmosphere. The effect of the heating rate on densification kinetics is then investigated.

a)   Effect of the silica layer stabilization

In Figure IV.11, the shrinkage curve and micrograph of a sample sintered at 1350 °C for 3 h under a silicon-silica powder bed is compared to a conventional sintering at the same temperature cycle under reducing atmosphere. The sample sintered under reducing atmosphere experienced a mass loss of 3.26 %, showing that the silica layer has been entirely reduced in the compact. The sample sintered under a silicon-silica powder bed did not experience any mass loss, showing that the silica layer has been stabilized. The following comments can be made as regards the stabilization of the silica layer:

- The beginning of shrinkage is retarded.

- The global shrinkage is twice larger.

- Pore growth and accordingly grain growth is about ten times smaller.

These observations are consistent with sintering kinetics calculations for surface diffusion as the presence of silica inhibits surface diffusion and grain coarsening as already mentioned in Chapter III. Although the silica layer seems to affect lattice diffusion kinetics as densification is retarded, inhibition of surface diffusion and grain coarsening allows lattice diffusion and densification to occur at higher temperatures.
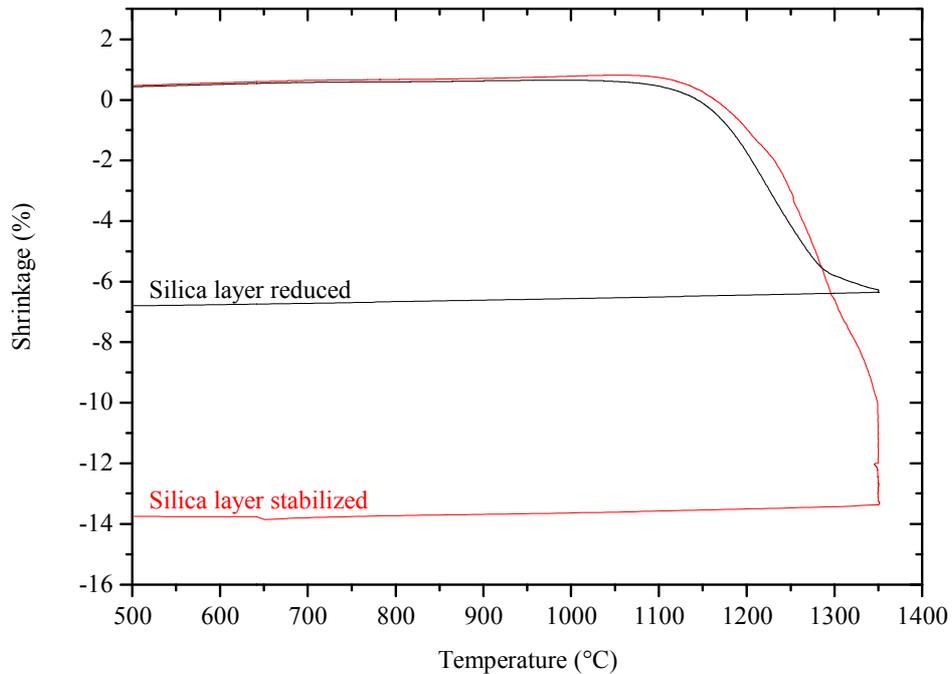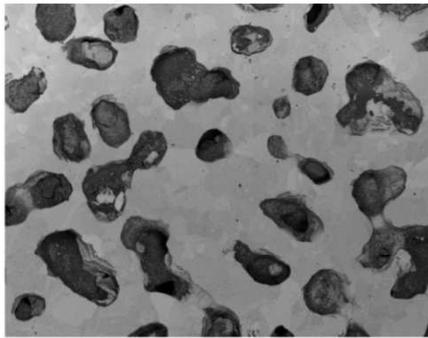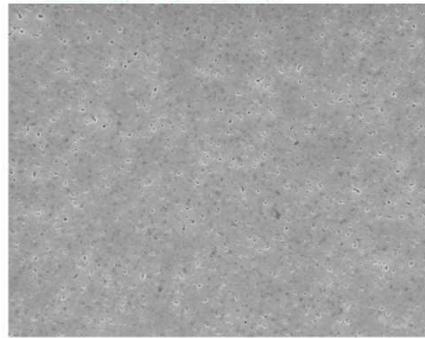
Figure IV.11: Shrinkage curves and microstructures of VF silicon powder compacts sintered 3 h at 1350 °C under 2 l h^{-1} He-4 mol.% H$_2$, with a heating rate of 1.25 °C min^{-1}. Black curve and left micrograph: sample sintered under reducing atmosphere, the silica being reduced. Red curve and right micrograph: sample sintered under a silicon-silica powder bed where the silica has been stabilized.

This conclusion is supported by our dilatometric and thermogravimetric measurements under reducing atmosphere, where the shrinkage is only observed before the complete reduction of the silica inside the compacts. In Figure IV.12, densification stops as soon as the silica layer is reduced with a density as low as 65 %. The presence of two peaks on the shrinkage rate curve may be explained by a differential shrinkage between the edge and the inner part of the compact. At the edge of the compact, the silica is reduced (reduced area), surface diffusion dominates and no shrinkage occurs. In the inner compact, a silica layer covers silicon particles, surface diffusion is inhibited and shrinkage occurs through lattice diffusion from grain boundary. The reduced area propagates inside the sample (r_g decreases) and surface diffusion progressively impedes the densification of the non-reduced area (first peak, sample (d)) which eventually becomes "chaotic" (second peak, sample (e)).
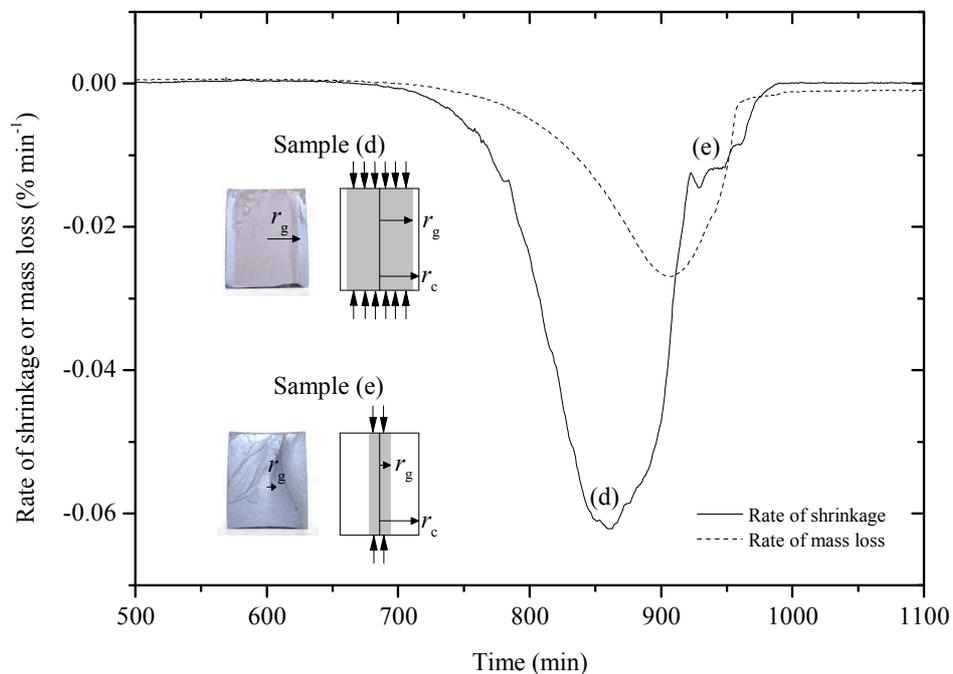
Figure IV.12: Rate of shrinkage and rate of mass loss for a VF silicon powder compact, heated up to 1350 °C with a heating rate of 1.25 °C min^{-1} and a holding time of 3 h under He-4 mol.% H$_2$. Two distinct peaks can be seen on the rate of shrinkage curve (corresponding interrupted samples (d) and (e)) which are related to the differential shrinkage between the edge and the inner of the compact as the coarsened area (reduced area) enlarges during sintering (r_g decreases).

b)   Effect of the heating rate

- *Sintering under reducing atmosphere, the silica layer being reduced*

In Figure IV.13, the rate of shrinkage is plotted along with the mass loss rate for samples sintered under reducing atmosphere for 3 h at 1350 °C at the heating rates of 0.625, 1.25 and 2.5 °C min^{-1}.
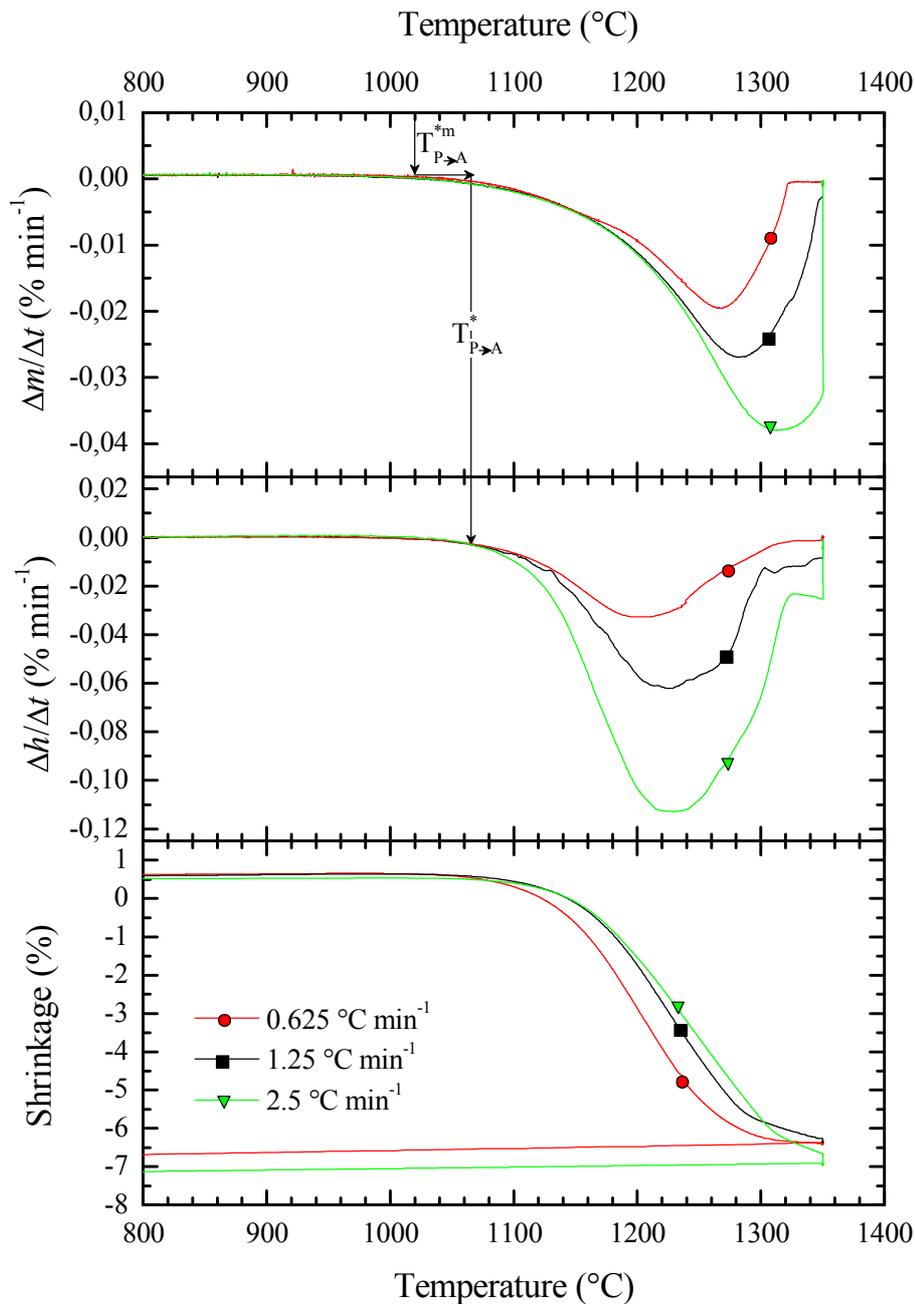
Figure IV.13: Rate of mass loss, rate of shrinkage and shrinkage as a function of the temperature for a VF silicon powder compact, heated up to 1350 °C with heating rates of 0.625, 1.25 and 2.5 °C min^{-1} under He-4 mol.% H$_2$.

From the results of oxidation kinetics in Chapter III.4 and as discussed in section IV.2.2 (Figure IV.8), holes would be present in the silica layer as soon as the partial pressure of silicon monoxide at the compact surface, P_{SiO}, is less than the equilibrium partial pressure from reaction (R$_5$), $P_{SiO}^{R_5}$. This corresponds to the passive to active transition temperature, $T_{P \to A}^*$, which is estimated from the temperature at which the mass loss rate is nil in thermogravimetric measurements, $T_{P \to A}^{*m}$. This temperature is independent of the heating rate and always coincides with the onset of densification as shown on the curve of shrinkage rate in Figure IV.13.

If lattice diffusion kinetics were not affected by the silica layer, the onset temperature of densification would increase with the heating rate as the process would be thermally activated. However, the onset of densification always occurs at the same temperature which corresponds to the onset of reduction of the silica layer at the passive to active transition. Accordingly, the silica layer affects lattice diffusion kinetics.

The beginning of the silica layer reduction also corresponds to the activation of surface diffusion and concomitant grain coarsening. Small densification may then also arise from particle coalescence which can significantly affect shrinkage as shown by Chen and Chen [CC96, CC97] during the sintering of ultrafine (nanometric) powder particles.

- *Sintering under a silicon-silica powder bed, the silica layer being stabilized*

In Figure IV.14, the rate of shrinkage is plotted for samples sintered under a silicon-silica powder bed at 1400 °C for 1 h at the heating rates of 10, 20 and 40° C min^{-1}. The silica layer is then stabilized and two peaks are clearly indentified on the shrinkage rate curve. Archimedes' densities of the samples increase slightly with the heating rate and are respectively, 82.5 %, 83 % and 85.5 %.

The microstructure evolution during sintering is observed in Figure IV.15 on samples that are quenched at several steps of the 10 °C min^{-1} cycle:

(g) Sample quenched at the top of the first shrinkage peak, (T = 1310 °C).

(h) Sample quenched at the valley between the two peaks, (T = 1340 °C).

(i) Sample quenched at the top of the second peak, (T = 1370 °C).

(j) Sample sintered for 1 h at 1400 °C.
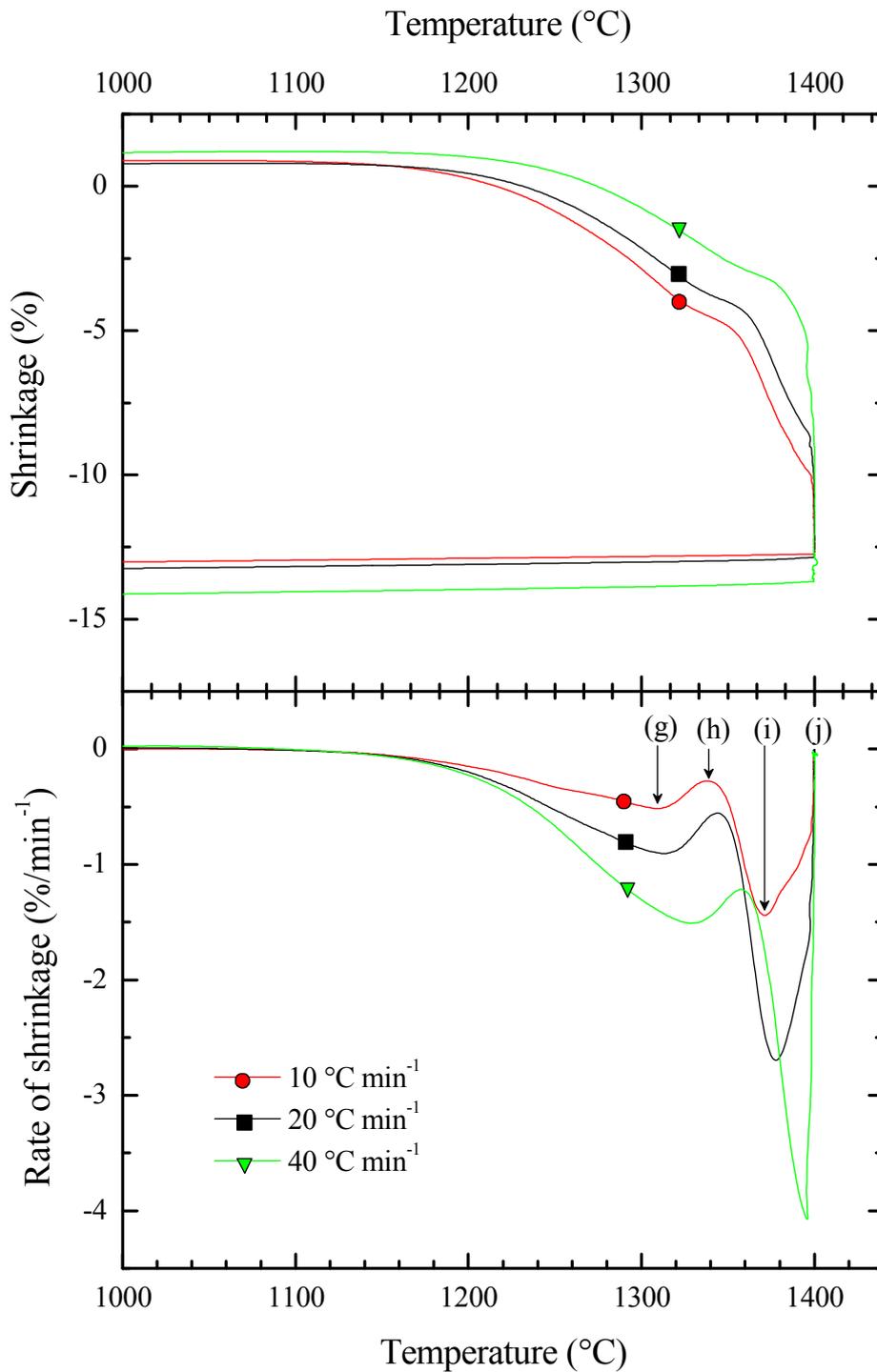
Figure IV.14: Shrinkage and rate of shrinkage as a function of the temperature for VF silicon powder compacts, heated up to 1400 °C with heating rates of 10, 20 and 40 °C min^{-1} under a silicon-silica powder bed in a 2 l h^{-1} flux of He-4 mol.% H$_2$.
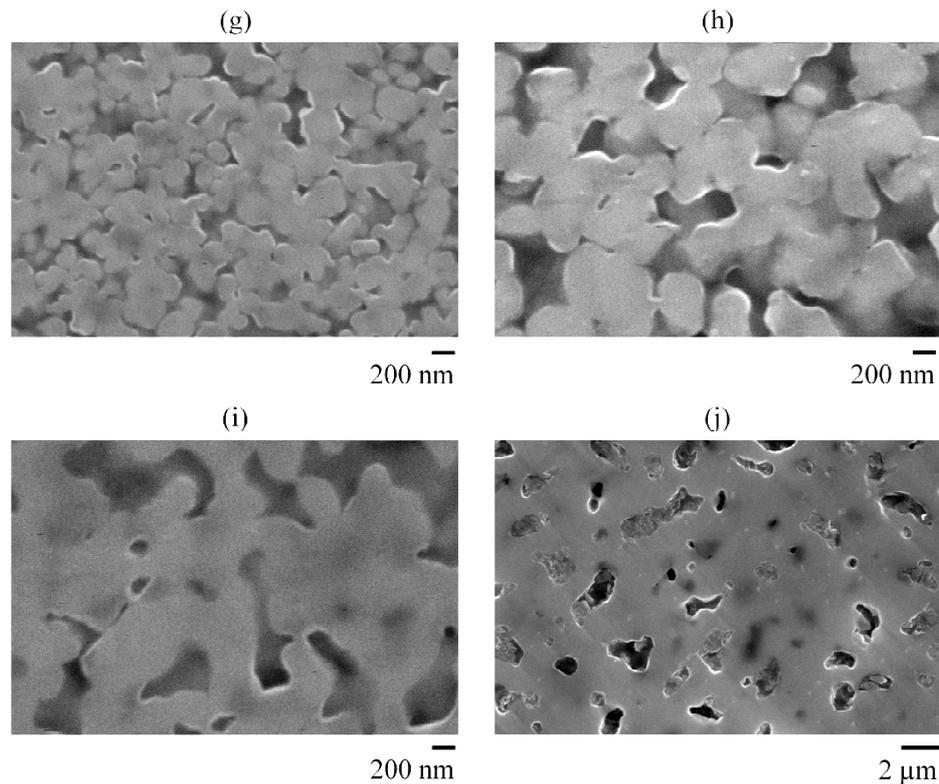
Figure IV.15: (g), (h), (i) *and* (j)*, FEG micrographs of quenched samples heated along the 10 °C min^{-1} cycle.*

As a major difference compared to sintering under reducing atmosphere, the microstructure evolution is homogeneous all over the compacts.

- Sample (g) micrograph is typical of the first stage of sintering and shows connected particles close to the initial particle size. Necks between particles are few tens percent of the particle size and the densification rate reaches a maximum.

- Sample (h) micrograph shows larger particles. Necks have grown and surface curvature gradients have been smoothed. Sintering is now driven by the concave curvatures of interconnected pores which are typical of the intermediate stage of sintering.

- Sample (i) micrograph shows that initial particles merged in dense agglomerates. The densification rate has reached the maximum rate.

- Sample (j) micrograph shows large interconnected pores, about ten times larger than the initial size. The densification rate is now very low and no densification occurs.

Multiple accelerations and drops of the densification rate are commonly observed during sintering of multi-phase materials, or even mono-materials that undergo phase transformations. But densification rate of pure materials like silicon is expected to exhibit only one peak. Indeed, the shrinkage (or densification) rate of single-phase material is conventionally expressed as Equation (IV.37), where K is a rate constant, E_a is the apparent activation energy of the mechanism responsible for densification, $f(SD)$ is a function of the sample density, SD, and G is the grain size [HRTJ92].

$$\frac{1}{h}\frac{dh}{dt} = K\,\frac{f(SD)}{G^n}\exp\left(-\frac{E_a}{RT}\right) \tag{IV.37}$$

The function, $\exp\left(-E_a/RT\right)$, increases with the temperature due to thermal activation of diffusion. On the contrary, the function of the density, $f(SD)$, decreases as sintering proceeds since the diffusion distances increase and the driving force originating from the surface energy is gradually reduced.

In our case, the first and second shrinkage peaks seem to be respectively associated with the initial and intermediate stages of sintering. But since the microstructural evolution is continuous throughout the initial and intermediate stages, the two peaks on the shrinkage rate curve are probably due to some change in the sintering mechanisms.

Using at least three different heating rates, three distinct values of the shrinkage rate, $\left.\frac{1}{h}\frac{dh}{dt}\right|_{D,T_1}$, $\left.\frac{1}{h}\frac{dh}{dt}\right|_{D,T_2}$ and $\left.\frac{1}{h}\frac{dh}{dt}\right|_{D,T_3}$, can be measured at three distinct temperatures, T_1, T_2 and T_3, at a constant density, D. Assuming that no grain growth occurs, these correspond to the same sintering progression or microstructure, *i.e.* to the same value of the function f. Then, plotting $\ln\left(\left.\frac{1}{h}\frac{dh}{dt}\right|_{D,T_n}\right)$ as a function of $-1/T_n$ gives a straight line of which slope is directly the apparent activation energy for densification.

Only limited grain growth occurs during the first stage of sintering (first peak), the measured apparent activation energy for the densification is then between 470 and 560 KJ mol^{-1} (Figure IV.16). The value of 500 KJ mol^{-1}, measured by Möller and Welsch [MW85], who actually measured the apparent activation energy for densification of very fine particles that were unintentionally covered with silica ($10 < 2a < 50$ nm) fits in that range.

Our measurements associated with Möller and Welsch ones show that the apparent activation energy for densification is between the activation energy for the diffusion of silicon into silicon [SUI07] and for the diffusion of silicon into silica [BSS+80]. Lattice diffusion kinetics

and densification is then affected by the diffusion of silicon into silica as considered in Equation (IV.36), where an effective diffusion coefficient has been estimated. Lattice diffusion kinetics would then be controlled by the lattice diffusion coefficient of Brebec *et al.* rather than the chemical diffusion coefficient of Sasse and Köning (Table IV.4).
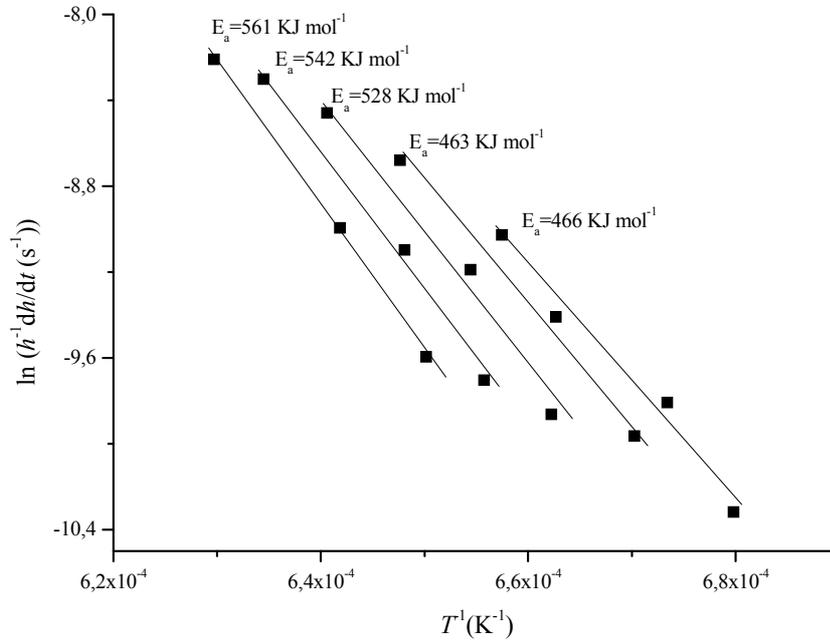
Figure IV.16: Apparent activation energies estimated from dilatometric measurements performed at three distinct heating rates on VF silicon powder compacts.

Apparent activation energy from Sintering		Solid state activation energy from lattice diffusion coefficients		
Möller and Welsh	This work	Shimizu *et al.*	Brebec *et al.*	Sasse and Köning
[MW85]		[SUI07]	[BSS+80]	[SK90]
		$D_{Si}^{l,Si}$	D_{Si}^{l,SiO_2}	D_{SiO}^{l,SiO_2}
500 KJ mol^{-1}	470 to 560 KJ mol^{-1}	347 KJ mol^{-1} to 477 KJ mol^{-1}	579 KJ mol^{-1}	308 KJ mol^{-1} (apparent)

Table IV.4: Activation energies for densification, E_a, measured from sintering compared to the activation energies for lattice diffusion of silicon into silicon, silicon into silica and silicon monoxide into silica.

In the following, modeling of the initial stage of densification kinetics (first peak) is proposed in order to estimate lattice diffusion kinetics and to clarify the role of the silica layer. In a second part, the modeling of the second stage (second peak) is considered by taking into account the microstructure growth observed on the micrographs of samples (i) and (j) (Figure IV.15).

IV.3 **Modeling of densification kinetics**

Until now, sintering mechanisms have been considered separately, assuming that they do not interact each other. However, in real systems several mechanisms acting together account for the neck growth and affect the shrinkage rate eventhough they may be non-densifying. Indeed, even though they do not directly contribute to densification, non-densifying mechanisms affect the neck shape, so the driving forces, and eventually the rate of densifying mechanisms.

IV.3.1 Initial stage of sintering

In the following, sintering rates of first stage mechanisms, taking into account the role of the silica layer, are brought together to calculate step by step the global neck growth rate and densification rate. The calculations are compared to dilatometric measurements in order to understand the direct role of the silica layer on lattice diffusion and vapor transport kinetics.

a)   Introduction of the initial stage model

In order to understand how sintering mechanisms affect the neck growth and densification rates during the first stage, it is important to return to the model geometry in Figure IV.17. When non-densifying and densifying mechanisms are acting together, the geometry of the first stage model is not univocal. Densifying mechanisms are responsible for interpenetration of the particles, *i.e.* shrinkage, while non-densifying mechanisms are not. During sintering, the geometry changes depending on the particle size (a) and neck size (x) but also depending on the particle interpenetration (i) as shown in Appendix A. The curvature radius of the neck, ρ, is then given by Equation (IV.38) and is neither as low as the radius of curvature for densifying mechanisms, ρ_d (Equation (IV.20)), nor as large as the radius of curvature for non-densifying mechanisms, ρ_{nd} (Equation (IV.14)).

$$\rho_d < \rho = \frac{x^2 - i(2a - i)}{2(a - x)} < \rho_{nd} \tag{IV.38}$$
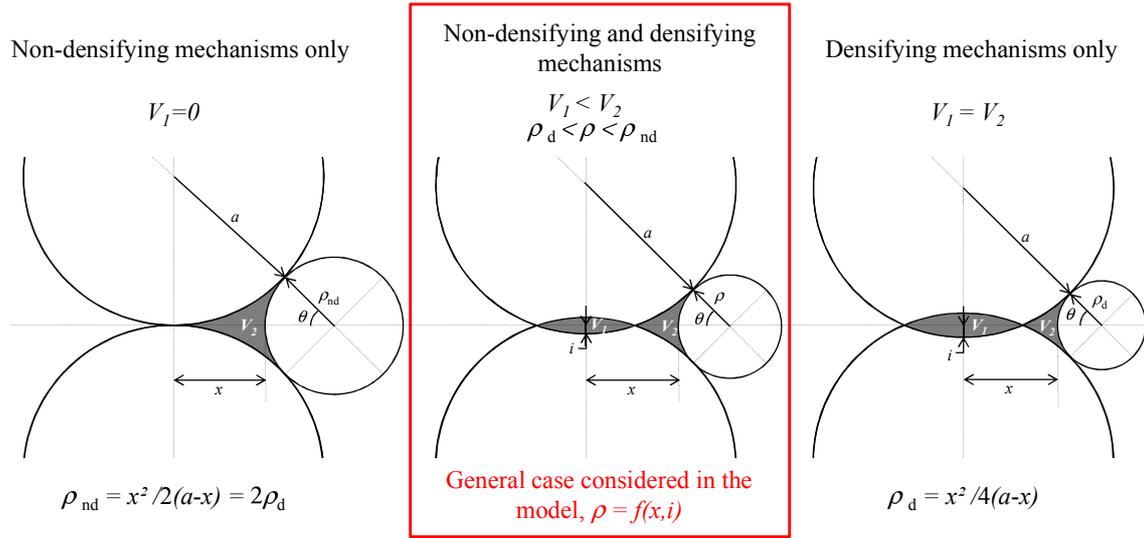
Figure IV.17: Model geometry for the first stage of sintering. When only non-densifying mechanisms or only densifying mechanisms operate, the curvature radius of the neck is directly related to the neck size. When both types of mechanisms operate simultaneously, the curvature radius of the neck also depends on the interpenetration of the spheres, i, that depends on the magnitude of each mechanism.

The elementary volume dV_1 is given in Equation (IV.39) and corresponds to the volume of the spherical caps which is transferred to the neck by densifying mechanisms. The total volume transferred to the neck surface dV_2 is given in Equation (IV.40) and is the sum of the contributions of densifying ($dV_{2,d}$) and non-densifying ($dV_{2,nd}$) mechanisms, in Equations (IV.41) and (IV.42) respectively.

$$dV_1 = 2\pi\left(2ai - i^2\right)di \tag{IV.39}$$

$$dV_2 = dV_{2,d} + dV_{2,nd} = 4\pi\theta\rho x \times \left(dx_d + dx_{nd}\right) \tag{IV.40}$$

$$dV_{2,d} = 4\pi\theta\rho x \times dx_d \tag{IV.41}$$

$$dV_{2,nd} = 4\pi\theta\rho x \times dx_{nd} \tag{IV.42}$$

From mass balance, dV_1 equals $dV_{2,d}$, and a relation between the increase of the interpenetration distance, di, and the neck size increase arising from densifying mechanisms, dx_d, can be written in Equation (IV.43).

$$di = \frac{2\theta\rho x}{(2a - i)i} dx_d \tag{IV.43}$$

The neck size increase, dx (Equation (IV.44)), is simply the sum of the contribution of densifying mechanisms, dx_d (grain boundary diffusion, dx_d^{gb}, and lattice diffusion from grain boundary, dx_d^l, Equation (IV.45)), and non-densifying mechanisms, dx_{nd} (surface diffusion, dx_{nd}^s, vapor transport, dx_{nd}^v, and lattice diffusion from surface, dx_{nd}^l, Equation (IV.46)).

$$dx = dx_d + dx_{nd} \tag{IV.44}$$

$$dx_d = dx_d^{gb} + dx_d^l \tag{IV.45}$$

$$dx_{nd} = dx_{nd}^s + dx_{nd}^v + dx_{nd}^l \tag{IV.46}$$

Finally, the neck growth rate as well as the interpenetration rate can be estimated using an iterative approach as described in Figure IV.18. The shrinkage rate is then extrapolated from the interpenetration rate using Equation (IV.47).

$$\frac{1}{h}\frac{dh}{dt} = -\frac{1}{a}\frac{di}{dt} \tag{IV.47}$$
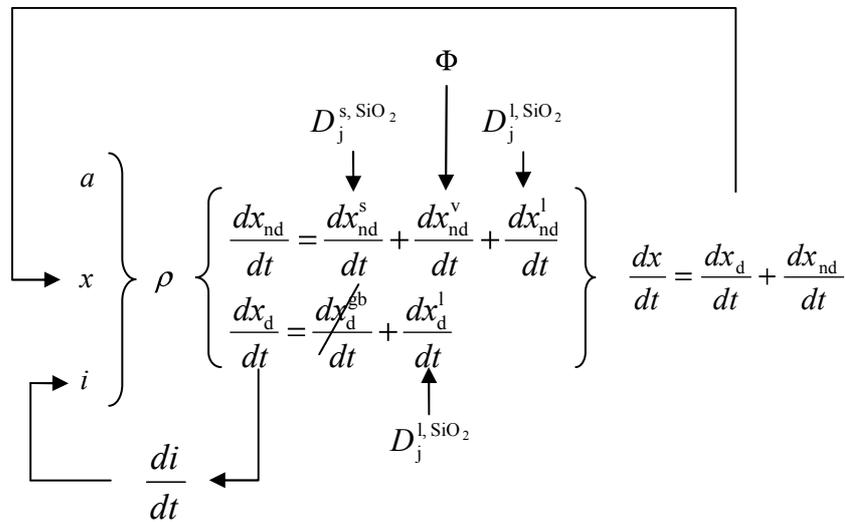
Figure IV.18: Iterative approach for the estimation of densification kinetics (contribution of grain boundary diffusion is negligible). The particle size, a, neck size, x, radius of curvature, ρ, and indenting parameter, i, are entering geometrical parameters of the model. The sintering rates are calculated step by step and x, ρ, and h, are modified accordingly while the particle size, a, remains constant. Physical parameters of the model are those of sintering rate equations presented in Table IV.1 and Table IV.2.

b)   Parameters of the model

All accessible parameters of the model are physical parameters used to derive neck growth rate equations in Table IV.1 and Table IV.2. The model is used to estimate densification kinetics in the presence of silica. The assumptions for the sintering mechanism are (Figure IV.18):

- Surface diffusion: The surface diffusion coefficient of silicon onto silica is ten times the lattice diffusion coefficient of silicon into silica (Equation (IV.33)).

- Vapor transport: only silicon monoxide vapor is assumed to affect neck growth kinetics. The vapor pressure is then the equilibrium partial pressure, $P_{\text{SiO}}^{\text{R}_s}$, and the surface area fraction of holes, Φ, which taken as 2.5×10^{-5} as estimated from fitting of densification kinetics in the next section c) "Effect of vaport transport".

- Lattice diffusion: The lattice diffusion coefficient of silicon into silicon is estimated from the measurements of Shimizu *et al.* [SUI07]. The silica layer is assumed to affect lattice diffusion kinetics. An effective diffusion coefficient is then estimated using Equations (IV.35) and (IV.36) for lattice diffusion from surface and grain boundary, respectively.

- Grain boundary diffusion: Grain boundary diffusion is assumed not to affect sintering kinetics (see section IV.2.2) and is not considered in the model calculations.

The dilation of the sample is taken into account assuming a constant coefficient of thermal expansion of 4.26×10^{-6} °C^{-1} [Hul99]. From previous considerations in section IV.2.2, one parameter remains undetermined, the diffusion coefficient of silicon into silica. This parameter affects surface diffusion as well as lattice diffusion kinetics.

c)   Modeling

- *Effect of the diffusion coefficient of silicon into silica*

In Figure IV.19, the shrinkage rate is estimated from the model and compared to experimental measurements for the heating rate of 10 °C min^{-1}, the silica layer being stabilized under a silicon-silica powder bed.
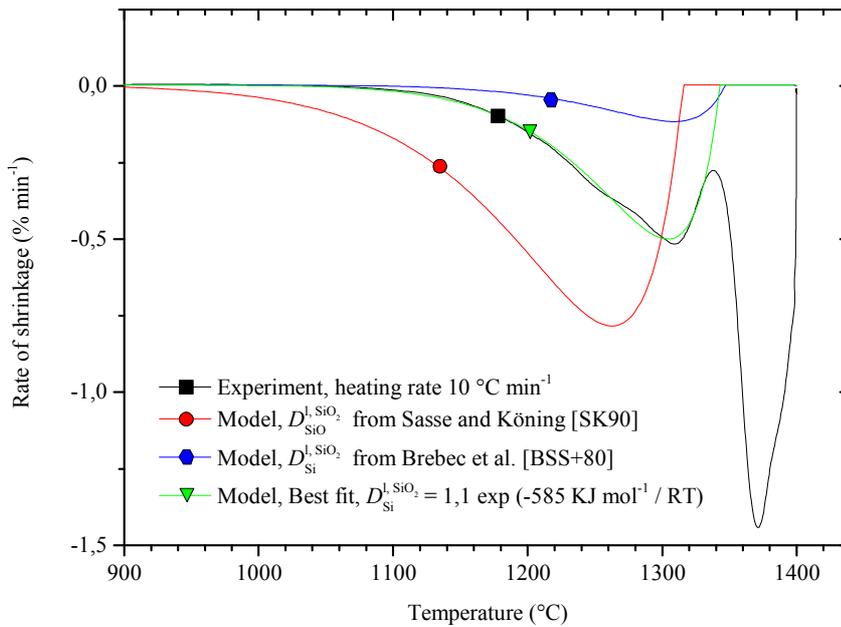
Figure IV.19: Modeling of the shrinkage rate of a VF powder compact using several values of the diffusion coefficient of silicon atoms into silica. Model parameters are, $e_{SiO_2} = 0.52$ nm, and $\Phi = 2.5 \times 10^{-5}$.

The shrinkage rate is calculated assuming two diffusion coefficients for the diffusion of silicon into silica:

- The diffusion coefficient of silicon into silica measured by Brebec *et al.* [BSS+80] from diffusion profiles of a stable isotope Si^{30} in a silica bulk material. In this case, the silica layer strongly affects lattice diffusion kinetics as shown in section IV.2.2, Figure IV.10.

- The diffusion coefficient of silicon monoxide into silica estimated by Sasse and Köning [SK90] during the decomposition of a silica layer of nanometric thickness. In this case, the silica layer slightly affects lattice diffusion kinetics as shown in section IV.2.2, Figure IV.10.

As can be seen in Figure IV.19, both coefficients do not fit the experimental curve.

- If the diffusion coefficient of silicon into silica measured by Brebec *et al.* [BSS+80] is considered, the shrinkage rate is largely underestimated.

- If the diffusion coefficient of silicon monoxide into silica estimated by Sasse and Köning [SK90] is considered, the shrinkage rate is largely overestimated.

Experimental measurements have been fitted in Figure IV.19 using the model, by changing the apparent activation energy and the pre-exponential factor in the diffusion coefficient of silicon into silica. As shown in Table IV.5, the best fit gives a diffusion coefficient with an apparent activation energy close to the activation energy measured by Brebec *et al.* [BSS+80]. However, the pre-exponential factor is approximately 30 times larger.

	Brebec *et al.*	Sasse and Köning	Model
Reference	[BSS+80]	[SK90]	Figure IV.19
Pre-exponential factor	3.3×10^{-2} m² s^{-1}	1.48×10^{-7} m² s^{-1}	1.1 m² s^{-1}
Activation energy	579 KJ mol^{-1}	308 KJ mol^{-1}	585 KJ mol^{-1}

Table IV.5: Activation energies for densification, E_a, estimated from sintering model compared to the activation energies for lattice diffusion of silicon into silica and silicon monoxide into silica.

Accordingly, the silica layer affects lattice diffusion and then densification kinetics. The appropriate diffusion coefficient for the diffusion of silicon into silica during sintering is the coefficient measured by Brebec *et al.* [BSS+80], as the activation energy is very close to the apparent activation energy estimated from the model. Although our experimental conditions are closer to the configuration of Sasse and Köning [SK90], i.e, a nanometric silica layer covering a silicon surface, the diffusion is not of the same type. Sasse and Köning diffusion is activated under a chemical gradient through the silica layer, as considered by Celler and Trimble [CT89b, CT89a, CT88, TCWS89] to explain the fast diffusion observed. However, during sintering, matter transport is driven by a vacancy gradient and the self-diffusion coefficient in the lattice has to be considered, as measured by Brebec *et al.* [BSS+80]. The discrepancy in the pre-exponential factors between Brebec's coefficient and the best fit from our dilatometric results is discussed in the next section.

- *Effect of stresses in the silica layer on the diffusion coefficient of silicon into silica*

Densification kinetics is strongly underestimated if the pre-exponential factor measured by Brebec *et al.* [BSS+80] is considered. The inconsistency is removed if the occurrence of tensile stresses in the silica layer which can accelerate the diffusion is considered.

A general expression for the diffusion coefficient is given in Equation (IV.48) [Kit56, She89, ADPQ78], where ΔG_f is the Gibbs free energy for the formation of a defect (vacancy), Z is the number of neighboring atoms, ΔG_m is the free energy for the migration of the defect and ν the jumping frequency of the atoms. c is a correlation factor and l the jumping length of the defect.

$$D = \frac{l^2 c}{6} \nu \exp\left(-\frac{\Delta G_f}{RT}\right) Z \exp\left(-\frac{\Delta G_m}{RT}\right) \tag{IV.48}$$

Assuming that a pressure P is applied to the material, the effect on the diffusion coefficient can be estimated in Equation (IV.50) using Equations (IV.48) and (IV.49). ΔV corresponds to the volume variation related to the change in Gibbs free energy, ΔG.

$$\left.\frac{\partial \Delta G}{\partial P}\right|_T = \Delta V \tag{IV.49}$$

$$\left.\frac{\partial \ln D}{\partial P}\right|_T = -\frac{\Delta V_f + \Delta V_m}{RT} \tag{IV.50}$$

$\Delta V_f + \Delta V_m$ being positive, when the pressure is increased $(\Delta P > 0)$, the diffusion coefficient decreases as commonly observed. The variation of diffusion coefficient with respect to the pressure is then a function of the temperature, the volume of vacancy formation, ΔV_f, and the volume variation resulting from the migration of the vacancy, . ΔV_f is close to the atomic molar volume, that is to say, approximately $\Omega_{SiO_2}/3$ for silicon atoms into silica. ΔV_m is usually small, approximately ten times smaller than the atomic molar volume, and negligible [ADPQ78], so that Equation (IV.50) simplifies in Equation (IV.51).

$$\left.\frac{\partial \ln D}{\partial P}\right|_T \approx -\frac{\Omega_{SiO_2}}{3RT} \tag{IV.51}$$

Considering the thermal expansion coefficient of silicon (4.26×10^{-6} °C^{-1} [Hul99]) and vitreous silica (0.55×10^{-6} °C^{-1} [Smi83]) at 1000 °C, tensile stresses should continuously develop in the silica layer. These tensile stresses result in a pressure drop, $(\Delta P < 0)$, that accelerates diffusion.

By integration of Equation (IV.51), the diffusion coefficient of silicon into silica from Brebec *et al.* [BSS+80] can be modified to take into account the effect of the pressure drop in Equation (IV.52).

$$D_{\mathrm{Si}}^{\mathrm{l,SiO_2}}(\Delta P) = D_{\mathrm{Si}}^{\mathrm{l,SiO_2}}\Big|_{\Delta P=0} \exp\left(-\frac{\Omega_{\mathrm{SiO_2}}\Delta P}{3\mathrm{R}T}\right) \tag{IV.52}$$

Equation (IV.52) is included in the model. In Figure IV.20, the best fit for the heating rates of 10, 20 and 40 °C min^{-1} corresponds to a tensile stress of 4500 MPa which is approximately half the rupture modulus of silica at room temperature [AJ80]. This is consistent if one assumes that stresses are released by the formation of holes, as already discussed, as soon as the rupture tensile stress of silica is overpassed.
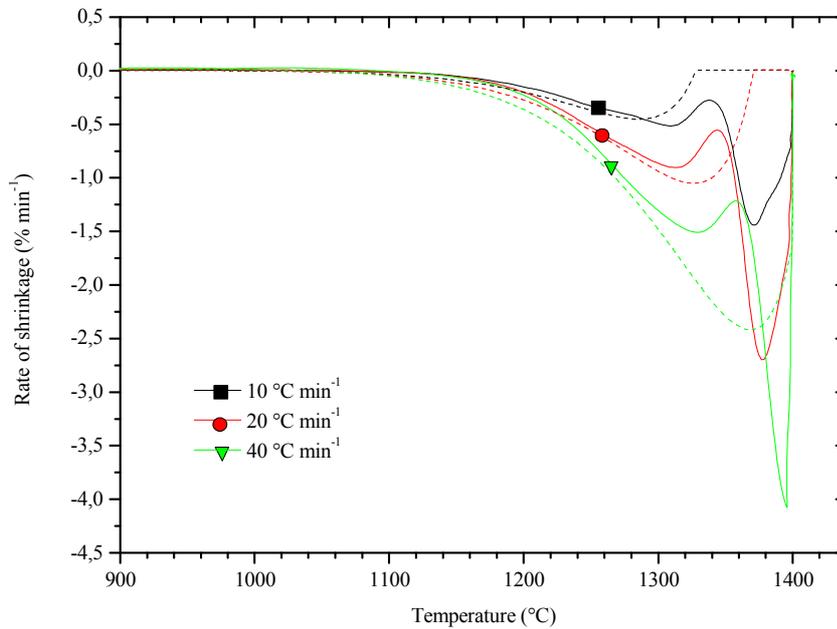
Figure IV.20: Modeling of the shrinkage rate of a VF powder compact using the diffusion coefficient of silicon into silica, $D_{\mathrm{Si}}^{\mathrm{l,SiO_2}}$, taking into account the effect a pressure drop ($\Delta P = -4500$ MPa) in the silica layer on the diffusion coefficient. Model parameters are, $e_{\mathrm{SiO_2}} = 0.52$ nm, and $\Phi = 2.5 \times 10^{-5}$.

As the temperature increases, $D_{\mathrm{Si}}^{\mathrm{l,SiO_2}}(\Delta P)\Big/ D_{\mathrm{Si}}^{\mathrm{l,SiO_2}}\Big|_{\Delta P=0}$ only slightly decreases (Figure IV.21). Pressure effects in the silica layer then only slightly affect the activation energy for the diffusion which is consistent with experimental results in Table IV.5.
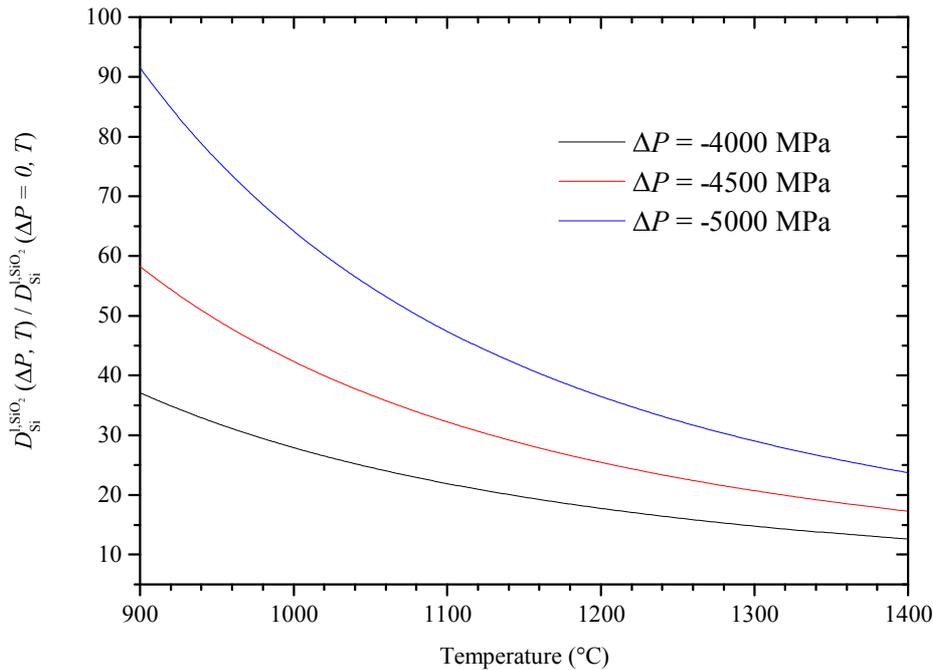
Figure IV.21: $D_{\mathrm{Si}}^{\mathrm{l,SiO_2}}(\Delta P)\Big/ D_{\mathrm{Si}}^{\mathrm{l,SiO_2}}\Big|_{\Delta P=0}$ *as a function of the temperature for several pressure drops, ΔP.*

Nevertheless, according to the Pilling-Bedworth ratio, close to 2.1, the silica layer, once formed, should be under compressive stresses.[4]

Another explanation for the rapid diffusion of silicon into silica might then be the increment of vacancies generated by the reaction (R_5).

- *Effect of vapor transport*

The effect of silicon vapor transport on densification kinetics is plotted in Figure IV.22, where the shrinkage rate is modeled and compared to experimental data for the 10 °C min^{-1} heating rate. Vapor transport kinetics depends on the surface area fraction of holes at the passive to active transition which is approximately 4×10^{-5} from discussion in Chapter III.4.

As can be seen in Figure IV.22, varying the surface area fraction of holes from 10^{-6} to 10^{-4}, does not affect the beginning of densification kinetics, but strongly affects the end. As sintering goes on, vapor transport dominates lattice diffusion which is consistent with the scaling law presented in Table IV.3. As the surface area fraction of holes is increased, densification kinetics is slowed down as vapor transport, which is a non-densifying

---

[4] Note added to the manuscript following a discussion with the comitee during the PhD defence.

mechanism, is enhanced compared to lattice diffusion. A surface area fraction of holes, $\Phi = 2.5 \times 10^{-5}$, is used in the following, as it gives the best fit.
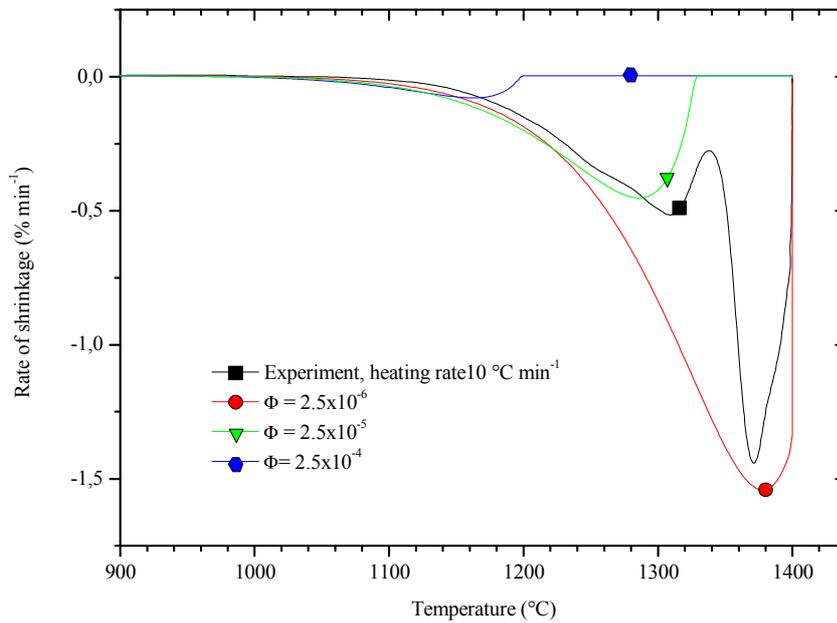
Figure IV.22: Effect of vapor transport on the densification rate of a VF powder compact for several surface fractions of holes, Φ. Important model parameters are, $e_{SiO_2} = 0.52$ nm and $\Delta P = -4500$ MPa.

d)   Summary: initial stage densification kinetics

When the silica layer is reduced, the onset of densification coincides with the apparition of holes in the silica layer at the passive to active transition. On the contrary, when the silica layer is stabilized, the densification is retarded.

Lattice diffusion is actually affected by the presence of a silica layer as the diffusion of silicon atoms in the silica layer is not as fast as in the silicon particle volume. An effective diffusion coefficient can be estimated assuming the serial diffusion of atoms in the particle volume and in the oxide thickness. The apparent activation energy for lattice diffusion and densification kinetics is then between the activation energy for the diffusion of silicon into silicon [SUI07] and for the diffusion of silicon into silica [BSS+80].

Densification kinetics has been modeled and compared to experimental results during the first stage of sintering (first peak of the densification rate). The suitable diffusion coefficient for silicon into silica is then the coefficient measured by Brebec *et al.* [BSS+80]. It corresponds to the diffusion of atoms through point defects as usually considered in sintering. The diffusion coefficient measured by Sasse and Köning [SK90] is comparatively too large and

cannot account for the experimental densification kinetics. It actually corresponds to the diffusion of silicon atoms under a chemical gradient through the silica layer.

But the diffusion coefficient of Brebec *et al.* [BSS+80] largely underestimates densification kinetics. The inconsistency is removed, by assuming the presence of tensile stresses in the silica layer that accelerates the diffusion. These stresses may be explained by the thermal expansion mismatch between silicon and silica. Estimated values are lower but of the order of magnitude of the silica tensile strength, since cracks should form to release those stresses above this limit.

Eventually, at the end of the first stage, vapor transport of silicon monoxide, which is controlled by the surface area fraction of holes, seems to dominate sintering and slows down densification kinetics. The migration of the silicon-silica interface is not precluded as the silica layer continuously evaporates and condensates at the particle surface through the continuous formation and healing of thermal holes.

IV.3.2 Intermediate stage of sintering

Until now, only the first stage of sintering has been considered, where limited grain growth has been observed. This corresponds to the first peak on the dilatometric curves:

- Lattice diffusion, even though retarded by the presence of silica, first dominates sintering kinetics. Accordingly, the densification accelerates as the temperature increases.

- Then, vapor transport dominates sintering kinetics. The densification rate slows down, although the density is very low and the temperature is increased.

Sintering during the second stage involves densification and grain growth, or more precisely, pore growth (Figure IV.15, samples (i) and (j)). Both mechanisms are first treated separately and put together to explain the second peak observed on the dilatometric curves.

a)   Densifying mechanism

At the end of the first stage, curvature gradients around the neck are smoothed, as can be seen on sample (h) microstructure (Figure IV.15) which has been quenched at the end of the first peak. Sintering is now driven by the curvatures of the pores which are interconnected.

Since the curvature of the pores is mostly uniform, non-densifying mechanisms cannot operate on the scale of a pore. We are therefore left with lattice diffusion from grain boundary since grain boundary diffusion has been assumed to never dominate sintering kinetics of silicon. Accordingly, as the temperature increases, densification kinetics should accelerate again during the second stage, as observed experimentally.

Assuming that the microstructure can be assimilated to a packing of tetrakaidecahedrons [Cob61] with cylindrical pores along their edges, the shrinkage rate can be estimated in Equation (IV.53) from the pore shrinkage calculated in Equation (IV.26). $D_{Si}^{l,eff}$ is an effective lattice diffusion coefficient taking into account the presence silica at the pore surface by assuming a diffusion distance of order of magnitude l_p (Equation (IV.54)). The pore segment length, l_p, can be related to the initial particle size, a, and to the porosity, p, from Equations (IV.23) to (IV.25), assuming that the volume of the tetrakaidecahedron equals the volume of the initial particles, *i.e.* assuming that no grain growth occurs (Equation (IV.55)). Equation (IV.56) simply links the pore radius, ρ_p, to the pore length according to the geometry considered.

$$\frac{1}{h}\frac{dh}{dt} = \frac{1}{3}\frac{dp^1}{dt} = -\frac{7}{3}\pi\sqrt{2}\frac{D_{Si}^{l,eff} F_{Si}}{l_p^{\ 3}} \tag{IV.53}$$

$$D_{Si}^{l,eff} = l_p \left(\frac{e_{SiO_2}}{D_{Si}^{l,SiO_2}} + \frac{l_p - e_{SiO_2}}{D_{Si}^{l,Si}} \right)^{-1} \tag{IV.54}$$

$$l_p = \left(\frac{\pi}{6\sqrt{2}(1-p)} \right)^{1/3} a \tag{IV.55}$$

$$\rho_p = \left(\frac{2\sqrt{2}p}{3\pi} \right)^{1/2} l_p \tag{IV.56}$$

b)   Mechanism of pore coarsening

Although the surface of one pore is more or less uniform, pores are not of equal size. The radius of curvature, ρ_p, differs from one pore to another. Chemical potential gradients and then pressure gradients exist between the pores. The porosity being interconnected, we can easily assume that vapor transport, which already dominates at the end of the first stage, occurs between the pores and leads to pore coarsening by a mechanism of Ostwald ripening. The largest pores grow and the smallest disapear, increasing the inter-pore distance. This is indeed observed on the final microstructure of the sample (j) in Figure IV.15. This mechanism which occurs at the scale of several pores is non-densifying but affects the densification kinetics: if the geometry of tetrakaidecahedron is maintained, l_p increasing in Equation (IV.53), the shrinkage rate progressively decreases.

A system consisting of a dispersion of cylindrical pores with different radius of curvature, ρ_p, is considered in Figure IV.23. From Equation (IV.9), the silicon monoxide vapor pressure at

the surface of one pore, $P_{SiO}(\rho_p)$, with respect to the pressure over a flat surface $P_{SiO}^{R_5}$ is given in Equation (IV.57).

$$\frac{P_{SiO}(\rho_p) - P_{SiO}^{R_5}}{P_{SiO}^{R_5}} = -\frac{F_{SiO}}{\rho_p} \qquad (IV.57)$$

The higher pressure inside a pore of larger radius gives rise to a net flux of matter from the larger pores to the smaller ones. The largest pores grow while the smallest shrink and eventually close as the criterion of morphological instability of Rayleigh is reached.
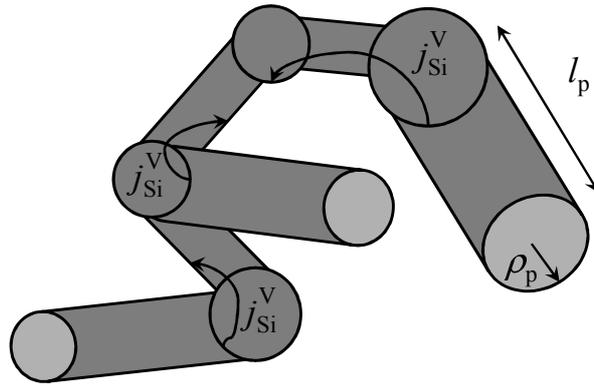
Figure IV.23: Network of connected cylindrical pores. Coarsening is assumed to occur through vapor transport from the larger to the smaller pores.

A rough estimation of pore coarsening kinetics is proposed in the following. It is based on the basic theory of Ostwald ripening, which was developed independently by Wagner [Wag61] and Lifshitz and Slyozov [LS61]. It is referred to as the LSW theory.

Returning to Figure IV.23, two steps may control the rate of coarsening, either the interface reaction (*i.e.* the evaporation or condensation) or the diffusion through the pores. Assuming that evaporation condensation controls the kinetics, the rate of transfer of atoms is then proportional to the difference between the vapor pressure in a pore of radius ρ_p, $P_{SiO}(\rho_p)$, and an average pressure, $P_{SiO}(\rho_p^*)$, defined as the pressure that is in equilibrium with pores of critical radius, ρ_p^*, that neither grow nor shrink. The molar flux density of silicon monoxide at the surface of one pore through vapor transport, j_{SiO}^v, can be then estimated from the gas kinetic theory and Equation (IV.57) in Equation (IV.58).

$$j_{SiO}^v = \Phi \frac{P_{SiO}(\rho_p^*) - P_{SiO}(\rho_p)}{\sqrt{2\pi M_{SiO}RT}} = \frac{-\Phi F_{SiO}P_{SiO}^{R_5}}{\sqrt{2\pi M_{SiO}RT}}\left(\frac{1}{\rho_p^*} - \frac{1}{\rho_p}\right) \qquad (IV.58)$$

Assuming that the rate of change of the pore volume, dV_p/dt, through vapor transport is much higher than the rate of change through lattice diffusion, i.e, assuming a rapid pore coarsening compared to densification, the rate of change of the pore volume can be directly related to the molar flux density of atom at the pore surface from vapor transport, j_{SiO}^v, in Equation (IV.59).

$$\frac{dV_p}{dt} = -2\pi\rho_p l_p j_{SiO}^v \Omega_{SiO} \tag{IV.59}$$

Eventually, the rate of volume pore change can be written in Equation (IV.60) from Equations (IV.56), (IV.58) and (IV.59) assuming that pore coarsening is homothetic, *i.e.* the ratio between the pore length, l_p, and the pore radius, ρ_p, remains constant.

$$\frac{dV_p}{dt} = -2\pi\rho_p^2 \left(\frac{3\pi}{2\sqrt{2}p}\right)^{1/2} j_{SiO}^v \Omega_{SiO} \tag{IV.60}$$

Moreover, from geometrical considerations, the rate of pore volume change can also be written in Equation (IV.61).

$$\frac{dV_p}{dt} = \pi\rho_p^2 \frac{dl_p}{dt} + 2\pi\rho_p l_p \frac{d\rho_p}{dt} = 3\pi\rho_p^2 \left(\frac{3\pi}{2\sqrt{2}p}\right)^{1/2} \frac{d\rho_p}{dt} \tag{IV.61}$$

From Equations (IV.58) to (IV.61), the rate of pore radius change can be written in Equation (IV.62).

$$\frac{d\rho_p}{dt} = \frac{2\Phi F_{Si} P_{SiO}^{R_5} \Omega_{Si}}{3\sqrt{2\pi M_{SiO} RT}} \left(\frac{1}{\rho_p^*} - \frac{1}{\rho_p}\right) \tag{IV.62}$$

The rate of change of the pore radius is then proportional to the difference between the critical curvature, $1/\rho_p^*$, and the curvature of the pore, $1/\rho_p$. Accordingly, if the pore radius is less than the critical radius, ρ_p^*, the pore will shrink while if the pore radius is larger, the pore will grow.

Evolution of the pore size distribution is not trivial to be deduced. Wagner [Wag61] analyzed the coarsening of a population of grains in a matrix, assuming that kinetics was limited by an interfacial reaction. Original assumptions were:
-   Population of grains with a specified shape as considered in Equation (IV.56).

- Constant volume of grains.

Wagner's model [Wag61] can be applied in our case to derive the growth kinetics of a pore with a critical radius, ρ_p^*, in Equation (IV.63), assuming homothetic pore shapes.

$$\frac{d\rho_p^*}{dt} = \frac{1}{6} \frac{\Phi F_{SiO} P_{SiO}^{R_5} \Omega_{SiO}}{\sqrt{2\pi M_{SiO} RT}} \frac{1}{\rho_p^*} \tag{IV.63}$$

The critical size may be approximated to the average size, $\overline{\rho_p}$, within a multiplying factor of 8/9. Eventually, the mean pore radius and pore length due to pore coarsening may be estimated using Equations (IV.64) and (IV.65).

$$\frac{d\overline{\rho_p}}{dt} = \frac{1}{6} \frac{\Phi F_{SiO} P_{SiO}^{R_5} \Omega_{SiO}}{\sqrt{2\pi M_{SiO} RT}} \frac{1}{\overline{\rho_p}} \tag{IV.64}$$

$$\frac{d\overline{l_p}}{dt} = \frac{1}{6} \left(\frac{3\pi}{2\sqrt{2}p} \right)^{\frac{1}{2}} \frac{\Phi F_{SiO} P_{SiO}^{R_5} \Omega_{SiO}}{\sqrt{2\pi M_{SiO} RT}} \frac{1}{\overline{\rho_p}} \tag{IV.65}$$

The influence of the pore growth on the rate of shrinkage is then assessed from Equation (IV.53) by replacing the pore segment length, l_p, by the mean pore segment length, $\overline{l_p}$ calculated from Equation (IV.65). The effect of the densification on the evolution of the pore segment length is assessed iteratively by uploading the value of the porosity, p, in the same equation.

c)   Model parameters

Since the equations of pore coarsening have been derived, the initial pore sizes have to be settled prior to any model estimation. Until now, it has been assumed that pore coarsening is initiated once the pore curvature is more or less uniform, *i.e.*, at the beginning of the intermediate stage. However, it would be fair to assume that pore coarsening is initiated before. Indeed, once a neck is formed, part of the pore surface is concave as shown in Figure IV.24. Once the concave surfaces are higher than the convex ones, smaller pores should exhibit a lower pressure than the larger ones, i.e, pore coarsening should be initiated. The fraction of concave surface plotted in Figure IV.24, can be expressed in Equation (IV.66). The neck surface is related to the concave surface while the surface of the particle minus the surface of the particle cap at the neck position corresponds to the convex surface, nc being the coordination number.

$$\frac{\text{Concave surface}}{\text{Solid vapor surface}} = \frac{n_c 2\pi\rho\theta x}{4\pi a^2 - n_c 2\pi a\rho(\sin\theta + i) + n_c 2\pi\rho\theta x} \qquad \text{(IV.66)}$$
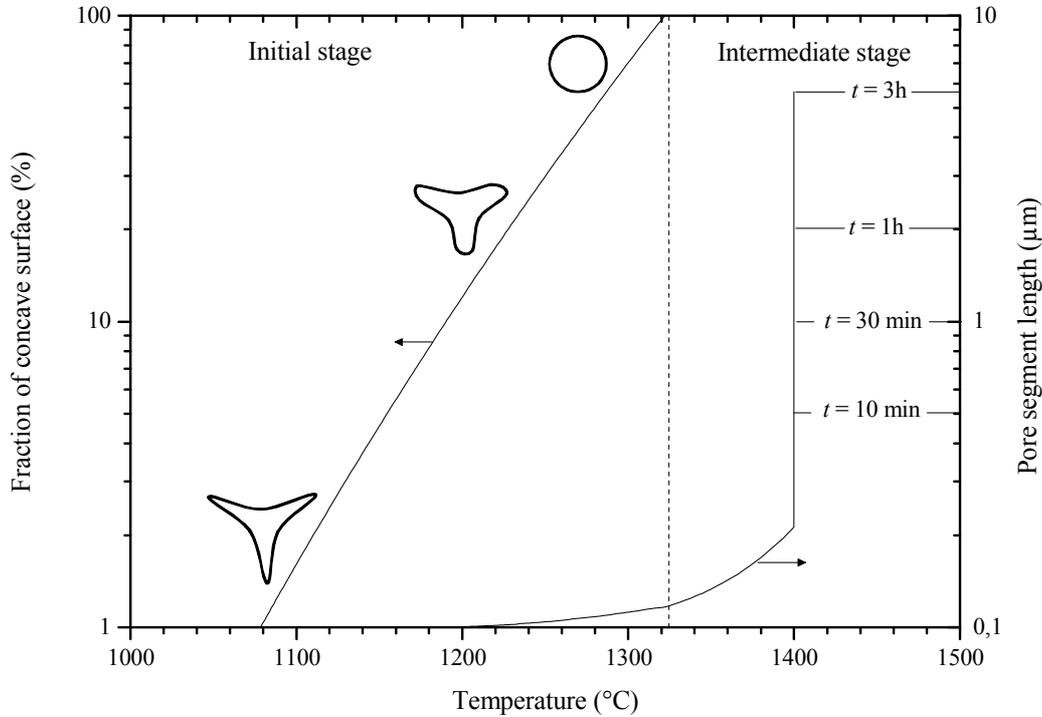
Figure IV.24: Left axis: evolution of fraction of concave surface (coordination number, n_c = 6) and corresponding pore shape from the initial stage model. Right axis: evolution of the pore segment length from the LSW model. The heating rate is 10 °C min^{-1} and t corresponds to the dwell time on the sintering plateau at 1400 °C.

In the model, the pore growth is initiated from the early stage of sintering. Although the geometry cannot be assimilated to cylindrical pores during the first stage, initial parameters, *i.e.*, mean pore segment length and pore radius, are estimated from Equations (IV.55) and (IV.56), using the initial mean particle radius and compact density, i.e, $2a$ = 220 nm and p = 0.47 for a VF powder compact.

In Figure IV.24, the fraction of concave surface and the growth of the pore segment length are plotted against the temperature. Actually, significant pore coarsening occurs only at temperatures higher than 1300 °C, when the fraction of concave surface is largely higher than 50 %, as experimentally observed in Figure IV.15 and expected. Initiating the pore coarsening at the early stage of sintering from the initial mean particle radius and compact density is then accurate, although the geometry considered is not.

In Figure IV.25, the LSW estimations of the final mean pore radius, $\overline{\rho}_p$, and pore segment length, $\overline{l}_p$, which is characteristic of the distance between pores, corroborate the microstructure observations for samples sintered for 1 and 3 h at 1400 °C. Of particular interest is the grain size which is much smaller than $\overline{l}_p$. This shows that grain boundary migration kinetics is not slowed down by pore pinning as usually observed during sintering but is intrinsically low. Here, the presence of silica at the triple junction of the grain may inhibit the mobility of the grain boundaries.

1400°C - 1h
$\overline{\rho}_p = 0.1$ μm - $\overline{l}_p = 2.2$ μm

1400°C - 3h
$\overline{\rho}_p = 0.2$ μm - $\overline{l}_p = 5.8$ μm
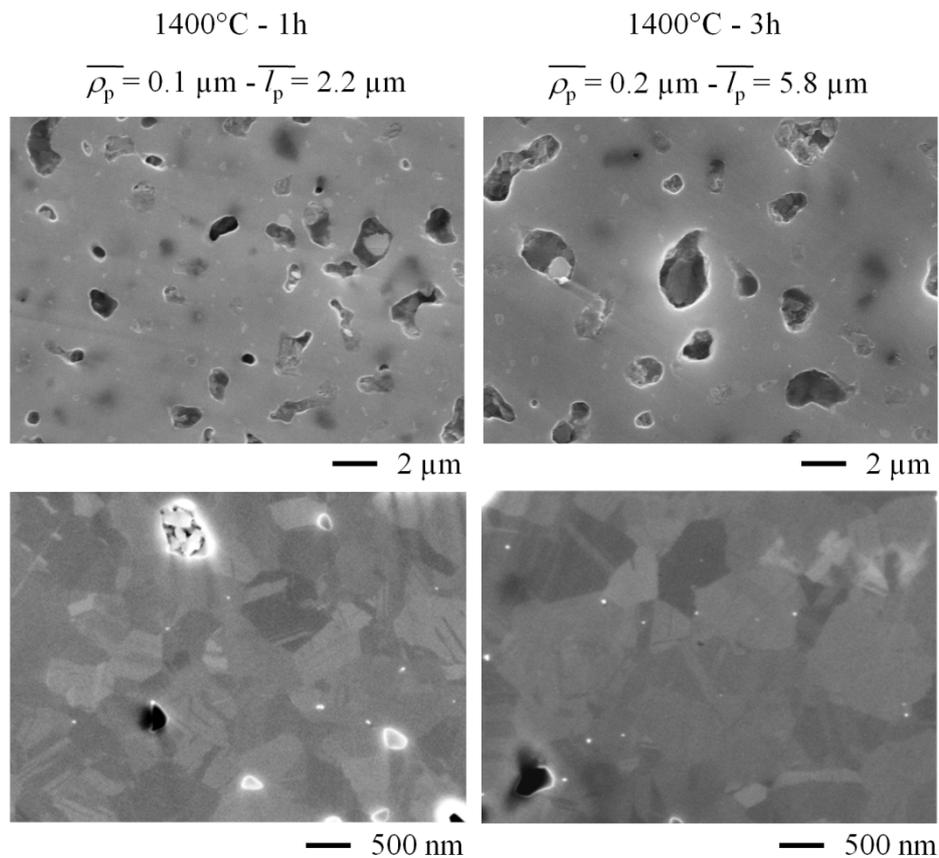
Figure IV.25: Microstructures of the samples sintered under a silicon-silica powder bed at 1400°C for 1 and 3 h with a heating rate of 10 °C min⁻¹. The microstructures can be compared to the pore size estimations from the LSW model.

d)   Discussion: model accuracy?

Some questions arise as regards the consistency between the models of Coble and pore coarsening by the LSW theory. Coble's model has been derived for pores of equal size and is in contradiction with the mean field approach of the LSW theory dealing with a pore size distribution. Also, according to the LSW theory, the total volume of pores should be constant,

that is to say, no densification should occur. The coupled approach derived here is then questionable.

However, although the pore size distribution is affected by the densification, it is fair to assume that the mean pore size is unaffected: densification occurs by elimination of the small pores and reduction of the pore size of the larger ones. These two effects may compensate on the mean pore radius, $\overline{\rho_p}$, or pore length, $\overline{l_p}$, even if they decrease the width of the pore size distribution. Indeed, for materials that do not undergo grain or pore growth, the mean pore radius, which can be estimated from the mean pore intercept, is usually constant during the intermediate stage of sintering [VRM+08, MR00, Arl82, AD01, GR01]. The effect of densification on the mean pore size can be then neglected, as a first approximation.

Variation of the total volume of pores due to densification should disturb coarsening kinetics as compared with the LSW model. Calculated kinetics of pore coarsening is then only valid if coarsening kinetics is rapid enough compared to densification kinetics.

IV.3.3 Combination of initial and intermediate stage models

Densification kinetics is then modeled using the following assumptions:

- The initial stage of sintering occurs as long as the compact density is less than approximately 60 % TD_{Si}, which corresponds to the position where the second peak appears. Lattice diffusion kinetics is estimated using the diffusion coefficient of silicon into silica, $D_{Si}^{l,SiO_2}(\Delta P)$, defined in Equation (IV.52), assuming that the silica layer is under tensile stresses ($\Delta P = -4500$ MPa). The surface area fraction of holes is $\Phi = 2.5 \times 10^{-5}$.

- The intermediate stage of sintering starts from a compact density of approximately 62 % TD_{Si}. This corresponds to a temperature of 1330 °C, right after the convex surfaces have disappeared (Figure IV.24). The initial value of the mean pore length is estimated from Equation (IV.55) from the initial particle size ($2a = 220$ nm) and porosity ($p = 0.47$) of a VF powder compact. Pore growth kinetics and densification kinetics are then calculated from Equations (IV.64) and (IV.65) assuming that densification does not affect the mean pore size.

- The final stage (pore closure) is not taken into account, which is justified by the limited value of the final density of the samples.

Modeled shrinkage kinetics is compared to experimental measurements in Figure IV.26 for the heating rates of 10, 20 and 40 °C min^{-1}. The shape of the shrinkage curve is now clearly explained as follows:

- The first peak is related to the first stage of sintering where the first acceleration is related to densification through lattice diffusion and where the drop is related to neck growth through vapor transport which is a non-densifying mechanism.

- The second peak accounts for the second stage of sintering. The curvature around the pores becomes uniform and non-densifying mechanisms, which occur at the scale of one pore, are inhibited. Lattice diffusion from the grain boundary is still driven by the curvature of the pore and the rate of shrinkage accelerates again as the temperature is increased. In the mean time, Ostwald ripening occurs by vapor transport between the pores which coarsen, increasing the pore to pore distance. The shrinkage rates decrease again before full densification can be reached.
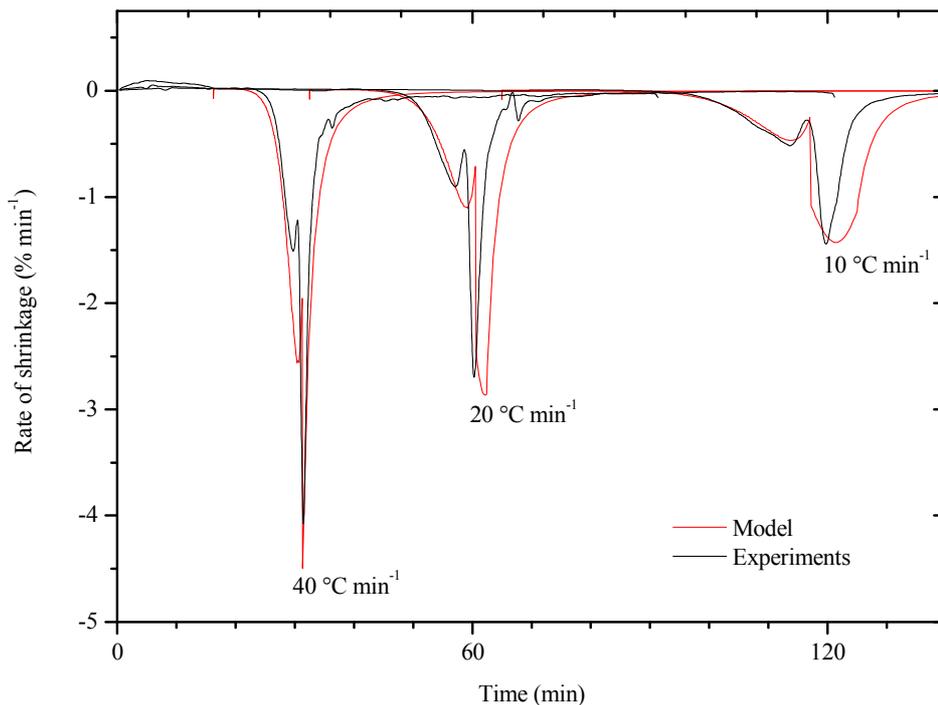
Figure IV.26: Experimental and modeled shrinkage rate curves of samples sintered for 1 h at 1400 °C, under a silicon-silica powder bed, at the heating rates of 10, 20 and 40 °C min^{-1}. Model parameters are, $2a = 220$ nm, $p = 0.47$, $e_{SiO_2} = 0.52$ nm, $\Delta P = -4500$ MPa, and $\Phi = 2.5 \times 10^{-5}$.

IV.4 Sintering maps: effect of silica and particle size

Ashby [Ash74] sintering maps for silicon are now plotted in order to summarize the results obtained. An Ashby map shows the dominant mechanism in a given temperature / neck size domain. Lines of constant neck growth rate are also added. These are simply the summation of the neck growth rate of all sintering mechanisms.

a)   Effect of silica on VF powder

In the case of silicon, two distinct maps should be plotted, one assuming silicon particles free from silica, the other assuming silicon particles covered with silica. Sintering maps are first plotted assuming spherical particles of 220 nm diameter that can be assimilated to the VF powder particles.

- *Pure silicon*

For pure silicon, the conclusion is straightforward (Figure IV.27). Surface diffusion s (nd) largely dominates sintering kinetics at all temperatures. This conclusion is consistent with SEM observations in the reduced area (Figure IV.5), where the large grain coarsening observed is the signature of such rapid neck growth through a non-densifying mechanism.
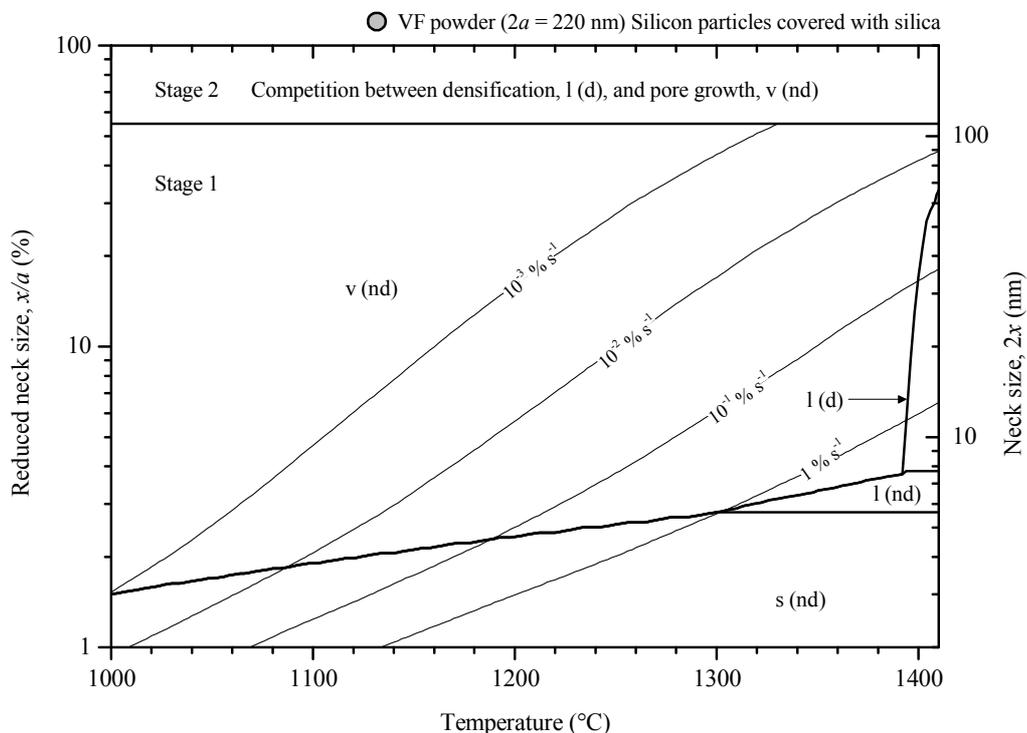
Figure IV.27: Ashby sintering map for pure silicon particles of 220 nm diameter (VF powder).

- *Silicon particles covered with silica*

For silicon particles covered with silica, assumptions made in the previous section are used to draw an Ashby sintering map (Figure IV.28). Sintering kinetics is clearly more complex than for pure silicon:

- Surface diffusion (s (nd)) still dominates the first step of sintering but is strongly slowed down compared to pure silicon. Accordingly, neck growth rate is strongly decreased compared to pure silicon.

- As the neck grows, vapor transport (v (nd)) and lattice diffusion (l (nd) and l (d)) dominate surface diffusion. Between the surface diffusion (s (nd)) and the lattice diffusion from grain boundary (l (d)) domains, lattice diffusion from the particle surface (l (nd)) dominates. Vapor transport (v (nd)) dominates lattice diffusion from grain boundaries (l (d)) for temperatures less than 1380 °C and for neck to particle ratio larger than 20%.

- Then, for neck to particle size ratio higher than 55 %, sintering enters in the second stage. Competition between densification through lattice diffusion (l (d)) and pore growth through vapor transport (v (nd)) occurs.
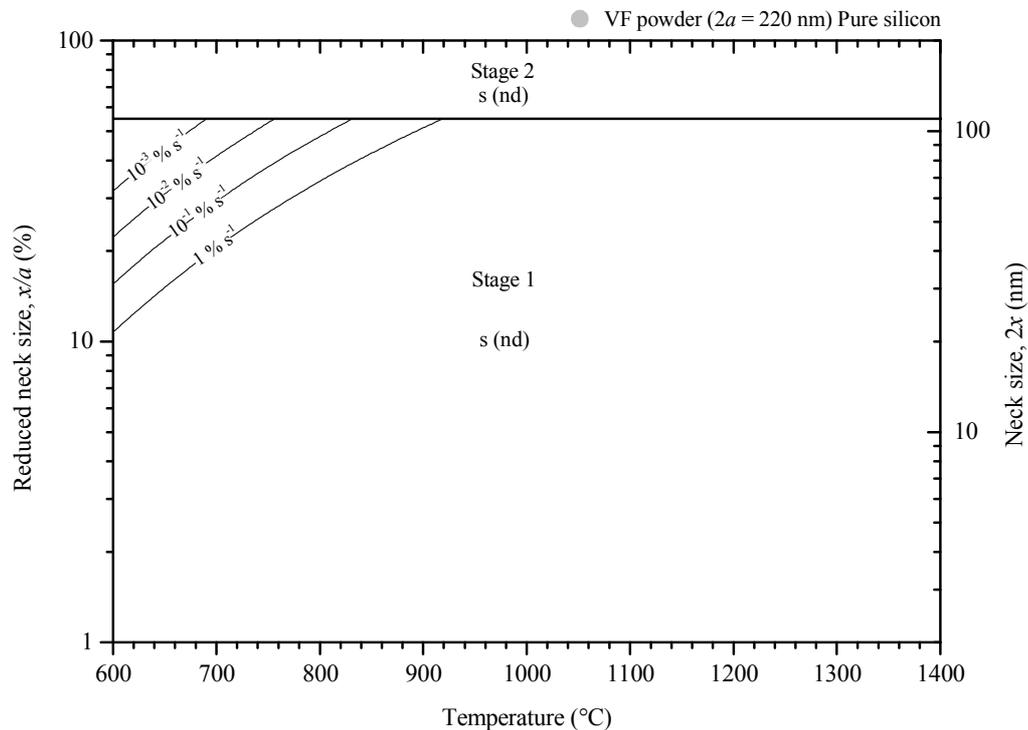
Figure IV.28: Ashby sintering map for 220 nm diameter silicon particles (VF powder) covered with silica.

This diagram is consistent with SEM observations in Figure IV.5, where neck growth and then grain coarsening is inhibited by the presence of silica. Lattice diffusion from grain boundary ensures densification of silicon at high temperature and at the beginning of the first stage and second stages.

b)   Effect of the particle size

The particle size strongly affects sintering kinetics. As the particle size is decreased, neck growth rates are always enhanced as the radius of curvature, ρ, which drives sintering kinetics, decreases. But, a particle size change does not affect homothetically the kinetics of the different mechanisms. One of the main interests of Ashby's diagram is then to plot the effect of a change in particle size on the movement of the boundaries between sintering domains. This allows a better visualization of the well-known Herring's scaling law.

Here, lines of constant neck growth rates are replaced by lines of constant sintering time which are of more practical use. These lines give the expected neck to particle size ratio after a sintering treatment of time t. More precisely, neck growth rate equations are summed and integrated, step by step, to give the neck growth after a given time at a constant temperature.

Experimental densities for several powder compacts made of various particle sizes sintered under reducing atmosphere and under a silicon-silica powder bed are shown in Table IV.6 and can be compared to the diagrams plotted in Figure IV.29 and Figure IV.30 for particles diameter of 100 nm, 220 nm (VF powder), 1 µm and 10 µm.

Powder	C	M	F	VF
$2a_{\text{BET}}^{\text{sphere}}$ (µm)	28	0.9	1	0.220
Initial density (% TD_{Si})	73	63	66	53
Sintering under reducing atmosphere, the silica layer being reduced - 1350 °C - 3 h				
Experimental final density (% TD_{Si})	75	66	68.5	65
Sintering under a silicon-silica powder bed, the silica layer being stabilized - 1350 °C - 3 h				
Experimental final density (% TD_{Si})				86

Table IV.6: Experimental densities for samples sintered under reducing atmosphere and under a silicon-silica powder bed.

- *Pure silicon*

As shown in Figure IV.29, for pure silicon, surface diffusion dominates at all particle sizes. Then, only neck growth kinetics is affected. As usually observed, as the particle size is increased, a higher temperature treatment is needed to reach an equivalent neck to particle size ratio in the same time.

These results are consistent with experiments performed under reducing atmosphere in Table IV.6. Densification is not favored when the particle size is changed. The better densification of the VF powder arises from partial densification of the sample before the complete reduction of the silica layer. Particle coalescence during grain growth, may also explain the densification observed.

Figure IV.29: Effect of a particle size change on sintering kinetics of pure silicon, free from silica.

Pure silicon - $2a$ = 100 nm

Pure silicon - $2a$ = 220 nm - VF powder
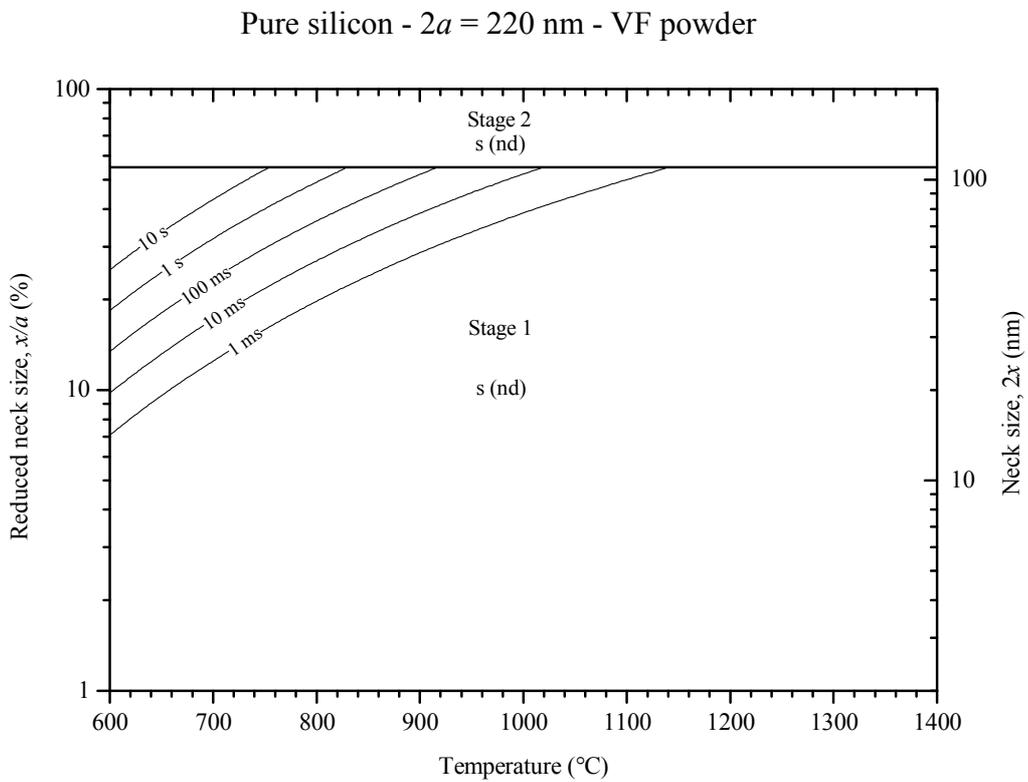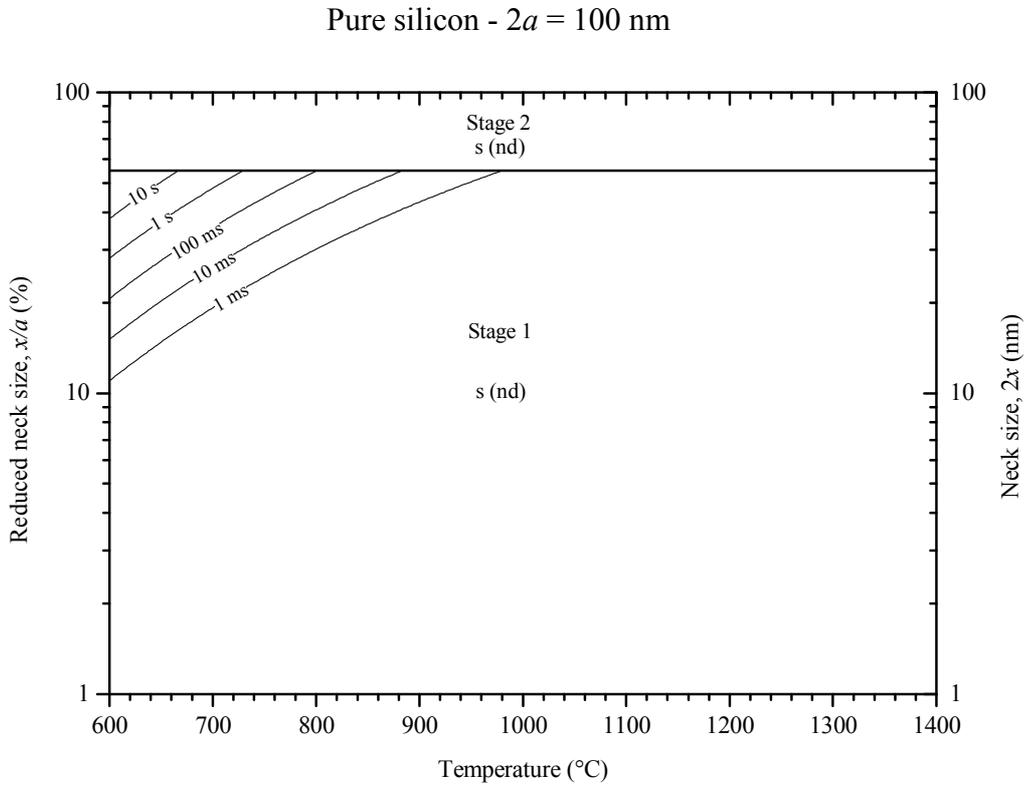
Figure IV.29 : (following) Effect of a particle size change on sintering kinetics of pure silicon, free from silica.

Pure silicon - 2*a* = 1 μm

Pure silicon - 2*a* = 10 μm
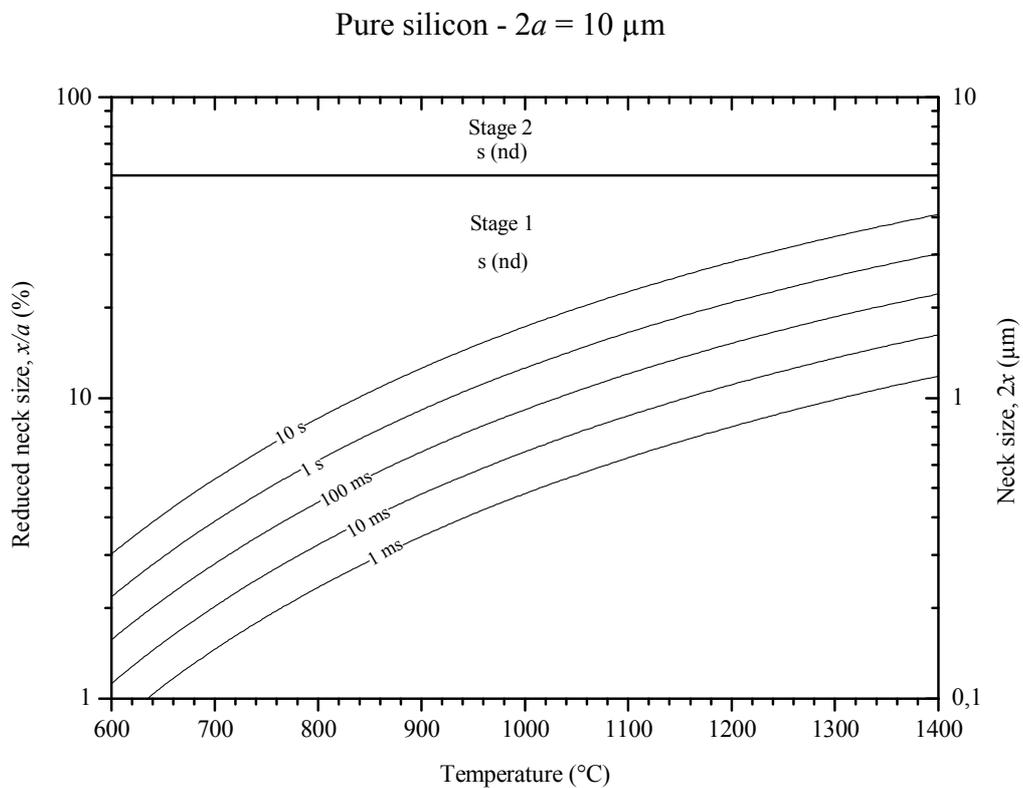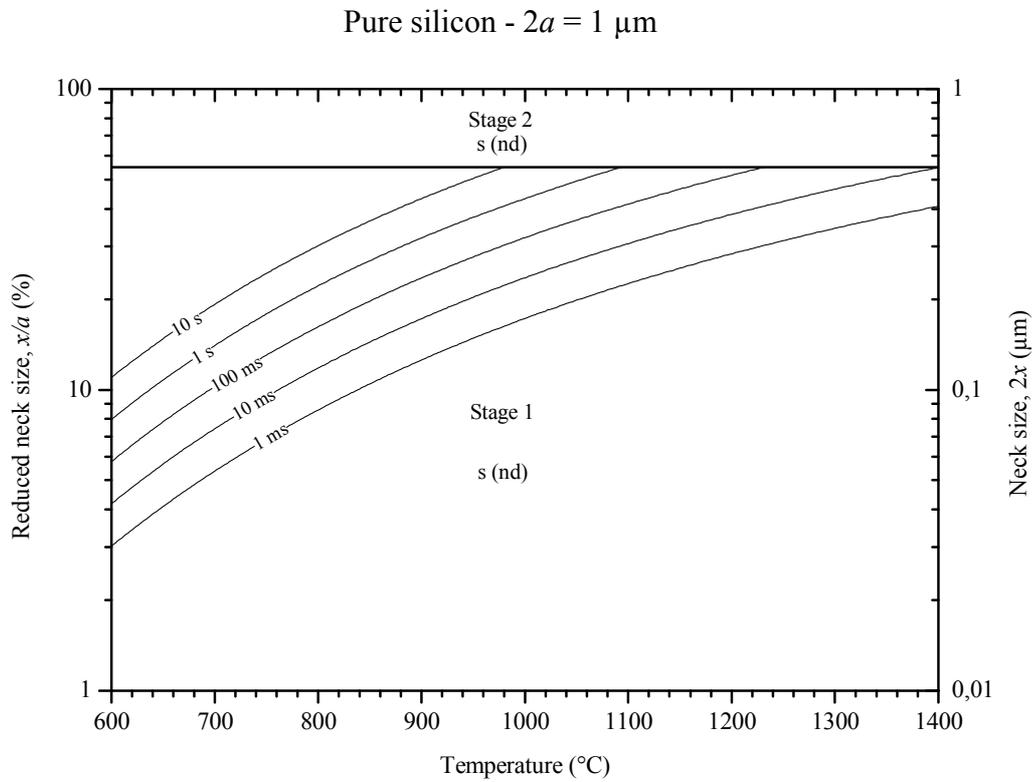
- *Silicon particles covered with silica*

For silicon particles covered with silica, a particle size change significantly affects the boundary positions between sintering mechanism domains (Figure IV.30).

As the particle size is decreased, the surface diffusion domain (s (nd)) grows towards higher neck to particle size ratio and the vapor transport domain (v (nd)) shrinks towards higher temperature and neck to particle size ratio. For particle diameters larger than 1 μm, vapor transport dominates sintering kinetics at all neck to particle size ratios. These results are consistent with the Herring's scaling law (Table IV.3).

Lattice diffusion domains (l (nd) and l (d)) are sandwiched between the surface diffusion (s (nd)) and vapor transport (v (nd)) domains at temperatures higher than $\sim$ 1300 °C. As the particle size is decreased, the lattice diffusion domain moves towards lower temperatures and higher neck to particle size ratios. For particle diameters lower than 1 μm, lattice diffusion occurs preferentially from grain boundaries (l (d)). For particle diameter higher than 1 μm, however, lattice diffusion occurs essentially from the surface of the particles (l (nd)). This result is consistent with observations made in Appendix C.2 where lattice diffusion from grain boundary was found to be favored at higher neck to particle size ratios compared to lattice diffusion from the surface of the particles. Densification, which can only occur through lattice diffusion from grain boundary, is then likely to occur only for fine particles ($2a < 500$ nm) covered with silica as observed in Table IV.6 and in the literature [GR76, SH83, MW85, Cob90].

Figure IV.30: Effect of a particle size change on sintering kinetics of silicon particles covered with silica.

Silicon particles covered with silica - 2*a* = 100 nm

## Silicon particles covered with silica - 2*a* = 220 nm - VF powder
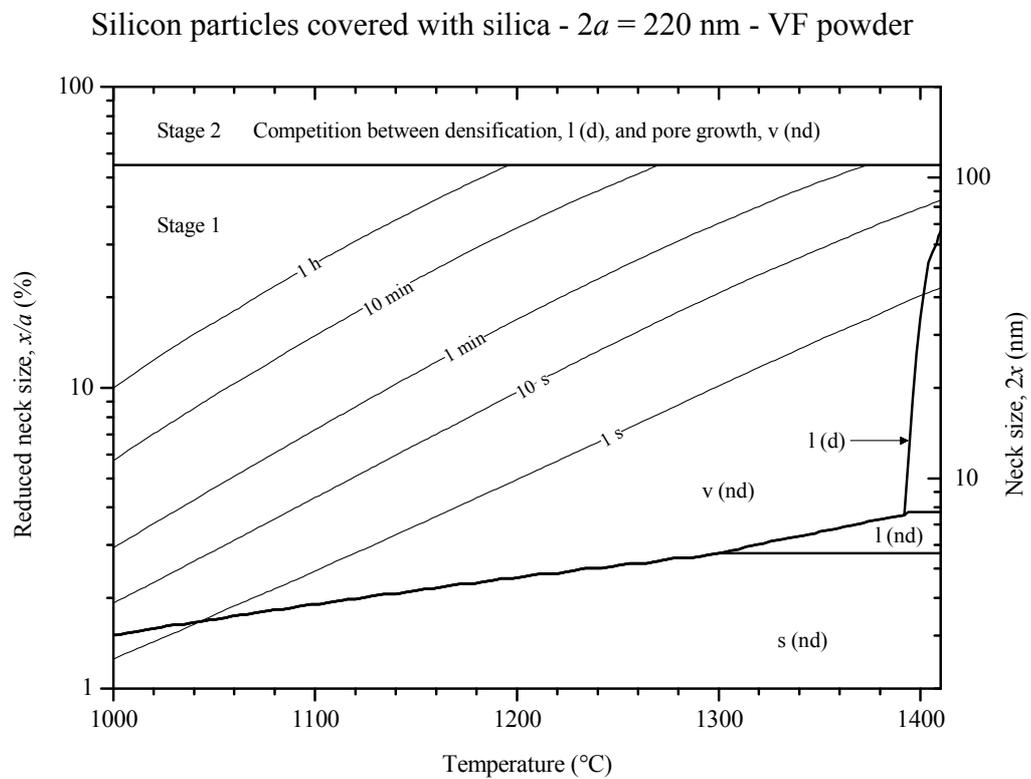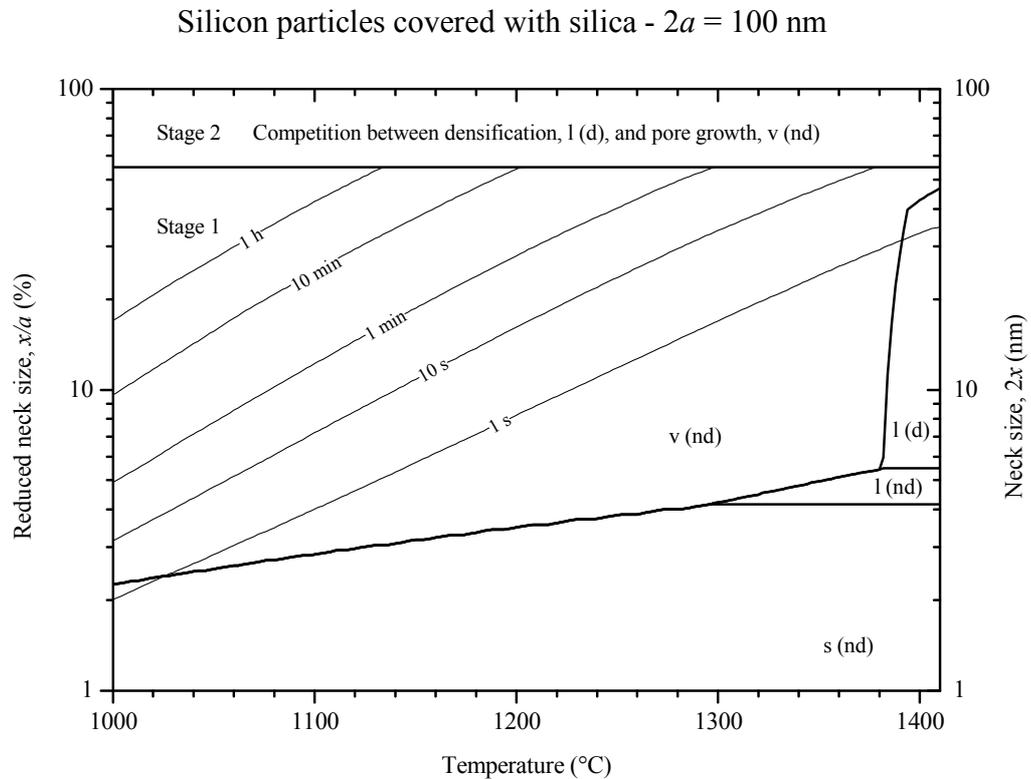
Figure IV.30: (following) Effect of a particle size change on sintering kinetics of silicon particles covered with silica.

Silicon particles covered with silica - $2a = 1\ \mu m$

Silicon particles covered with silica - $2a = 10\ \mu m$
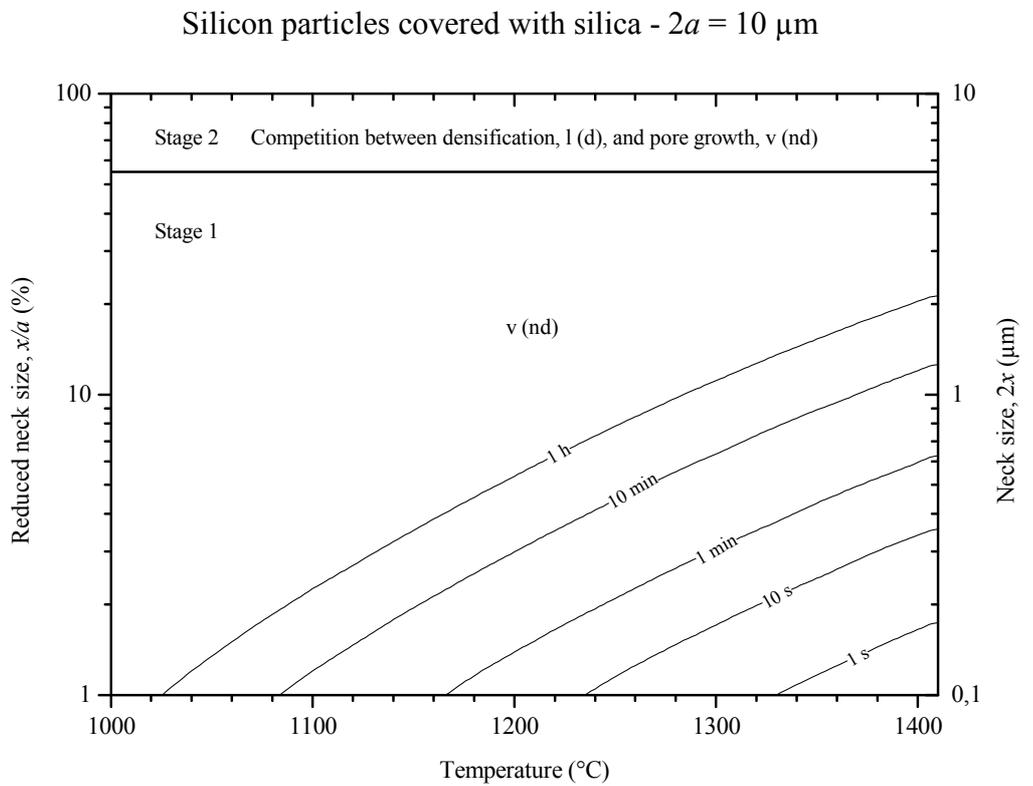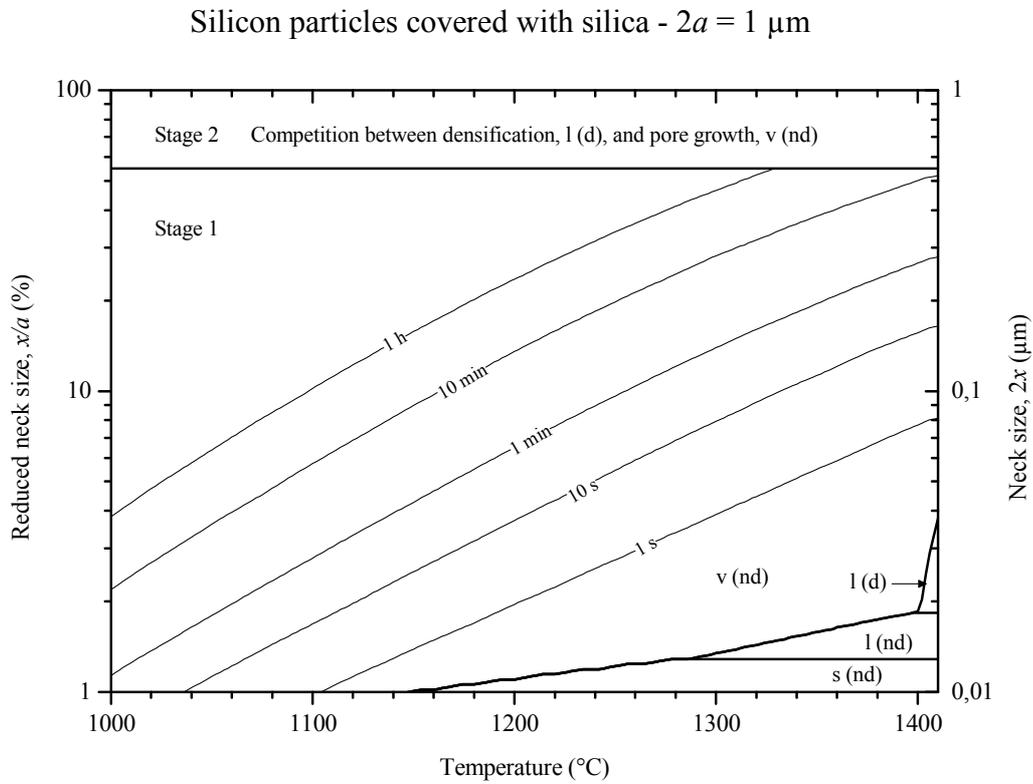
IV.5 **Conclusion and perspectives**

Sintering kinetics has been investigated theoretically and experimentally for pure silicon particles as well as for silicon particles covered with silica. The conclusion is that the silica layer stability strongly affects silicon sintering mechanisms.

Experimentally, the silica layer was stabilized by embedding the powder compact in a sacrificial silicon-silica powder bed. The silica layer at the particle surface prevents surface diffusion and then grain coarsening. This conclusion is confirmed by SEM observations and kinetics considerations. Densification kinetics was measured using dilatometric experiments on VF powders. The sintering behavior could be divided into two sequential stages that were clearly visible on the shrinkage curve and on the sample microstructures. These two stages were modeled using appropriate geometrical simplifications.

The initial stage corresponds to neck growth between particles. First, lattice diffusion and densification occur, although affected by the presence of silica. The activation energy for the diffusion of silicon atoms into silica [BSS+80] is much larger than the activation energy for the diffusion of silicon atoms into silicon [SUI07]. The densification rate of fine powders ($2a < 500$ nm) is then significantly affected and the measured apparent activation energy for densification is between the activation energy for the diffusion of silicon into silica and silicon into silicon. An effective lattice diffusion coefficient can be estimated from the diffusion paths of silicon atoms into the silicon particle and into the silica layer [Mun79]. This effective diffusion coefficient accounts for the measured densification kinetics, provided that the presence of thermal tensile stresses in the silica layer, which enhance lattice diffusion, is considered. Then, as the neck grows, vapor transport of silicon monoxide eventually dominates sintering kinetics and is responsible for a slowdown of the shrinkage rate. The first stage is then clearly identified as a first peak on the shrinkage rate curve during which only limited particle coarsening occurs.

As the curvature of the pores becomes uniform, sintering enters in the intermediate stage. The driving force for non-densifying mechanisms being nil, lattice diffusion from grain boundaries dominates sintering kinetics and the shrinkage rate accelerates once again. However, vapor transport still occurs between pores. Small pores shrink and larger ones grow. The average pore size and pore to pore distance progressively increases, lowering densification kinetics again. The second stage is then clearly identified as a second peak on the shrinkage rate curve during which pore and then grain growth occurs.

If the sample is sintered under reducing atmosphere, the silica layer is progressively reduced from the edge to the center of the compact. Once the reduction of the silica is initiated, defects or holes appear in the silica layer and sintering mechanisms are then activated. Lattice

diffusion allows small densification, while surface diffusion, which is much more rapid, induces large neck growth and finally particle coarsening. At the edge of the compact, in the reduced area, sintering enters rapidly in the second stage where grain coarsening impedes densification. At the center of the compact, in the non-reduced area, the silica layer is stabilized and densification occurs although affected by the presence of silica. Differential shrinkage occurs between the center and the edge of the compact. As the silica layer is reduced, the grain coarsening area increases to the detriment of the non-reduced area, densification is then progressively precluded and the shrinkage becomes "chaotic" before the complete reduction of the silica layer.

Eventually, silicon sintering behavior has been represented using Ashby's diagram approach and the effect of the particle size has been investigated. For pure silicon, surface diffusion dominates at all particle sizes. For silicon particles covered with silica, vapor transport dominates at large neck to particle size ratios and for large particles ($2a > 1$ µm). If the particle size is decreased, lattice diffusion and surface diffusion domains progressively grow towards vapor transport. Accordingly, lattice diffusion from grain boundary and then densification, is significant only if the particles are fines enough ($2a < 500$ nm). These conclusions are consistent with literature observations [GR76, SH83, MW85, Rob81, Cob90] and our interpretations.

- *In-situ control of the silicon monoxide pressure*

In order to control silicon densification and microstructure, the stability of the silica layer has to be monitored. From Chapter III, reaction (R_5) determines the stability of the silica layer:

$$Si_{(s)} + SiO_{2(s)} = 2SiO_{(g)} \tag{R_5}$$

Assuming that the silicon monoxide pressure can be controlled at the sample surrounding, the sintering behavior may be sketched as follow in a Temperature – Pressure – Sintering (TPS) diagram (Figure IV.31):

- If densification has to be favored, the silica layer must be stabilized and the effective silicon monoxide partial pressure at the sample surface should equal the silicon monoxide equilibrium partial pressure of reaction (R_5), $P_{SiO}^{R_5}$. Neck growth kinetics is then given in the upper part of the diagram which is equivalent to Figure IV.28.

- If grain growth has to be favored, the silica layer must be reduced and effective silicon monoxide partial pressure should be lower than $P_{SiO}^{R_5}$. Neck growth kinetics is then given in the lower part of the diagram which is equivalent to Figure IV.27.
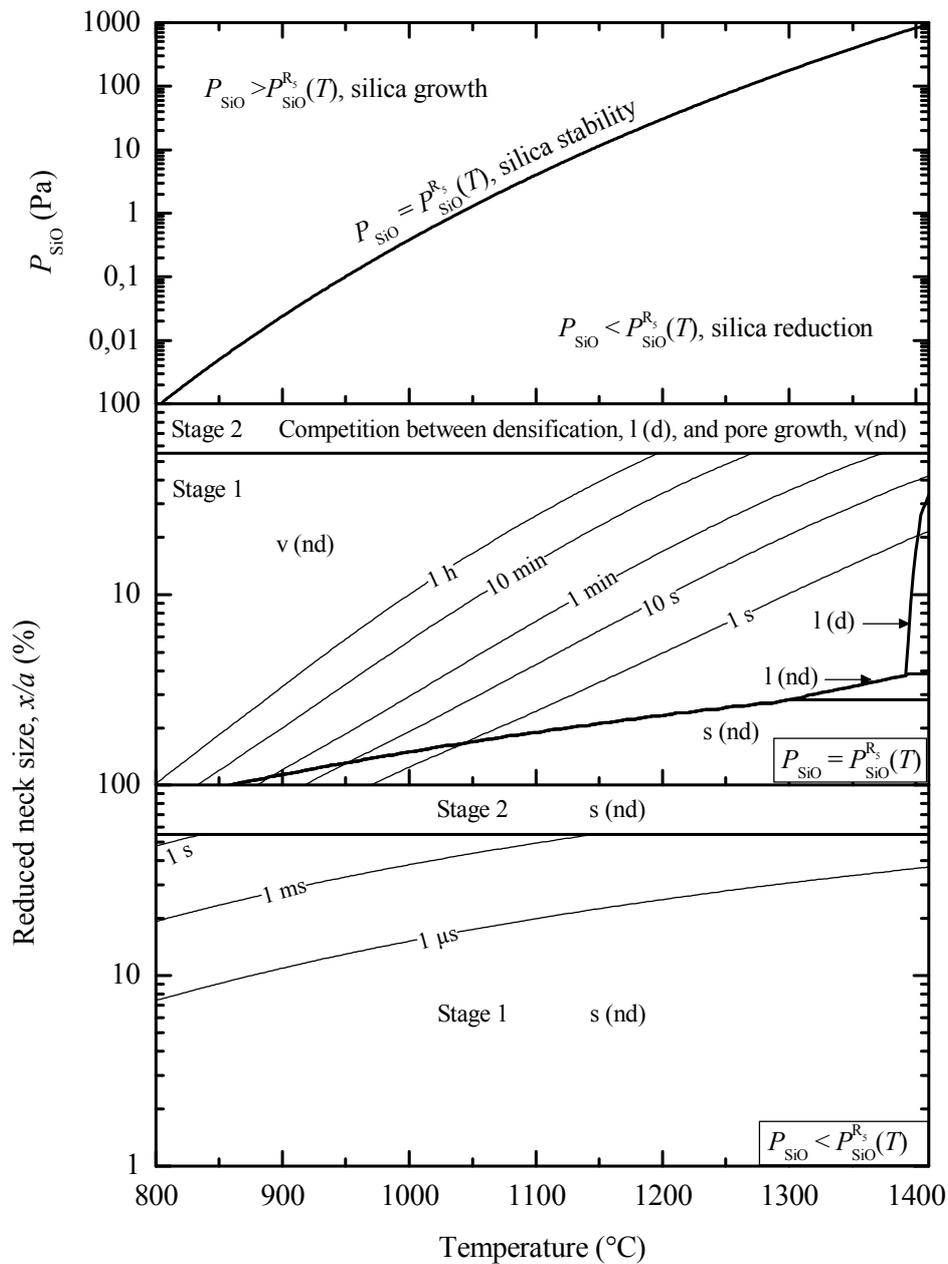
Figure IV.31: Temperature – Pressure – Sintering (TPS) diagram for silicon particles of 220 nm diameter (VF powder).

The first condition can be achieved using a sacrificial silicon-silica powder bed, while the second condition is fulfilled if the sample is sintered under reducing atmosphere. However, none of these solutions allows passing from one domain to another. An alternative solution

involves an in-situ control of the silicon monoxide pressure through the control of water pressure in the gas flux.

- *Decreasing the particle size*

For silicon particles covered with silica, as the particle size is decreased, lattice diffusion domain grows at the expense of vapor transport one. Using finer particles should then enhance densification in the late stage, assuming that the silica layer is still stable.

- *Increasing the initial density of the compact*

For silicon particles covered with silica, improving the initial density of the powder compact should accelerate the transition to the second stage of sintering and then limit the influence of vapor transport during the initial stage. This should also accelerate the pore closure and give rise to lower pore coarsening through vapor transport in the intermediate stage, eventually allowing a better densification.

Chapter V. Silicon sintering processes towards photovoltaic applications

S ilicon sintering mechanisms have now been identified. From Ashby's diagram, only fine silicon particles ($2a < 500$ nm), can experience densification. The final grain size of the material is then limited to few μm after sintering for 1 h at 1400 °C. However, as regards the application, large grain materials are sought. The sintering of thin layer bimodal powder compact is then addressed. The objective here is to find the better compromise between the sinterability and the required final microstructure and geometry for photovoltaic applications. Two solutions are investigated, either the introduction of coarse particles in a fine particle matrix or the sintering of two-layer materials.

During sintering of silicon, the issue relies on the stability of the silica layer that depends on the silicon monoxide vapor pressure at the silicon particle surface, as introduced in a TPS diagram (Figure IV.31). In this chapter, we provide one solution in order to experimentally implement such diagrams. This solution consists in a control of the water vapor pressure (or any other oxidizing specie with respect to silicon) in the incoming gas flux. The silicon monoxide pressure at the sample surface is then in situ controlled and the sample is either placed in the silica reduction domain ($P_{\mathrm{SiO}} < P_{\mathrm{SiO}}^{\mathrm{R_5}}$) or at the equilibrium condition ($P_{\mathrm{SiO}} = P_{\mathrm{SiO}}^{\mathrm{R_5}}$). This solution is attractive as regards the development of an industrial solution and is addressed in the second section of this chapter. Using TGA experiments, it will be shown that the reliability of the silicon monoxide pressure control strongly depends on the furnace geometry.

Finally, the Spark Plasma Sintering method is proposed in order to overcome the difficulties regarding silicon densification. This method is a derivative of the Hot Pressing process and usually allows higher processing rates and better densifications at lower temperatures.

V.1 **Sintering of bimodal thin layer compacts**

Silicon densification during sintering is limited by significant grain or pore coarsening. For pure silicon, grain coarsening is initiated from the very beginning of sintering through surface diffusion. For silicon particles covered with silica, pore coarsening is promoted at the end of the initial stage with the formation of large polycrystalline clusters.

The first conclusion is that full densification cannot be reached. But regarding the application, the realization of pore free wafers is not always necessary. Rather, large grain size materials are sought in order to reach suitable electronic properties or to allow the growth of high crystalline quality thin silicon layer through Chemical Vapor Deposition in a EpiWE process (Chapter I.3).

Sintering of VF powder compact (1400 °C for 1 h) actually leads to low grain size materials (few µm) and final densities less than 90 %. A compromise between densification and grain growth, is expected to be achieved through the sintering of bimodal powder compacts. The use of large particles allows higher green densities and would initiate grain growth, while fine particles are expected to favor densification.

V.1.1   Sample geometries and sintering conditions

The effect of particle size and of bimodal particle mixtures on the sintering behavior of thin powder compacts is then investigated. Two configurations of bimodal powder compacts were studied (Figure V.1):

i.   Bi-layer compact prepared by co-compaction of VF (80 vol%) and C (Coarse, 20 vol%) Si powders.
ii. One layer compact with various initial densities prepared from VF (Very Fine) and M (Medium) Si powder mixtures. Ratios of M in VF powders are 20, 40 and 60 vol%.
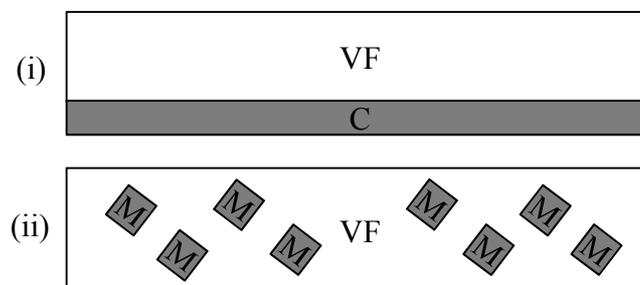
Figure V.1: Sample geometries, two-layer compact (i.) *and one layer bi-modal compact* (ii.).

The compacts were 800 µm thick and 10 mm diameter and were obtained using uniaxial compaction at 550 MPa.

Specimens were sintered in the TGA equipment under silicon monoxide equilibrium pressure ensured by embedding the compacts in a silicon-silica powder bed in order to maintain the silica layer at the particle surface and enhance densification. The heating rate was 40 °C min^{-1} and sintering temperature was 1400 °C for 1 h. After sintering, Archimedes' densities were measured and sample cross-sections were observed using SEM.

V.1.2   Experimental results

a)   Bilayer materials

After sintering, the global density was about 75% instead of 85% for powder VF. The two layers exhibited a strong differential shrinkage with two main consequences (Figure V.2):

- Mechanical stress at the VF/C interface resulting in strong bending distortions and delamination.

- Porosity gradient between the bottom and the top of the sample.

As for mono-modal compacts, layer VF did not reveal grain growth. Moreover, layer C did not initiate grain growth toward layer VF. An important observation is that coarse particles were initially polycrystalline as the grain size is much lower than the initial particle size.
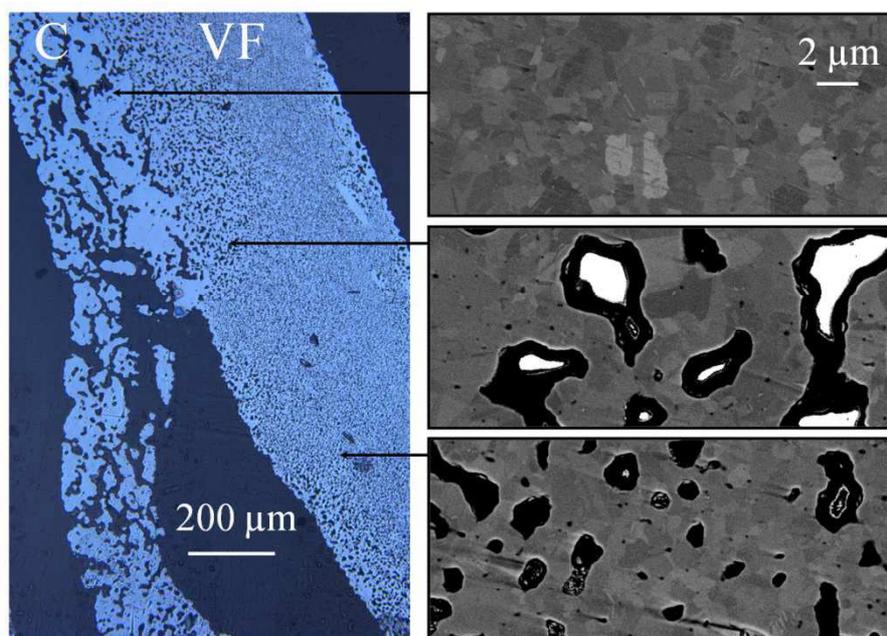
Figure V.2: Microstructure of the bi-layer compact VF/C after sintering at 1400 °C for 1 h under a silicon-silica powder bed.

b)   Bimodal powder compacts

As the volume percent of M powder increases, the green density increases and the final density decreases (Figure V.3) which is consistent with Ashby's diagram in Chapter IV.4.
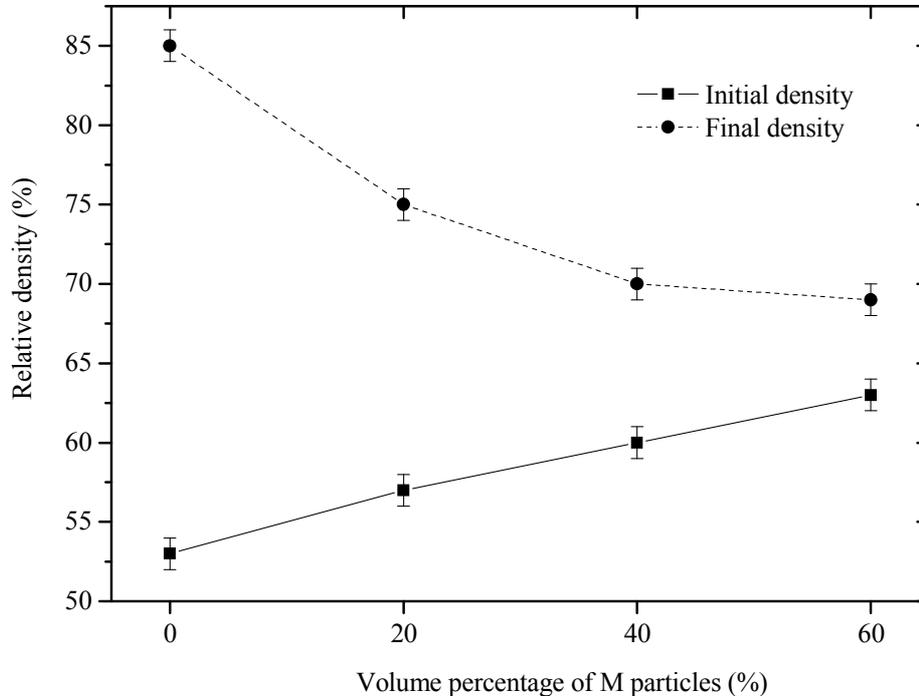
Figure V.3: Green and final densities evolution with vol% of M in VF powder compacts.

Sample microstructures in Figure V.4 were homogeneous and no bending was observed. M particles were monocrystallines which is *a priori* suitable to initiate grain growth. However, grain growth did not take place, may be because it was impeded by silica layer at the Si particle surfaces.

However, pore coarsening occurred during the intermediate stage of sintering through an Ostwald ripening process as described in Chapter IV.3.2. The presence of coarse particles in the compact actually enhances pore growth kinetics compared to mono-modal compacts of VF powders (Figure V.4, bottom) as the pore size distribution width (or particle size distribution width) is much larger. Although vapor transport kinetics is significant, there is no change in the order of magnitude of the cluster size as experimentally observed.
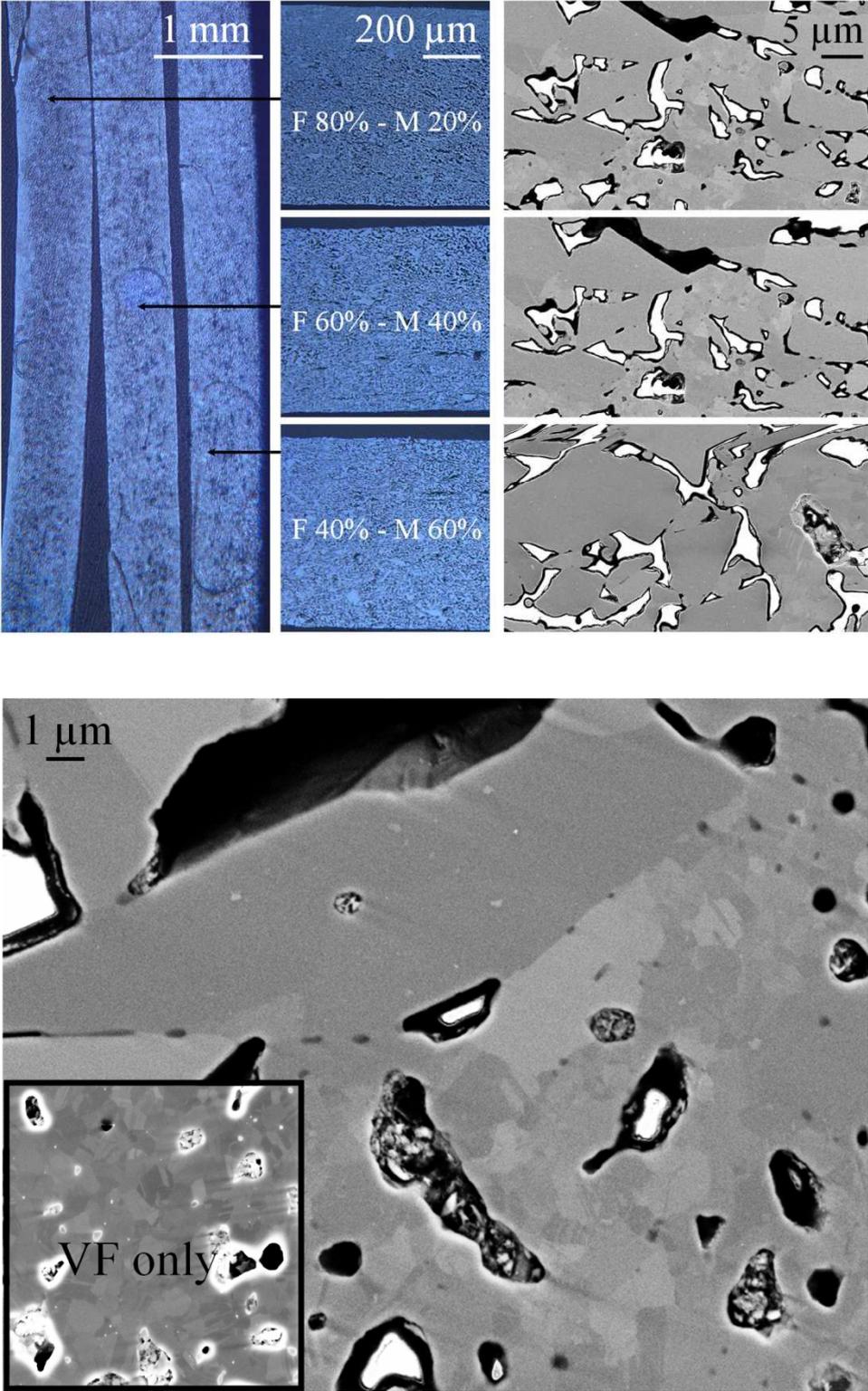
Figure V.4: Microstructure of (M + VF) mixtures after sintering at 1400 °C during 1 h under a silicon-silica powder bed (top) and microstructure at a M/VF grain boundary (bottom).

V.1.3   Conclusion

Sintering of bimodal and of two-layer fine/coarse Si powder mixtures was studied in order to find the better compromise between the sinterability and the required final microstructure for photovoltaic applications. The introduction of coarse particles in a fine particle matrix improves the green density but inhibits sintering densification and the final density is decreased. Sintering of two-layer materials results in delamination and porosity gradients due to differential shrinkage. In both cases, growth of large grains at the interface with the fine grain matrix is not observed, probably because the presence of silica at the grain boundary. An increase of the pore size is however noticed, probably due to vapor transport from larger pores to the fine ones. But the total mass transport is limited and this mechanism cannot change the order of magnitude of the particle size.

V.2 **Sintering under controlled water vapor partial pressure**

In Chapter III, the temperature at which the silica layer started to dissociate has been shown to depend on the water vapor partial pressure surrounding the sample. Under dry reducing atmosphere, the water vapor pressure surrounding the sample is 1 to 1.8 Pa and does not allow a stabilization of the silica layer at the silicon particle surface for temperatures higher than 1050 °C.

Basically, controlling the water vapor pressure at the sample surrounding would allow controlling the stability of the silica layer and therefore the sintering kinetics at any temperature. Here, we propose to control the water vapor pressure in the gas flux using a water vapor pressure controller specifically designed (Chapter II.2.4).

V.2.1 Design of the water vapor pressure controller

From oxidation kinetics studies in Chapter III and Appendix A, reaction (R_5) controls the stability of the silica layer at the silicon particle surface.

$$Si_{(s)} + SiO_{2(s)} = 2SiO_{(g)} \tag{R_5}$$

This reaction is a combination of two others, (R_1) and (R_2) that describes the oxidation of silicon under hydrogenated and humidified atmospheres.

If the supply of water from the atmosphere is lower than the silicon monoxide which could be produced through reaction (R_5), then the sample is under active oxidation (R_2):

$$Si_{(s)} + H_2O_{(g)} = SiO_{(g)} + H_{2(g)} \tag{R_2}$$

The amount of water molecules heating the silicon surface is not large enough to maintain the equilibrium partial pressure of silicon monoxide, $P_{SiO}^{R_5}$. The silica layer is reduced as equilibrium (R_5) is shifted to the right.

If the supply of water to the sample is higher than the silicon monoxide produced through reaction (R_5), then the sample is under passive oxidation (R_1):

$$Si_{(s)} + 2H_2O_{(g)} = SiO_{2(s)} + 2H_{2(g)} \tag{R_1}$$

The silicon monoxide pressure at the silicon-silica interface then overpass the equilibrium partial pressure of silicon monoxide, $P_{SiO}^{R_5}$. The silica layer grows as equilibrium (R_5) is shifted to the left.

Accordingly, in order to stabilize the silica layer, *i.e.* to prevent both growth and dissociation, the molar flux density of water, j_{H_2O}, should equal the silicon monoxide flux produced through reaction (R$_5$), j_{SiO} (Equation (V.1)).

$$j_{SiO} + j_{H_2O} = 0 \tag{V.1}$$

The atmosphere surrounding the sample (in vertical position) can still be approximated to a quasi stagnant gas mixture in Figure V.5. Assuming steady-state conditions for the diffusion (Appendix B.3.2), the molar flux density of a molecule j, can be derived in linear coordinates in Equation (V.2), where P_j is the partial pressure of the molecule, z the vertical position in the furnace tube, D_j^{mol} the molecular diffusion coefficient and R the gas constant. The temperature T, is assumed constant at the sample surroundings.
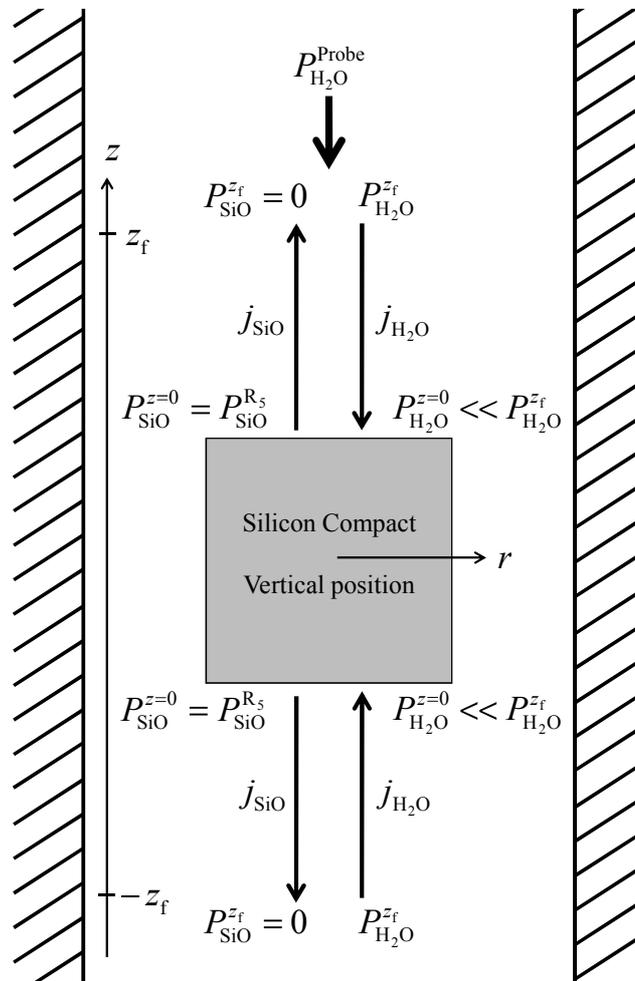
Figure V.5: Schematic representation of mass transport kinetics involved in the furnace tube during sintering under equilibrium conditions, $j_{SiO} + j_{H_2O} = 0$.

$$j_j = -\frac{D_j^{mol}}{RT} \frac{P_j^z - P_j^{z=0}}{z} \tag{V.2}$$

The molar flux density of silicon monoxide is expressed in Equation (V.3) assuming the following boundary conditions:

- $P_{SiO}^{z=0} = P_{SiO}^{R_5}$ as the silica layer ought to be stabilized at the particle surfaces.

- $P_{SiO}^{z_f} = 0$ as the silicon monoxide condensate at the z_f position.

$$j_{SiO} = \frac{D_{SiO}^{mol}}{RT} \frac{P_{SiO}^{R_5}}{z_f} \tag{V.3}$$

The molar flux density of water is expressed in Equation (V.4) assuming $P_{H_2O}^{z=0} \ll P_{H_2O}^{z_f}$ since the water is entirely consumed through reaction (R_2) at the sample surface.

$$j_{H_2O} = -\frac{D_{H_2O}^{mol}}{RT} \frac{P_{H_2O}^{z_f}}{z_f} \tag{V.4}$$

The molar flux density of water in one direction corresponds to half the amount of water supplied by the water vapor pressure controller in Equation (V.5), where Q is the volumic gas flux, S^{tube} is the section of the furnace tube, $P_{H_2O}^{Probe}$ is the water vapor pressure at the probe position (in the incoming gas flux), and T° the room temperature.

$$j_{H_2O} = \frac{1}{2} j_{H_2O}^{Probe} = -\frac{Q}{2 S^{tube} RT°} P_{H_2O}^{Probe} \tag{V.5}$$

The water vapor pressure to be controlled, $P_{H_2O}^{Probe*}$, such as to stabilize the silica layer at the transition temperature, T^*, can be estimated from Equations (V.1), (V.3) and (V.5) in Equation (V.6).

$$P_{H_2O}^{Probe*} = 2 \frac{D_{SiO}^{mol}(T^*) S^{tube}}{Q z_f} \frac{T°}{T^*} P_{SiO}^{R_5}(T^*) \tag{V.6}$$

$P_{H_2O}^{Probe*}$ corresponds to a water vapor pressure at the sample surroundings, $P_{H_2O}^{z_f*}$, calculated from Equations (V.1), (V.3) and (V.4) in Equation (V.7), as done in the pioneer work of Wagner [Wag58].

$$P_{H_2O}^{z_f*} = \frac{D_{SiO}^{mol}\left(T^*\right)}{D_{H_2O}^{mol}\left(T^*\right)} P_{SiO}^{R_5}\left(T^*\right) \tag{V.7}$$

Depending on the temperature at which the sample is to be sintered, T^*, the water vapor pressure to be controlled to stabilize the silica layer, $P_{H_2O}^{Probe*}$, is plotted in Figure V.6. Using $z_f = 40$ mm, as estimated from the model derived in Chapter III, sintering temperatures of 1100 °C to 1350 °C corresponds to water vapor pressures at the probe position of 100 to 2000 Pa.

Using Finite Element Methods (FEM, Appendix B.3), the matter transport equation (involving the diffusive as well as the convective component of the flux), has been solved for the silicon monoxide and water molecules assuming the same boundary conditions. The value of T^* ensuring vapor transport balance, as expressed by Equation (V.1), has been estimated for several water vapor pressure in the incoming gas flux, $P_{H_2O}^{Probe}$ (Figure V.6).
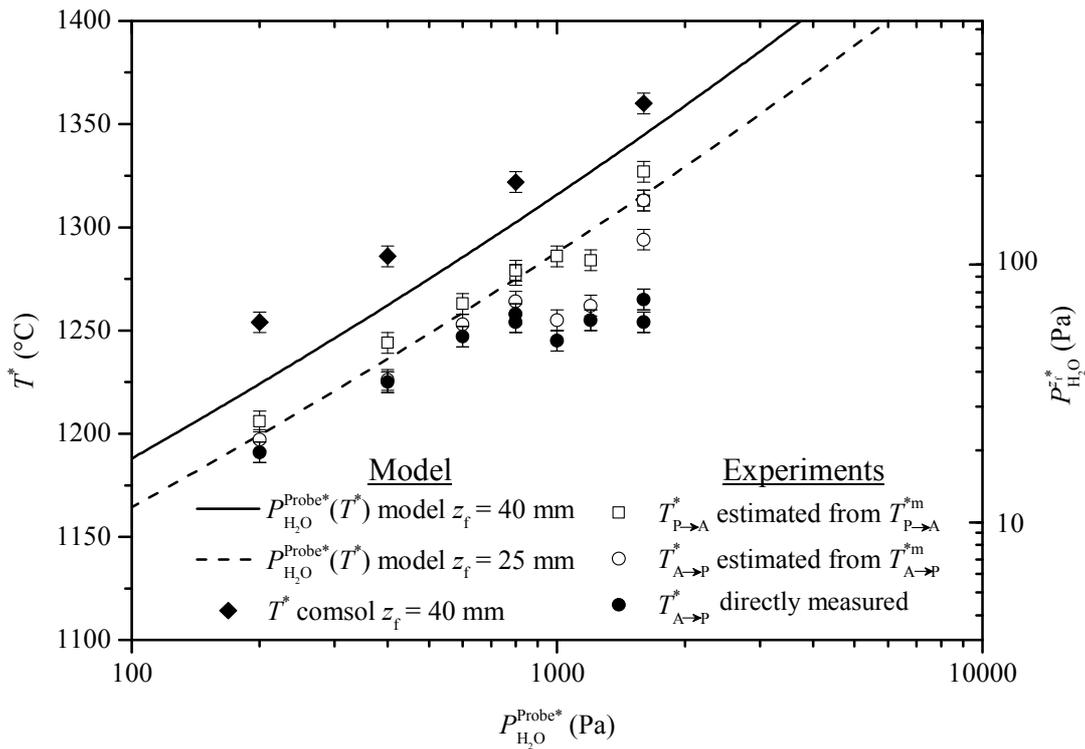
Figure V.6: Model and experimental transition temperatures, T^*, for several water vapor pressure in the incoming gas flux, $P_{H_2O}^{Probe}$.

V.2.2 Calibration of the water vapor pressure controller

a) Experimental approach

Experiments are realized in the TGA apparatus. The water vapor pressure in the incoming gas flux is controlled using the water vapor pressure controller introduced in Chapter II.2.4. Mass loss rates for VF powder compacts sintered under dry and humidified atmospheres (200, 400, 800 and 1600 Pa) are given in Figure V.7. Samples were heated along the same temperature cycle which is described below (Figure V.7 (a)):

- Heating to 1350 °C at 40 °C min^{-1}. A rapid heating rate was chosen such as to limit the formation of silica at the sample surface which might delay the beginning of silica reduction, *i.e.* the passive active transition temperature, $T^{*}_{P \rightarrow A}$.

- Holding time of 1h30 at 1350 °C, in order to remove the silica covering the silicon particles at the sample surface.

- Cooling to 1100 °C at 2.5 °C min^{-1}. A slow cooling rate was chosen to better identify the temperature at which silica starts to grow again at the sample surface, *i.e.* the active to passive transition temperature, $T^{*}_{A \rightarrow P}$.

According to observations made in Chapter III, the passive to active, $T^{*}_{P \rightarrow A}$, and active to passive, $T^{*}_{A \rightarrow P}$, transition temperatures should be equal and controlled by the equilibrium (R$_5$).

b) Experimental results

Four steps are identified for all investigated water vapor pressures (Figure V.7 (b)):

i. During heating, samples experience a mass gain attributed to passive oxidation (R$_1$).

ii. Then, still during heating, all samples start to experience the passive to active transition. The mass loss rate becomes nil at a temperature $T^{*m}_{P \rightarrow A}$ depending on the water vapor pressure. The observed mass loss corresponds to the reduction of the silica according to reaction (R$_5$). As the water vapor pressure is increased, $T^{*m}_{P \rightarrow A}$ is also increased (Figure V.7 (c)).

iii. During the holding at 1350 °C, the mass loss rate reaches a plateau and is related to the continuous active oxidation of silicon (R$_2$), as the silica has been removed.

iv. During cooling, the rate of mass loss suddenly takes-off and the active to passive transition occurs. This moment corresponds to the active to passive transition, $T^{*}_{A \rightarrow P}$, since the silica, which eventually becomes thermodynamically stable, starts to grow again at the sample surface according to reaction (R$_1$). Then the sample mass loss rate becomes nil at a temperature $T^{*m}_{A \rightarrow P}$. As the water vapor pressure is increased, $T^{*}_{A \rightarrow P}$ as well as $T^{*m}_{A \rightarrow P}$ increase (Figure V.7 (d)).
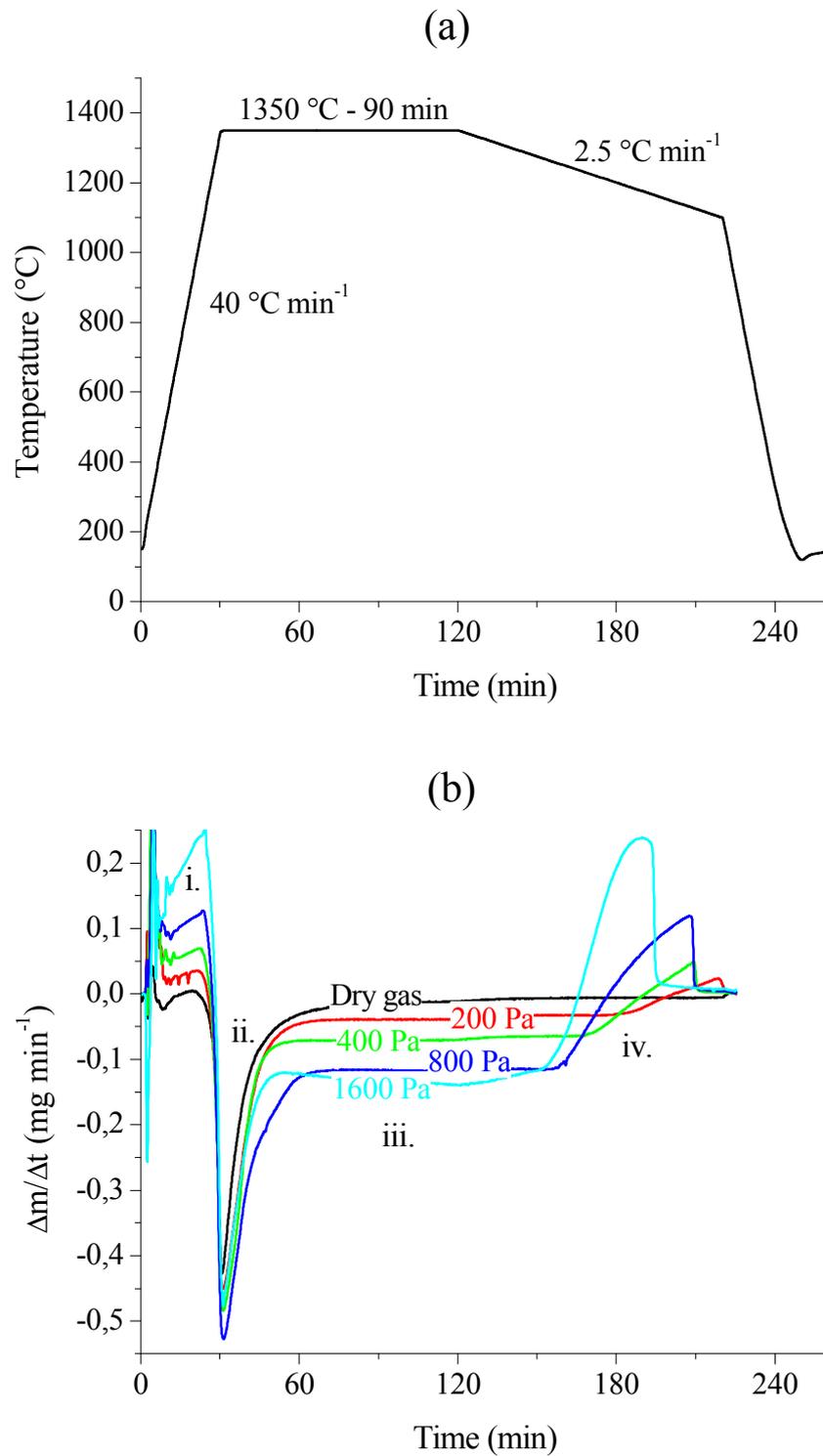
Figure V.7: TGA curves of VF powder compacts under 2 l h^{-1} He-4mol.% H$_2$ atmosphere, dry or humidified (P$_{H_2O}^{Probe}$ = 200, 400, 800 and 1600 Pa). (a) Thermal cycle. (b) Sample mass variation rate during the whole experiment.
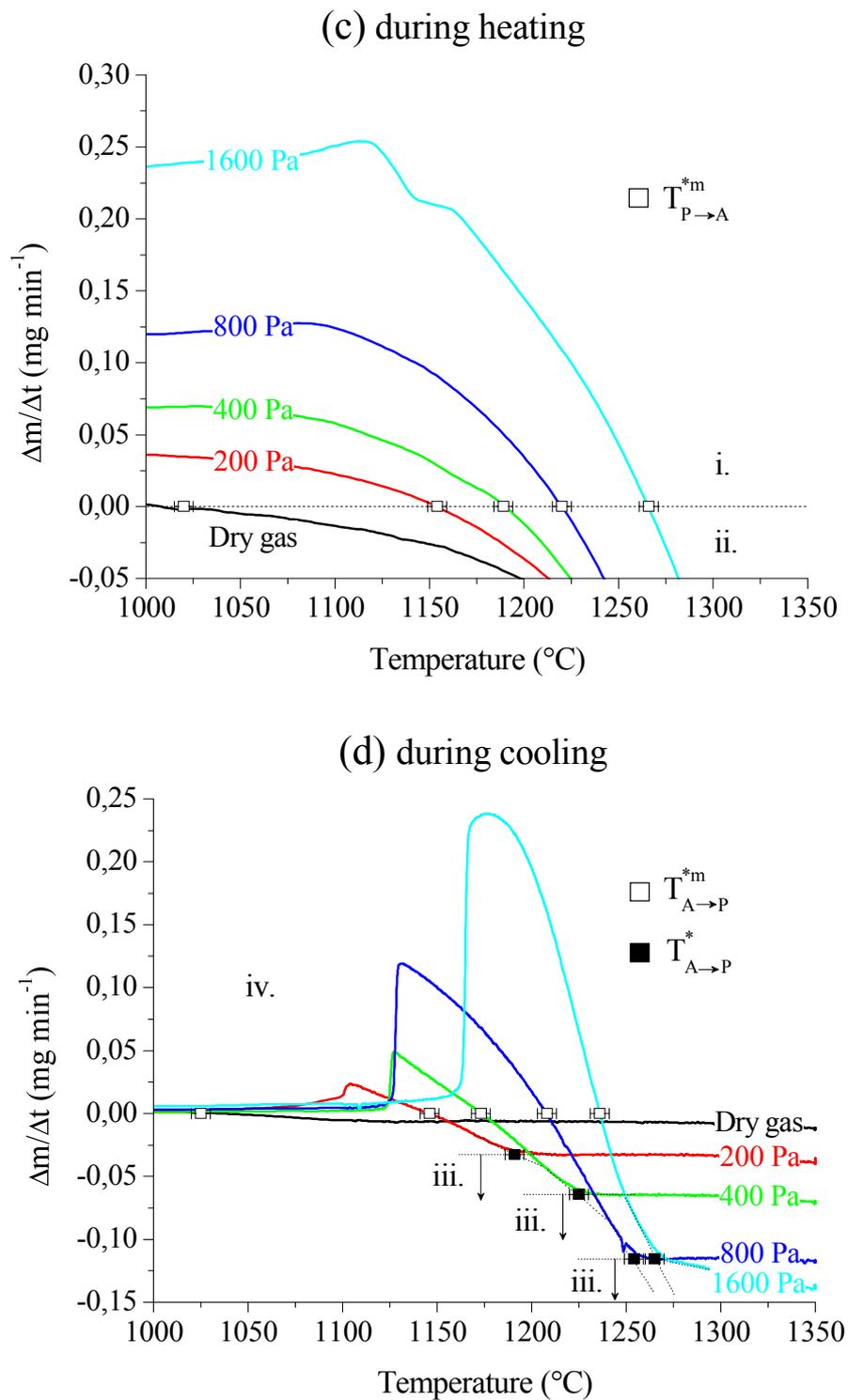
Figure V.7 (following): TGA curves of VF powder compacts under 2 l h⁻¹ He-4mol.% H₂ atmosphere, dry or humidified ($P_{H_2O}^{Probe}$ = 200, 400, 800 and 1600 Pa). (c) Mass variation rate during heating (passive to active transition). (d) Mass loss rate during cooling (active to passive transition).

The temperature at which the mass loss rate is nil, T^{*m}, both during heating (P-A) and cooling (A-P), corresponds to a mass flux equality between $H_2O_{(g)}$ arrival and $SiO_{(g)}$ departure (Equation (V.8)).

$$M_{SiO}\, j_{SiO} + M_O\, j_{H_2O} = 0 \qquad\qquad\qquad\qquad (V.8)$$

At T^{*m}, the molar flux of silicon monoxide is lower than the molar flux of water, as $M_{SiO} > M_O$. Silica is then growing on silicon particles at the sample surface and Equation (V.3) is valid. Using Equations (V.3), (V.5) and (V.8), $P_{H_2O}^{Probe*}$ can be estimated from T^{*m} in Equation (V.9).

$$P_{H_2O}^{Probe*} = 2\frac{M_{SiO}}{M_O}\frac{D_{SiO}^{mol}\!\left(T^{*m}\right)S^{tube}}{Q\,z_f}\frac{T^{\circ}}{T^{*m}}\,P_{SiO}^{R_5}\!\left(T^{*m}\right) \qquad\qquad (V.9)$$

Equation (V.10) is derived using Equations (V.6) and (V.9) since the molecular diffusion coefficient of $SiO_{(g)}$ is almost constant within the temperature range $(T^{*m};T^{*})$.

$$P_{SiO}^{R_5}\!\left(T^{*}\right) = \frac{M_{SiO}}{M_O}\frac{D_{SiO}^{mol}\!\left(T^{*m}\right)}{D_{SiO}^{mol}\!\left(T^{*}\right)}\frac{T^{*}}{T^{*m}}\,P_{SiO}^{R_5}\!\left(T^{*m}\right) \approx \frac{M_{SiO}}{M_O}\,P_{SiO}^{R_5}\!\left(T^{*m}\right) \qquad (V.10)$$

Temperatures at which the mass loss rate is nil, T^{*m}, are converted in transition temperature at which the molar fluxes of silicon monoxide and water are equal, T^{*}, using Equation (V.10). This is done for the passive to active (heating, Figure V.7 (c)) as well as the active to passive (cooling, Figure V.7 (d)) transitions. These temperatures are reported in Figure V.6 and so called "T^{*} estimated from T^{*m}". During cooling the transition temperatures, T^{*}, can be directly estimated from the moment where the rates of mass loss suddenly collapse (Figure V.7 (d)). These temperatures are then simply called $T_{A\to P}^{*}$ and are reported in Figure V.6.

c)   Interpretation of the results

First, the measured transition temperatures, are lower than those predicted from Equation (V.6) or FEM simulations, using $z_f = 40$ mm. A lower value of z_f (25 mm), leads to a very good fit of the experimental data, as if the silicon monoxide would condensate closer to the sample. This shift of the z_f value compared to experiments carried out under dry atmospheres is not clearly understood. We can first allege the model simplicity to explain this discrepancy. We can also propose that the condensate of silicon monoxide, partly made of silicon, consumes some water molecules before they can reach the sample. The water vapor pressure at the sample surroundings, $P_{H_2O}^{z_f}$, would be then lower than expected. Otherwise

speaking, the water vapor pressure to be imposed in the incoming flux ought to be larger than the value given in Equation (V.6), as experimentally observed in Figure V.6.

Measured passive to active transition temperatures, $T^*_{P \to A}$, are slightly larger than the active to passive ones $T^*_{A \to P}$. During cooling (iv.), the active to passive transition actually requires the germination of silica on a bare silicon compact surface through reaction (R_1). Supersaturation of $SiO_{(g)}$ and $H_2O_{(g)}$ may be necessary to activate the nucleation and silica growth, thus shifting the active to passive transition to lower temperatures. Accordingly the measured passive to active transition temperatures would give a better estimation of T^*. During active oxidation (iii.), (R_2) is assumed to be controlled by the diffusion of water vapor to the powder compact and the rate of weight loss should increase when increasing $P^{Probe}_{H_2O}$ as observed for experimentations carried out under water vapor pressures less than 800 Pa. However, experiments realized under higher water vapor pressures deviates from this prediction:

- Measured active to passive transition temperatures, $T^*_{A \to P}$, are lower than the predicted ones (Figure V.6).

- Mass loss rates measured during step (iii.) do not increase (Figure V.7 (c) and (d)).

Nucleation of silica along reaction (R_1) may occur in the furnace tube during step (iii.) and would decrease the water vapor pressure at the sample surroundings and explain these observations. At high temperatures and vapor pressures, $SiO_{(g)}$ and $H_2O_{(g)}$ activities are higher, and deviation from the model would be more important, as observed in Figure V.6.

Model and experiments are then consistent, at least when looking at the sample behavior during the passive to active transition, $T^{*m}_{P \to A}$. The water probe vapor pressure to be controlled, $P^{Probe*}_{H_2O}$, in order to stabilize the silica layer at a temperature, T^*, can then be estimated from Equation (V.6) using $z_f = 25$ mm.

V.2.3   Sintering under control water vapor pressure

a)   Experimental approach

The experimental approach is summarized in a TPS diagram in Figure V.8. First, the water vapor pressure to be controlled in order to stabilize the silica layer, $P^{Probe*}_{H_2O}$, is given as a function of the temperature. Then, two diagrams are plotted depending on the probe water vapor pressure:

- If the effective partial pressure of water is equal to $P^{Probe*}_{H_2O}$, the silica layer is stabilized. Neck growth kinetics is given in the upper part of the diagram from

calculations made in Chapter IV.5. Surface diffusion and lattice diffusion dominate sintering kinetics in the early stage of sintering depending on the temperature while vapor transport dominates in the late stage. Lattice diffusion domains (l (nd) and l (d)) are sandwiched between the surface diffusion (s (nd)) and vapor transport (v (nd)) domains at temperatures higher than $\sim 1300 \, °C$.

- If the effective partial pressure of water is lower than $P_{H_2O}^{Probe^*}$, the silica layer is reduced. Neck growth kinetics is given in the lower part of the diagram from calculations made in Chapter IV.5 and surface diffusion controls the neck growth rate at all temperatures and neck to particle sizes.

For a given sintering temperature, T^s, the water vapor pressure in the incoming gas is chosen:

- Equal to $P_{H_2O}^{Probe^*}(T^* = T^s)$, such as to keep the silica layer stable. A rapid heating of $40 \, °C \, min^{-1}$ is chosen in order to reach the equilibrium state rapidly. Such rapid heating rate should also favor lattice diffusion and densification against surface diffusion and vapor transport. Sintering temperatures, T^s, for the samples a^*, b^* and c^* are 1225, 1260 and 1315 °C (3 h dwelling time), corresponding to water vapor pressures, $P_{H_2O}^{Probe^*}$, of 400, 800 and 1600 Pa, respectively.

- As low as possible, under dry reducing atmosphere, for the same sintering temperatures ($T^s = 1225$, 1260 and 1315 °C - 3 h dwelling time) with a high heating rate ($40 \, °C \, min^{-1}$), such as to favor silica reduction and coarsening through surface diffusion. These conditions correspond to samples a, b and c respectively.

b)   Results

Samples microstructures and densities are given in Figure V.9:

- Samples a^*, b^* and c^* show a fine porous microstructure from 200 nm (close to the VF particle size) for the sample sintered at 1225 °C to approximately 500 nm for the sample sintered at 1315 °C. These microstructures were typically observed when the silica was stabilized in Chapter IV.

- Samples a, b and c microstructures are about ten times coarser than the microstructures of samples a^*, b^* and c^*. Large grains ($\sim 1 \, \mu m$), highly twinned, are surrounded by very coarse pores (5-10 μm). These microstructures were previously observed in our investigations under reducing atmosphere in which surface diffusion occurred after the silica layer reduction.
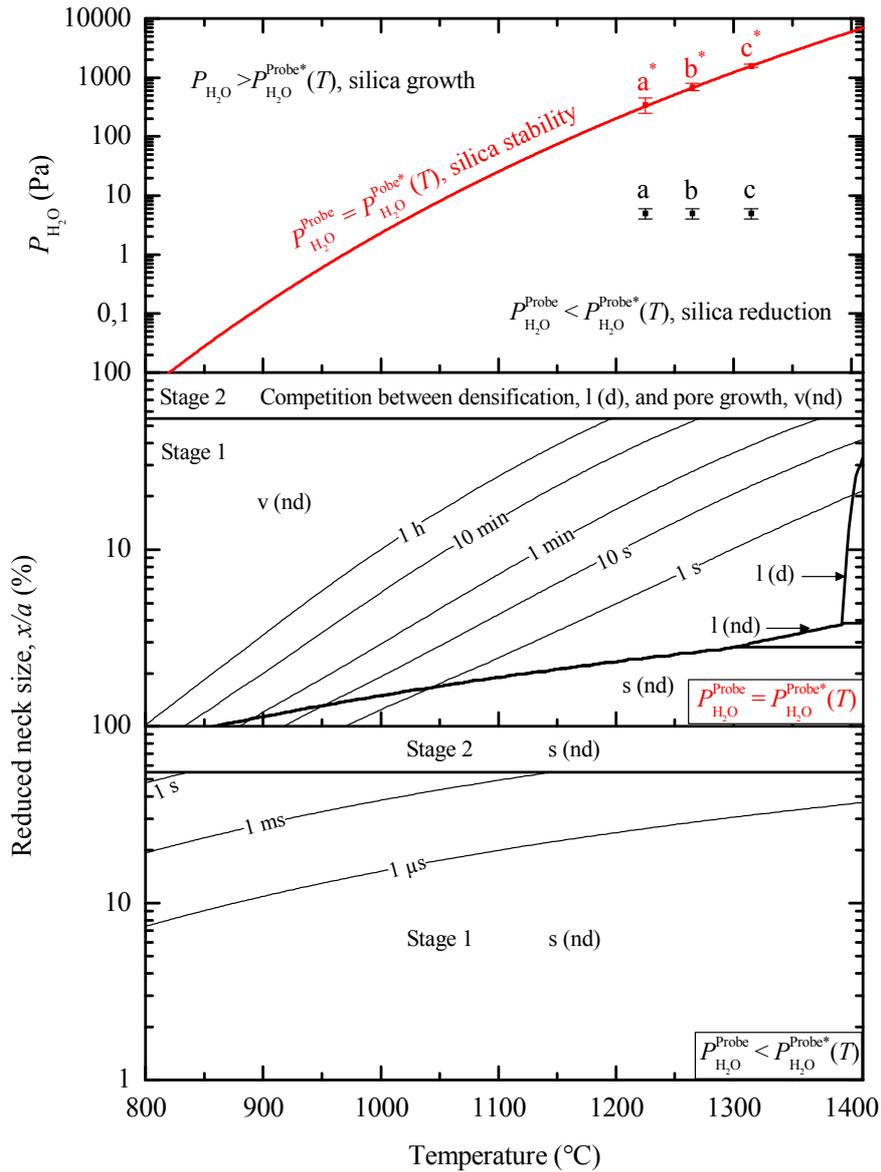
Figure V.8: Temperature - (water vapor) Pressure - Sintering rate (TPS) diagram. Lines of constant sintering time are calculated for particles with a diameter 2a = 220 nm. At the top of the diagram, the probe water vapor pressure at which the silica layer ought to be stabilized, $P_{H_2O}^{Probe*}$, is given with respect to the temperature. If the probe partial pressure of water is equal to $P_{H_2O}^{Probe*}$, the silica layer is stabilized. Neck growth kinetics is given in the section $P_{H_2O}^{Probe} = P_{H_2O}^{Probe*}$ of the diagram. If the effective partial pressure of water is lower than $P_{H_2O}^{Probe*}$, the silica layer is reduced. Neck growth kinetics is given in the section $P_{H_2O}^{Probe} < P_{H_2O}^{Probe*}$ of the diagram. At 1225, 1260 and 1315 °C, samples a^*, b^* and c^*, are respectively sintered at the corresponding critical water vapor pressures, 400, 800 and 1600 Pa and refers to the $P_{H_2O}^{Probe} = P_{H_2O}^{Probe*}$ section of the diagram, while samples a, b and c are sintered in the silica reduction domain and refers to the section $P_{H_2O}^{Probe} < P_{H_2O}^{Probe*}$ of the diagram.
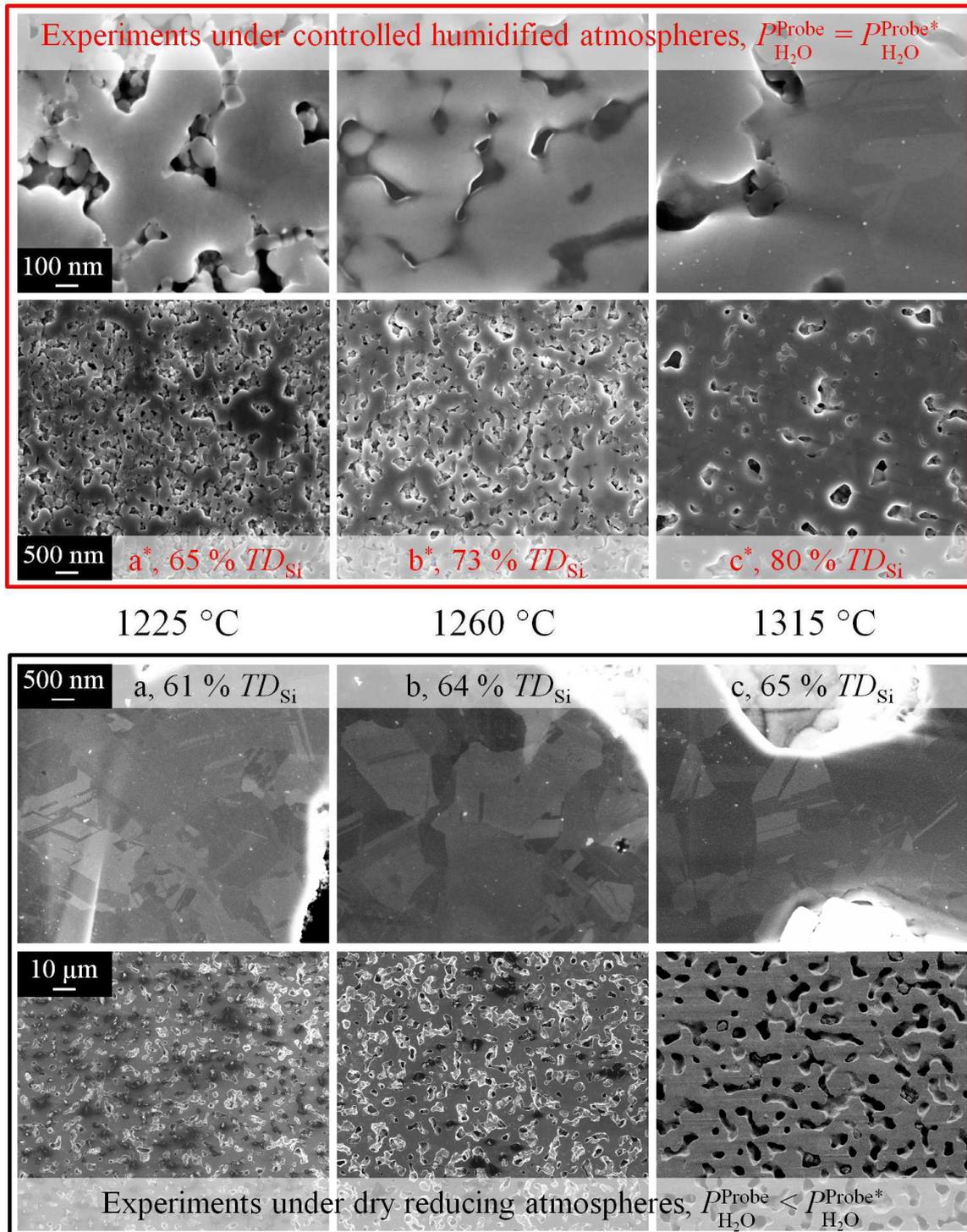
Figure V.9: Red frame: microstructures and Archimedes' densities of samples a*, b* *and* c*, *sintered under controlled humidified atmospheres for 3 h at respectively 1125 °C, 1260 °C and 1315 °C. Black frame: microstructures and Archimedes' densities of samples* a, b *and* c *sintered at the same temperatures but under dry reducing atmospheres. The heating rate is 40 °C min⁻¹ and the carrier gas is 2 l h⁻¹ He-4mol.% H_2 flow.*

Stabilizing the silica layer at high temperatures (> 1300 °C) inhibited surface diffusion and grain coarsening to enable neck growth through lattice diffusion. Accordingly, samples a^*, b^* and c^* relative densities are higher than samples a, b and c densities. As the temperature is increased, the relative density increases which is consistent with Figure V.8 where the lattice diffusion domain expanses at higher temperature when the silica layer is stabilized. Sample c^* density is 80 % TD_{Si} while sample c is only 65% TD_{Si}, showing that the control of the silica layer enables a wide control of the grain size and densification.

However, full densification is not observed (sample c^*) because of neck growth through vapor transport occurring at the end of the first stage (Figure V.8). Then vapor transport continues during the intermediate stage of sintering and is responsible for Ostwald ripening of the pores as described in Chapter IV.3.2. The silica layer also retards densification from lattice diffusion as previously discussed in Chapter IV.2.

V.2.4 Discussion on the control of the water vapor pressure

Controlling the water vapor pressure allows a direct control of the silicon monoxide pressure at the sample surrounding. This solution is interesting as the silica layer can be real time controlled. For example, in order to improve the densification the sample might first be placed in the silica stability domain. Then, as regards the electronic properties of the material the water vapor pressure may be decreased (or the temperature increased for the same water vapor pressure), in order to eliminate silica and increase the grain size through surface diffusion.

However, the control of the water vapor pressure is not as suited as it seems. Increasing the water vapor pressure leads to a concomitant oxidation of the sample and to important material losses. Indeed, for every water molecule reaching the sample, a silicon atom is lost in the form of silicon monoxide. Actually, the experimental mass loss in Equation (V.11), is directly related to the flux of water (Equation (V.6)) coming to the sample and to the duration, t^* (h), of the sintering treatment during which the silica layer is stabilized, *i.e.* during which the water vapor pressure is maintained to the equilibrium value, $P_{H_2O}^{Probe} = P_{H_2O}^{Probe*}$.

$$\Delta m_{Si} = -2S^{tube} \times M_{Si} \times t^* \times \left| j_{H_2O}^* \right| = -M_{Si} \times t^* \frac{Q}{RT^\circ} P_{H_2O}^{Probe*}$$

$$\Delta m_{Si} = -2 \frac{M_{Si} S^{tube} t^* D_{SiO}^{mol}(T^*)}{RT^* z_f} P_{SiO}^{R_5}(T^*)$$

(V.11)

As the sintering temperature, $T^s = T^*$ is increased, the water vapor pressure, $P_{H_2O}^{Probe*}$, must be increased to stabilize the silica layer. In Figure V.10, mass losses are plotted as a function of the sintering temperature for a typical sintering time, t^*, of 3 h and a sample mass of 400 mg.

For temperatures higher than 1350 °C, and for the diffusion length $z_f = 25$ mm, the mass loss exceeds 50 %. Actually, the control of the diffusion length, z_f, which is directly related to the furnace thermal profile, seems more appropriate than the control of the water vapor pressure. Typically, if the homogeneous temperature range is increased, supersaturation and accordingly condensation of silicon monoxide occurs further from the sample and z_f increases. z_f being increased, the flux of water and silicon monoxide decreases and the material loss is less important.
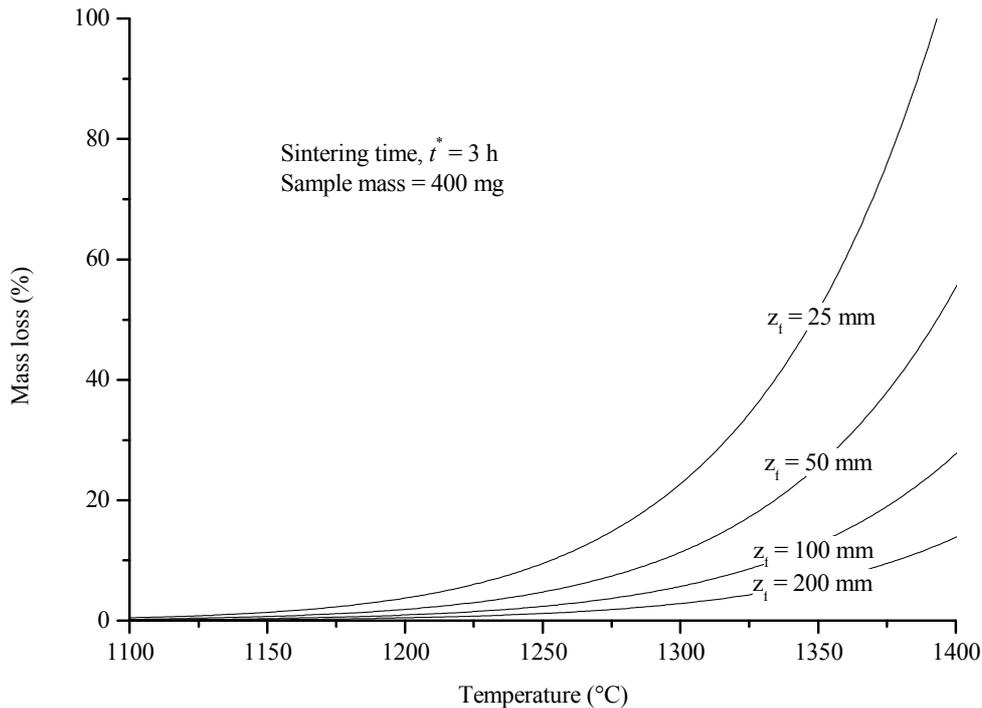
Figure V.10: Mass losses for samples sintered under equilibrium conditions, $j_{SiO} + j_{H_2O} = 0$, *for diffusion length between 25 and 200 mm.*

Mass transport kinetics strongly depends on the furnace thermal profile. Sintering treatments were also conducted under controlled water vapor partial pressure in the dilatometer ($P_{H_2O}^{Probe}$ = 400 Pa, $T^s = 1250$ °C $> T^*$). Although the dilatometer and TGA furnaces are similarly designed (Chapter II.2), mass transport kinetics are significantly different. Both samples have inhomogeneous microstructures as $T^s > T^*$ (Figure V.11). In both compacts, part of the silica had been reduced but the reaction front position (r_r) moved further in the compact sintered in the dilatometer than in the compact sintered in the TGA. Actually, it is assumed that the homogeneous temperature zone of the dilatometer is not as large as in the TGA. The diffusion length, z_f, in the dilatometer is then smaller than in the TGA and the flux of silicon monoxide is larger, leading to higher amounts of reduced silica. For a given temperature, the sample

must be sintered to higher water vapor pressure in the dilatometer in order to stabilize the silica layer.

$$P_{H_2O}^{Probe} = 400 \text{ Pa}, T^s = 1250 \text{ °C}$$

TGA   Dilatometer

$$r_r^{TGA} > r_r^{Dilatometer}$$
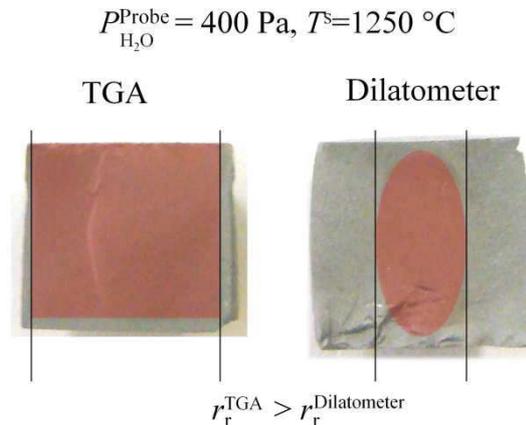
Figure V.11: Sample sintered at 1250 °C for 3 h with $P_{H_2O}^{Probe}$ = 400 Pa. Left: sample sintered in the TGA. Right: sample sintered in the dilatometer.

V.2.5 Conclusion

Experiments under controlled humidified atmospheres have been performed. A water vapor pressure controller was designed in order to fit our experimental requirements. In order to stabilize the silica layer, the incoming flux of water must equal the flux of silicon monoxide produced by the sample. Two parameters define the water vapor pressure to be controlled:

- The sintering temperature. As the sintering temperature is increased, the flux of silicon monoxide produced by the sample is increased as $P_{SiO}^{R_5}$ increases. The flux of water to be applied in order to counter act the silicon monoxide departure must then be increased.

- The furnace geometry. Matter transport kinetics strongly depends on the furnace tube section (area of the flux) as well as on the diffusion length of the species, z_f, which corresponds to the position where silicon monoxide condensates. As z_f is increased, the flux of water to be applied in order to balance the silicon monoxide departure must be decreased. Controlling the temperature profile of the furnace should allow controlling the z_f position. More precisely, enlarging the homogeneous temperature range should move away from the sample the position of silicon monoxide supersaturation and condensation.

Sintering under controlled water vapor pressure eventually permitted the stabilization of the silica layer at high temperatures. Grain coarsening through surface diffusion was then inhibited, and densification through lattice diffusion could occur. For a sintering temperature of 1315 °C, the sample density is 80% TD_{Si} under controlled humidified atmosphere while it

is only 65 % under dry reducing atmosphere. Vapor transport, which is assumed to dominate in the late stage of sintering, is responsible for coarsening of the microstructure and explains the incomplete densification of the samples.

V.3 Spark Plasma Sintering route as an alternative for complete densification

The Spark Plasma Sintering (SPS) method is a variation of the traditional Hot Pressing (HP) method of densification. The difference is that the die, usually made of graphite is heated electrically by applying an electric field through the die and the specimen. Higher densities at lower sintering temperatures are often achieved using this technique. The question that usually arises is as follows: is the lowering of sintering temperature in SPS a result merely of the high pressures applied, or is there an additional effect from the electric field? The question is rather difficult to answer and the reader may refer to the critical reviews of Raj *et al.* [RCF11] and Munir *et al.* [MATO01] about the question. Here, we rather attempt to introduce the method and present experimental densification results obtained on various types of silicon powders. Then, we shall focus our discussion on silica reduction kinetics which is affected by the higher densification rates measured.

V.3.1 Spark Plasma Sintering technique

Spark Plasma Sintering is a current and pressure controlled process where powders are densified in a graphite die that is simultaneously heated with electrical current. The applied pressure can be very high, up to 1000 MPa and the current can be several kiloAmpers. The voltage applied across the graphite die and the specimen ranges up to 10 V, bringing the total electrical power expended in the process to several kW [RCF11].

In these experiments, the graphite die and the specimen act like two resistors in parallel (Figure V.12), both experiencing the same applied voltage, but the current between them being partitioned according to their relative conductivity. Fundamental differences are then expected depending on the conductivity of the material. While the current will be the important variable for conductive material, the applied voltage is likely to be more important in applying the method to insulating materials.

At the origin of this process, it was supposed that the application of pulsed DC currents can generate a plasma discharge between the particles of powdered material, thus enhancing the creation of necks at low temperatures. This was supposed to accelerate the matter diffusion and densification at low sintering temperatures, which could prevent from grain growth. This assumption of the existence of plasma or another specific SPS effect has never been verified, although the possibilities offered by the SPS are proven.

Generally, for a given initial grain size the SPS process results in a finer grain size. Since sintering is achieved more quickly, there is little time for grain growth. As regards photovoltaic applications, where large grain sizes are sought, this is not an advantage. However, activation of sintering by the electric field and the applied load, as well as the rapid

heating, allow better densification of large grain specimens. Moreover, high heating rate processes potentially increase the productivity compared to the conventional HP process.
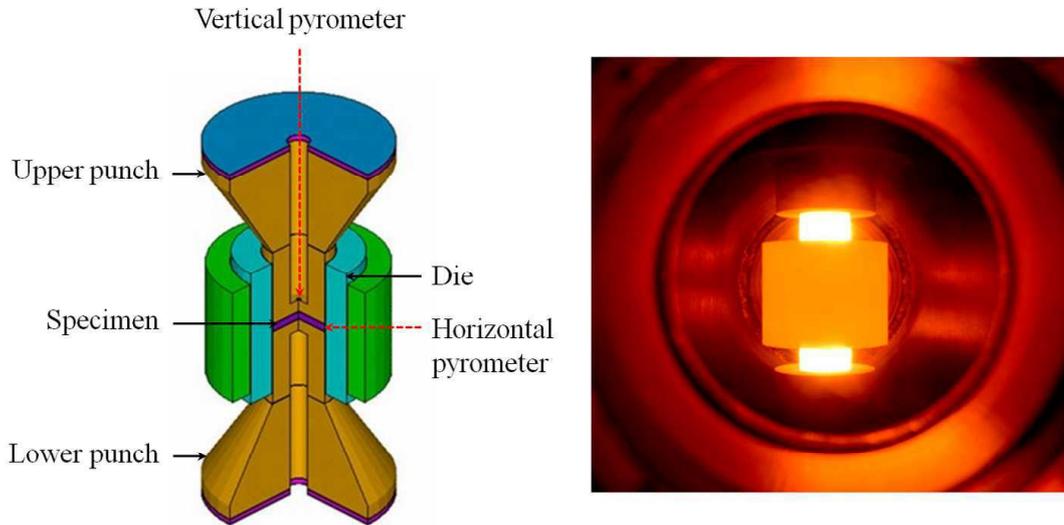
Figure V.12: Illustration of the SPS tool setup and photograph of a heated graphite die during the process.

V.3.2   Experimental conditions

The SPS apparatus type HD P 25/1 (FCT Gmbh, Germany) was used in the present investigation. The as-received powders were loaded in a 10 mm-inner diameter graphite die. The pulses pattern was constant and it consisted of a 2 pulses lasting 10 ms, followed by time out of 5 ms. The applied uniaxial pressure was constant and equal to 63 MPa during the whole process. This is the minimum pressure to be applied in order to ensure a good electrical contact between the specimen and the punch and to avoid powder dissemination out of the die under the effect of the current at the beginning of the sintering process.

One of the main issues of SPS techniques relies in the control of the temperature during the sintering process. Here, the temperature is measured using the horizontal pyrometer (Figure V.12). As the sample is heated by Joule effect under vacuum, significant thermal losses occurs at the surface of the sample by radiation. During one experiment, the sample has been found to reach its melting temperature (1414 °C) while the pyrometer was indicating approximately 1300 °C at the surface of the sample. Although rough, this measurement is taken as reference for the estimation of the inner sample temperature, T, which is calculated from the temperature indicated by the pyrometer, $T_{\text{pyrometer}}$ in Equation (V.12).

$$T = T_{\text{pyrometer}} \frac{1414}{1300} \tag{V.12}$$

C, M and VF powders were sintered at 1350 °C for 5 min using a heating rate of 50 and 100 °C min^{-1}. Final sample densities were measured by the Archimedes' method in ethanol. Samples could be densified to almost full density for the C and VF powders, while it was 91 % TD_{Si} for the M powder. As regards the photovoltaic application, the realization of fully dense materials with very coarse powders is encouraging. Therefore, in the following, our investigation focuses on the C powder.

V.3.3   Silica reduction kinetics and oxygen contamination

Starting C powder is contaminated with 263 ppm of oxygen. After sintering, the sample is contaminated with 350 ppm of oxygen. Oxidation of the powder may arise from desorption of oxygen impurities inside the furnace while heating. Under the passive to active transition of silicon, the powder is then contaminated with oxygen by the formation of silica at the particle surface. Assuming that the sample densifies to rapidly, the silica cannot be reduced in the compact after the passive to active transition.

Experiments have been performed in order to reduce the silica layer using isothermal plateau at 1040 and 1140 °C, which are assumed to be higher than the passive to active transition temperature. By keeping the sample for one hour at these temperatures, the silica is assumed to be reduced as the porosity inside the sample is not closed yet. Then the sample is heated to 1350 °C for 5 min using the standard heating rate of 50 °C min^{-1}. Eventually, another sample has been prepared using HF-etched powders.

Sample shrinkages curves with respect to the temperature are plotted in Figure V.13. By the end of the sintering process, all samples reached almost full density (99.7 %). Sample processed at 1040 and 1140 °C for 1 h experienced shrinkage during the isothermal plateau. The sample processed at 1040 °C experienced approximately half of the total shrinkage while the sample processed at 1140 °C was fully densified by the end of the isothermal plateau. As for HF-etched powders, they started to shrink at lower temperatures compared to the reference sample. This behavior may be attributed to the fact that by removing the silica layer the apparent activation energy for densification has been decreased.
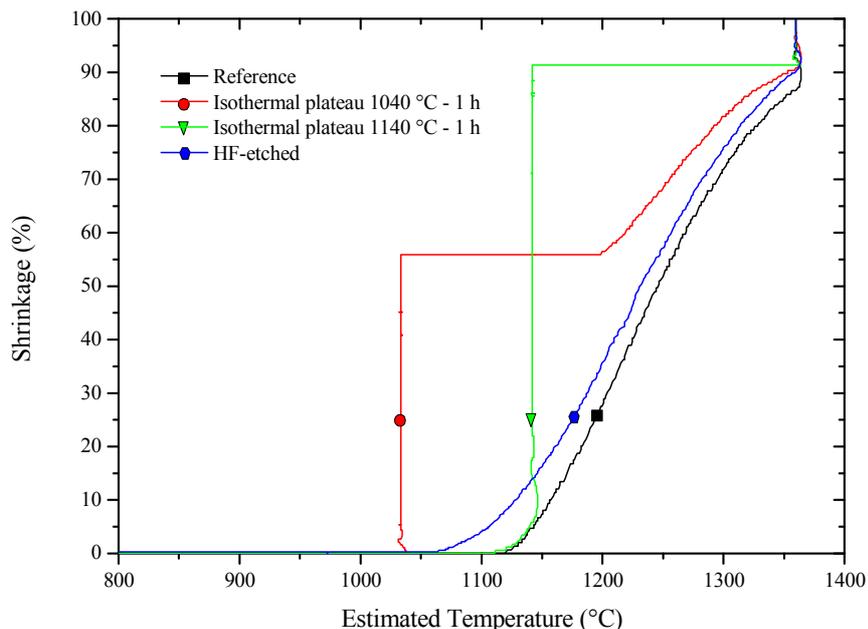
Figure V.13: SPS Shrinkage curves of C powders. The reference cycle corresponds to a shrinkage at a heating rate of 50 °C min^-1 and a sintering temperature of approximately 1350 °C for 5 min.

Results regarding sample oxygen contaminations are summarized in Table V.1 and compared to the reference sample sintered for 5 min at 1350 °C.The sample processed for one hour at 1040 °C shows a higher level of oxygen impurities than the reference sample, while the sample processed for one hour at 1140 °C shows a lower oxygen content. The passive to active transition temperature is then probably within this range of temperature.

Sintering Process	Oxygen contamination
Reference	350 ppm
Isothermal plateau 1040 °C – 1h	420 ppm
Isothermal plateau 1140 °C – 1h	250 ppm
HF-etched	200 ppm

Table V.1: Oxygen contamination levels of samples made of C powder and sintered at 1350 °C for 5 min.

The isothermal temperature could be further increased in order to accelerate silica reduction kinetics. However, sample density would then increase too rapidly to allow the silica removal. Another solution could be to decrease the applied pressure during the isothermal plateau such as to prevent sample shrinkage. The use of oxidation kinetics model such as presented in Chapter III, could be very useful to estimate the appropriate dwelling time and temperature conditions.

Actually, the sample made of HF-etched powder shows the lower oxygen contamination levels, showing that it might be a more competitive route to remove oxygen, although chemical batch processes are needed.

V.3.4   Conclusion

SPS results are promising. Coarse powders (~ 120 µm diameter) were fully densified in less than 5 min at 1350 °C. As regards the application, large grain size material can be obtained by sintering large powder particles in very short times. For instance, powders recycled from the wafering process could be used.

Issues regarding the contamination of the sample have to be discussed. Here, our discussion focused on silica reduction kinetics. However contamination by metallic impurities is probably the main issue to be considered.

General conclusion and perspectives

Photovoltaic conversion is a promising energy resource. Bulk crystalline silicon technologies currently dominate the market but suffer from high material losses that are highly detrimental to solar cell production cost. Accordingly, amorphous thin-film technologies emerged as new alternatives. By using less amount of material, CdTe and CIGS based solar cells have achieved lower retail prices and are gaining significant market share. However, silicon-based technologies still have a great potential. Silicon being the second most abundant element material on earth, it can certainly meet the continuous growth of the photovoltaic industry.

Thin-film technologies have also been proposed for silicon solar cells. Unfortunately, amorphous silicon material displays low electronic properties that prevent the realization of sufficiently high performance devices. Crystalline Silicon Thin-Film (CSiTF) technologies have comparatively a greater potential but are facing higher technical issues than their amorphous counterparts. One of the main issues relies in the preparation of a low-cost substrate. This substrate must be heated to relatively high temperatures for the elaboration of the crystalline layer through Chemical Vapor Deposition processes. In order to avoid deterioration of the grown layer, the substrate must have thermo-mechanical and physico-chemical properties as close as possible to silicon. Actually, only silicon substrates fit these requirements.

The challenge is then the elaboration of low cost silicon substrates. The silicon powder metallurgy route seems suitable since it avoids the need for at least crystallization and wafering steps that represent approximately one fourth of the module price. In this manuscript, we focused our work on the pressureless sintering method which ought to be the most competitive route as the material would be produced and processed continuously.

The identification of silicon sintering mechanisms was controversial in the literature. Especially, the native oxide layer (SiO_2) at the powder particle surfaces was assumed to significantly affect sintering kinetics, but no experimental evidences supported the idea yet. Therefore, we first investigated the stability of the silica layer at the silicon particle surfaces depending on the experimental conditions, *i.e.* temperature, surrounding partial pressure of oxidizing species and compact size. Under atmospheric pressure and stagnant flow conditions, reaction (R_5) has been shown to control the stability of the silica layer.

$$Si_{(s)} + SiO_{2(s)} = 2\ SiO_{(g)} \tag{R_5}$$

The silica layer was shown to be fragmented as the solid state diffusion coefficient of silicon (or silicon monoxide) through the silica layer could not account for the rapidity of the silica removal, which is simply limited by the molecular diffusion of silicon monoxide and water in the gas phase. A closed-form model completed by finite difference calculations was developed. The model fits silica reduction kinetics pretty well.

Microstructural observations at different steps of the sintering and silica reduction process were also performed. Even though very fine (about 0.5 nm), the silica layer strongly influences sintering mechanisms of very fine powders (~ 200 nm diameter). Neck growth kinetics was then investigated for pure silicon particles as well as for silicon particles covered with silica. For pure silicon, surface diffusion dominates sintering and is responsible for a large grain growth without densification. In the presence of silica at the particle surface, surface diffusion and then grain coarsening is inhibited which allows densification through lattice diffusion at higher temperatures.

Densification kinetics in the presence of silica was also investigated throughout the whole sintering process. Experimentally, the silica layer was stabilized by embedding the powder compact in a sacrificial silicon-silica powder bed, in order to control the silicon monoxide pressure at the sample surface. Densification kinetics was measured using dilatometric experiments. The sintering behavior could be divided into two sequential stages marked by two shrinkage peaks on the dilatometric curves. This result is unusual for the sintering of single-phase materials. However, it could be explained with help of a kinetic model using appropriate geometrical simplifications and observations of the sample microstructures. It was conclude that:
- First, lattice diffusion and densification occurs, although significantly affected by the presence of silica, as the activation energy for the diffusion of silicon atoms into silica is much larger than the activation energy for the diffusion of silicon atoms into silicon. Then, as the necks grow, vapor transport of silicon eventually dominates sintering kinetics and is responsible for a slowdown of the shrinkage rate. This corresponds to the first peak on the shrinkage rate curve.

- As the curvature of the pores becomes uniform, sintering enters in the intermediate stage. The driving force for non-densifying mechanisms being nil, lattice diffusion from grain boundaries dominates sintering kinetics and the shrinkage rate accelerates once again. However, vapor transport still occurs between pores. Small pores shrink and large pores grow in a so called Ostwald ripening process. The average pore size and pore to pore distance progressively increases, lowering densification kinetics again. This corresponds to the second peak on the shrinkage rate curve.

Silicon sintering behavior was then represented in a simplified form using Ashby's diagram approach and the effect of the particle size was investigated. For pure silicon, surface diffusion dominates at all particle sizes. For silicon particles covered with silica, vapor transport dominates at large neck to particle size ratios and for large particles ($2a > 1$ µm). Lattice diffusion from grain boundary and then densification, is significant only if the particles are fines enough ($2a < 500$ nm). These conclusions are consistent with literature results.

Then, innovative sintering processes were investigated as new perspectives for the elaboration of low cost silicon substrates.

Sintering of thin bimodal powder compacts was first addressed. The objective was to find the better compromise between the sinterability, the required final microstructure and the geometry for photovoltaic applications. The introduction of coarse particles dispersed in a fine particle matrix improved the green density but inhibited densification and the final density was decreased as predicted by our sintering diagrams. Sintering of (coarse/fine particles) two-layer materials resulted in delamination and porosity gradients due to differential shrinkage. Growth of large grains at the interface with the fine grain matrix was not observed. Re-crystallization processes are then needed to enhance the final grain size in pressureless sintered powder compacts.

A processing route based on TPS (Temperature Pressure Sintering) diagrams and involving a control of the water vapor pressure was then proposed in order to control the silica layer stability during the whole sintering process. This solution is interesting as the sintering mechanisms can be real time controlled at any temperature. However, increasing the water vapor pressure leads to a concomitant oxidation of the sample and to important material losses. Actually, the control of the diffusion length of gaseous species, which is directly related to the furnace thermal profile, seems more appropriate. Typically, if the size of the

homogeneous temperature zone is increased, the flux of water and silicon monoxide decreases and the material loss is less important.

Eventually, another sintering method, so called Spark Plasma Sintering, was proposed in order to overcome the difficulties regarding silicon densification. First results are promising as coarse powders (~ 120 μm diameter) were fully densified in less than 5 min at 1350 °C. As regards the application, large grain size material can be obtained by sintering large powder particles in very competitive times. However, the elimination of silica in the final material is still an issue and contamination by metallic impurities during this process must be avoided.

During this thesis, our attention focused on the comprehension of silicon sintering mechanisms that essentially affect the final density, purity and grain size of the material. These three parameters will directly affect the elaboration process of the solar cell. Ideally, pore free, highly pure and large grain size (~ mm) materials are wanted.

Pure silicon sintering is actually dominated by a grain coarsening mechanism (surface diffusion) that impedes the densification. But a major breakthrough of our study is that grain coarsening can be avoided and densification enhanced by stabilizing the silica layer at high temperature, under controlled oxidizing atmospheres. In this work, the densification has been improved from 63 % TD_{Si}, under conventional reducing atmosphere, to 87 % TD_{Si} under controlled atmosphere (1400 °C - 3 h), for fine silicon powders of 200 nm diameter. However, full densification of silicon requires even finer particles that are not currently available. In any case, the final material, still porous, contains high levels of oxygen impurities and final grain sizes of about 10 μm, that are not suitable as regards the elaboration of wafer based solar cells.

Instead, sintering of silicon as a route for the elaboration of low-cost silicon substrates for CSiTF solar cells may be proposed. Such approach avoids the needs for pore free materials, making the pressureless sintering route peculiarly attractive as it can be processed continuously. Requirements regarding the amount of impurities and final grain size are also less stringent but depend on the proposed CSiTF solar cell elaboration process.

The elaboration of materials free from metallic impurities with final grain size of hundreds μm would be very interesting as epitaxial wafer equivalent processes (EpiWE) could be used. This technology currently gives the higher CSiTF solar cell efficiencies with a relative simple process of elaboration. To achieve this goal, the following developments may be proposed:
- Non-contaminating forming technologies should be investigated. The main issue, regarding pressureless technologies, actually relies in this step. As a major difference with Hot Pressing or Spark Plasma Sintering technologies, the

specimen must be shaped before sintering. The issue is actually highly challenging when thinking about the thickness and area of the silicon substrates that ought to be processed.

- The pressureless sintering of large area silicon substrates in industrial-scale furnaces that must be specifically designed. Silica reduction kinetics and then sintering strongly depends on the sample size, partial pressure of oxidizing species and furnace temperature profiles.

- Solid state re-crystallization processes should be studied. This would allow increasing the final grain size of the material without melting steps that are usually highly detrimental to the productivity and final cost.

- Eventually, new processes, such as Induction Sintering or Spark Plasma Sintering, could be proposed in order to increase the productivity of pressureless or Hot Pressing methods, respectively.

References

[AD01]   E. Aigeltinger and R. DeHoff. Quantitative determination of topological and metric properties during sintering of copper. *Metallurgical and Materials Transactions A*, 6(10):1853–1862, 1975-10-01.

[ADPQ78]   Y. Adda, J.M. Dupouy, J. Philibert, and Y. Quere. *Eléments de Métallurgie Physique, Tome 4: Diffusion Transformation*. La Documentation Française, 1978.

[Age11a]   International Energy Agency. Key world energy statistics, 2011.

[Age11b]   International Energy Agency. Trends in photovoltaic applications survey report of selected iea countries between 1992 and 2010, 2011.

[AJ80]   M.F. Ashby and D.R.H. Jones. *Matériaux 1. Propriétés et applications*. Pergamon Press, Oxford, 1980.

[Arl82]   E. Arlt. The influence of an increasing particle coordination on the densification of spherical polders. *Acta Metallurgica*, 30(10):1883–1890, October 1982.

[AS62]   Roger A. Svehla. Estimated viscosities and thermal conductivities of gases at high temperatures. Technical Report TR R-132, NASA, 1962.

[Ash74]   M.F Ashby. A first report on sintering diagrams. *Acta Metallurgica*, 22(3):275–289, March 1974.

[Ass11]   European Photovoltaic Industry Association. Solar generation 6, 2011.

[Ass12]   European Photovoltaic Industry Association. Global market outlook for photovoltaics until 2016, May 2012.

[BA93]   Didier Bernache-Assolant. *Chimie-physique du frittage*. FORCERAM, 1993.

[Bau03]   S. Bau. High temperature CVD silicon films for crystalline silicon thin-film solar cells. PhD thesis, Universität Konstanz, 2003.

[Bea09]   Mickael Beaudhuin. Étude expérimentale et numérique de la précipitation d'impuretés et de la formation des grains dans le silicium photovoltaïque. PhD thesis, Institut polytechnique de Grenoble - Ecole doctorale IMEP2, Décembre 2009.

[Bel10]   P. Bellanger. Etude d'un procédé de re-crystallisation de plaquettes de silicium fritté pour la réalisation de cellules solaires photovoltaïques. PhD thesis, Institut National des Sciences Appliquées de Lyon, 2010.

[BLCC07]   K.G. Barraclough, A. Loni, E. Caffull, and L.T. Canham. Cold compaction of silicon powders without a binding agent. *Materials Letters*, 61(2):485–487, January 2007.

[BMZ+08]   A.F.B. Braga, S.P. Moreira, P.R. Zampieri, J.M.G. Bacchin, and P.R. Mei. New processes for the production of solar-grade polycrystalline silicon: A review. *Solar Energy Materials and Solar Cells*, 92(4):418–424, April 2008.

[BPP11]   K. Branker, M. Pathak, and J. Pearce. A review of solar photovoltaic levelized cost of electricity. *Renewable and Sustainable Energy Reviews*, 15(9):4470–4482, 2011.

[BSL01]   R. Byron Bird, Warren E. Stewart, and Edwin N. Lightfoot. *Transport phenomena*. John Wiley & Sons, Inc., 2001.

[BSS+80]   G. Brebec, R. Seguin, C. Sella, J. Bevenot, and J.C. Martin. Diffusion du silicium dans la silice amorphe. *Acta Metallurgica*, 28(3):327–333, March 1980.

[CC96]   Pei-Lin Chen and I-Wei Chen. Sintering of fine oxide powders: I, microstructural evolution. *Journal of the American Ceramic Society*, 79(12):3129–3141, 1996.

[CC97]   Pei-Lin Chen and I-Wei Chen. Sintering of fine oxide powders: Ii, sintering mechanisms. *Journal of the American Ceramic Society*, 80(3):637–645, 1997.

[CHC95]   B. Caussat, M. Hemati, and J.P. Couderc. Silicon deposition from silane or disilane in a fluidized bed part II: Theoretical analysis and modeling. *Chemical Engineering Science*, 50(22):3625–3635, November 1995.

[CL03]   B. Ceccaroli and O. Lohne. *Handbook of photovoltaic Science and Engineering*, Chapter 5, pages 153–204. John Wiley & Sons, 2003.

[Cob61]   R. L. Coble. Sintering crystalline solids. I. intermediate and final state diffusion models. *Journal of Applied Physics*, 32(5):787–792, May 1961.

[Cob90]   W. S. Coblenz. The physics and chemistry of the sintering of silicon. *Journal of Materials Science*, 25(6):2754–2764, June 1990.

[Cor09]   L.A. Corathers. *2009 Minerals Yearbook*. U.S. Department of the Interior, U.S. Geological Survey, 2009.

[Cou10]   World Energy Council. Survey of energy resources, 2010.

[CT88]   G. K. Celler and L. E. Trimble. High-temperature stability of Si/SiO_2 interfaces and the influence of SiO flux on thermomigration of impurities in SiO_2. *Applied Physics Letters*, 53(25):2492–2494, 1988.

[CT89a]   G. K. Celler and L. E. Trimble. Catalytic effect of SiO on thermomigration of impurities in SiO_2. *Applied Physics Letters*, 54(15):1427–1429, 1989.

[CT89b]   G.K. Celler and L.E. Trimble. Formation of SiO at Si/SiO_2 interface and its influence on transport of group V dopants and Ge in SiO_2. *Applied Surface Science*, 39(1-4):245–258, October 1989.

[Der06]   K. Derbouz. Etude du frittage du silicium pour application aux cellules solaires photovoltaïques. PhD thesis, Université de Poitiers, 2006.

[Dor01]   Robert H. Doremus. Diffusion of oxygen and silicon in silicon: Silicon monoxide model. *Journal of Materials Research*, 16(1):185–191, Jan 2001.

[Dor02]   Robert H. Doremus. Viscosity of silica. *Journal of Applied Physics*, 92(12):7619–7629, 2002.

[END99]   N. Eustathopoulos, M.G. Nicholas, and B. Drevet. *Wettability at high temperatures*. Pergamon Materials Series, 1999.

[FHHS98]   F. Faller, V. Henninger, A. Hurrle, and N. Schillinger. Optimization of the cvd process for low-cost crystalline silicon thin film solar cells. In *Proceedings of the 2nd World Conference And Exhibition On Photovoltaic Solar Energy Conversion*, 1998.

[FM67]   J. M. Fairfield and B. J. Masters. Self-diffusion in intrinsic and extrinsic silicon. *Journal of Applied Physics*, 38(8):3148–3154, July 1967.

[GAB66]   Earl A. Gulbransen, Kenneth F. Andrew, and Fred A. Brassart. Oxidation of silicon at high temperatures and low pressure under flow conditions and the vapor pressure of silicon. *Journal of The Electrochemical Society*, 113(8):834–837, 1966.

[GBL⁺09]   M. Grau, D. Blangis, S. Lindekugel, S. Janz, S. Reber, and A. Straboni. High voc crystalline silicon thin film solar cells through recrystallized wafer equivalent applied to sintered silicon. In *Proceedings of the 24ᵗʰ European Photovoltaic Solar Energy Conference*, number 3AV.1.42, 2009.

[GC85]   S.H. Garofalini and S. Conover. Comparison between bulk and surface self-diffusion constants of Si and O in vitreous silica. *Journal of Non-Crystalline Solids*, 74(1):171–176, September 1985.

[GCG⁺08]   I. Gordon, L. Carnel, D.V. Gestel, G. Beaucarne, and Poortmans J. Fabrication and characterization of highly efficient thin-film polycrystalline silicon solar cells based on aluminium-induced crystallization. *Thin Solid Films*, 516:6984–6988, 2008.

[GCG01]   C. Gelain, A. Cassuto, and P. Goff. Low-pressure, high-temperature siliconizing of tungsten-i. *Oxidation of Metals*, 3(2):115–138, 1971-03-01.

[Ger94]   Randall M. German. *Powder Metallurgy Science*. Metal Powder Industries Federation, 1994.

[Ger96]   Randall M. German. *Sintering Theory and Practice*. Wiley-Interscience, 1996.

[Gho66]   R. N. Ghoshtagore. Method for determining silicon diffusion coefficients in silicon and in some silicon compounds. *Physical Review Letters*, 16(20):890–, May 1966.

[GJ01]   Earl A. Gulbransen and Sven A. Jansson. The high-temperature oxidation, reduction, and volatilization reactions of silicon and silicon carbide. *Oxidation of Metals*, 4(3):181–201, 1972-09-01.

[GR76]   C. Greskovich and J. H. Rosolowski. Sintering of covalent solids. *Journal of the American Ceramic Society*, 59(7-8):336–343, 1976.

[GR01]   R. Gregg and F. Rhines. Surface tension and the sintering force in copper. *Metallurgical and Materials Transactions B*, 4(5):1365–1374, 1973-05-01.

[Gra12]   M. Grau. Réalisation de nouvelles structures de cellules solaires photovoltaïques à partir de couches minces de silicium sur substrat de silicium préparé par frittage de poudres. PhD thesis, Institut National des Sciences Appliquées de Lyon, 2012.

[HA79]   J. Hirvonen and A. Anttila. Self-diffusion in silicon as probed by the (p,gamma) resonance broadening method. *Applied Physics Letters*, 35(9):703–705, 1979.

[HB98]   C. Honsberg and S. Bowden. Photovoltaic devices, systems and applications, 1998.

[Her50]   Conyers Herring. Effect of change of scale on sintering phenomena. *Journal of Applied Physics*, 21(4):301–303, 1950.

[HRTJ92]   James D. Hansen, Richard P. Rusin, Mao-Hua Teng, and D. Lynn Johnson. Combined-stage sintering model. *Journal of the American Ceramic Society*, 75(5):1129–1135, 1992.

[Hul99]   Robert Hull. *Properties of crystalline silicon*. INSPEC, London, 1999.

[IN85]   Yoshiko Itoh and Tadashi Nozaki. Solubility and diffusion coefficient of oxygen in silicon. *Japanese Journal of Applied Physics*, 24(Part 1, No. 3):279–284, 1985.

[Joh69]   D. Lynn Johnson. New method of obtaining volume, grain-boundary, and surface diffusion coefficients from sintering data. *Journal of Applied Physics*, 40(1):192–200, 1969.

[Kan05]   Suk-Joong L. Kang. SINTERING Densification, grain growth & microstructure. Elsevier, 2005.

[KBGA08]   T. Kunz, I. Burkert, N. Gawehns, and R. Auer. Crystalline silicon thin-film solar cells on graphite or sic ceramic substrates. In *Proceedings of the 23rd European Photovoltaic Solar Energy Conference*, 2008.

[KDC+10]   J. Kraiem, B. Drevet, F. Cocco, N. Enjalbert, S. Dubois, D. Camel, and D. Grosset-Bourbange. 35th ieee photovoltaic specialists conference. In *Conference Record of the 35th IEEE Photovoltaic Specialists Conference*, pages 1427–1431, 2010.

[KEF+03]   W. Koch, A. L. Endrös, D. Franke, C. Häbler, J.P. Kalejs, and Möller H. J. *Handbook of photovoltaic Science and Engineering*, chapter 6, pages 205–252. John Wiley & Sons, 2003.

[Kit56]   C. Kittel. *Introduction to Solid States Physics*. John Wiley & Sons, Inc., 1956.

[KPES03]   T. Kieliba, J. Pohl, A. Eyer, and C. Schimiga. Optimization of c-si films formed by zone-melting recrystallization for thin-film solar cells. In *Proceedings of the 3rd World Conference on Photovoltaic Energy Conversion*, 2003.

[KS79]   Ludomir Kalinowski and Remy Seguin. Self-diffusion in intrinsic silicon. *Applied Physics Letters*, 35(3):211–213, 1979.

[LM62]   J. J. Lander and J. Morrison. Low voltage electron diffraction study of the oxidation and reduction of silicon. *Journal of Applied Physics*, 33(6):2089–2092, 1962.

[LS61]   I.M. Lifshitz and V.V. Slyozov. The kinetics of precipitation from supersaturated solid solutions. *Journal of Physics and Chemistry of Solids*, 19(1-2):35–50, April 1961.

[MATO01]   Z. Munir, U. Anselmi-Tamburini, and M. Ohyanagi. The effect of electric field and pressure on the synthesis and consolidation of materials: A review of the spark plasma sintering method. *Journal of Materials Science*, 41(3):763–777, 2006-02-01.

[MC98]   W. Malcolm and Jr. Chase. Nist-janaf thermochemical tables. In *Journal of Physical and Chemical Reference Data*, volume 9. American Chemical Society, American Institue of Physics, 4th edition, 1998.

[MG09]   C. Miquel and B. Gaiddon. Systèmes photovoltaïques : fabrication et impact environnemental. Technical report, Hespul, 2009.

[MOH+90]   M. Morita, T. Ohmi, E. Hasegawa, M. Kawakami, and M. Ohwada. Growth of native oxide on a silicon surface. *Journal of Applied Physics*, 68(3):1272–1281, 1990.

[MR00]   J.-M. Missiaen and S. Roure. Automatic image analysis methods for the determination of stereological parameters - application to the analysis of densification during solid state sintering of wc-co compacts. *Journal of Microscopy*, 199(2):141–148, 2000.

[Mun79]   Z. A. Munir. Analytical treatment of the role of surface oxide layers in the sintering of metals. *Journal of Materials Science*, 14(11):2733–2740, 1979.

[MW85]   H. J. Möller and G. Welsch. Sintering of ultrafine silicon powder. *Journal of the American Ceramic Society*, 68(6):320–325, 1985.

[NOT+03]   Yukio Nakabayashi, Hirman I. Osman, Kazunari Toyonaga, Kaori Yokota, Satoru Matsumoto, Junichi Murota, Kazumi Wada, and Takao Abe. Self-diffusion in intrinsic and extrinsic silicon using isotopically pure [30]silicon/natural silicon heterostructures. *Japanese Journal of Applied Physics*, 42(Part 1, No. 6A):3304–, 2003.

[NPKF+09]   K.V. Nieuwenhuysen, M.R. Payo, I. Kuzma-Filipek, J.V. Hoeymissen, and Poortmans J. Epitaxial thin film solar cells with efficiencies up to 16.9% by combining

advanced light trapping methods and cvd emitters. In *Proceedings of the 24th European Photovoltaic Solar Energy Conference*, 2009.

[Pie95]   G. J. Pietsch. Hydrogen on si - ubiquitous surface termination after wet-chemical processing. *Applied Physics A-materials Science & Processing*, 60(4):347–363, April 1995.

[Pro06]   Prometheus. Supply, demand, & implications for the pv industry. Technical report, Rapport du Prometheus Institute for Sustainable Development, 2006. http://www.prometheus.org/research/polysilicon2006.

[Rah95]   M. N. Rahaman. *Ceramic Processing and Sintering*. Marcel Dekker, Inc., 1995.

[RCF11]   Rishi Raj, Marco Cologna, and John S. C. Francis. Influence of externally imposed and internally generated electrical fields on grain growth, diffusional creep, sintering and related phenomena in ceramics. *Journal of the American Ceramic Society*, 94(7):1941–1965, 2011.

[RCJMJWWB01]   Kylie R. Catchpole, Michelle J. McCann, Klaus J. Weber, and Andrew W. Blakers. A review of thin-film crystalline silicon for solar cell applications. part 2: Foreign substrates. *Solar Energy Materials and Solar Cells*, 68(2):173–215, May 2001.

[REC12]   Solar REC. High purity silicon materials. Technical report, REC Solar, 2012. recgroup.com.

[RHEW04]   S. Reber, A. Hurrle, A. Eyer, and G. Willeke. Crystalline silicon thin-film solar cells - recent results at fraunhofer *ISE*. *Solar Energy*, 77(6):865–875, December 2004.

[Rob81]   Wayne M. Robertson. Thermal etching and grain-boundary grooving silicon ceramics. *Journal of the American Ceramic Society*, 64(1):9–13, 1981.

[SBBP02]   A. Slaoui, S. Bourdais, G. Beaucarne, and S. Poortmans, J.and Reber. Polycrysstalline silicon solar cells on mullite substrates. *Solar Energy Materials and Solar Cells*, 71(2):245–252, 2002.

[SH83]   N. J. Shaw and A. H. Heuer. On particle coarsening during sintering of silicon. *Acta Metallurgica*, 31(1):55–59, 1983.

[She89]   P. Shewmon. *Diffusion in solids*. The Minerals, Metals and Materials Society, 1989.

[SK90]   H-E. Sasse and U. Koening. SiO diffusion during thermal decomposition of SiO$_2$. *Journal of Applied Physics*, 67(10), 1990.

[Smi83]   Colin Smithells. *Smithells Metals Reference book*. Butterworth & Co, 6th edition, 1983.

[Sop03]   B. Sopori. *Handbook of photovoltaic Science and Engineering*, chapter 8, pages 307–354. John Wiley & Sons, 2003.

[SS63]   Charles N. Satterfield and Thomas K. Sherwood. *The Role of Diffusion in Catalysis*. 1963.

[SSR07]   E. Schmich, N. Schillinger, and S. Reber. Silicon cvd deposition for low cost applications in photovoltaics. *Surface and Coatings Technology*, 201(22-23):9325–9329, 2007.

[Str04]   Alain Straboni. Matériau semiconducteur obtenu par frittage, brevet WO 2004/093202, 2004.

[SUI07]   Yasuo Shimizu, Masashi Uematsu, and Kohei M. Itoh. Experimental evidence of the vacancy-mediated silicon self-diffusion in single-crystalline silicon. *Physical Review Letters*, 98(9):095901, Mar 2007.

[Sun10]   Suntech. 25th European Conference on Photovoltaic Energy (PVSEC). Oral Communication, 2010.

[Sve11]   J. Svensson. Ground-breaking technology for cost leadership. Technical report, Elkem Solar plant, 2011. http://www.elkem.com/dav/499fe289c6.pdf au 31/05/2011.

[TCWS89]   L. E. Trimble, G. K. Celler, K. W. West, and T. T. Sheng. Arsenic drift in SiO$_2$: Temperature, dose, and thermal gradient effects. *Journal of The Electrochemical Society*, 136(1):182–188, 1989.

[TDCA03]   I. Tobias, C. Del Cañizo, and J. Alonso. *Handbook of photovoltaic Science and Engineering*, Chapter 7, pages 255–303. John Wiley & Sons, 2003.

[TRB$^+$85]   R. Tromp, G. W. Rubloff, P. Balk, F. K. LeGoues, and E. J. van Loenen. High-temperature SiO$_2$ decomposition at the SiO$_2$/Si interface. *Physical Review Letters*, 55(21):2332–, November 1985.

[Vei11]   J. Veirman. Effets de la compensation du dopage sur les propriétés électriques du silicium et sur les performances photovoltaïques des cellules à base de silicium solaire

purifié par voie métallurgique. PhD thesis, Institut National des Sciences Appliquées de Lyon, 2011.

[VRM$^+$08]   A. Vagnon, J.P. Rivière, J.M. Missiaen, D. Bellet, M. Di Michiel, C. Josserond, and D. Bouvard. 3d statistical analysis of a copper powder sintering observed in situ by synchrotron microtomography. *Acta Materialia*, 56(5):1084–1093, March 2008.

[Wag58]   C. Wagner. Passivity during the oxidation of silicon at elevated temperatures. *Journal of Applied Physics*, 29(9):1295–1297, 1958.

[Wag61]   C. Wagner. Theorie der alterung von nieder schlagen durch umlosen (Ostwald-reifung). *Zeitschrift fur Elejtrochemie*, 65(7):581–591, 1961.

[WTT99]   Y. Wakayama, T. Tagami, and S. Tanaka. Three-dimensional islands of Si and Ce formed on SiO_2 through crystallization and agglomeration from amorphous thin films. *Thin Solid Films*, 350(1-2):300–307, August 1999.

[WZWG96]   A. Wang, J. Zhao, S. R. Wenham, and M. A. Green. 21.5% efficient thin silicon solar cell. *Progress in Photovoltaics*, 4(1):55–58, 1996.

[YO10]   Kouji Yasuda and Toru Okabe. Solar-grade silicon production by metallothermic reduction. *JOM Journal of the Minerals, Metals and Materials Society*, 62:94–101, 2010. 10.1007/s11837-010-0190-8.

[YSO11]   Kouji Yasuda, Kunio Saegusa, and Toru Okabe. Production of solar-grade silicon by halidothermic reduction of silicon tetrachloride. *Metallurgical and Materials Transactions B*, 42:37–49, 2011. 10.1007/s11663-010-9440-y.

[ZH92]   Junhong Zhao and Martin P. Harmer. Effect of pore distribution on microstructure development: Iii, model experiments. *Journal of the American Ceramic Society*, 75(4):830–843, 1992.

Autor's contributions

- *Reviewed articles*

Jean-Marie Lebrun, Jean-Michel Missiaen, and Céline Pascal. Elucidation of mechanisms involved during silica reduction on silicon powders. *Scripta Materialia*, 64(12):1102–1105, June 2011.

Jean-Marie Lebrun, Céline Pascal, and Jean-Michel Missiaen. The role of silica layer on sintering kinetics of silicon powder compact. *Journal of the American Ceramic Society*, 95(5):1514–1523, 2012.

Jean-Marie Lebrun, Céline Pascal, and Jean-Michel Missiaen. Temperature - Pressure - Sintering (TPS) diagrams approach for sintering of silicon. *Materials Letters*, 83:65–68, 2012.

- *Published peer reviewed congress papers*

Jean-Marie Lebrun, Céline Pascal, and Jean-Michel Missiaen. Sintering of silicon under slightly oxidizing atmospheres. *Oral and Paper communication at the International Conference on Sintering, Jeju Island, South Korea, to be published in Ceramic Transactions*, 2011.

- *Congress communications and papers*

Jean-Marie Lebrun, Jean-Michel Missiaen, Céline Pascal, Florence Servant, Jean-Paul Garandet, Gilbert Fantozzi, and Guillaume Bonnefont. Elaboration de silicium polycristallin par frittage naturel pour applications photovoltaïques. *Acte de congrès et communication orale à la conférence Matériaux Nantes*, 2010.

Jean-Marie Lebrun, Jean-Michel Missiaen, and Céline Pascal. Réduction de la silice au cours du frittage du silicium. *Communication Orale, Journées d'Etude sur la Cinétique Hétérogène, JECH42, La Rochelle*, 2011.

Jean-Marie Lebrun, Jean-Michel Missiaen, Céline Pascal, Florence Servant, Jean-Paul Garandet, Gilbert Fantozzi, and Guillaume Bonnefont. Sintering for photovoltaic applications. *Poster Communication at the European Congress and Exhibition on Advances Materials and Processes*, 2011.

Jean-Marie Lebrun, Céline Pascal, Jean-Michel Missiaen, Florence Servant, Jean-Paul Garandet, Gilbert Fantozzi, and Guillaume Bonnefont. Pressure-less sintering of silicon bimodal powder compacts under controlled atmosphere. *Oral Communication at the European Powder Metallurgy Congress, Basel, Switzerland*, 2012.

Jean-Marie Lebrun, Jean-Michel Missiaen, and Céline Pascal. Pressure-less sintering of silicon powder compacts : experimental approach and modeling. *Oral Communication at the Powder Metallurgy World Congress and Exhibition, Yokohama, Japan*, 2012.

- *Patent*

Jean-Marie Lebrun, Jean-Michel Missiaen, Céline Pascal, Jean-Paul Garandet, and Florence Servant. Elaboration de silicium polycristallin par frittage naturel pour applications photovoltaïques, 2010, FR 296628, PCTWO2012049300A1.

Appendixes

Appendix A.   Wagner's approach extended under hydrogen

In 1958, Carl Wagner [Wag58] first established the stability conditions of silica layers covering silicon surfaces. These conditions were calculated assuming a laminar flow at the sample surrounding (Figure A.1, (i)). More precisely, assuming molecular diffusion in a boundary layer at the sample gas interface, he determined the silica layer stability in terms of temperature and oxygen vapor pressure.

These calculations can be extended to hydrogenated atmosphere assuming a steady-state diffusion of oxidizing species in a furnace tube along a height $\pm z_f$ from the sample position (Figure A.1, (ii)). This corresponds more or less to our experimental conditions (see Appendix B.3.3).
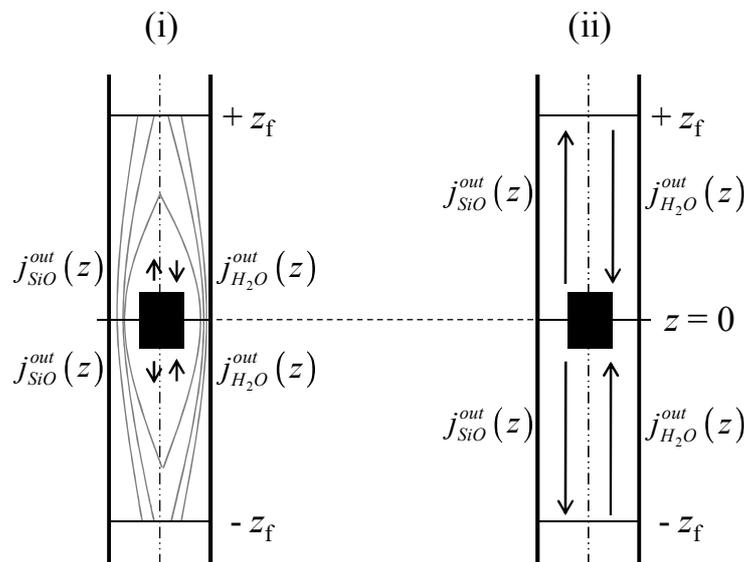

Figure A.1: (i) *Matter transport of silicon monoxide and water in a boundary layer at the sample gas interface according to Wagner's initial approach.* (ii) *In our experimental conditions, matter transport of silicon monoxide and water can be considered entirely diffusive over a height* $\pm z_f$ *(~ 40 mm).*

Wagner's approach can be divided into two distinct cases (Figure A.2). The first case (a) considers that the sample is initially free from oxide and corresponds to the so-called active to passive transition. This case can be assimilated to the passive to active transition when a discontinuous silica layer covers the sample (or particle) surface. On the contrary, the second case (b) considers that the sample is covered by a continuous and passive silica layer and corresponds to the passive to active transition.
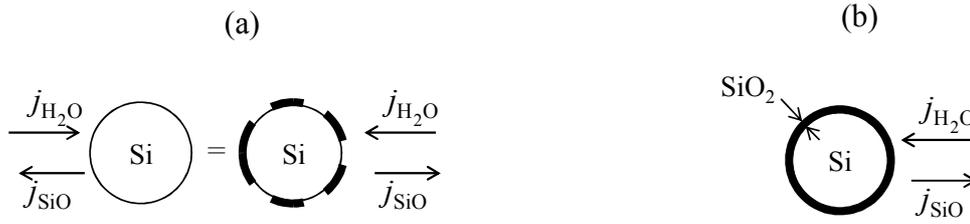
Figure A.2: (a) *Active to passive transition.* (b) *Passive to active transition. In both cases, the balance of water and silicon monoxide flux determines the temperature or corresponding water vapor pressure at which silica will grow or dissociate.*

A.1 Active to passive transition

The silicon sample is under low water vapor pressure and initially free from oxide, *i.e.* under active oxidation conditions, (R$_2$), (Figure A.2 (a)). Reaction (R$_5$) determines the active to passive transition.

$$Si_{(s)} + H_2O_{(g)} = SiO_{(g)} + H_{2(g)} \qquad (R_2)$$

$$Si_{(s)} + SiO_{2(s)} = 2SiO_{(g)} \qquad (R_5)$$

If the effective partial pressure of silicon monoxide generated at the sample surface, P_{SiO}, is less than $P_{SiO}^{R_5}$ the silicon surface remains bare. If the supply of H$_2$O is increased, P_{SiO} eventually reaches $P_{SiO}^{R_5}$ and accordingly a protective silica layer is formed. Thus Equation (A.1) controls the active to passive transition where K_5 is the equilibrium constant of reaction (R$_5$).

$$P_{SiO} = P_{SiO}^{R_5} = P^\circ K_5^{1/2} \qquad (A.1)$$

To calculate the effective partial pressure of silicon monoxide on a bare silicon surface, P_{SiO}, Wagner proposed the following procedure.

The H$_2$O molecules hitting the bare silicon surface are assumed to react readily since the equilibrium constant of reaction (R$_2$), K_2, is high. Then, as far as the water partial pressure in the flowing gas is large compared to the equilibrium value of (R$_2$), the water vapor partial pressure at the silicon surface is much lower than the partial pressure at the z_f position, $P_{H_2O}^{z_f}$.

The water flux toward the silicon surface can be expressed as Equation (A.2) where $D_{H_2O}^{mol}$ is the molecular diffusion coefficient of water vapor, R the gas constant, and z_f the diffusion length of molecular species in the furnace tube.

$$j_{H_2O}^{out} = -\frac{D_{H_2O}^{mol}}{RT} \frac{P_{H_2O}^{z_f}}{z_f} \qquad (A.2)$$

Silicon monoxide molecules generated at the sample surface along reaction (R_2) diffuse outwards the sample. These molecules condensate out of the heated zone and therefore the silicon monoxide pressure at the z_f position, $P_{SiO}^{z_f}$, can be neglected with respect to the pressure close to the sample, P_{SiO}. Accordingly their flux is expressed as a function of the molecular diffusion coefficient of silicon monoxide, D_{SiO}^{mol} in Equation (A.3).

$$j_{SiO}^{out} = \frac{D_{SiO}^{mol}}{RT} \frac{P_{SiO}}{z_f} \qquad (A.3)$$

Under steady-state conditions, the net flux of oxygen atoms towards the sample surface vanishes.

$$j_{SiO}^{out} + j_{H_2O}^{out} = 0 \qquad (A.4)$$

According to Equations (A.2), (A.3) and (A.4), the effective partial pressure of silicon monoxide at the sample surface, P_{SiO}, can be estimated in Equation (A.5).

$$P_{SiO} = \frac{D_{H_2O}^{mol}}{D_{SiO}^{mol}} P_{H_2O}^{z_f} \qquad (A.5)$$

The maximum water vapor pressure far from the sample at which the silicon surface remains bare, $P_{H_2O}^{W\,R_5}$, is calculated in Equation (A.6) using Equations (A.1) and (A.5), where $T_{A\to P}^{W}$ corresponds to the active to passive transition temperature calculated by Wagner.

$$P_{H_2O}^{W\,R_5} = \frac{D_{SiO}^{mol}}{D_{H_2O}^{mol}} P^{\circ} \left(K_5 \left(T_{A\to P}^{W} \right) \right)^{1/2} \qquad (A.6)$$

The mass loss rate, $\frac{\Delta m}{\Delta t}$, during active oxidation calculated using Equations (A.3) and (A.5) is directly proportional to the water vapor pressure away from the sample, $P_{H_2O}^{z_f}$, as expressed in Equation (A.7) where M_{Si} is the silicon molar mass and r_t the furnace tube radius.

$$\frac{\Delta m}{\Delta t} = -M_{Si}\, 2\pi r_t^2\, j_{H_2O}^{tube} = -M_{Si}\, 2\pi r_t^2\, \frac{D_{H_2O}^{mol}}{RT} \frac{P_{H_2O}^{z_f}}{z_f} \qquad (A.7)$$

A.2   Passive to active transition

A silicon particle completely covered with a continuous and passive silica layer is now considered (Figure A.2 (b)). Reaction (R$_6$), of equilibrium constant K_6, determines the passive to active transition as silicon monoxide cannot leave the $Si_{(s)}$-$SiO_{2(s)}$ interface.

$$SiO_{2(s)} + H_{2(g)} = SiO_{(g)} + H_2O_{(g)} \tag{R$_6$}$$

$$K_6 = \frac{P_{H_2O} P_{SiO}}{P^\circ P_{H_2}} \tag{A.8}$$

If the water vapor at the sample surface, P_{H_2O}, becomes lower than the value imposed by Equation (A.8), the silica layer starts to dissociate. The molar flux of water vapor and silicon monoxide towards the surface are now given by Equation (A.9) and (A.10), where P_{SiO} is related to P_{H_2O} using Equation (A.8).

$$j_{H_2O}^{out} = -\frac{D_{H_2O}^{mol}}{RT} \frac{P_{H_2O}^{z_f} - P_{H_2O}}{z_f} \tag{A.9}$$

$$j_{SiO}^{out} = \frac{D_{SiO}^{mol}}{RT} \frac{P_{SiO}}{z_f} = \frac{D_{SiO}^{mol}}{RT} \frac{P^\circ P_{H_2} K_6}{P_{H_2O}} \tag{A.10}$$

Using Equations (A.4), (A.9) and (A.10), P_{H_2O} can be related to the water vapor pressure far from the sample $P_{H_2O}^{z_f}$ in Equation (A.11).

$$P_{H_2O}^2 - P_{H_2O}^{z_f} P_{H_2O} + \frac{D_{SiO}^{mol}}{D_{H_2O}^{mol}} P^\circ P_{H_2} K_6 = 0 \tag{A.11}$$

If after the formation of a silica layer, the water vapor pressure away from the sample is gradually decreased, the silica layer will be stable as long as a real solution for the water vapor pressure at the sample surface, P_{H_2O}, can be found using Equation (A.11), *i.e.* as long as the discriminant of Equation (A.11) is positive. Accordingly in Equation (A.12), $P_{H_2O}^{W\,R_6}$ corresponds to the minimum water vapor pressure at which the silica layer remains stable and $T_{P\rightarrow A}^W$ to the corresponding passive to active transition temperature calculated by Wagner.

$$P_{H_2O}^{W\,R_6} = 2\left(\frac{D_{SiO}^{mol}}{D_{H_2O}^{mol}}\right)^{1/2} P_{H_2}^{1/2} P^{\circ\,1/2} \times \left(K_6\left(T_{P\rightarrow A}^W\right)\right)^{1/2} \tag{A.12}$$

In thermogravimetric analysis (TGA), the transitions can be identified when the mass loss rate is nil, T^{Wm}, as the mass flux of water equals silicon monoxide one. Equation (A.4) changes to Equation (A.13) and accordingly Equations (A.6) and (A.12) become Equations (A.14) and (A.15) respectively.

$$M_{\text{SiO}}\, j_{\text{SiO}}^{\text{out}} + M_{\text{O}}\, j_{\text{H}_2\text{O}}^{\text{out}} = 0 \tag{A.13}$$

$$P_{\text{H}_2\text{O}}^{\text{WR}_5} = \frac{M_{\text{SiO}} D_{\text{SiO}}^{\text{mol}}}{M_{\text{O}} D_{\text{H}_2\text{O}}^{\text{mol}}} P^\circ \left(K_5 \left(T_{\text{A}\to\text{P}}^{\text{Wm}} \right) \right)^{\!\!1/2} \tag{A.14) or (III.4}$$

$$P_{\text{H}_2\text{O}}^{\text{WR}_6} = 2 \left(\frac{M_{\text{SiO}} D_{\text{SiO}}^{\text{mol}}}{M_{\text{O}} D_{\text{H}_2\text{O}}^{\text{mol}}} \right)^{\!\!1/2} P_{\text{H}_2}^{1/2} P^{\circ\,1/2} \times \left(K_6 \left(T_{\text{P}\to\text{A}}^{\text{Wm}} \right) \right)^{\!\!1/2} \tag{A.15) or (III.5}$$

The active to passive and passive to active transitions temperatures, $T_{\text{A}\to\text{P}}^{\text{Wm}}$ and $T_{\text{P}\to\text{A}}^{\text{Wm}}$, are plotted depending on the partial pressure of water vapor surrounding the sample, $P_{\text{H}_2\text{O}}$, in Figure III.1.

Appendix B.   Matter transport

B.1   Equation of matter transport

In the most general case, the flux of a diluted specie j in a gas mixture can be described using Equation (B.1), where:

$$j_j = j_j^{conv} + j_j^{diff} + j_j^{elec}$$ (B.1)

- j_j^{conv} represents the convective component which accounts for pressure forces acting on the gas mixture.

- j_j^{diff} represents the diffusive component which accounts for matter transport under the effect of a chemical potential gradient in the gas mixture.

- j_j^{elec} represents the electrical component which accounts for the motion of particles under the effect of an electrical field.

Silicon monoxide, hydrogen and helium are uncharged molecules, thus electrical interactions with water do not exist and the last component of Equation (B.1) is removed. The flux gradient in the furnace tube can be written in Equation (B.2).

$$\nabla j_j = \nabla j_j^{conv} + \nabla j_j^{diff}$$
$$u \frac{\nabla P_j}{RT} - \nabla\left(D_j \frac{\nabla P_j}{RT}\right) = V + S + \frac{1}{RT}\frac{\partial P_j}{\partial t}$$ (B.2)

In the left side of Equation (B.2), P_j is the partial pressure of the specie j, u is the velocity vector and D_j is the diffusion coefficient of the molecules. The flux gradient is related to the right side term of Equation (B.2), where:

- V is the amount of specie j produced or consumed by a hypothetic volume reaction.

- S is the amount of specie j produced or consumed by a hypothetic surface reaction.

- $\frac{\partial P_j}{\partial t}$ is the amount of accumulated species.

In Chapter III.3.3, the transport equation has been solved assuming that:

(a) The steady state condition was reached, $\dfrac{\partial P_{\mathrm{j}}}{\partial t} = 0$.

(b) The temperature was homogeneous over a range z_{f}.

(c) The convective component of the flux could be neglected in front of the diffusive one.

(d) Surface reactions occurring on the sample (formation of silicon monoxide) and at the tube ends (condensation of silicon monoxide) were fairly rapid. It was thus emphasized that the concentration of species at the sample surface and at the tube ends could be fixed.

(e) No volume reaction occurred over the range z_{f}.

Equation (B.2) could be thus simplified in Equation (B.3), so called the steady state equation for diffusion.

$$j_{\mathrm{j}} = -D_{\mathrm{j}} \frac{\nabla P_{\mathrm{j}}}{\mathrm{R}T} \qquad\qquad \text{(B.3) or (III.11)}$$

One of the aims of this appendix is to verify the validity of such simplifications by solving Equation (B.2) with Comsol 4.0 and comparing the results with Equation (B.3).

B.2   Equation coupling

The temperature is calculated by coupling Equation (B.2) with the heat transfer Equation (B.4) for fluids, where ρ is the gas density, C_{p}, the gas heat capacity, k the gas thermal conductivity and Q is the heat source or sink.

$$\rho C_{\mathrm{p}} \frac{\partial T}{\partial t} + \rho C_{\mathrm{p}} u \nabla T = \nabla(k \nabla T) + Q \qquad\qquad \text{(B.4)}$$

The gas properties are those of helium. Rather than to set a heat source, the furnace temperature is fixed as a boundary condition on the inner surface of the tube at the sample position over a height of 30 mm which corresponds to the homogeneous temperature range. The ambient temperature is set at the upper and lower ends of the tube.

The convective component of the flux relies on the velocity vector, u, which can be calculated by coupling Equation (B.2) with the Navier-Stokes equations. Actually, when coupling these

equations, the velocity field is found almost constant all over the tube, showing that no boundary layers form at the surface of the sample or on the wall surface of the tube. As a first approximation it thus fair to assume that the velocity field is directly given by the gas flow rate, G, and the tube section, S^{tube}, in Equation (B.5).

$$u = \frac{G}{S^{tube}}$$
(B.5)

B.3 Solution of the equation of matter transport

B.3.1 Geometry

The furnace tube is modeled in a two dimensional axisymmetric geometry, r corresponding to the radial position, z to the height position from the center of the tube, so called the sample position. Matter transport inside the sample is not considered.

B.3.2 Steady state assumption validity

Equation (B.2) is solved along with Equation (B.4) assuming a time dependent solution. The purpose of this study is to check the steady state assumption validity (a) during the reduction of the silica layer. In this approach the assumptions (d) and (e) are assumed valid and the following boundary conditions apply:

- At the surface of the sample, the reduction of the silica layer is assumed to occur and reactions (R$_5$) and (R$_2$) set the partial pressures of silicon monoxide and water.

$$\text{Si}_{(s)} + \text{SiO}_{2(s)} = 2\text{SiO}_{(g)}$$
(R$_5$)

$$P_{\text{SiO}}^{z=0} = P_{\text{SiO}}^{R_5} = P^\circ K_5^{1/2}$$
(B.6)

$$\text{Si}_{(s)} + \text{H}_2\text{O}_{(g)} = \text{SiO}_{(g)} + \text{H}_{2(g)}$$
(R$_2$)

$$P_{\text{H}_2\text{O}}^{z=0} = \frac{P_{\text{SiO}}^{R_5} P_{\text{H}_2}}{P^\circ K_2}$$
(B.7)

- At the z_f position, the partial pressure of silicon monoxide is assumed to be negligible in front of $P_{\text{SiO}}^{z=0}$, as the silicon monoxide condensed in the tube.

- As for the partial pressure of water at the z_f position, the value of 1.8 Pa estimated from the model in section III.3.3 is applied.

As can be seen in Figure B.1, steady state conditions for the partial pressures of water and silicon monoxide are reached in less than 2 s. When referring to the highest heating rate of 40 °C min^{-1} used in our experimental work, this time corresponds to a temperature change of approximately 1 °C, showing that the steady state assumption is fairly valid.
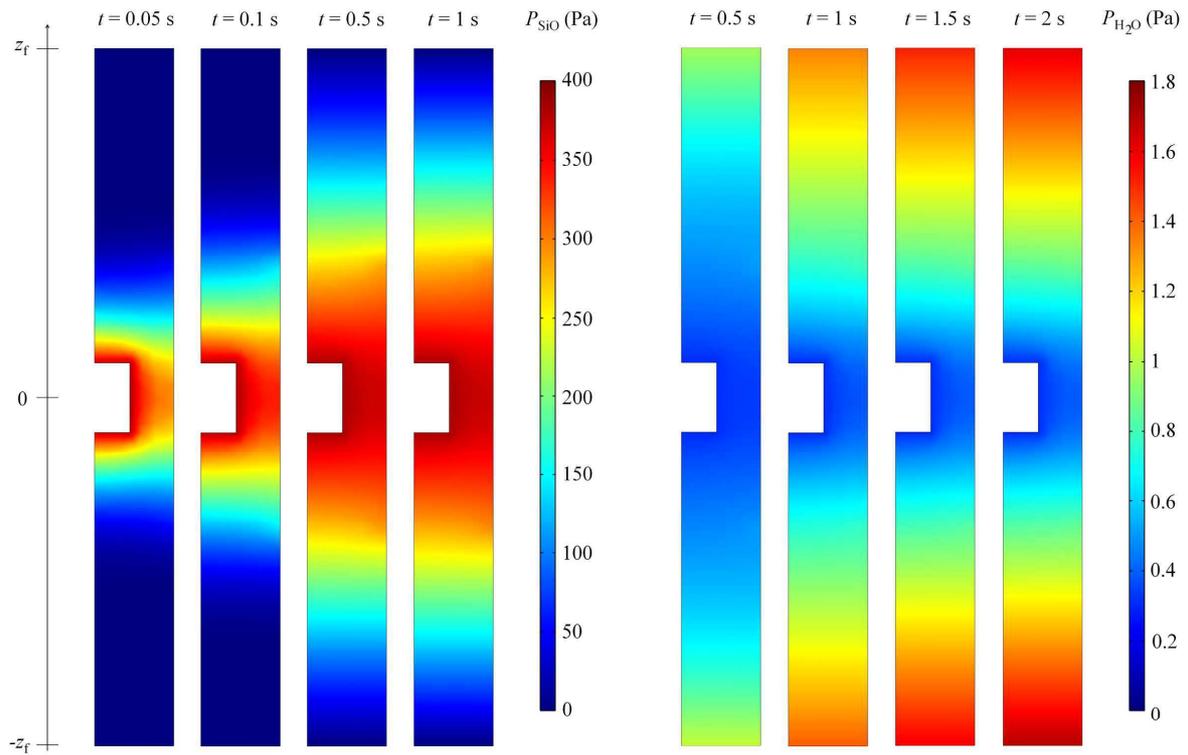
Figure B.1: Time dependent solutions for the partial pressure of silicon monoxide and water in the furnace tube for a furnace temperature of 1350 °C. The steady state conditions are shown to be reached within a few seconds.

B.3.3 Diffusive flux assumption validity

Equations (B.2) and (B.4) are now solved in steady state conditions using the same boundary conditions as in the previous section B.3.2. In Figure B.2, the convective and the diffusive component of the flux are plotted for the silicon monoxide along the height of the tube for a furnace temperature, $T_f = 1350$ °C. The diffusive component is seen as one order of magnitude larger than the convective one, showing that the controlled diffusive flux assumption (c) used for the derivation of the model in section III.3.3 is correct.
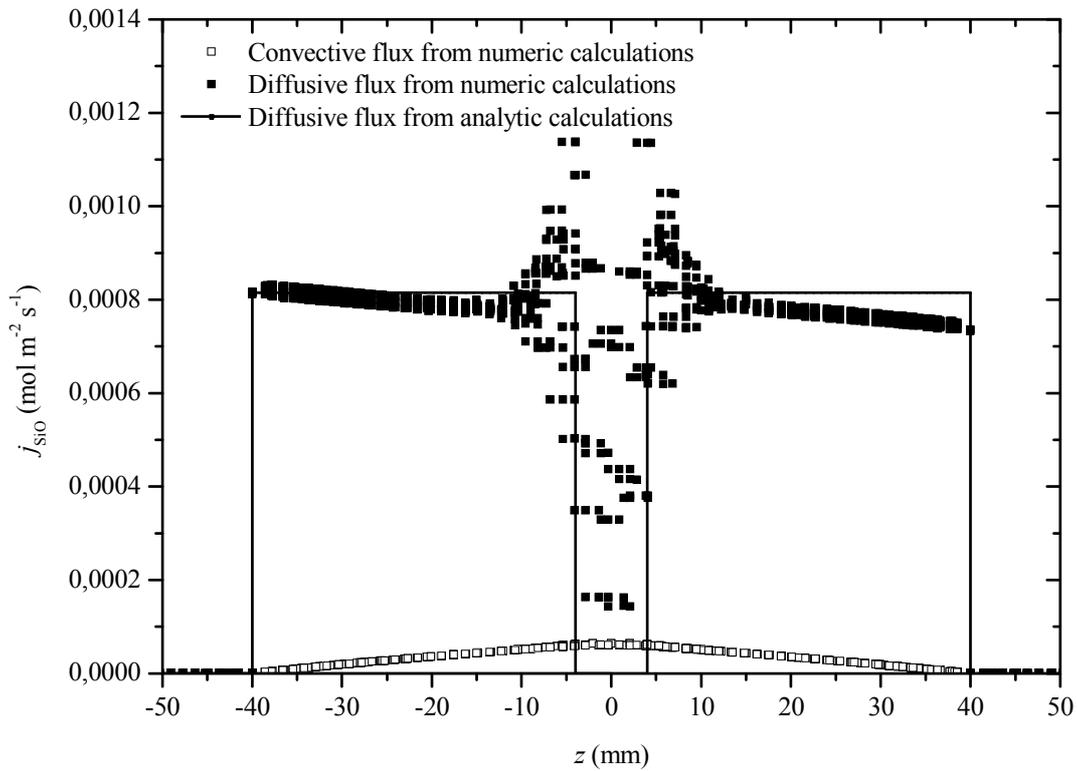
Figure B.2: Numeric calculations of the silicon monoxide flux along the height of the tube from Equations (B.2) and (B.4) for a furnace temperature of 1350 °C. The convective and the diffusive component are drawn separately. These calculations are compared to analytical estimations of the flux from Equation (III.15) directly derived from Equation (B.3) assuming simplifications (a), (b), (c), (d) *and* (e).

B.3.4 Condensation of silicon monoxide

Assumptions (d) and (e) are now considered. The boundary condition at the z_f position assumes that silicon monoxide rapidly condensate when leaving the high temperature furnace area. The experimental observation of a condensate film of silicon and silica (Figure III.4) is a strong evidence of the occurrence of this phenomenon. However, kinetics was not analyzed in Chapter III and is now considered.

Silicon and silica nucleates on the tungsten thermocouple along reaction (R_5). Nucleation kinetics is controlled by the supersaturation, β, of the silicon monoxide gas phase, which corresponds to the ratio of the actual gas phase concentration (P_{SiO}) to the equilibrium concentration ($P_{SiO}^{R_5}$), in Equation (B.8).

$$\beta = \frac{P_{SiO}}{P_{SiO}^{R_5}}$$ (B.8)

Considering the nucleation of one spherical germ of radius g, made of j solid molecules, the change in Gibbs free energy for homogeneous nucleation, *i.e.* spherical nuclei, is given by Equation (B.9), where the first term corresponds to the volume energy and the second one to the surface energy of the nuclei.

$$\Delta G_j^{hom} = \frac{-4\pi g^3}{3\Omega_j} RT \ln(\beta) + 4\pi g^2 \gamma^{SV}$$ (B.9)

The nuclei will be stable and grow once $\frac{\partial}{\partial t}(\Delta G)$ is negative, corresponding to a critical radius, g_c, given by Equation (B.10).

$$g_c = \frac{2\Omega_j \gamma^{SV}}{RT \ln(\beta)}$$ (B.10)

In the case of heterogeneous nucleation, as considered here, the nucleation occurs on a support and the shape of the nuclei is semi-spherical. The critical radius for the heterogeneous nucleation is the same as for homogeneous nucleation. The Gibbs free energy for the nucleation of a semi-spherical germ is given by Equation (B.11), where f is a geometrical factor which depends on the contact angle, ω, of the nucleated material (silicon or silica) with the support (tungsten).

$$\Delta G_j^{het} = f(\omega)\Delta G_j^{hom} = \left(\frac{1}{2} - \frac{3}{4}\cos(\omega) + \frac{1}{4}\cos^3(\omega)\right)\Delta G_j^{hom}$$ (B.11)

The equilibrium contact angle between silicon and tungsten is close to zero, as silicon readily reacts with W to form WSi_2. Thus, f approaches zero and the nucleation is likely to occur even for low supersaturations. The equilibrium contact angle between silica and tungsten is close to 70°, corresponding to a geometrical factor, f, equal to 0.25, showing that the silica nucleation is less favorable than silicon [END99]. Then, silica nucleation most likely controls nucleation kinetics and the rate of silicon monoxide consumption by the volume reaction (R_5), which is finally given by Equation (B.12). A_{SiO} corresponds to the colliding frequency, in mol m^{-3} s^{-1} of silicon monoxide molecules in the furnace tube volume, V^{tube}, at the surface of the tungsten thermocouple, $S^{thermocouple}$, that can be estimated from gas kinetic theory in Equation (B.13), using the frequency of molecular collision of SiO, ζ_{SiO}.

$$V_{SiO} = -A_{SiO} \exp\left(-f(\omega)\frac{\Delta G_{SiO_2}^{hom}(r_c)}{RT}\right) = -A_{SiO} \exp\left(-\frac{4\pi\Omega_{SiO_2}^2 \gamma^{SiO_2 V\,3}}{3(RT\ln(\beta))^2}\right) \qquad \text{(B.12)}$$

$$A_{SiO} = \frac{S^{thermocouple}}{V^{tube}} \zeta_{SiO} \qquad \text{(B.13)}$$

The surface energy of amorphous silica, $\gamma^{SiO_2 V}$, is estimated from wettability measurements of liquid silica at 1720 °C in Equation (B.14) [END99].

$$\gamma^{SiO_2 V}(T) = 0.307 - 0.0002 \times (T - 1720\,°C) \ \text{J m}^{-2} \qquad \text{(B.14)}$$

Equations (B.2) and (B.4) are now solved in steady state conditions assuming new boundary conditions:

- At the surface of the sample, the reduction of the silica layer is still assumed to set the partial pressures of silicon monoxide and water reaction from reactions (R_5) and (R_2).

- The boundary condition for silicon monoxide at the z_f position is no longer considered and is replaced by the volume reaction rate of silicon monoxide derived in Equation (B.13).

- The boundary condition for water at the z_f position is replaced by a constant water flow that is assumed to originate from gas impurities. The concentration of oxygen gas impurities inside the gas cylinder is less than 5 ppm (0.5 Pa) from supplier specifications.

In Figure B.3, the temperature and pressure profiles are plotted for a furnace temperature of 1350 °C. The pressure profile of silicon monoxide and water are compared to the previous profiles calculated in section B.3.3 assuming statements (d) and (e) valid. The profiles of silicon monoxide are almost undifferentiated, showing that the nucleation of silicon and silica occurs rapidly at the z_f position as assumed previously. The comparison of water profiles is less satisfying. Even when assuming that the amount of impurities in the gas cylinder is 2 Pa the water pressure at the z_f position is less than 1.8 Pa as previously measured. The presence of water in the furnace tube certainly originates from other sources such as leaks close to the sample position.

In Figure B.4, the silicon monoxide flux is plotted for several furnace temperatures. It can be seen that the silicon monoxide nucleates always the same position, $z_f \# 40$ mm. At this position, the temperature is 200 to 250 °C lower than the furnace temperature. The silicon monoxide fluxes calculated from Equations (B.2) and (B.4) are closed to those derived from the analytic model in section III.3.3, showing that assumptions (d) and (e) are valid.
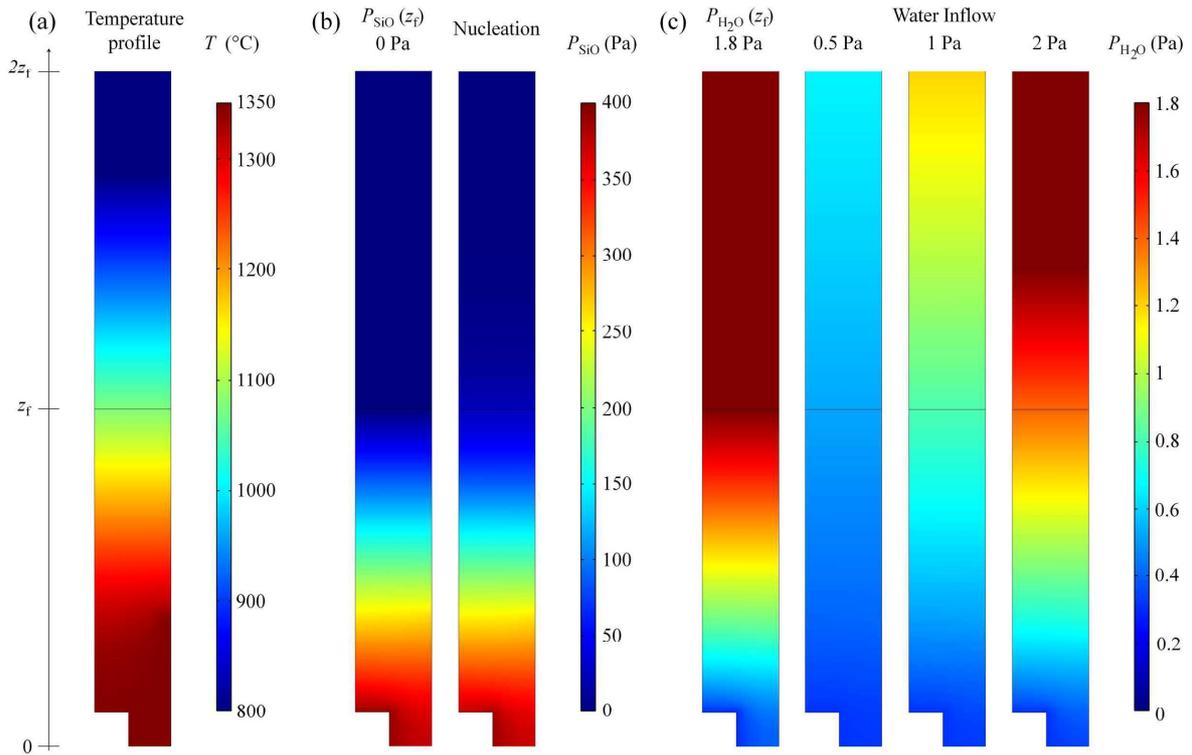
Figure B.3: Numeric calculations of the temperature (a), *silicon monoxide* (b) *and water* (c) *pressure profiles along the height of the tube, from Equations (B.2) and (B.4) for a furnace temperature of 1350 °C.* (b), *the silicon monoxide pressure profile is calculated assuming* $P_{SiO}^{z_f} = 0 \, \text{Pa}$ *and nucleation in the furnace tube.* (c), *the water pressure profile is calculated assuming* $P_{H_2O}^{z_f} = 1.8 \, \text{Pa}$ *and a water supply from impurities in the gas cylinder where,* P_{H_2O} = *0.5, 1 and 2 Pa.*
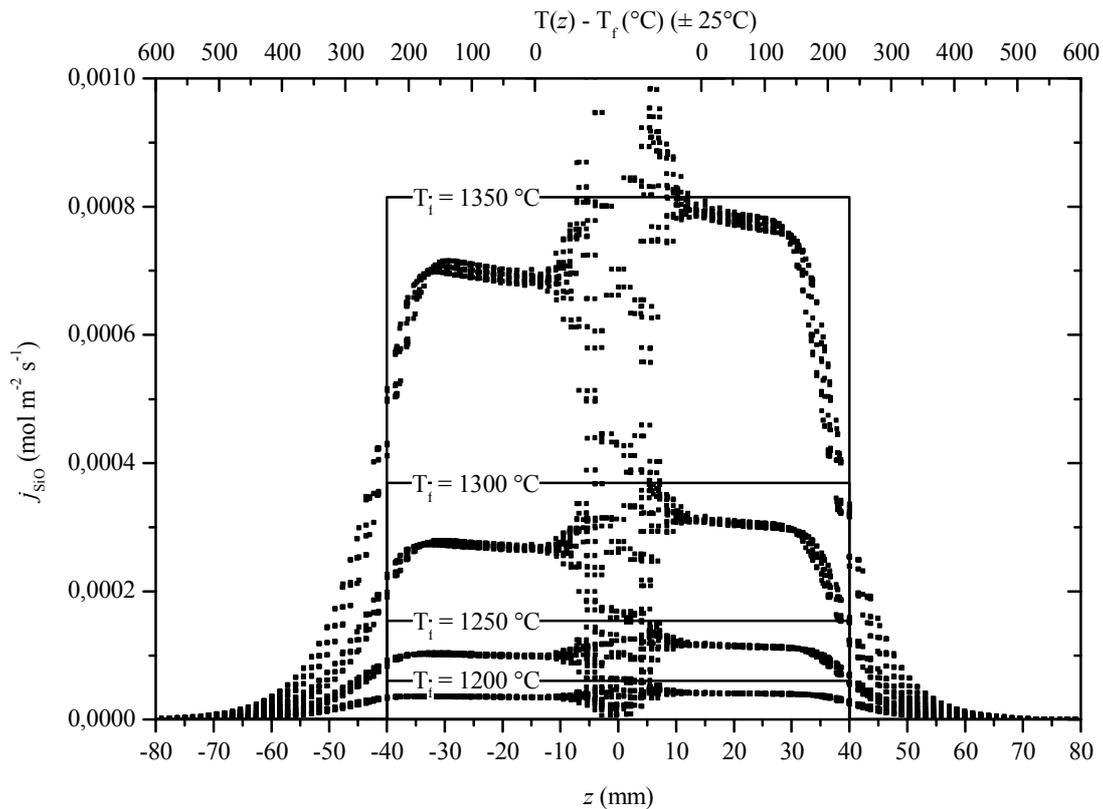
Figure B.4: Dot, numeric calculations of the silicon monoxide flux along the height of the tube from Equations (B.2) and (B.4), assuming nucleation of silicon and silica in the volume of the furnace tube. Line, silicon monoxide flux as derived from the analytic model in Equation (III.15) directly derived from Equation (B.3) and assumptions (a), (b), (c), (d) and (e). Calculations are performed for several furnace temperatures, T_f.

B.4 Estimation of the molecular diffusion coefficients

B.4.1 Diffusion in gases

The mass diffusivity for binary mixtures of non-polar gases is predictable using the gas kinetic theory. Such simplified derivation is useful for a rapid estimation of the diffusion coefficient. Then the semi-empiric approach of Chapman-Enskog is presented as a more accurate method for the estimation of such diffusion coefficient.

Gas kinetic theory

Consider a pure gas composed of rigid, non-attracting spherical molecules j of diameter d_j, and molar mass, M_j. The pressure of gas molecules, P_j, is presumed to be sufficiently small (less than 10 $P°$), that the average distance between molecules is many times larger than their

diameter, d_j. At equilibrium, the mean molecular velocity, υ_j, can be calculated from the Maxwell-Boltzmann statistic in Equation (B.15).

$$\upsilon_j = \sqrt{\frac{8RT}{\pi M_j}} \tag{B.15}$$

The frequency of molecular collision of molecule j in mol per unit area and unit time, ζ_j, on one side surface exposed to the gas is given by Equation (B.16).

$$\zeta_j = \frac{1}{4}\frac{P_j}{RT}\upsilon_j \tag{B.16}$$

The molecular mean free path, λ_j, which can be seen as the distance between two molecular collisions, is given by Equation (B.17), where P corresponds to the total pressure.

$$\lambda_j = \frac{RT}{\sqrt{2}\pi d_j^2 N_A P} \tag{B.17}$$

From the expression of the molecular flux, the molecular diffusion coefficient can be estimated in Equation (B.18).

$$D_j^{mol} = \frac{1}{3}\upsilon_j\lambda_j \tag{B.18}$$

The Equation (B.18) for a gas composed of identical spherical and rigid molecules j becomes Equation (B.19), in which $P = P_j$.

$$D_j^{mol} = \frac{2}{3\pi^{3/2}}\frac{(RT)^{3/2}}{M_j^{1/2}d_j^2 N_A P} \tag{B.19}$$

The calculation for the diffusion of molecules j (or k) in a binary mixture is given by Equation (B.20), in which $P = P_j + P_k$.

$$D_{jk}^{mol} = \frac{2}{3\pi^{3/2}}\frac{(RT)^{3/2}}{N_A P}\left(\frac{1}{2M_j}+\frac{1}{2M_k}\right)^{1/2}\left(\frac{2}{d_j+d_k}\right)^2 \tag{B.20}$$

Chapman-Enskog theory

The Chapman-Enskog theory [BSL01] gives expressions for the transport properties in terms of the intermolecular potential energy, $\varphi_j(d)$, where d is the distance between a pair of molecules undergoing a collision. The intermolecular force acting on the molecules is simply given by the derivative of this potential. This potential is directly calculated from the empirical expression of the Lennard-Jones potential given by Equation (B.21).

$$\varphi_j(d) = 4\varepsilon_j \left[\left(\frac{\sigma_j}{d} \right)^{12} - \left(\frac{\sigma_j}{d} \right)^6 \right] \tag{B.21}$$
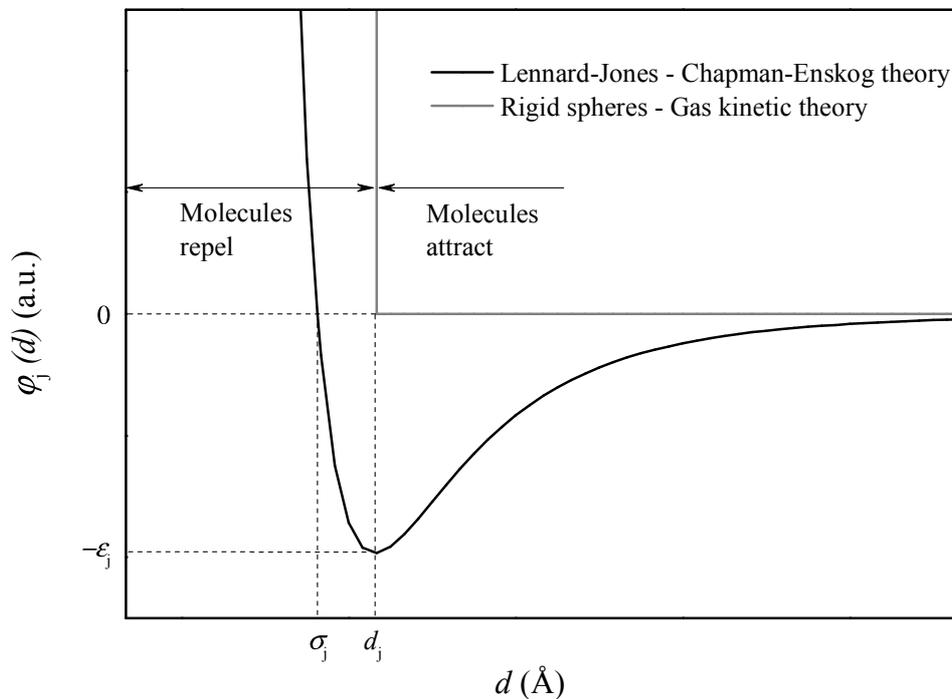

Figure B.5: Potential energy function describing the interaction between spherical molecules according to the gas kinetic theory (grey) and to the Chapman-Enskog theory (black).

In Equation (B.21), σ_j is a characteristic diameter of the molecules, often called the collision diameter, while ε_j is a characteristic energy corresponding to the maximum attraction energy between two molecules. The diffusion coefficient for the molecules j (or k) in a binary mixture is given by Equation (B.22), in which $P = P_j + P_k$ is in Pa, D_j^{mol} is in m^2 s^{-1}, P in Pa, M_j in g mol^{-1}, σ_j in Å and T in K.

$$D_{jk}^{mol} = 0.018583 T^{3/2} \left[\phi(T, \varphi_{jk}) P \right]^{-1} \left(\frac{1}{M_j} + \frac{1}{M_k} \right)^{1/2} \left(\frac{2}{\sigma_j + \sigma_k} \right)^2 \qquad (B.22)$$

ϕ is a dimensionless function of T and φ_{jk}, where σ_{jk} and ε_{jk} are effective Lennard-Jones parameters as defined in Equations (B.23), (B.24) and (B.25).

$$\phi = \frac{1.06036}{\left(\dfrac{k_B T}{\varepsilon_{jk}} \right)^{0.15610}} + \frac{0.193}{\exp\left(0.47635 \dfrac{k_B T}{\varepsilon_{jk}} \right)} + \frac{1.03587}{\exp\left(1.52996 \dfrac{k_B T}{\varepsilon_{jk}} \right)} + \frac{1.76474}{\exp\left(3.89411 \dfrac{k_B T}{\varepsilon_{jk}} \right)} \quad (B.23)$$

$$\sigma_{jk} = \frac{\sigma_j + \sigma_k}{2} \qquad (B.24)$$

$$\varepsilon_{jk} = \sqrt{\varepsilon_j \varepsilon_k} \qquad (B.25)$$

For rigid spheres, $\phi(T, \varphi_{jk})$ would be simply equal to one at all temperatures and a result similar to Equation (B.20), derived from the gas kinetic theory would be obtained.

Molecule	d_j (Å)	ε_j/k_B	σ_j (Å)
SiO	3.8	569	3.37
H_2O	3	809	2.64
He	2.9	102	2.55
H_2	3.2	597	2.83

Table B.1: d_j and Lennard-Jones parameters for the calculation of the molecular diffusion coefficients according to the gas kinetic theory and to the Chapman-Enskog theory respectively [AS62].

Equation (B.22) applies only to binary gas mixtures, but many cases involving more than two components are encountered. Equation (B.26) allows a good estimation of effective molecular diffusion coefficients when the diffusing molecules are present in low concentrations [SS63].

$$D_j^{mol} = \frac{1 - P_j/P}{\sum\limits_{k}^{n} \dfrac{P_k}{P} \dfrac{1}{D_{jk}}} \qquad (B.26)$$

Equation (B.26) was used to estimate the diffusion coefficient of silicon monoxide and water in He-4%H_2 mixtures using the Lennard-Jones parameters given in Table B.1 from literature reference [AS62] in which a large number of molecules are tabulated.

In Figure B.6, the molecular diffusion coefficient of silicon monoxide calculated from the Chapman-Enskog theory can be compared to the one calculated from the gas kinetic theory.
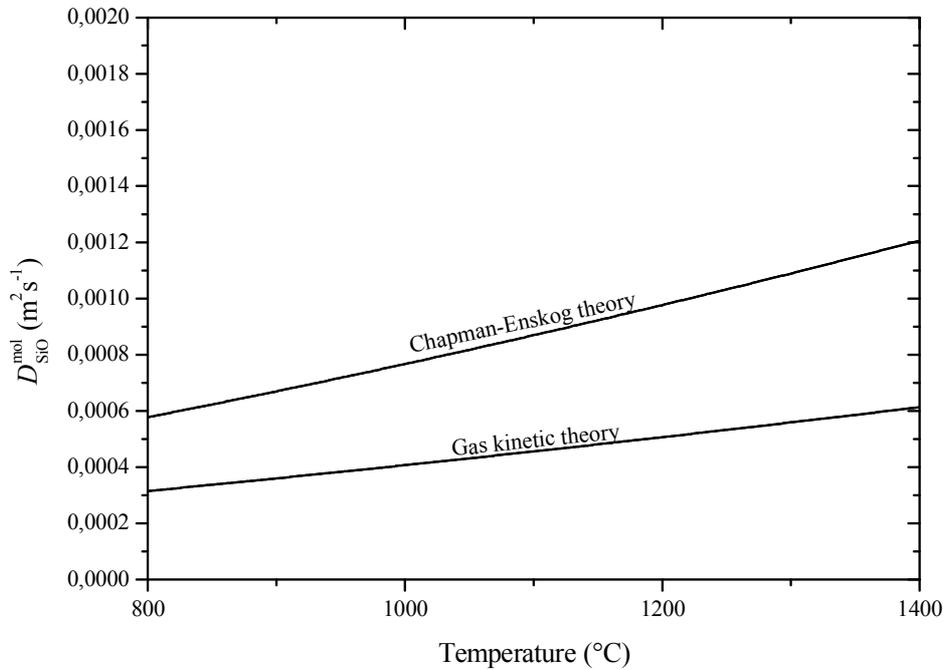

Figure B.6: Calculated molecular silicon monoxide diffusion coefficient into He-4 mol.% H_2 mixtures according to the gas kinetic theory and to the Chapman-Enskog theory.

B.4.2   Diffusion in pores

Pore diffusion may occur by ordinary diffusion, as described in the previous section, or by Knudsen diffusion. The transition between both mechanisms is defined by the mean molecular free path, λ_j.

If the mean molecular free path is lower than the pore size, the process is that of ordinary diffusion, as the number of collisions between molecules is much higher than the number of collisions between the molecules and the pore surface. This is usually the case at relatively high pressure, low temperature or large pore size.

If the mean molecular free path for molecular diffusion is larger than the pore size, the molecules collide with the pore surface much more frequently than each other. This is usually the case at low pressure, high temperature or low pore size and is known as "Knudsen

diffusion". In this case, the molecular diffusion coefficient is replaced by a Knudsen diffusion coefficient, D_j^{Knudsen}, taking into account the collisions with the pore surface. More precisely, Equation (B.18) is used and λ_j is replaced by the pore diameter [SS63].

Actually, the transition between both processes is not clearly defined and an effective diffusion coefficient is used as given in Equation (B.27). The pore fraction, p, as well as the tortuosity, τ, are taken into account for the two diffusion processes. The tortuosity simply accounts for the longer path travelled by the molecule as compared to the straight line in the direction of the diffusion flux.

$$D_j^{\text{eff}} = \frac{p}{\tau}\left(\frac{1}{D_j^{\text{mol}}} + \frac{1}{D_j^{\text{Knudsen}}}\right)^{-1} \tag{B.27}$$

The effect of the pore size on the diffusion coefficient of silicon monoxide is plotted in Figure B.7. The diffusion coefficient is affected by the porosity only for pores less than 10 μm in diameter.
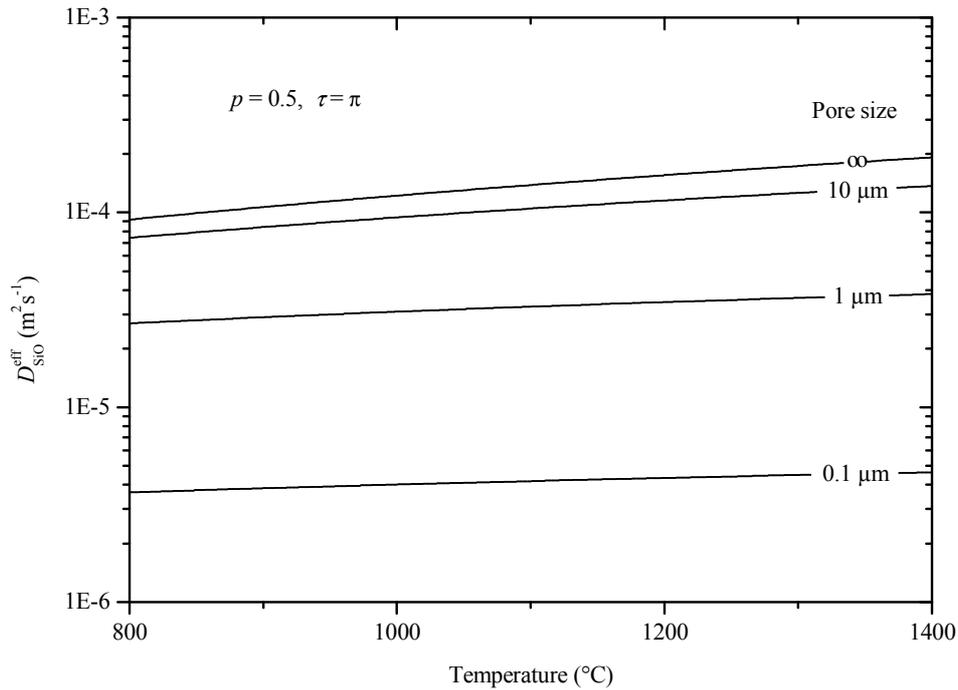

Figure B.7: Calculated effective silicon monoxide diffusion coefficient for a pore fraction of 0.5, a tortuosity of π and different pore sizes. The diffusion coefficient is affected by the collisions with the pore surface only for a pore diameter smaller than 10 μm.

Appendix C.   Initial sintering stage equations

C.1   Geometrical assumptions

The sintering of powder compacts with complex-shaped particles of various sizes cannot be explained in a simple manner. The simplest model for the initial stage consists of two spheres in contact of equal radius a, connected with a neck of radius x (Figure C.1) [Rah95, Kan05, BA93, Ger94, Ger96].
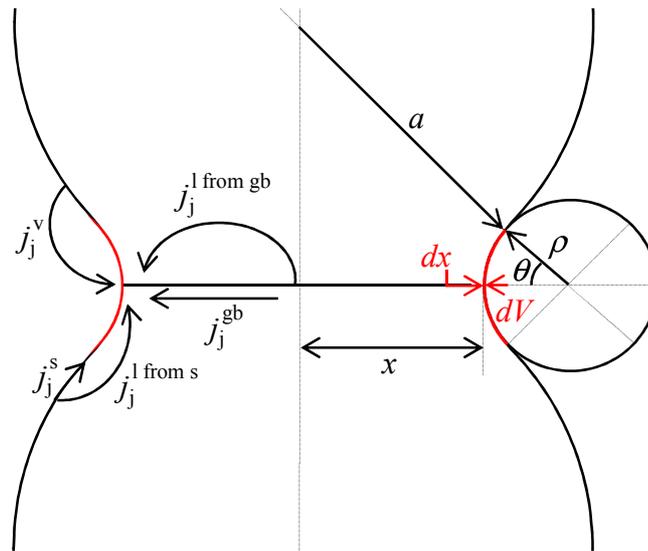

Figure C.1: Two spherical particles model for initial stage sintering. Matter transport is driven by the negative curvature around the neck (in red). Matter transport can occur through five distinct paths. Three of them transport atoms from the surface of the particles and are then non-densifying: vapor transport, j_j^v, surface diffusion, j_j^s, and lattice diffusion from the surface of the particles, $j_j^{l\,from\,s}$. Two of them transport atoms from the grain boundary and are then densifying: grain boundary diffusion, j_j^{gb}, and lattice diffusion from the grain boundary, $j_j^{l\,from\,gb}$.

The negative curvature around the neck region, ρ, induces atoms migration towards this area and increases the neck size. Sintering equations are derived by equaling the neck volume increase, dV, and the volume of atoms coming to the neck, which depends on the flux density of atoms j, j_j, the surface of the flux, A, and the molar volume of the specie, Ω_j, as expressed in Equation (C.1).

$$\frac{dV}{dt} = 4\pi x \rho \theta \frac{dx}{dt} = j_j A \Omega_j \tag{C.1}$$

The atom flux is related to the atom concentration difference in the solid phase (Equation (C.2)) and to the vapor pressure difference in the vapor phase with respect to a planar surface (Equation (C.3)), as shown in Chapter IV.1.2.

$$\frac{C_j^S - C_j^0}{C_j^0} = 2\frac{\gamma^{SV}\Omega_j}{RT}\kappa = 2F_j\kappa \tag{C.2}$$

$$\frac{P_j^V - P_j^0}{P_j^0} = 2\frac{\gamma^{SV}\Omega_j}{RT}\kappa = 2F_j\kappa \tag{C.3}$$

Depending on the diffusion path (Figure IV.3), matter transport either contributes to shrinkage (densification) or not. Sintering mechanisms are then respectively classified in densifying or non-densifying mechanisms. Shrinkage actually corresponds to interpenetration or indentation of the spheres, i, and affects the radius of curvature around the neck, ρ, as can be seen in Figure C.2, from which Equation (C.4) is written. Whatever the sintering mechanism involved, densifying or non-densifying, Equation (C.5) then gives a general expression of the neck curvature radius that is always accurate.
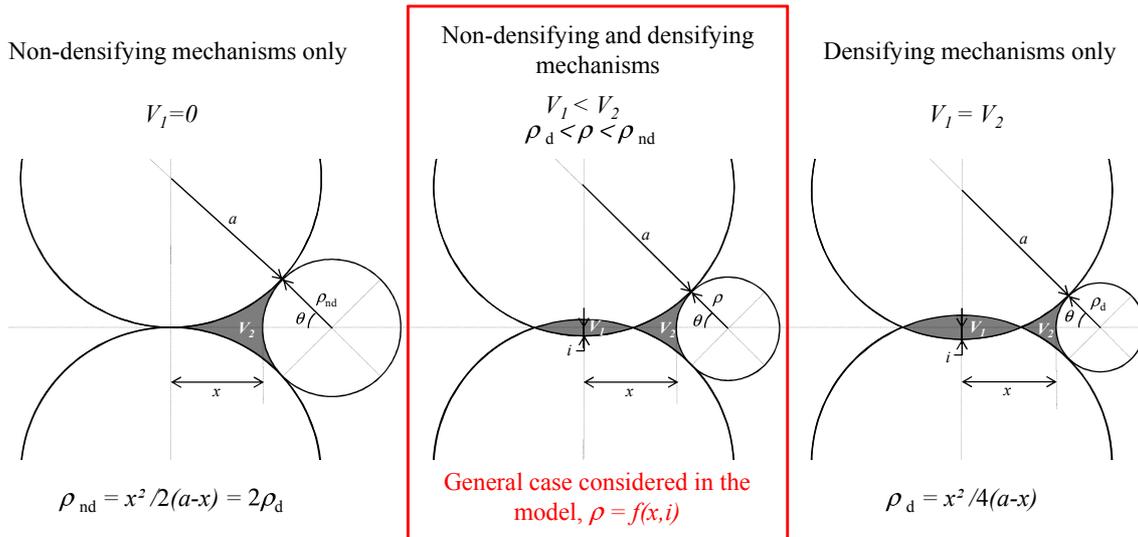

Figure C.2: Model geometry for the first stage of sintering. When only non-densifying mechanisms or only densifying mechanisms operate the radius curvature of the neck is directly related to the neck size. When both types of mechanisms operate simultaneously, the radius curvature of the neck also depends on the shrinkage, h, that depends on the intensity of each mechanism.

$$(\rho + a)^2 = (a - i)^2 + (x + \rho)^2 \tag{C.4}$$

$$\rho = \frac{x^2 - i(2a - i)}{2(a - x)} \tag{C.5}$$

C.2 Sintering mechanism kinetic equations

C.2.1 Non-densifying mechanisms

Non-densifying mechanisms transport matter from the convex surface of the particle to the concave surface around the neck. When the neck size is small, the mean curvature difference, κ_{nd}, is given by Equation (C.6).

$$\kappa_{nd} = \frac{1}{2}\left(\frac{1}{\rho_{nd}} - \frac{1}{x} + \frac{2}{a}\right) \tag{C.6}$$

The geometry (Figure C.2) accounts for the particle size, a, and the growth of the neck which is assumed circular with a radius x. Assuming that there is no shrinkage ($i=0$), the principal radius of curvature ρ_{nd} can be estimated in Equation (C.7) from Equation (C.5).

$$\rho_{nd} = \frac{x^2}{2(a-x)} \tag{C.7}$$

a) Vapor transport

In this mechanism atoms evaporate from the particle surface, diffuse in the vapor phase and condense in the neck region. Two equations are derived depending on the step limiting transport kinetics.

- *Vapor transport limited by condensation*

In this case the condensation of atoms at the particle neck is assumed to limit vapor transport kinetics. The molar flux density of atom at the neck surface, j_j, is estimated from the gas kinetic theory using Equation (C.8), where, M_j is the molar mass of the specie j, α is the sticking coefficient, representing the number of effective collisions.

$$j_j = \alpha \frac{\Delta P_j}{\sqrt{2\pi M_j RT}} \tag{C.8}$$

ΔP_j is the pressure difference between the average partial pressure of specie j in the vapor phase, and the equilibrium pressure at the neck surface. Assuming diffusion is not the limiting step, the average partial pressure is the equilibrium partial pressure, P_j, with particles of radius a. The pressure difference is then related to the curvature difference, κ_{nd}, from Equation (C.3).

$$\Delta P_j = 2 P_j^0 F_j \, \kappa_{nd} \tag{C.9}$$
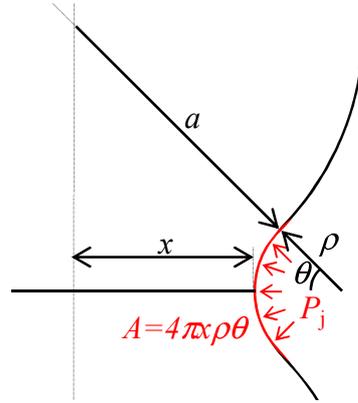
*Figure C.3: Neck surface area, A, for vapor transport limited by condensation.*

The flux surface, A, corresponds to the surface of the neck, $4\pi x \rho \theta$, (Figure C.3) and Equation (C.10) is derived from Equation (C.1).

$$\frac{dx_{nd}^v}{dt} = \alpha \frac{2 P_j^0 F_j \Omega_j}{\sqrt{2\pi M_j \mathrm{R} T}} \kappa_{nd} \tag{C.10}$$

- *Vapor transport limited by diffusion*

In this case the diffusion of atoms from the particle surface to the neck is assumed to limit vapor transport kinetics. The atom flux density, j_j, is estimated in Equation (C.11), where D_j^{mol} corresponds to the molecular diffusion coefficient of the specie j in the gas phase calculated from the semi-empiric approach of Chapman-Enskog [BSL01, AS62] in Appendix B.4.1.

$$j_j = -\frac{D_j^{mol}}{\mathrm{R}T} \nabla P_j \tag{C.11}$$

∇P_j corresponds to the pressure gradient which is assumed to extend over a distance $\theta \rho$ and is calculated from Equation (C.3) where ΔP_j is the difference between the equilibrium partial pressure of specie j near the neck surface and near the convex surface of radius a.

$$\nabla P_j = \frac{\Delta P_j}{\theta \rho_{nd}} = -2 \frac{P_j^0 F_j}{\theta \rho_{nd}} \kappa_{nd} \tag{C.12}$$
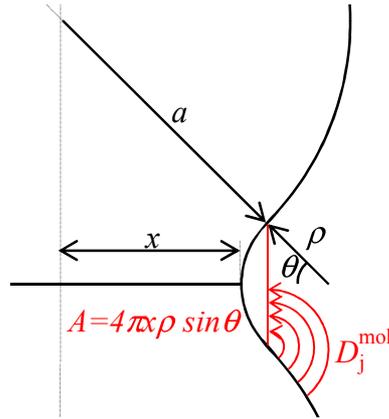
*Figure C.4: Neck surface area, A, for vapor transport limited by diffusion.*

The surface of the flux, A, is assumed to be $4\pi x\rho\sin\theta$ (Figure C.4) and Equation (C.13) is derived from Equation (C.1).

$$\frac{dx_{\text{nd}}^{\text{v}}}{dt} = 2\frac{\sin\theta}{\theta^2}\frac{D_j^{\text{mol}}}{RT}\frac{P_jF_j\,\Omega_j}{\rho_{\text{nd}}}\kappa_{\text{nd}} \tag{C.13}$$

- *Vapor transport limited by condensation or diffusion?*

One way to estimate whether vapor transport is limited by condensation or diffusion is to calculate the ratio of Equations (C.10) and (C.13). This ratio depends on the pressure, P, temperature, T, as well as particle size, a, and neck size, x, as shown in Equation (C.14), where the molecular diffusion coefficient, D_j^{mol}, has been estimated from Equation (B.20) in Appendix B.4.1. M_j corresponds to the molar mass of the diffusing specie j, while M_k corresponds to the molar mass of the main constitutive gas specie, k. Finally, d_j and d_k correspond to the mean molecular diameter of the respective species, j and k.

$$\frac{\left.\dfrac{dx}{dt}\right|_{\text{Evaporation-Condensation}}}{\left.\dfrac{dx}{dt}\right|_{\text{Diffusion}}} = \frac{3\pi\alpha}{4\sqrt{2}}\frac{\theta^2}{\sin\theta}\left(\frac{x^2}{a-x}\right)\frac{PN_A}{RT}\left(M_j\left(\frac{1}{2M_j}+\frac{1}{2M_k}\right)\right)^{-\frac{1}{2}}\left(\frac{d_j+d_k}{2}\right)^2 \tag{C.14}$$

In Figure C.5, the transition between both mechanism is plotted as a function of the pressure, P, initial particle size, a, and neck growth, x/a. The temperature is 1000 °C, the diffusing specie, j, is silicon and the main constitutive gas specie, k, is He. Under atmospheric pressure (0.1 MPa), vapor transport at the beginning of sintering is limited by evaporation-condensation for all particle size, as usually considered in most sintering models. As the pressure is increased or as the neck grows, vapor transport may become diffusion limited

since the molecular diffusion coefficient, D_j^{mol}, and the diffusion length, $\theta\rho_{nd}$, respectively increases.
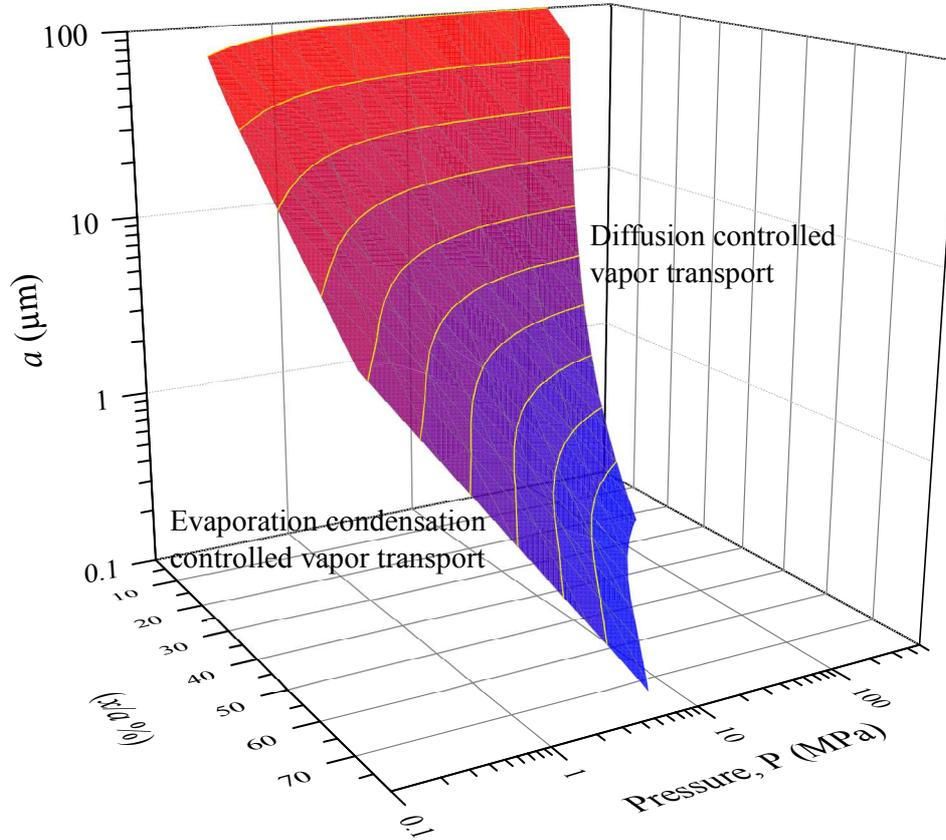
*Figure C.5: Boundary between the evaporation condensation and diffusion controlled domains for vapor transport for a temperature of 1000 °C.*

b)   **Surface diffusion**

This mechanism occurs *via* atom movement at the solid surface from the particle surface to the neck region.

The atom flux density is estimated from Equation (C.15), where D_j^s corresponds to the diffusion coefficient of the specie j.

$$j_j = -D_j^s \nabla C_j \tag{C.15}$$

∇C_j corresponds to the concentration gradient of the specie j which is assumed to extend over a distance $\theta\rho_{nd}$ and is calculated from Equation (C.2).

$$\nabla C_j = \frac{\Delta C_j}{\theta \rho_{nd}} = -2\frac{C_j^0 F_j}{\theta \rho_{nd}}\kappa_{nd} = -2\frac{F_j}{\Omega_j \theta \rho_{nd}}\kappa_{nd} \qquad (C.16)$$
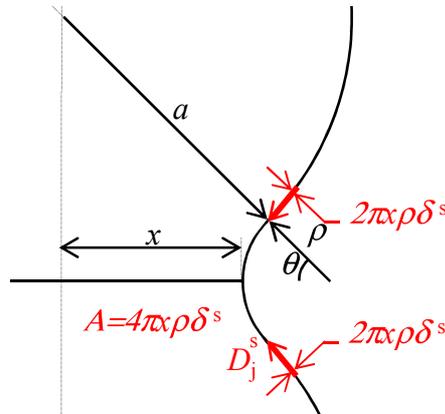
*Figure C.6: Neck surface area, A, for surface diffusion.*

The surface of the flux, A, is $4\pi x \delta^s$, where δ^s corresponds to diffusion thickness at the surface (Figure C.6). The neck growth rate (Equation (C.17)) is deduced from Equation (C.1).

$$\frac{dx_{nd}^s}{dt} = \frac{2}{\theta^2}\frac{D_j^s \delta^s F_j}{\rho_{nd}^2}\kappa_{nd} \qquad (C.17)$$

c)   Lattice diffusion from surface sources

This mechanism transport atoms from the surface of the particle to neck through the volume of the particle.

The atom flux density is estimated from Equation (C.18), where D_j^l corresponds to the lattice diffusion coefficient of the specie j.

$$j_j = -D_j^l \nabla C_j \qquad (C.18)$$

The concentration gradient of the specie j is still given by Equation (C.16). The surface of the flux, A, is assumed to be $4\pi x \rho(1-\cos\theta)$ (Figure C.7) and the neck growth rate (Equation (C.19)) is deduced from Equation (C.1).

$$\frac{dx_{nd}^l}{dt} = 2\frac{1-\cos\theta}{\theta^2}\frac{D_j^l F_j}{\rho_{nd}}\kappa_{nd} \qquad (C.19)$$

$A=$
$4\pi x \rho\ (1-\cos\theta)$

a

$2\pi x\rho(1-\cos\theta)$

x

ρ

θ

$2\pi x\rho(1-\cos\theta)$

D_j^l
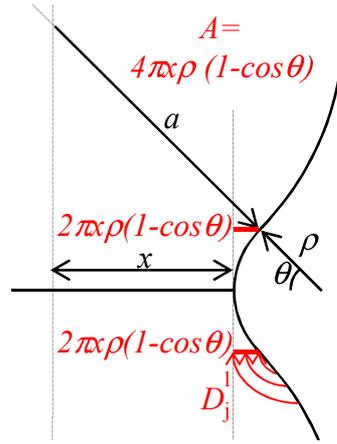
*Figure C.7: Neck surface area, A, for lattice diffusion from the surface of the particle.*

C.2.2 Densifying mechanisms

The grain boundary acts as a source of atoms for densifying mechanisms. The corresponding curvature difference, κ_d, is calculated in Equation (C.20).

$$\kappa_d = \frac{1}{2}\left(\frac{1}{\rho_d} - \frac{1}{x}\right) \tag{C.20}$$

The geometry (Figure C.2) accounts for interpenetration of the spheres (*i.e.*, shrinkage) as well as neck growth. Assuming that densifying mechanisms dominate during the whole sintering process, the volume V_1 equals the volume V_2 and the interpenetration parameter can be approximated to $i \approx x^2/4a$. Then, from Equation (C.5) the principal radius of curvature at the neck, ρ_d, should be twice lower than ρ_{nd} (Equation (C.21)).

$$\rho_d \approx \frac{x^2}{4(a-x)} \tag{C.21}$$

d)   Grain boundary diffusion

According to this mechanism, atoms are driven along the grain boundary to the particle neck.

The atom flux density is estimated from Equation (C.22), where D_j^{gb} corresponds to the diffusion coefficient of the specie j at the grain boundary.

$$j_j = -D_j^{gb}\nabla C_j \tag{C.22}$$
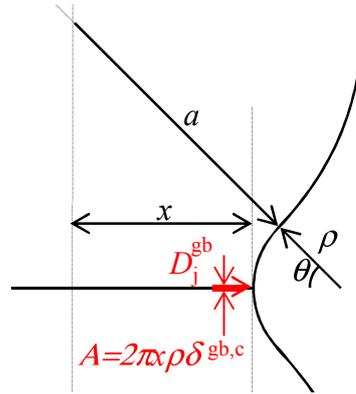
Figure C.8: Neck surface area, A, for grain boundary diffusion.

The concentration gradient can be estimated in a simple way by considering that the vacancy concentration is at equilibrium in the grain boundary, and is related to the curvature at the neck surface, κ_d. This approach gives rise to an underestimated value of the gradient. Actually, from mechanical equilibrium considerations [Joh69], the grain boundary is under compressive stress and the gradient is four times larger than expected. The value of the gradient is modified accordingly assuming that the gradient is homogeneously distributed along the neck, x.

$$\nabla C_j = 4\frac{\Delta C_j}{x} = -8\frac{C_j F_j}{x}\kappa_d = -8\frac{F_j}{\Omega_j x}\kappa_d \tag{C.23}$$

The surface of the flux, A, is $2\pi x \delta^{gb}$, where δ^{gb} corresponds to the grain boundary thickness (Figure C.8). Equation (C.1) can be used to calculate the neck growth rate (Equation (C.24)).

$$\frac{dx_d^{gb}}{dt} = \frac{4}{\theta}\frac{D_j^{gb}\delta^{gb}F_j}{\rho_d x}\kappa_d \tag{C.24}$$

e)   Lattice diffusion from grain boundaries

In this mechanism, atoms are driven from the grain boundary to the particle neck through the volume of the particle.
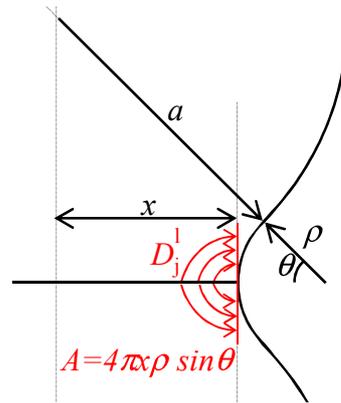
Figure C.9: Neck surface area, A, for lattice diffusion from the grain boundary.

The atom flux is estimated from Equation (C.18).

The concentration gradient is calculated from Equation (C.23).

The surface of the flux, A, is assumed to be $4\pi x\rho \sin\theta$ (Figure C.9) and the neck growth rate (Equation (C.25)) is derived from Equation (C.1).

$$\frac{dx_{\mathrm{d}}^{\mathrm{l}}}{dt} = 8\frac{\sin\theta}{\theta}\frac{D_{\mathrm{j}}^{\mathrm{l}}F_{\mathrm{j}}}{x}\kappa_{\mathrm{d}} \tag{C.25}$$

Lattice diffusion from grain boundaries can be easily compared to lattice diffusion from surface sources, as the mechanism involved for the diffusion is the same. Calculating the ratio of Equations (C.25) and (C.19) gives Equation (C.26) which determines the dominant transport mechanism. This ratio only depends on the geometry, *i.e.*, the neck to particle size ratio, x/a, as shown in Figure C.10.

$$\frac{\left.\dfrac{dx}{dt}\right|_{\text{lattice from grain boundary}}}{\left.\dfrac{dx}{dt}\right|_{\text{lattice from surface}}} = \frac{\theta\sin\theta}{1-\cos\theta}\frac{\rho_{\mathrm{nd}}\kappa_{\mathrm{d}}}{x\kappa_{\mathrm{nd}}} \tag{C.26}$$
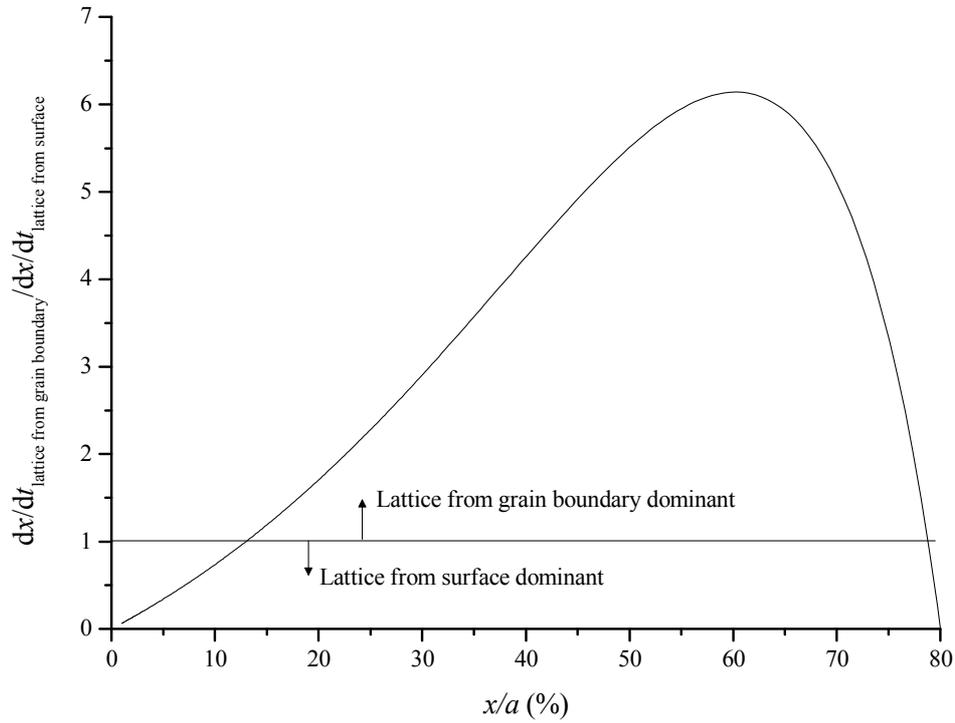
Figure C.10: Ratio of lattice diffusion from grain boundary to lattice diffusion from surface kinetics as a function of the neck to particle size ratio, x/a.

Lattice diffusion from surface is often neglected in sintering models. However, this mechanism always dominates lattice diffusion from grain boundary at the beginning of sintering, *i.e.*, for neck to particle size ratio less than 15 %. Still at the beginning of sintering, surface diffusion or grain boundary diffusion often dominates lattice diffusion.

Etude des mécanismes d'oxydation et de frittage de poudres de silicium en vue d'applications photovoltaïques

La conversion photovoltaïque présente de nombreux avantages. Actuellement, les technologies basées sur l'élaboration de wafers de silicium cristallins dominent le marché, mais sont responsables de pertes de matières importantes, très néfastes au coût de production des cellules. Le défi à relever est donc la réalisation de matériaux bas coûts en silicium par un procédé de métallurgie des poudres. Cependant, le frittage du silicium est dominé par des mécanismes de grossissement de grains qui rendent la densification difficile par frittage naturel. Dans la littérature, l'identification de ces mécanismes est sujette à controverse. En particulier, le rôle de la couche d'oxyde natif (SiO_2) à la surface des particules de silicium reste inexploré. Dans ce manuscrit, l'influence de l'atmosphère sur la réduction de cette couche de silice au cours du frittage est étudiée par analyse thermogravimétrique. Les cinétiques de réduction sont en accord avec un modèle thermochimique prenant en compte, les quantités d'oxygène initialement présentes dans poudre, la pression partielle en espèces oxydantes autour de l'échantillon et l'évolution de la porosité du fritté. Pour la première fois, des données expérimentales permettent de montrer que la couche de silice inhibe le grossissement de grain. Des nouveaux procédés, basés sur un contrôle de l'atmosphère en monoxyde de silicium ($SiO_{(g)}$) autour de l'échantillon, sont alors proposés afin de maitriser la stabilité de cette couche. Bien que la couche d'oxyde retarde les cinétiques de diffusion en volume, son maintien à des températures de 1300 – 1400 °C permet d'améliorer significativement la densification. Dans ces conditions, le comportement au frittage du silicium peut être séparé en deux étapes, clairement mises en évidences par la présence de deux pics de retrait sur les courbes de dilatométrie. Ce résultat est inhabituel compte tenu de l'aspect monophasé du matériau étudié. Cependant, il peut être expliqué à l'aide d'un modèle cinétique de frittage, basé sur des simplifications géométriques en accord avec l'évolution microstructurale du matériau.

Mots clés : Photovoltaïque, Silicium, Silice, Frittage, Oxydation, Microstructure, Cinétiques, Diagrammes TPS, Procédés, Thermogravimétrie, Dilatométrie.

Investigation of Oxidation and Sintering mechanisms of Silicon powders for photovoltaic applications

Photovoltaic conversion is a promising energy resource. Bulk crystalline silicon technologies currently dominate the market but suffer from high material losses that are highly detrimental to solar cell production costs. The challenge is then the elaboration of low cost silicon materials through a powder metallurgy route. However, silicon sintering is dominated by grain coarsening mechanisms that preclude densification. Identification of these mechanisms is controversial in the literature. Especially, the role of the native oxide layer (SiO_2) at the powder particle surfaces has remained unexplored yet. In this manuscript, the influence of the atmosphere on the reduction of this silica layer is studied using thermogravimetric analysis. Reduction kinetics is consistent with a thermochemical model taking into account the powder oxygen content, the partial pressure of oxidizing species and the pore morphology of the sintered material. For the first time, experimental evidences support the idea that the silica layer inhibits grain coarsening. New sintering processes, involving a control of the silicon monoxide atmosphere ($SiO_{(g)}$) surrounding the sample are then proposed and investigated in order to monitor the stability of this layer. Stabilization of the silica layer at temperatures as high as 1300 – 1400 °C is shown to enhance densification although it retards lattice diffusion kinetics. In these conditions, the sintering behavior can be divided into two sequential stages marked by two shrinkage peaks on the dilatometric curves. This result is unusual for the sintering of single-phase materials. However, it can be explained with help of a kinetic model using appropriate geometrical simplifications and observations of the sample microstructures.

Keywords: Photovoltaic, Silicon, Silica, Sintering, Oxidation, Microstructure, Kinetics, TPS Diagrams, Processes, Thermogravimetry, Dilatometry.